To the Graduate Council:

I am submitting herewith a dissertation written by Rejanah Vernice Steward entitled "A Lifetime-Prediction Approach to Understanding Corrosion: The Corrosion-Fatigue and the Corrosion Behavior of a Nickel-Based Superalloy and a Nanocrystalline Alloy." I have examined the final electronic copy of this dissertation for form and content and recommend that it be accepted in partial fulfillment of the requirements for the degree of Doctor of Philosophy, with a major in Materials Science and Engineering.

Peter K. Liaw
Major Professor

We have read this dissertation
and recommend its acceptance:

David Joy

Charles Feigerle

Claudia Rawn

Accepted for the Council:

Anne Mayhew
Vice Chancellor and Dean of
Graduate Studies

(Original signatures are on file with official student records.)

A Lifetime-Prediction Approach to Understanding Corrosion: The Corrosion-Fatigue and Corrosion Behavior of a Nickel-Based Superalloy and a Nanocrystalline Alloy

A Dissertation Presented
For the
Doctor of Philosophy
Degree
The University of Tennessee, Knoxville

Rejanah Vernice Steward
December 2006

Copyright ® 2006 by Rejanah V. Steward
All rights reserved.

ACKNOWLEDGEMENTS

First, the author would like to thank her Creator, Savior, and Lord – Jesus Christ, for imparting her with a zeal for mathematical and scientific concepts and a strong propensity for art. Secondly, the author acknowledges her parents, Mr. and Mrs. Harry and Yvonne Steward of Alcorn State University, Alcorn State, MS, for their wise counsel, strong upbringing, and ongoing love and support. Special family acknowledgements are extended to the author's siblings, Mr. Daryl Steward, a Head Football Coach and Health Instructor of Lexington, MS; Ms. Nacole Steward, a 10th grade English Instructor of Jackson, MS; a great-aunt, Evangelist Anna Crawford of Amory, MS; three especially caring aunts, Mrs. Artricia Matthews of Pasadena, MD; Ms. Jeanette Ramsey of Detroit, MI; and Ms. Sophia Steward of Carson, CA. Other relatives who have been supportive during this endeavor include: Mrs. Ora Dean Caldwell, Mrs. Joe Ann Guillory, Mrs. Sharon Jefferson, Mrs. Earlean Jones, Mrs. Annell Potts, Mrs. Debra Sykes, Ms. Jackie Steward, Mr. Carl Marshall, Mr. Clifford Marshall, Mr. Stephen Steward, Mr. Lee Steward, Mr. Kenneth Steward, Mr. Rufus Steward, Mr. Reginald Steward, and a host of cousins too numerous to list.

Over the course of years, many friends, mentors, and colleagues have played an integral part in helping the author reach this milestone. Of her many comrades, Attorney Tonya Boga, Attorney and Counsleor of Law, Marietta, GA, has always been a God-sent friend and sister in the Lord. Special thanks to Attorney Boga for her constant petitions and supplications on behalf of the author unto the Lord. The best is yet to come concerning God's plan for our careers, families, and other divine appointments. Thanks are also extended to Mrs. Emayet Spencer and Ms. Glynis Hopskins-Peters for their

many prayers, dinners, and loving care of the author during her stay in Knoxville. Thanks are due to many sisters and brothers in Christ who include: Rev. and Sis. Tommie Mims and the Mt. Zion Baptist Church of Oak Ridge, TN, the members of New Covenant Baptist Church, Rev. and Sis. James Brown and family, Mr. and Mrs. Harold Conner, Mrs. Ruth Graham, Rev. and Sis. A. Gwathney and family, Sis. Frances Strickland and family, Rev. and Sis. N. Nevels and family, Dea. and Sis. A. Smith and family, Dr. Edith Smith-Cheek Williams and family, Mr. and Mrs. M. Walker and family, Ms. Tammy McCoy, Mrs. Daryce Love, Mrs. Myrtle Robinson, Dr. Eddie Moore, Mrs. Glorious Brooks, Ms. Philandra Dorsette, Mrs. Joyce Echols, Ms. Kristie Tillery, Ms. Jowana Dunlap, Ms. Sonia Roberts and a little one and two big ones – Jaonia Settles (little one), E. J. Roberts, and Destiny Kirkland.

Additionally, four special mentors are worthy of many thanks for scholarly directions: Dr. George Adebiyi, Dr. Lesia Crumpton-Young, Dr. Clara Young, and Dr. Marcus Shute. Two very special individuals, Drs. Joe and Linda Horton, affectionately referred to as the author's surrogate parents in the field of Materials Science and Engineering, have earned the right as distinguished mentors in that they have gone beyond the call of duty in providing academic direction, advice, and continuous active support in the author's research endeavors. The author cannot express her gratitude for their presence and involvement in her life.

Lastly, but certainly not least, the author would like to thank her advisors, Dr. Peter K. Liaw and the late Dr. Raymond A. Buchanan for their guidance and intellectual discussions while completing her Ph.D. studies in the field of corrosion-fatigue and failure analyses at the University of Tennessee-Knoxville. The author is extremely

grateful to Dr. Peter Liaw for his patience and kindness shown toward her in such a challenging season of her life. She will always be grateful to Dr. Liaw for embracing her unique style and expressive character. Moreover, the author is appreciative to her committee members and other supportive faculty for their fruitful discussions. These individuals include: Dr. David Joy, Dr. Charles Fiergerle, Dr. Charlie Brooks, Dr. Claudia Rawn, Dr. Yangfei Gao, Dr. Denise Jackson, Dr. Roberto Benson, Dr. John Dunlap, and Dr. Tom Meek. The author is extremely grateful to Dr. Sabrina Meck and Dr. Dwaine Klarstrom of Haynes International for kindly supplying the materials for this research. Several colleagues and supporters who have been instrumental in more ways than one include: Dr. Tarik Saleh, Mr. Robert McDaniels, Mr. Gongyao Wang, Mr. Haden Janda, Mr. Kyle Gwathney, Ms. Brandice Green, Mr. Mike Benson, Mr. Ervin Huang, Dr. Gouijang Fan, Dr. Bing Yang, Mr. Greg Jones, Ms. Carol Winn, Ms. Roberta Campbell, Mrs. Carla Lawrence, Mrs. Sandy Maples, Mr. Doug Fielden, Mr. Dan Hackworth, Mr. Larry Smith, Mr. Stephen Stiner, Mr. Mike Neal, Mr. Frank Holiway, Mr. Randy Stooksbury, Dr. Mike Brady, Dr. Mike Miller, Mr. Jackie Mayotte, Mr. Tom Greer, Mr. Cecil Carmichael, Dr. Stan David, Dr. C. T. Liu, Mr. Larry Walker, the UT Chemical Engineering Department, and the Materials Science and Technology, MS&T, Division, formerly known as the Metals and Ceramics, M & C, Division, of the Oak Ridge National Laboratory.

ABSTRACT

Lifetime-prediction models are useful for simulating a material's in-service behavior or outcome. Perhaps the greatest advantage of these models is the ability to use the predicted results to help optimize engineering designs and reduce costs. The Hastelloy® C-2000® superalloy is a single-phase material and face-centered cubic in structure at all temperatures. The C-2000® alloy is a commercially designed alloy manufactured to function in both reducing and oxidizing solutions. C-2000® is used as a fabrication material for heat exchangers, piping for chemical refineries, and storage repositories. The corrosion properties of C-2000® are excellent, and the ductility and fatigue properties are good. In this study, C-2000® is used to verify the theoretical basis of an electrochemical-micromechanical crack-initiation corrosion-fatigue model for materials under passive electrochemical conditions. The results from electrochemical and mechanical experiments, along with the findings from the conventional electron microscopy and a laser interferometer will be presented.

A nanocrystalline Ni-18 weight percent (wt.%) Fe alloy is examined to investigate its electrochemical behavior in a 3.5 wt.% NaCl solution. Three Ni-18 wt.% Fe samples were annealed at 400ºC for 3, 8, and 24 hours (hrs.) to study the effects of grain sizes on the electrochemical properties of bulk Ni-18 wt.% Fe. The electrochemical results from the annealed samples are compared with those measured for the as-received Ni-18 wt.% Fe material consisting of an average grain size of 23 nanometers (nm). The samples annealed for times longer than 8 hrs. appear to have undergone an abnormal grain growth, where nanometer and micrometer (μm) grain sizes are present. Unlike the electrochemical results for the as-received material, the annealed nanocrystalline

materials appear to be susceptible to localized corrosion. Consequently, these larger grains within the nanoncrystalline-grain matrix are preferentially attacked during electrochemical corrosion. Of the four materials studied, the as-received nanocrystalline alloy possesses the best corrosion properties, and the nanocrystalline material coarsened to an average grain size of 23 μm has the poorest electrochemical properties.

TABLE OF CONTENTS

PART I: LITERATURE REVIEW 1

1.0 OVERVIEW 2

2.0 INTELLECTUAL MERITS 4

3.0 BROADER IMPACTS 6

4.0 RESEARCH APPROACH 8

4.1 Theoretical Approach 8

4.2 Design Approach 8

4.3 Advantages of Factorial Design 9

4.4 Experimental Facilities and Setups 11

4.4.1 Cyclic-Polarization Experiments 12

4.4.2 Surface Finish and Geometrical Constraints 13

4.4.3 Electropolishing 14

4.4.4 Investigative Tools 15

4.4.4.1 Weaker Material Interactions Tools 15

4.4.4.2 Stronger Material Interactions Tools 16

4.4.5 Crack-Initiation Tools 17

4.4.5.1 Potential Drop 17

4.4.5.2 Acoustic Emission 18

4.4.5.3 Replica Technique 18

4.4.5.4 Thermography 18

5.0 SUMMARY 20

6.0 RESEARCH BACKGROUND 21

6.1 Superalloys 21

6.1.1 Emergence of Superalloys and Attributes 21
6.1.2 Synopsis of Investigate Material 21
6.1.3 Corrosion of Nickel Superalloys 22
6.2 Corrosion 24
6.2.1 Anodic and Cathodic Reactions for Corrosion 24
6.3 Mechanically-Induced Deformation 26
6.3.1 Fatigue-Crack Initiation and Propagation 26
6.3.2 Damage Mechanisms 27
6.3.2.1 Persistent Slip Bands 29
6.4 Environmentally-Enhanced Deformation 30
6.4.1 Stress-Corrosion Cracking (SCC) 30
6.4.2 Corrosion Fatigue or Cyclic-Loading Influences 31
6.4.2.1 Variable Effects 34
6.5 Corrosion-Fatigue 35
6.5.1 Corrosion-Fatigue Modeling 35
7.0 CONCLUSION 38
REFERENCES 39
APPENDICES 50
APPENDIX A 51
APPENDIX B 55
PART II: IN-SITU ELECTROCHEMICAL INVESTIGATIONS OF A NICKEL-BASED ALLOY SUBJECTED TO FATIGUE 78
1.0 INTRODUCTION 79
2.0 EXPERIMENTAL SETUP 81
2.1 Metallographic Preparations and Electrochemical Experiments 81

2.2 Electrochemical Cell 81
2.3 Mechanical Scratch Tests 82
2.4 Corrosion-Fatigue Experiments and Surface Preparation 83
2.5 Characterization 84
3.0 RESULTS 85
4.0 DISCUSSION 91
5.0 CONCLUSION 99
REFERENCES 100
APPENDICES 103
APPENDIX A 104
APPENDIX B 106
PART III. VALIDATION OF AN ELECTROCHEMICAL MODEL FOR A PASSIVATING NICKEL ALLOY 122
1.0 INTRODUCTION 123
2.0 EXPERIMENTAL PROCEDURE 125
2.1 Corrosion-Fatigue Experiments and Surface Preparation 125
3.0 BACKGROUND ON C2000 127
4.0 FORMULATION OF CORROSION-FATIGUE CRACK-INITIATION MODEL 128
4.1 Mueller's Model Approach 128
4.2 Daeubler's Model Approach 128
4.3 Chan's Model Approach 130
5.0 REFINED MODEL APPROACH 132
6.0 DISCUSSION 135
7.0 CONCLUSION 138

RFERENCES 139

APPENDICES 142

APPENDIX A 143

APPENDIX B 146

PART IV. PITTING OF A BULK NI-18 WT.% FE NANOCRYSTALLINE ALLOY 152

1.0 INTRODUCTION 153

2.0 EXPERIMENTAL PROCEDURE 155

2.1 Specimen Preparation 155

2.2 Optical Microscopy 155

2.3 X-Ray Diffraction 155

2.4 Scanning-Electron Microscopy 155

2.5 Transmission-Electron Microscopy 156

2.6 Electrochemical Experiments 156

2.7 Atom-Probe Tomography 156

3.0 RESULTS 158

3.1 Optical Microscopy 158

3.2 Transmission-Electron Microscopy 158

3.3 X-Ray Diffraction 158

3.4 Electrochemical Experiments 158

3.5 Atom-Probe Tomography 161

4.0 DISCUSSION 162

4.1 Pit Initiation 162

4.2 Pit Propagation 162

5.0 CONCLUSION 166

REFERENCES 167
APPENDICIES 171
APPENDIX A 172
APPENDIX B 174
DISSERTATION APPENDICES 188
APPENDIX A 189
APPENDIX B 219
VITA 230

LIST OF TABLES

Part I

Table 1. Typical Roughness Values for Various Materials 52

Table 2. Nominal Composition of Haynes C2000 52

Table 3. Chemical Composition of Various Corrosion-Resistant Nickel Alloys 53

Table 4. Cyclic Polarization Electrochemical Parameters for Various Corrosion-Resistant Nickel Alloys 53

Table 5. Common ASTM Standards Related to Fatigue 54

Part II Tables

Table 1. Chloride Content for C2000 in 3.5 wt.% NaCl 105

Table 2. Corrosion-Fatigue Data for C2000 in 3.5 wt.% NaCl 105

Part III Tables

Table 1. Parameter Descriptions 144

Table 2. Values Used in the Calclulation of the Present Model 145

Part IV Tables

Table 1. Electrochemical Data for Nickel and Nickel-Based Materials . 173

LIST OF FIGURES
Part I

FIGURE 1. Fatigue Pie Chart: a) Distribution of Different Failure Modes in Jet Engines, b) Susceptibility of Different Components to HCF Problems 56

FIGURE 2. Research Tasks Flowchart 58

FIGURE 3. A Depiction of the Logic Process for the Design of Experiments for C2000 59

FIGURE 4 The 2^3 Full Factorial Spreadsheet for C2000 60

FIGURE 5. Typical Representation of Cyclic Anodic Polarization Curve 61

FIGURE 6. The Fatigue Properties of Materials for Various Surface Finishes 62

FIGURE 7. Electrochemical Cell and Circuitry Model for Electropolishing C2000 63

FIGURE 8. Unpolished and Polished Images of C2000 Samples 64

FIGURE 9. X-Ray Diffraction Data of FCC C2000..... 65

FIGURE 10. SEM Micrograph of C2000 Grain Morphology 66

FIGURE 11. Effects of Increasing Temperature on Protective Oxide 67

FIGURE 12. Cyclic Polarization Curve for Haynes C2000 Alloy in Deaerated 3.5 wt.% NaCl..... 68

FIGURE 13. Cyclic Anodic Polarization Curve for Haynes C2000 in Concentrated Metal-Ion Solution..... 69

FIGURE 14. A Schematic of Persistent Slip Bands (PSB) 70

FIGURE 15. Different Phases of Fatigue Life and Relevant Factors..... 71

FIGURE 16. Different Regimes of Saturation Stress-Strain 72

FIGURE 17. A Schematic for the Stress-Corrosion Cracking Behavior for Active Corrosion (Region I), Passivity (Region II), and Pitting (Regions III) 73

FIGURE 18. Types of Corrosion-Fatigue: a) Categories of Corrosion-Fatigue for Passivating Materials, b) Type II Embrittlement Postulates for Passivating Materials..... 74

FIGURE 19. Frequency Effects on Corrosion Fatigue..... 76

FIGURE 20. Waveform Effects on Corrosion Fatigue..... 77

Part II Figures

FIGURE 1. Electrochemical-Cell Apparatus for Scratch Tests..... 107

FIGURE 2. Corrosion Cell Interfaced with a MTS Fatigue Machine 108

FIGURE 3. Schematic of Flat Tensile Specimen Geometry 109

FIGURE 4 . S-N Curve for C2000 and a Nickel Alloy Studied by Asphanani 110

FIGURE 5. Potentiodynamic Scratch Test Curve in 3.5 wt.% NaCl 111

FIGURE 6. Cyclic-Anodic-Polarization Corrosion-Fatigue Curve in 3.5 wt.% NaCl at a Frequency of 20 Hz and a Stress Amplitude of 574 MPa..... 112

FIGURE 7. Slip Steps Emerging to the Surface Throughout the Gage Volume for C2000 113

FIGURE 8. Critical Current Range Corresponding to the Critical Potential Range 114

FIGURE 9. Constant Potential of 350 mV against SCE Graph Monitoring Current vs. Time for C2000 114

FIGURE 10. Fracture Morphology and Corresponding EDS Spectrum for Corrosion-Fatigue of C2000 in Air at R = 0.1, f = 20 Hz and σa = 574 MPa..... 115

FIGURE 11. A) Fracture Morphology and Corresponding EDS Spectrum for Corrosion-Fatigue of C2000 in 3.5 wt.% NaCl at R = 0.1, f = 5 Hz, and σa = 574 MPa. B) Fracture Morphology and Corresponding EDS Spectrum for Corrosion-Fatigue of C2000 in 3.5 wt.% NaCl at R = 0.1, f = 1 Hz, and σ_a = 574 MPa 116

FIGURE 12. Chloride Channels at Secondary Crack-Initiation Sites 117

FIGURE 13. Distinctive Fracture-Morphology Regions Associated with Fatigue of C2000 in Air at R = 0.1 and f = 20 Hz 118

FIGURE 14. Distinctive Fracture Regions Washed-Out Due to the Anodic Dissolution After Long-Term Exposure Times (7 Days) to 3.5 wt.% NaCl Before Commencing Corrosion-Fatigue at R = 0.1, f = 20 Hz 119

FIGURE 15. Crack-Initiation Site for C2000 at Slip Bands..... 119

FIGURE 16. Transmission-Electron-Microscopy Image of a Secondary Crack at a Slip Interface..... 120

FIGURE 17. Stahle Model for Crack Propagation in a Corrosive Environment..... 121

Part III Figures

FIGURE 1. Electrochemical Chamber Interfaced with Electrohydraulic Fatigue Testing Machine..... 147

FIGURE 2. Rupture Process: Case (A): The Nucleation of a Crack Due to Dislocation Pile-Up at a Twin or Grain Boundary. Case (B): The Nucleation of a Crack Due to Pile-Up at Precipitates 148

FIGURE 3. Temporal Representation of Fatigue Events: A) Number of Current Transients Recorded Over Time at a High Stress Amplitude of 574 MPa. B) Intermediate Stress Amplitude of 485 MPa. C) And at the Endurance Limit of 384 MPa at a Frequency of 20 Hz..... 149

FIGURE 4. Refinement of Mueller's and Daeubler's Model for Predicting the Lifetime for C2000 150

FIGURE 5. A Cartoon Showing the Various Refinement Effects of Mueller's Model Fit for Predicting the Lifetime for Crack-Initiation in Structural Materials..... 151

Part IV Figures

FIGURE 1. Nanocrystalline Ni-18 wt.%Fe As-Received Material..... 175

FIGURE 2. 3 hrs. Anneal at 400ºC of Nanocrystalline Ni-18 wt.%Fe..... 175

FIGURE 3. 8 hrs. Anneal at 400ºC of Nanocrystalline Ni-18 wt.%Fe..... 176

FIGURE 4. 24 hrs. Anneal at 400ºC of Nanocrystalline Ni-18 wt.%Fe..... 176

FIGURE 5. Nanocrystalline Ni-18 wt.%Fe Transmission Electron Micrograph B) And Grain-Size Distribution..... 177

FIGURE 6. X-Ray Diffraction Results for Ni-18 wt.%Fe Nanocrystalline Samples After 3 hrs., 8 hrs., and 24 hrs. Annealing 178

FIGURE 7. Typical Representation of Cyclic Anodic Polarization Curve .. 179

FIGURE 8. Cyclic Anodic Polarization Curve for Ni-18wt. % Fe Nanocrystalline Sample in 3.5 wt.% NaCl Solution..... 180

FIGURE 9. SEM Micrograph of Mud Cracking in Pit on Ni-18 wt.% Fe Nanocrystalline Surface..... 181

FIGURE 10. Qualitative X-Ray Mapping Data: A) Chloride Concentrations; B) Fe_2O_3 Concentrations; and C) Nickel Concentrations..... 182

FIGURE 11. Magnification of Localized Corrosion in 3.5 wt.% NaCl Solution for Nanocrystalline Ni-18 wt.%Fe Annealed for 24 hrs. at 400ºC at Field of View 1 (FOV 1) 183

FIGURE 12. Magnification of Localized Corrosion in 3.5 wt.% NaCl Solution for Nanocrystalline Ni-18 wt.%Fe Annealed for 24 hrs. at 400º C at FOV 2..... 184

FIGURE 13. Secondary Electron SEM Image of Nanocrystalline Ni-18 wt.%Fe Annealed at 400ºC for 24 hrs. with EDS Profile 185

FIGURE 14. EDS Profiles for the 24-hrs. Annealed NC Material: a) Larger Grain Region. b) Smaller Grain Region 186

FIGURE 15. Atom Probe Reconstruction: a) Ni-Compositional Matrix for 3-hrs. Post Treatment of Ni-18wt.%Fe. b) Ni Compositional Matrix for 24 hrs. Post Treatment of Ni-18wt.% Fe..... 187

Dissertation Appendices Figures
Appendix A

FIGURE 1. Optical Micrograph of the As-Received C2000 in Viewing Direction 1 190

FIGURE 2. Optical Micrograph of the As-Received C2000 in Viewing Direction 2 190

FIGURE 3. Optical Micrograph of the As-Received C2000 in Viewing Direction 3 191

FIGURE 4. SEM Micrograph of the As-Received C2000 at Field of View Field 1 (FOV 1) 192

FIGURE 5. SEM Micrograph of the As-Received C2000 at FOV 2 193

FIGURE 6. SEM Micrograph of the As-Received C2000 at FOV 3 194

FIGURE 7. Grain-Boundary Mobility Region in the As-Received Fabricated C2000 195

FIGURE 8. TE M Micrograph of the As-Received C2000 in FOV 1 196

FIGURE 9. TE M Micrograph of the As-Received C2000 in FOV 2 197

FIGURE 10. TE M Micrograph of the As-Received C2000 in FOV 3 198

FIGURE 11. Higher-Resolution TEM Micrograph of the As-Received C2000 199

FIGURE 12. The Evolution of Dislocations: a) As-Received C2000, b) Less Than 1,000,000 cycles, c) Greater Than 1,000,000 Cycles d) A Secondary Crack Observed After 1,000,000 Cycles 200

FIGURE 13. Crack Propagation of C2000 Fatigued at 574 MPa in 3.5 wt.% NaCl and an R-Ratio of 0.1 201

FIGURE 14. FOV Showing Primary and Secondary Crack-Propagation of C2000 Fatigued at 574 MPa in a 3.5wt.% NaCl Solution and at an R-Ratio of 0.1 202
FIGURE 15. Primary Crack-Propagation of C2000 Fatigued at 574 MPa in a 3.5 wt.% NaCl Solution and at an R-Ratio of 0.1 203
FIGURE 16. Secondary-Crack Propagation of C2000 Fatigued at 574 MPa in a 3.5 wt.% NaCl Solution and at an R-Ratio of 0.1 204
FIGURE 17. Fractographs of C2000 Fatigued at 574 MPa in Air and an R-Ratio of 0.1 205
FIGURE 18. Fractographs of C2000 Fatigued at 425 MPa in Air and an R-Ratio of 0.1 206
FIGURE 19. Fractographs of C2000 Fatigued at 400 MPa in Air and an R-Ratio of 0.1 207
FIGURE 20. Fractographs of C2000 Fatigued at 382 MPa in Air at and an R-Ratio of 0.1 208
FIGURE 21. Interferometer Measurements of C2000 Gage Area Deformed at 574 MPa and an R-Ratio of 0.1 209
FIGURE 22. A Cartoon of the Possible Events that Transpire During Corrosion-Fatigue 210
FIGURE 23. Potential vs. Cycles to Failure for C2000 Subjectd to Fatigue at an R-Ratio of 0.1 211
FIGURE 24. Current vs. Time and Number of Cycles, Nf, for C2000 Subjected to Fatigue at 574 MPa and an R-Ratio of 0.1, While Maintaining a 350 mV Potential 212

FIGURE 25. A Cartoon Showing the Progressive Anodic Dissolution During Corrosion-Fatigue 213
FIGURE 26. The S-Ni and the S-N Curves for C2000 214
FIGURE 27. Daeubler and Mueller's Models Plotted With the Experimental Data 215
FIGURE 28. Top View of the Corrosion Cell Chamber 216
FIGURE 29. A Zoom Image of the Top View of the Corrosion Cell Chamber 217
FIGURE 30. Side View of the Corrosion Cell Chamber 218

Appendix B

FIGURE 1. SEM of the 8 hrs. Anneal at 400ºC of the Nanocrystalline Ni-18wt.%Fe at Field of View 1 (FOV 1) 220
FIGURE 2. SEM of the 8 hrs. Anneal at 400ºC of the Nanocrystalline Ni-18wt.%Fe at FOV2 221
FIGURE 3. SEM of the 8 hrs. Anneal at 400ºC of the Nanocrystalline Ni-18wt.%Fe at FOV 3 222
FIGURE 4. SEM of the 8 hrs. Anneal at 400ºC of the Nanocrystalline Ni-18wt.%Fe at FOV 4 223
FIGURE 5. SEM of the 24 hrs. Anneal at 400ºC of the Nanocrystalline Ni-18wt.%Fe at FOV1 224
FIGURE 6. SEM of the 24 hrs. Anneal at 400ºC of the Nanocrystalline Ni-18wt.%Fe at FOV 2 225
FIGURE 7. SEM of the 24 hrs. Anneal at 400ºC of the Nanocrystalline Ni-18wt.%Fe at FOV 3 226

FIGURE 8. SEM of the 24 hrs. Anneal at 400ºC of the Nanocrystalline Ni-18wt.%Fe at FOV 4 227

FIGURE 9. Magnification of Localized Corrosion in a 3.5wt.% NaCl Solution for the Nanocrystalline Ni-18wt.% Fe Annealed for 24 hrs. at 400ºC at FOV 1 228

FIGURE 10. Magnification of Localized Corrosion in a 3.5wt.% NaCl Solution for the Nanocrystalline Ni-18wt.% Fe Annealed for 24 hrs. at 400ºC at FOV 2 229

Nomenclature

K_{1c}	Fracture Toughness in Plane Strain
K_{1SCC}	Fracture Toughness in Plane Strain under Stress Corrosion Cracking
K_c	Fracture Toughness
υ_c	Frequency
HCF	High-Cycle Fatigue
K_{max}	Maximum Stress-Intensity Factor
PSB	Persistent Slip Band
γ_{pl}	Plastic Strain
SCC	Stress-Corrosion Cracking
SFE	Stacking Fault Energy
K_t	Stress-Concentration Factor
S-N	Stress to Number of Cycles to Failure (Wöhler Diagram)
K	Stress-Intensity Factor
ΔK	Stress-Intensity Range
$\Delta\sigma$	Stress Range
τ_s	Shear Stress
$(da/dt)_f$	Change in Crack Length per Change in Time under Fatigue
$(da/dt)_{sc}$	Change in Crack Length per Change in Time under Stress Corrosion
da/dN	Change in Crack Length per Change in Cycles
I	Current
ρ	Density
F	Faraday's Constant
M	Mass
mA/cm^2	Milliamp per Square Centimeter
mm/cycle	Millimeter/Cycle
MPa	MegaPascal
$MPa\sqrt{m}$	Megapascal Times One-Half Power of a Meter
mV	Millivolt
n	Valence Electrons
V	Volt
ºC	Temperature

Abbreviations

ads	Adsorption
C	Carbon
Cr	Chromium
Cr_3O_2	Chromium Oxide
Cu	Copper
e^-	Electron
Fe	Iron
g	Gas
H	Atomic Hydrogen
H^+	Hydrogen Ion
H_20	Water
M	Metal
$M(OH)_2$	Metal Hydroxide
M^+	Metal Ion
Mn	Manganese
Mo	Molybdenum
NaCl	Sodium Chloride
Ni	Nickel
O_2	Oxygen
OH^-	Hydroxide Ion
UTS	Ultimate Tensile Strength
W	Tungsten
wt.%	Weight Percent
Yield	Yield Strength

PART I

Literature Review

1. Overview

The Haynes C2000® Alloy is a commercially designed material manufactured to function in reducing and oxidizing environments [1]. Its industrial applications have tremendous potentials in automotive, structural, aviation, and storage components. Albeit its good reducing and oxidizing traits in extremely aggressive media are attractive features of its chemistry, changes in the mechanical properties are believed to be insignificant due to its strong propensity to passivate. Compared to stainless steels, C2000® exhibits both comparable tensile and fatigue properties and superior corrosion characteristics.

The objective of this study is to understand the microstructural mechanisms influencing the incipient crack initiation within C2000® subjected to mechanical stresses in air and corrosive solutions. The results from the aforementioned will serve as useful data toward the development of an electrochemical micro-mechanistic (EMM) model. Thus, a thorough characterization of the material is required to accomplish this task. Additionally, a systematic approach to determine the governing mechanisms influencing corrosion fatigue is necessary to design experiments and isolate critical corrosion-fatigue testing conditions. The objectives of this research are addressed within three parts. The first part is entitled "In-situ Electrochemical Investigations of a Nickel-Based Superalloy Subjected to Fatigue," which identifies and discusses the experiments for extracting useful electrochemical parameters. Moreover, the mechanism for the crack initiation and the contribution of the chlorides from the bulk electrolyte are discussed. The second part, "Validation of an Electrochemical Model for a Passivating Nickel Alloy," discusses the modeling considerations for developing a corrosion-fatigue crack-initiation model. A

comparison of two of the best crack-initiation models is presented. A new model developed to correct key parameters necessary to predict the crack-initiation in a structural material is presented and discussed. The third part is entitled, "Pitting of a Bulk Ni-18 weight percent (wt.%)Fe Nanocrystalline Material," which reports the research findings of a nanocrystalline material having a much smaller grain size than C2000. Thus, the data findings are reported for a point of comparison. Also, the inclusion of the experimental findings for nanocrystalline materials provides useful insights into the corrosion behavior and the possibilities of using nanocrystalline alloys as a new material for structural applications. A dissertation appendix is included at the end, which is comprised of useful figures that do not necessarily provide clarity to the written contexts of the dissertation.

2. Intellectual Merits

Attempts to model microstructural characteristics and establish relationships between macroscopic and microscopic behavior require careful experimental data. Modeling heavily relies upon basic physical and mechanical properties that are always material specific. Without circumspection, bias can easily be introduced. Consequently, useful models have to be based upon data obtained in extremely controlled environments. Additionally, models have to incorporate ways to filter out errors introduced due to experimental setups and measurement techniques. Models serve as the best method and most cost-efficient means of predicting or extrapolating the information that is difficult to resolve or monitor due to apparatus limitations. They also aim to provide universal equations and more representative depictions of a material's behavior under a set of in-service conditions.

Over the course of years, advances in technologies have aided the computational and modeling community tremendously in helping them better predict and represent a material's behavior under adverse or in-situ settings. Infrared thermography, atomic-force microscopy, acoustic emission, electrochemical-impedance spectroscopy, and electron microscopy are certainly at the forefront when it comes to microanalyses of materials. In this study, additional advanced instrumentations were used to complement the conventional techniques, such as x-ray photoelectron-spectroscopy, atomic-force microscopy, transmission-electron microscopy (TEM), and scanning-electron microscopy (SEM) with the energy-dispersive spectroscopy (EDS), all of which are available to the researcher through shared facility programs supported by the University of Tennessee at

Knoxville and the Oak Ridge National Laboratory. Partnerships with leading researchers within the governmental and academic arenas enable a more thorough research study for providing solutions to the scientific issues, and the joint collaborations allow the students to develop strong research skills by having access to a gamut of researchers.

3. Broader Impacts

Since nickel has a face-centered-cubic (fcc) structure, the solubility of chromium in nickel is higher than the conventional iron-based, body-centered-cubic (bcc) structure. This trend lends nickel as a promising alloying material for applications demanding superior mechanical and corrosion-resistant properties. The potential for nickel alloys to possess excellent mechanical and corrosion properties deems nickel alloys as very attractive suitors for vessels, piping, pumps, turbine blades, and almost any corrosive environment applications. The majority of nickel-based alloys are used in the aircraft industry, and the greatest concerns are fatigue-related problems. In a review by Cowles [1], fatigue is responsible for the majority of damages in jet-engine components. Figure 1a (All figures and tables are listed in the appendices) shows the effects of the important factors for jet-engine components, and Figure 1b presents the susceptibility of various components to high-cycle fatigue (HCF) and low-cycle fatigue (LCF) problems, and other environmental and external influences.

Nickel, molybdenum, and copper alloys with high chromium contents are excellent candidates for manufacturing piping, valves, containers, and tubing for environments exposed to both reducing and oxidizing solutions. For waste repositories, the waste container has to possess superior corrosion properties, since the long-term exposure to stagnant solutions may give rise to the occurrence of localized corrosion. Additionally, for applications where nickel alloys serve as pressure housings, hydrogen-charging effects of nickel alloys are of interest, since the accumulation of hydrogen gas

can increase lattice strains, which may cause a premature failure similar to brittle fracture, i.e., hydrogen embrittlement.

Thus, the findings of this research possess tremendous industrial impact. Limited corrosion-fatigue research on the crack-initiation behavior in superalloys has been conducted, while none have been reported on the rich Cr and Mo alloy known as C2000®. For this reason, the research on nickel-based superalloys can provide the information that will aid in improving the processing, microstructures, mechanical and chemical properties, and also provide data for refining lifetime-prediction models in order to better understand the scientific issues as they relate to high-cycle corrosion-fatigue characteristics.

4. Research Approach

4.1 Theoretical Approach: The development of a lifetime-prediction model requires the background knowledge of the underlying mechanisms associated with the material under study in both the electrochemical and mechanical environments. The determination of the governing mechanisms in each environment provides the platform for pinpointing key mechanisms for synergistic effects. The development of a suitable electrochemical micro-mechanical lifetime model involves research in three separate tasks to yield pertinent modeling parameters. Task 1 is the isolation of mechanical influences on C2000 when the material is subjected to cyclic stresses. Task 2 is the isolation of electrochemical influences on C2000 while the material is exposed to a 3.5 wt.% NaCl solution and a Cr_2Cl_3 solution. Task 3 is the synergistic investigation of C2000 under fatigue. A schematic delineating the conceptual approach for this research is depicted in Figure 2. Additionally, the examinations of pre-existing models were scrutinized for revamping to develop a feasible electrochemical micro-mechanical (EMM) model. Currently, Dr. M. Dauebler [2] and Dr. Kwai Chan [3] have developed microstructure-based fatigue-crack-initiation models that appear to provide a useful platform for either incorporating an electrochemical component or refining the existing models.

4.2 Design Approach: The Design of Experiment (DOE) technique was used to create a systematic experimental matrix. DOE is useful for understanding synergistic effects, reducing the experimental time, and isolating factors and conditions that most influence the process under study. Additionally, statistical analyses and interpretations of data can be performed in order to determine the path ascent for corrosion-fatigue experiments.

DOE is a useful tool for developing an experimental matrix to determine the research path for analyzing a problem involving many parameters. Comparative experiments allow the researcher to make inferences about the differences in means and randomized designs. Hypothesis testing and confidence intervals are two methods utilized to perform comparative analyses. Several treatments or influences on the data are conditioned by means of several schemes, which may include one-way models, block designs, and factorial designs, to develop experimental setups; while regression analyses and response surfaces are useful for determining the path of ascent for the experiment of interest.

In this investigation, the full factorial method was the choice for analyzing the critical external influences. A 2^3 full factorial experiment (FFE) requires eight permutations for two external influences. Air and 3.5 wt.% NaCl were the two factors controlled in this study. Within each factor, high and low levels were assigned to develop a scheme to monitor the fatigue response, i.e., the number of cycles to failure.

4.3 Advantages of Factorial Designs: The effects of multiple interactions or influences can be determined efficiently using a factorial design. In factorial designs, the fluctuations in levels produce a change in the response. As explained above, influences are given high and low levels. The difference between the average responses at both levels of each factor provides the main effect. Parallel lines imply a lack of interactions between the two influences, and intersecting lines indicate interactions between the two factors. The advantages of a factorial design lie within the statistics, which are heavily influenced by the number of events and data runs. In other words, holding the high level of a factor, X, and varying another factor, Y, between high and low levels, yields two

combinations of X and Y, X1Y1 and X1Y2. If the experimenter holds Y constant at the high level and varies X, the Y1X1 and Y1X2 permutations are observed. Usually, one factor is altered several times, and the responses are recorded. Since a bias is introduced in any experimental setup, average responses are more meaningful, which requires several runs of the data to provide a better representation. Thus, with two factors and four levels, a minimum of six observations are required if two runs are recorded for the three combinations. Planning experiments in this fashion is referred to as a one-factor-at-a-time representation. Factorial designs would consider the additional factor of X2Y2 to evaluate the responses to four observations. This approach clearly reduces the number of replicates and gives a similar representation of the data as in the one-at-a-time method without additional experiments. The disadvantage of this method is introduced when interactions are present. Hence, factorial designs help avoid such conclusions because they provide a better range to examine the data. Figure 3 shows a depiction of the conceptual logic process for the design of experiments regarding the study of C2000 in 3.5 wt.% NaCl.

Eight experiments at various permutations of potential, stress, and frequency are performed in both states, which are air and 3.5 wt.% NaCl. From these experiments, data, such as electrochemical, mechanical property, and time/life results, were extracted and used as input for the lifetime-prediction model. The experimental matrix used as a guideline for conducting fatigue experiments is shown in Figure 4, where the number (1) represents the high-level condition, and the number (-1) represents the low-level condition. The subset table in the upper right of Figure 4 is a legend listing the states, the level assignments, and the experimental values.

4.4 Experimental Facilities and Setups: Electrochemical, fatigue, and corrosion-fatigue experiments were performed at the University of Tennessee-Knoxville. Specimen machining and the necessary apparatus design were completed at the Machine Shop at the University of Tennessee. Mechanical grinding, polishing, and electropolishing were used to obtain optimal surface finishes. The characterization of the material for surface anomalies and defects was examined, using the conventional optical and electron microscopes along with advanced techniques, such as transmission-electron microscopy, x-ray photoelectron spectroscopy, and laser interferometry. Data retrieved from the aforementioned include monitoring the free potential vs. time, the current transients vs. time, and the spatial-temporal evolution of the fatigue damage.

The components of the design of an electrochemical cell include an insulated container capable of supporting the working electrode, which is the material under study, a counter or auxillary electrode to support the cathodic reaction, and a reference electrode to monitor relative potential changes. The final electrochemical assemblage is referred to as the Stew-Field electrochemical cell, which is capable of testing uniaxial and bend specimens. The load frame used is a servohydraulic machine developed by the Materials Testing Systems (MTS). All fatigue experiments will be performed in tension-tension using a pin-joint assembly fixture. The observation of the deformed states has been captured using SEM and TEM. A Princeton Applied Research Potentiostat was interfaced with the electrochemical cell to control the potential while monitoring corrosion, and the data analysis will be performed with the ECorr Software. Electrochemical experiments were designed to observe how pH changes and deaerated solutions affect the corrosion properties of C2000. Scratch tests were performed to monitor the repassivation kinetics,

which could provide insights into the potential corrosion mechanisms operating during fatigue. The optical microscopy, scanning-electron microscopy (SEM), and transmission-electron microscopy (TEM) were employed to probe the microstructure of the as-received and deformed states.

4.4.1 Cyclic-Polarization Experiments: Electrochemical data can be determined via cyclic-polarization experiments. Cyclic-anodic-polarization curves are generated by connecting a sample known as the working electrode, a platinum counter electrode, and a reference electrode in the circuitry to polarize the working electrode toward anodic (positive) or cathodic (negative) potentials. Figure 5 shows the various properties that can be retrieved from cyclic-polarization curves [4]. The free potential or corrosion potential, commonly referred to as E_{corr}, is the natural potential of a material within a given electrolyte at the open-circuit potential. The protective potential is the potential value at which the passivation is maintained. A constant current density maintained over a particular potential range denotes the passive current density of the material. The passivity region on the cyclic-anodic-polarization diagram is an indication of the material's ability to resist dissolution or passive film breakdown within a given electrolyte. The point at which the oxide/hydroxide layer experiences the dissolution is referred to as the pitting potential (E_{pit}). Although the pitting potential is commonly taken as the potential at the onset of pitting, pitting or localized corrosion may actually occur at potential values lower than those manifested on the cyclic-polarization curve. Hence, a more accurate definition of E_{pit} is the potential representing a pit or other form of the localized corrosion of a critical size. The intersection of the passive potential range and the reversed potential marks the protection potential (E_{pp}) of the material. Therefore,

a hysteresis is formed and provides useful information about the amount of material loss due to the localized corrosion phenomenon. In some cases, such as inadvertent scratches or handling, the protection potential does not follow path 2 (Figure 5). There is a possibility that the protection potential can intersect the cathodic (negative) region of the curve. Thus, the protection potential is not in the anodic region.

The degree to which a material has the ability to resist localized corrosion can be determined by evaluating the difference between E_{pit} and E_{corr} and E_{pp} and E_{corr}. A large difference between E_{pit} and E_{pp} in relation to E_{corr} implies a strong resistance to localized corrosion. A set of results following path 3 (Figure 5) implies the material's susceptibility to immediate pitting upon the immersion into the solution, if an inadvertent scratch or nick occurs. Although many materials behave according to the trend depicted in Figure 5, the electrochemical behavior is not limited to the three paths discussed.

Other important parameters, such as the corrosion-current density (i_{corr}), and the passivation-current density are extremely useful. The corrosion current density provides a reasonable estimate of the corrosion-penetration rate (CPR) by means of the following equation.

$$CPR(mpy) = 0.0129\frac{M \cdot icorr}{n\rho} \qquad \textbf{(1)}$$

In the above equation, mpy represents mils per year, M represents the mass, and ρ represents the density. The mols of electrons released are represented by n.

4.4.2 Surface Finish and Geometrical Constraints: The effects of the surface finish on fatigued samples have been studied extensively in the literature [5-8]. Figure 6 shows the effects of surface finishes on the fatigue properties. The development of a micro-

mechanistic understanding is heavily dependent upon observing and monitoring microstructural features, such as extrusions and slip steps. Optimal finishes provide the best data for characterization tools, such as an atomic-force microscope (AFM), to provide the topographic contrast between normally indistinguishable features. Consequently, an optimal surface finish has to be achieved on C2000®, and electropolishing is the best method for obtaining an extremely smooth finish. Table 1 [9] lists some common materials, such as steels and nickel alloys, and surface-roughness values (Ra) associated with mechanical, chemical, and electrochemical polishing preparation methods. As clearly shown from the data listed in Table 1, the electropolished finish provides the optimal surface finish, which corresponds with the lowest Ra value.

4.4.3 Electropolishing: Electropolishing is an electrochemical process, which produces a luster on a metallic surface by removing metal ions. The sample acts as the anode and is connected to the positive terminal of the power supply. As shown in Figure 7, a stainless-steel container serves as the cathode, and a lead wire connects the cathode to the negative terminal of the power supply. The material under study acts as the anode, and a lead is spot-welded to the sample and connected to the positive terminal of the power supply. An electrical circuit is maintained via ionic conduction through the polishing electrolyte. A 4.22 ohms resistor, R1, is added to the circuitry to increase the power source (Vs) to 12.4 V. The parameters Rm, Rs, and Rc, represent the components that make up the total resistance in the circuit, which are the electrical leads, the polishing solution, and the stainless steel container, respectively. The objective is to remove hills and burrs, which become areas of higher current densities, compared to those in valleys.

The removal of hills creates a smooth surface or even terrain to provide a highly reflective surface. In the setup for electropolishing C2000, a circular container houses the electrolyte. The advantage of a circular container is that it provides a radial conductive path for a uniform removal. Corrosion effects are better studied on flat specimens to minimize bias due to roughness. Since crack initiation is of importance to this study, the samples were designed to include a continuous radius to ensure crack initiation in the same proximity and ease microstructural probing with SEM. Additionally, the sample rotation is eliminated and the polishing time is reduced (Figure 7).

The C2000® specimens were electropolished in a 15 volume percent (vol. %) sulfuric acid and 85 vol. % methanol at 10 V for 45 minutes. A liter of the electrolyte is required to submerse a 101.6 mm tensile sample. The results of electropolishing for C2000 are shown in Figure 8.

4.4.4 Investigative Tools: Conventional characterization tools, such as x-rays and electron microscopy, are still two of the most powerful means of gaining insight about a material's structure, constituents, and grain morphology. These characterization tools can be catergorized into two types: weaker interactions and stronger interactions. A short summary of the two types is recorded below.

4.4.4.1 Weaker Material Interactions Tools: X-ray diffraction uses a copper target to produce a monochromatic beam of x-rays as a means of probing samples. A detector is positioned opposite the sample and target, while the sample is rotated to angles of up to 90 degrees to provide a good count average for peak intensities. Both bulk and powder samples are common samples studied using x-ray diffraction. X-ray diffraction operates

on the basis of constructive interferences manifested as the maxima in the intensity for x-ray. Diffraction or constructive interference occurs when the incident waves are in phase, and the diffracted beam is a multiple of the incident wavelength. This condition is referred to as the Bragg condition. The purpose of using x-ray diffraction on C2000 sheets is to verify the structure and texture properties, and to identify the formation of possible second phase particles. Although C2000 is reported as being homogeneous and face-centered-cubic (fcc) at all temperatures, the possibility of second phases is only plausible, if the alloy is not truly homogeneous as reported. In-situ neutron diffraction, although costly, can provide the answer to such questions with less preparation.

4.4.4.2 Stronger Material Interactions Tools: Electron diffraction is another very useful tool for examining materials. Since electrons are charged particles, they interact strongly with metallic materials. For this reason, the information about the material is constrained within the interaction envelope, which has a limited depth. The interaction of several electrons can be detected and used for imaging purposes via a scanning-electron microscope (SEM). Depending on the type of detector device, the SEM can provide both topical and phase variations in the material.

TEM provides the structural information by examining the diffraction pattern, and the nano-scale features, such as dislocations, can be resolved using bright-field or dark-field imaging techniques. However, the preparation is tedious, and the interpretation can present an erroneous picture if the evolution of events is not captured. Unlike x-ray and neutron diffraction, the selected area diffraction with the energy-dispersive spectroscopy (EDS) can be used to isolate key features within the microstructure.

Surface-analysis tools, such x-ray photoelectron spectroscopy (XPS), are useful for understanding the chemistry of the oxide layer and determining the thickness. With XPS, a characteristic energy profile can be determined, which reports the binding energy associated with each core atomic orbital. The information obtained from XPS can be extremely useful for corrosion studies, since the migration of detrimental species, such as chlorides, are of interest. Furthermore, the transportation of the chlorides to copious regions within the oxide depends upon the oxide composition and density, which can also be determined by XPS.

4.4.5 Crack-Initiation Tools: The potential drop, lasers, replica techniques, acoustic emissions, thermography, and SEM are techniques utilized throughout the fatigue and fracture community to detect early crack initiation [10-12]. However, each method must be carefully performed, which can be cumbersome. All require tedious set up and auxillary equipment to monitor crack initiation, with the exception of the SEM and replica technique. Choosing a suitable technique is determined by how early a crack needs to be detected. The short-crack initiation and long-crack initiation must be deciphered, and each technique requires judicious planning and practices to determine cracks smaller than the grain size of most metallic materials. A distinction between artifacts and authentic data becomes the challenge as the detection at lower scales is desired. Hence, a second method is needed to verify the findings using one of the methods introduced. Following is a brief description of the advantages and disadvantages of each method.

4.4.5.1 Potential Drop: The potential-drop method [13] can be conducted using direct current (DC) or alternating current (AC). In both cases, the change in the potential or

potential drop across the crack-tip opening of a compact-tension (CT) specimen is monitored. The difference in the potential at the initial crack tip site is recorded and monitored during the crack-growth period against a calibrated sample.

4.4.5.2 Acoustic Emission: Acoustic emission [14-16] is fairly simple to assemble onto a sample, given that the sample is relatively large compared to the contacting electrodes. To utilize this technique, two transducers are positioned across the gage section of the sample via glue, such as epoxy or another nondestructive polymeric resin. The material's response to acoustic emissions is captured, and the signal is amplified and recorded for data analyses.

4.4.5.3 Replica Technique: The replica technique [17-20] involves a capillary attachment of the polymeric film, acetate, to the fatigued-sample surface using acetone. At particular intervals chosen during the testing, squirts of acetone promote a capillary adhesion of the film to the deformed surface to create a negative film of the specimen. The negative is sputtered with conductive plasma, such as gold or carbon, to view in an SEM. The major challenge of the replica technique is the selection of polymeric films, choosing the optimal sputtering-processing parameters, and keeping the sample in the maximum stress amplitude mode during designated intervals to properly identify and monitor the crack.

4.4.5.4. Thermography: Thermography is a fairly new technique utilized for field engineering and research-related observation. Infrared (IR) wavelength energy released from a sample is detected with the IR camera. The energy is calculated against a calibrated scale and used to convert into a corresponding temperature. Data handling is one of the main issues with thermography; judicious planning is involved in determining

the acquisition time, field of view, and data analysis. Several authors [11, 21-28] have attempted to utilize an IR camera to detect the crack initiation during fatigue.

5. Summary

Corrosion alone presents unique challenges to the researcher. Yet, corrosion fatigue proves to present greater obstacles due to synergistic effects. Corrosion fatigue demands an adequate understanding of the material chemistry, a response to chemical environments and mechanical stresses, and an archive of events necessary to derive models capable of extrapolating solutions outside the span of the controlled research. The understanding of essential phenomena and parameters provides a platform to replace archaic models used to retire aging components, as well as new information useful for material and design optimizations. Nickel-based superalloy research is extremely promising due to superalloys' ability to remain immune to localized corrosion under various environments. Additionally, they possess good mechanical properties. In particular, Haynes C2000® possesses excellent corrosion properties, and the ductility is comparable to that observed for 304 stainless steel. Thus, Haynes C2000® is a promising candidate for lifetime predictions due to the ability of the material to remain a single phase alloy at all temperatures. A single phase alloy will require a micro-mechanistic model with fewer microstructural parameters.

6. Research Background

6.1 Superalloys:

6.1.1 Emergence of Superalloys and Attributes: Traditionally, the usage of iron alloys has dominated the structural commercial industry. However, applications of nickel alloys for a wide variety of service conditions are on the rise [29]. The interest in nickel superalloys emerged during the 1950-1960s. Superalloys, comprising 6 or more elemental additions, possess attractive qualities such as corrosion resistance, ductility, high fatigue strength, resilience, stiffness, durability, wear resistance, and the ability to withstand high temperatures [29, 30]. Additionally, nickel superalloys have recycle potentials. Nickel-based superalloys have mechanical properties competitive to that of stainless steels. They are superior in price when compared to cobalt-based superalloys, and are higher performing compared to iron-based superalloys.

6.1.2 Synopsis of Investigated Material: Haynes C2000® is a single-phased crystalline alloy comprised mostly of nickel, chromium, and molybdenum. The nominal composition of C2000® is listed in Table 2. X-ray diffraction confirms that C2000® is a homogeneous fcc structure (Figure 9). High-resolution imaging reveals a structure that is comprised of annealing twins (Figure 10).

The high content of chromium enables C2000® to exhibit resistance to oxidizing media, such as ferric ions or dissolved oxygen, while the addition of molybdenum and copper provides a chemistry conducive to the material's usage in reducing media, such as sulfuric acid. The material is processed by solid solution and hot rolling, followed by a

final anneal. The fabrication of the C2000® is available in bar, sheet, plate, wire, and tubular forms. C2000® possesses superior corrosion-resistance properties to alloys like an industry standard, C-276, which is comprised of 57Ni-16Cr-16Mo-5Fe-4W-2.5Co-1Mn-0.35V-0.08Si-0.01C (wt. %). Unlike Ni_3Al and other superalloys used for high-temperature applications, C2000® does not form second-phase precipitates at elevated temperatures. Therefore, C2000® is extremely stable in aqueous environments at lower temperatures due to the material's ability to maintain tenacious Cr_3O_2, $Mo(OH)^-$ and NiO barriers [31].

Determining the governing mechanisms for materials undergoing fatigue presents challenges due to their microstructural features, such as grain boundaries, precipitates, and grain sizes; and, synergistic influences on these features provide even greater challenges. Hence, C2000® is an attractive superalloy for undergoing lifetime-prediction studies during corrosion fatigue because of the stability of the microstructure under many environmental conditions.

6.1.3 Corrosion of Nickel Superalloys: The corrosion-resistant properties of nickel are dependent upon the selection of elemental additions. In the active state, pure nickel intrinsically possesses low corrosion rates in acidic solutions or reducing environments, while certain complex metal-ion additions in a given electrolyte may further decrease the corrosion rate. There are three categories of nickel-based superalloys: nickel-copper alloys, nickel-chromium-molybdenum alloys, and nickel-chromium-iron-molybdenum alloys. Each of these can attribute its inceptions to specific industry demands, such as the

resistance to deaerated hydrofluoric acid, oxidizers in acidic solutions, and chloride solutions.

The nickel superalloys' corrosion resistance is attributed to the high solubility content of chromium. Consequently, the resistance to corrosive media spans a wide range. Most nickel-based superalloys consist of additions of iron, molybdenum, cobalt, or niobium. Table 3 [32] manifests both the commercial names and chemical compositions for selected corrosion-resistant nickel-based alloys. Table 4 [32] outlines the electrochemical properties of some corrosion-resistant nickel superalloys. In both neutral and iodide solutions, nickel-based superalloys are immune to any form of localized corrosion [33] at room temperature. The breakdown of the stable chromium oxide layer made up of Cr(III) ions is heavily influenced by the temperature. For solution temperatures lower than approximately 150ºC, the increased oxygen solubility and oxidizing power do not cause the dissolution of oxide films. However, for temperatures greater than 150ºC, the protective oxide becomes less stable with the increased oxygen solubility. Additionally, further deterioration can easily be achieved by slight increases in the oxidizing power of the solution.

Although certain elemental additions are used to produce a protective layer, some oxides are vulnerable to dissolution in acidic solutions. As a result, larger contents of chromium are beneficial, since the formation of Cr(III) oxides [34-37] is thermodynamically stable at room temperature and at temperatures ranging up to 300ºC [35, 38] (Figure 11). In Figure 11, the effects of corrosive media and elevated temperatures on the corrosion of nickel-based alloys and stainless steels are schematically shown. The schematic shows that a passive state is maintained in the 200ºC – 300ºC

range, where the possible protective oxides are Cr_2O_3 or CrOOH. At an intermediate temperature of 350ºC, a breakdown in the oxide occurs. At this point a transpassive state is reached. At temperatures higher than 500ºC, a "density-controlled" passive state is reached, due to the high-density solution, which acts as a barrier to the material layer. For most alloys, chloride solutions are considered subcritical, since the chlorides depassivate the protective oxide. However, for most nickel-based superalloys, the presence of chlorides does not induce localized corrosion at room temperature. The pitting corrosion or localized corrosion is not prevalent until alloys are exposed to critical temperature values that depend upon the material's chemistry. The literature reports that most nickel superalloys require a breakdown of passive films to occur at temperatures above 100ºC - 400ºC [34].

In particularly, Haynes C2000® is incredibly immune to localized corrosion in 3.5wt.% sodium chloride solutions (Figure 12). The corrosion behavior of Haynes C2000® in the presence of neutral and concentrated metal-ion (pH=0) solutions does not support the dissolution of passive films (Figure 13). Overall, the performance of C2000® in various media is excellent. Evidently, element additions play an integral role in tailoring an alloy for a specific application, especially if the corrosion resistance is the predominate factor.

6.2 Corrosion:

6.2.1 Anodic and Cathodic Reactions for Corrosion: In general, cathodic reactions [39, 40] for the hydrogen ion reduction in an acidic solution follow the equation:

$$H^+ + e^- \rightarrow H(ads) \qquad \textbf{(2)}$$

The adsorbed hydrogen created by this reaction can combine with other adsorbed hydrogen on the deteriorating surface by the reaction:

$$H(ads) + H(ads) \rightarrow H_2(g) \quad \textbf{(3)}$$

The accumulation of sufficient atomic hydrogen on the surface evolves hydrogen gas. The electrochemical desorption can also give rise to the hydrogen-gas evolution through the reaction:

$$H^+ + H(ads) + e^- \rightarrow H_2(g) \quad \textbf{(4)}$$

Equation 5 accounts for neutral and alkaline conditions where dissolved oxygen in water produces hydrogen oxide ions.

$$O_2 + 2H_2O + 4e^- \rightarrow 4OH^- \quad \textbf{(5)}$$

The dissolution of the anodic materials reacts according to the following for both acidic and neutral and alkaline environments.

$$M \rightarrow M^+ + e^- \quad \textbf{(6)}$$

Therefore, corrosion is driven by the conjoint oxidation and reduction reactions occurring on the metallic surface. The corrosion rate is highly dependent upon the chemistry, surface imperfections, potentials, and coupling with dissimilar materials. The area of the anodic to cathodic ratio is of importance as well as choosing the correct combination of metals in design. In corrosion, most behavior can be described by the use of cyclic anodic or potentiodynamic curves. These curves provide the useful information about the material's response to the incremental potential increases in a particular electrolyte. Materials exhibit corrosion behavior within one or a combination of three regions: the active, the passive, and the transpassive, or the pitting.

6.3 Mechanically-Induced Deformation:

6.3.1 Fatigue-Crack Initiation and Propagation: Fatigue-crack initiation was believed to be a consequence of exceeding the limit of the local strain hardening [41]. In 1953, Head [42] created a model to account for the local saturation of ductility, which leads to an increase in stress and subsequent cracking. This ductility-exhaustion theory did not account for cracking on the atomic level. Therefore, Stroh [43, 44] attempted to develop a micro-model. These attempts yielded little value and proved unacceptable upon the advent of new and improved devices and techniques to image dislocations. Finally, the creation of crevices in the material was attributed to the correct sources. These sources are commonly known as intrusions and extrusions, which are surface phenomena (Figure 14) [45]. Thus, fatigue-crack initiation is a surface phenomenon. Cracks form in the crevices or recesses of the intrusions and extrusions due to newly created high-stress concentrators. Ensuing crack initiation, propagation occurs to yield failures. Crack initiation and propagation became pertinent issues for describing the fatigue life of a material. It was commonly observed that under low-cycle-fatigue conditions, most of the fatigue life is spent in the propagation region. For high-cycle-fatigue conditions, most of the fatigue life is spent in the crack-initiation stage. The block diagram adopted from Schijve [46] best describes the crack-initiation period and the growth period with corresponding quantifying parameters (Figure 15). The stress-concentration factor (K_t) was first demonstrated by Inglis [47] in an experiment that showed an increase in the applied stress at the ends of the major axis of an ellipse. Stress concentration is a measure of the ratio of the crack length to the crack radius. According to Dowling [48], the stress-intensity factor (K) is best defined as the parameter that characterizes the

severity of the cracking situation as affected by the crack size, stress, and geometry. For linearly-elastically-behaving materials, another term, known as the fracture toughness (K_{1c} or K_c), is the measure of a material's ability to withstand or resist fracture. Later in the 1960s, a correlation was established between the crack-growth rate per fatigue cycle, da/dN, and stress-intensity-factor range (ΔK). Paris, Gomez, and Anderson [49] were the first to release findings on their approach correlating the crack-growth rate and stress-intensity factor in which they adopted the use of the K-value proposed by Irwin [50].

Fatigue experiments yield various forms of the information. Perhaps of most importance is the applied stress to the number of cycles to failure (S-N) curve. Before the reference of the named S-N curve, these useful diagrams were known as the Wöhler diagrams. S-N diagrams allow the material's life to be analyzed over a period extending to millions of cycles. In engineering, the fatigue limit or endurance limit is the most critical designing parameter extracted from the S-N curve. Theoretically, failure does not occur below the fatigue limit. Standardized methods have been devised to determine the fatigue limit of materials. Table 5 lists the American Society for Testing and Materials (ASTM) standards associated with fatigue most commonly followed for simulating in-service fatigue problems and performing fatigue experiments for reporting findings.

6.3.2 Damage Mechanisms: Damage mechanisms vary with the nickel superalloy composition, service or test temperature, and frequency. For example, increasing the temperature alters the cracking mode by causing the alloy to exhibit an intergranular fracture. At even higher temperatures, service conditions may incorporate an additional mechanism due to creep. Such damage generally manifests itself via grain-boundary voids and cracks. Yet, in lower temperature conditions, the localization of a plastic strain

is the most common means of nucleating cracks [44]. Thus, on a macroscopic scale, fatigue experiments investigate a material's response to cyclic stresses. The mechanisms in which failure occurs can be described by localized stress risers at low temperatures and creep mechanisms at high temperatures.

During fatigue, lattice distortions produced by dislocations occur after the exertion of a force known as the Peierls-Nabarro force. Since this force is contingent on the dislocation width or distorted region, the force experienced by a given dislocation is variable. Edge, screw, and mixed (a combination of edge and screw) natures are the three types or characters of dislocations found in metallic materials. Each type consists of similar components, yet differ in the directional functionality and geometrical positioning in the crystal. The process by which the dislocation motion occurs is known as slip. Slip from one crystallographic plane to another is referred to as cross-slip. Positive-sense or negative-sense edge dislocations can exist within a crystalline structure. Similar-sign dislocations provide a lower resistance to mobility than dissimilar-sign dislocations. Dislocation interactions coalesce when the signs are alike.

Interactions between different senses cause the dislocations to repel. Consequently, this repelling promotes dislocation pile-ups, which can cause both a large stress concentration, and a barrier to further slip. These pile-up-initiated stress concentrations become primary regions for crack initiation. Other interactions can occur between dislocations and precipitates or inclusions. For instance, interactions between dislocations and particles can cause a pinning effect, which generates additional dislocations within the material. A common dislocation multiplier, known as the Frank-Reed source, pins the dislocation lines to particles at the outer edges of the dislocation,

causing a bowing effect. Upon applying shear stresses, a decreasing radius of curvature is experienced until the radius is half the length of the pinned dislocation. At this point, an instability is reached and an annihilation occurs due to the bowing of the dislocation unto itself. Subsequently, a new dislocation line is formed within the newly-generated loop developed by the aforementioned dislocation action. This action continues until the stress from the pile-up interactions counteracts the stress required to continue generating dislocations. Further complexity is introduced by the dissociation of edge dislocations into two partial dislocations. Partial dislocations occur when the total strain energy is reduced by the splitting of the primary dislocation into two dislocations, i.e., partial dislocations. The region formed between the two partial dislocations is called the stacking-fault width. This width is useful for determining the stacking-fault energy (SFE), since the SFE is inversely proportional to the SFE width or separation distance. Low-stacking-fault energy materials, such as nickel and nickel alloys, exhibit minimal cross slips, resulting in narrow and straight slip bands.

6.3.2.1 Persistent Slip Bands: Persistent slip bands (PSBs) [51] are local deformation phenomena that insistently occur during a loading sequence. Unlike monotonic testing, slip does not occur similar to a staircase. The slip morphology on the surface resembles hills and valleys known as extrusions and intrusions. PSBs are responsible for carrying the load during the cyclic deformation. Persistent slip bands form in stage B of Figure 16 during the fatigue process. Crack initiation in stage I initiates at 45 degrees along the direction of the maximum shear stress. PSBs consist of extrusions and intrusions on a material's surface by means of the backward and forward slip. This action continues until the crack traverses sufficient grains to deflect the propagation perpendicular to the

direction of the applied stress. The crack propagation 90 degrees to the loading stress is known as the stage-II propagation, which is illustrated in Figure 16 [52].

6. 4 Environmentally-Enhanced Deformation:

6.4.1 Stress-Corrosion Cracking (SCC): Overall, most stress-assisted cracking lies within two catergories: stress-corrosion cracking and corrosion-fatigue. Stress-corrosion cracking is attributed to a sustained-loading condition where the material, before the introduction of stresses, is susceptible to localized corrosion. The material can produce cracks at grain boundaries or pits. Cracking along grain boundaries is referred to as intergranular cracking. Cracks that emanate from pits, once these pit have reached a critical size, are most likely associated with the formation of atomic hydrogen as a by-product during metal hydrolyse. The increase in the local hydrogen relative to the bulk electrolyte creates a potential-difference gradient. Hence, the mass transport of detrimental species, such as chlorides to the pit, is permitted. Additionally, the increase in the atomic hydrogen within the pit decreases the pH to cause acidification. At a critical pit depth, a crack (or cracks) initiates from the pits to cause SCC. Whether the culprit site is attributed to chemistry inhomogeneities, surface flaws, or pits, the addition of a stress to corrosion introduces a more complex region of activities. Figure 17 shows a schematic of the corrosion regimes where cracking will most likely occur when coupled with stress. Region I is labeled as the active region of corrosion. Hydrogen embrittlement is dominant in this region, since the evolution of hydrogen is plentiful due to the low potential or cathodic currents imposed. Thus, cracking occurs, resulting from the lattice dilation of diffused hydrogen into interstitial sites within the metallic lattice. The dilation causes a local condition of plane strain, which requires an applied stress

equal to at least three times the yield strength to promote the crack growth and subsequent failure. The fracture behavior is a brittle one due to the large increase in the yield strength from the more macroscopic yield strength. Region II is known as the passivity region. The passivity region is marked by the formation of a protective film within a specific potential range. The transition from the active to the passive regions is one of the most susceptible areas to cracking since active processes and oxide-formation processes are in competition. Likewise, the transition from the passivity to pitting is also vulnerable to cracking, since the depassivation and oxide formation are occurring simultaneously. The mechanism for localized corrosion in Region III described in Figure 17 is known as pitting.

6.4.2 Corrosion Fatigue or Cyclic-Loading Influences: Unlike SCC, corrosion fatigue is caused by cyclic loading or alternating stress. Both forms of stress corrosion account for the influences of stresses on a material in a given electrolyte, and plausible crack-initiation phenomena can be explained with the linear-elastic-fracture mechanics. However, there are some subtleties. SCC occurs under conditions of constant stresses. The fracture-mechanics-parameter, K, the stress-intensity factor, can be used to quantify the stress in which corrosion will not enhance or expedite the propagation rate of a given crack size. The stress-intensity factor associated with the enhanced behavior is known as the critical stress-intensity factor, Kc, which is usually lower than that observed in air. However, corrosion fatigue is more complex in that the alternating stress is involved. Consequently, frequencies, R ($\sigma_{min.}/\sigma_{max.} = K_{min.}/K_{max.}$) ratios, mean stresses, and stress ranges or ΔK are of importance, since these parameters can strongly affect the fatigue life in the absence of corrosive media.

Another concern is differentiating the influences of pure mechanics from those induced by electrochemical means. Roughness effects on the influences of fatigue lives are well established in the literature [53]. The explanation for the expected decrease in the fatigue life must be identified by carefully examining and understanding the fatigue behavior in both ambient and severely detrimental environments. When studying the behavior of corrosive media during crack propagation, ΔK_{ICF}, the critical stress-intensity-factor range due to corrosion can serve as a marker for this type of distinction. Stress-intensity-factor ranges below ΔK_{ICF} are mostly dominated by mechanical stresses, while values above ΔK_{ICF} are generally dominated by electrochemical influences. Further studies have established a relationship to determine the susceptibility of a material to corrosion-fatigue by knowing the fatigue-endurance limit in both corrosive and ambient environments [54]. If the ratio of the corrosion-fatigue endurance limit to that observed in air is less than one, the material is likely to perform poorly in the corrosive media. Materials exhibiting ratios greater than one are deemed immune to corrosion under fatigue.

Corrosion-fatigue mechanisms for metals in the active and passive regimes differ. For metals in the passive regime, a perturbation in the passive film must occur, such as film rupture, before corrosive species can cause dissolution of the freshly exposed surface. Metals in the active regime experience dissolution more readily due to the inability to maintain a protective layer. Hence, the subjection to corrosion-fatigue exacerbates the corrosion behavior observed in the presence of aggressive solutions [54-58].

In general, corrosion-fatigue analyses require an understanding of the materials' chemical state, corrosion properties (such as the localized corrosion occurrences) and mechanisms, and the environmental influences, such as stress, exposure to varying pH solutions, and temperature [59]. Studies performed by Garcia [60] substantiate the aforementioned as key issues to understanding crack-initiation processes incurred under cyclic stresses coupled with the corrosive media. Given a sufficient time, corrosion species attack the bare metal exposed by the formation of extrusions and intrusions on the material surface. The mechanism commonly adopted is that by which dissolution of the freshly exposed material occurs, and the ease of plastic deformation or the localized surface plasticity is more favorable [57]. Moreover, corrosion fatigue is affected by the type of oxides present and their thickness [61]. Understanding corrosion influences on the fatigue process of structural materials is difficult, considering that the corrosion process for materials is intrinsic to the unique chemistry of these materials. The corrosion fatigue of materials can be categorized into two types: Type 1 - pitting, and Type 2 – Embrittlement (Figures 18a and 18b). Figure 18a shows the failure cascade for Type 1 and Type 2 cases. The major distinction between the two cases is whether the material state is homogeneous or inhomogeneous and whether the material can maintain a protective film. The response to the addition of stress is affected by the material state. Among the embrittlement postulates, two approaches are acceptable for the deterioration of material. These two categories are known as the slip-step anodic dissolution and hydrogen-embrittlement. In both cases, the crystal structure of the material is weakened and experiences dissolution. However, the mechanism by which slip-step anodic dissolution occurs is different than the mechanism for hydrogen embrittlement. In

hydrogen-embrittlement, local acidification occurs due to the saturation of atomic hydrogen. For slip-step anodic dissolution, the atomic hydrogen buildup is due to the local entrapping of the corrosive electrolyte, which produces hydrogen at a faster rate as opposed to having hydrogen readily available from the bulk electrolyte.

6.4.2.1 Variable Effects: Although nickel-based superalloys are widely used in various applications, limited studies on variable effects under corrosion fatigue of nickel-based superalloys are reported in the literature. The waveform, frequency, R-ratio, and solution conditions can strongly affect the corrosion-fatigue behavior of alloys. A careful inspection of the effects of the waveform, frequency, R-ratio, and solution has been summarized in the literature [51, 52]. Of the aforementioned, the authors have looked at the influences of these variables on the crack-growth rate but not the crack initiation. In Figure 19, the effects of variable frequencies on the fatigue properties of a titanium alloy are examined. The frequencies studied range from 5 Hz to 50 Hz. All the experiments were performed at an R-ratio of 0.05 and at room temperature. The plot shows that frequency does not affect the crack-growth rate in an inert environment, such as argon (Ar). However, the material's response to fatigue is dependent on frequency when studied in 3.5 wt.% NaCl.

Additionally, at a constant frequency, Figure 20 shows the type of wave forms that can influence the propagation results. The figure shows that a sinusoidal, a triangular, and a positive sawtooth waveform increases the fatigue-propagation rate, whereas the negative sawtooth, and square wave form do not affect the crack-propagation rates. In both figures, the K_{ISCC} marker is placed as a point of reference for the reader,

although K_{ISCC} is the value determined on constant-loading conditions and not variable-loading conditions.

6.5 Corrosion-Fatigue:

6.5.1 Corrosion-Fatigue Modeling: Modeling of corrosion-fatigue phenomena presents certain challenges since every material-environment system is a synergistic effect, coupling the material nature, surface reactions, and stress conditions. Thus, a universal model to describe the corrosion-fatigue behavior for classes of metallic materials remains to be developed. Researchers [60, 62-68] who have attempted to model corrosion fatigue have achieved some success by using the superposition approach, which assumes that the operating mechanisms under sustained loading (stress-corrosion cracking) and corrosion-fatigue hold true. In the early 1970s, a model to determine the crack-growth rate was derived according to Equation 7 [69].

$$\left(\frac{da}{dt}\right)_{SCF} = \left(\frac{da}{dt}\right)_{F} + \left(\frac{da}{dt}\right)_{SC} \qquad (7)$$

Although synergistic interactions between the purely mechanical and corrosion fatigue occur, the model does not account for such behavior. For this reason, others have tried to resolve this problem by incorporating a component to the above equation that would model synergistic effects and deem the model more representative. Modern models incorporate the use of parametric representations of statistical fits to experimental data, where the distribution trend is normal and the variance is homogeneous. Next, the

data is linked with probabilistic methods to determine life predictions. Harlow and Wei suggest the use of mechanistically-based models to examine the corrosion-fatigue behavior of a material not within the interpolation range of data, i.e., extrapolated beyond the experimental data [62, 70-72]. Assuming that the rate of the growth of the pit radius is proportional to Faraday's law, the following equation can be written.

$$\frac{da}{dt} = \frac{MI}{n\rho F} \tag{8}$$

In Equation 8, the crack-growth rate, da/dt, is proportional to the quotient of the molecular weight, M, current, I, and the valence electrons, n, the density, ρ, and Faraday's constant. Then the radius as a function of time is determined by the separation of variables and integrating Equation 8 over time to yield Equation 9, where a_{co} is a constant representing the critical stable nucleus size to precede the crack propagation.

$$a = a_{CO} + \frac{MI}{n\rho F} t \tag{9}$$

Once a critical pit size is reached, the fatigue-crack-growth rate follows the relation below.

$$\frac{da}{dN} = C_F (\Delta K - \Delta K_{th})^{n_C} ; \Delta K = \beta \Delta\sigma \sqrt{a} \tag{10}$$

The parameters in Equation 10 describe the relationship between the fatigue-crack-growth rate, da/dN, and the difference between the applied stress-intensity-factor range and the near–threshold stress-intensity-factor range, where crack growth is not permissible. The stress-intensity-factor range can also be expressed according to the

linear-elastic fracture-mechanics relationship, where the stress-intensity-factor range is proportional to the stress range, $\Delta\sigma$, and the square of the crack length, a. The C_F and β parameters in Equation 9 are the proportionality constants, and n_c is the fatigue exponent. A transition criterion for both the stress-intensity-factor range for the critical-pit size, ΔK_{Pit}, and the fatigue-crack-growth rate, $da/dt)_{fcg}$, is governed according to the following:

$$\Delta K_{Pit} \geq \Delta K_{th} and \left(\frac{da}{dt}\right)_{fcg} \geq \left(\frac{da}{dt}\right)_{Pit} \quad \textbf{(10)}$$

where ΔK_{th} represents the near-threshold stress-intensity factor range and (da/dt)pit represents the rate of the pit growth before the onset of cracks emanating from pits, respectively. Utilizing the above equations and their governing criteria, a mechanistic modeling approach is derived to relate the damage mechanisms induced by aging to fundamental scientific principles, which allows for extrapolation beyond the laboratory range of data, and better confidence intervals for life predictions.

7. Conclusion

Only a few materials exhibit a long range of passivity above their natural corrosion potential. Hence, the pitting potential is not prevalent at room temperature. In the presence of strongly acidic solutions and solutions with strong oxidizing powers, most materials have a strong propensity to pitting. Corrosion fatigue involves a competition between the mechanical and electrochemical influences. Under a given set of conditions, the control of the interdependent parameters can sway the deterioration of a material to be dominated by a purely mechanical or electrochemical process. There are many reports in the literature discussing the influences of the mean stress and other variables on the fatigue life of materials. Consequently, the effects of the mean stress on the corrosion-fatigue behavior of materials are suspected to exacerbate the fatigue life observed under the non-corrosive media. Generally, the mean stress, frequency, and solution oxidizing strength are expected to have the greatest influences on the fatigue lives of materials, whether or not they are susceptible to pitting for a given potential at the ambient temperature or not. An attempt to develop an experimental platform or approach for isolating the key parameters necessary for determining the cycles to crack initiation was the main thrust of this investigation. The baseline material selected for this study was the nickel-based superalloy, C2000. The advantages of C2000 are 1) the inability of the material to undergo pitting at room temperature for a range of potentials and 2) the fact that it is a single-phase material at all temperatures.

REFERENCES

1. Cowles, B.A., *High Cycle Fatigue in Aircraft gas Turbines - An Industry Perspective.* International Journal of Fracture, 1996. **80**(2-3): pp. 147-163.

2. Daeubler, M.A., Thompson, A.W. and Bernstein, I.M., *Crack Initiation and near-Threshold Surface Fatigue Crack-Propagation Behavior of the Iron-Base Superalloy a-286.* Metallurgical Transactions a-Physical Metallurgy and Materials Science, 1988. **19**(2): pp. 301-308.

3. Chan, K.S., *A Microstructure-Based Fatigue-Crack-Initiation Model.* Metallurgical and Materials Transactions A-Physical Metallurgy and Materials Science, 2003. **34**(1): pp. 43-58.

4. Peter, W.H., Buchanan, R.A., Liu, C.T., Liaw, P.K., Morrison, M.L., Horton, J.A., Carmichael Jr., C.A., and Wright, J.L., *Localized Corrosion Behavior of a Zirconium-Based Bulk Metallic Glass Relative to its Crystalline State.* Intermetallics, 2002. **10**: pp. 1157-1162.

5. Juvinall, R.C., and Marshek, K. M., *Fundamentals of Machine Component Design*. Second ed. 1991, New York: John Wiley and Sons.

6. Noll, C.G., and Lipson, C., *Allowable Working Stresses.* Proceedings of the Society of Experimental Stress Analysis, 1946. **3**(2): pp. 49.

7. Shigley, J.E., and Mischke, K. M., *Mechanical Engineering Design*. Fifth ed. 1989, New York: McGraw-Hill Book Company.

8. Reemsnyder, H.S., *Simplified Stress-Life Model.* Betheleham Steel Corporation Report, 1985.

9. Goken, M., *Studies of Metallic Surfaces and Microstructure with Atomic Force Microscopy*.

10. Schmidt, P.A. and J.C. Earthman, *Development of a Scanning Laser Crack Detection Technique for Corrosion-Fatigue Testing of Fine Wire.* Journal of Materials Research, 1995. **10**(2): pp. 372-380.

11. Yang, Liaw, P. K., Wang, G., Peter, W. H., Buchanan, R. A., Yokoyama, Y., Huang, J. Y., Kuo, R. C., Huang, J. G., Fielden, D. E., Klarstrom, D *Thermal-imaging technologies for detecting damage during high-cycle fatigue.* Metallurgical and Materials Transactions A-Physical Metallurgy and Materials Science, 2004. **35A**(1): pp. 15-23.

12. Talbot, Martin, J. W., Chandler, C., Sanderson, M. I *Assessment of Crack Initiation in Corrosion Fatigue by Oscilloscope Display of Corrosion Current Transients.* Metals Technology, 1982. **9**(MAR-): pp. 130-134.

13. Merah, N., Buiquoc, T. and Bernard, M., *Calibration of DC Potential Technique Using an Optical-Image Processing System in LCF Testing.* Journal of Testing and Evaluation, 1995. **23**(3): pp. 160-167.

14. Cakir, A., Tuncell, S., and Aydin, A., *AE Response of 316L SS During SSR Test Under Potentiostatic Control.* Corrosion Science, 1999. **41**(6): pp. 1175-1183.

15. Crowell, J.J. and Pickering, F., *Acoustic-Emission Failure Criterion for FRP Pipe.* Materials Evaluation, 1982. **40**(3): pp. A14-A15.

16. Jiang, L., Brooks, C. R., Liaw, P. K., Wang, H., Rawn, C. J., Klarstrom, D. L. *High-Frequency Metal Fatigue: The High-Cycle Fatigue Behavior of ULTIMET (R) Alloy.* Materials Science and Engineering A-Structural Materials Properties Microstructure and Processing, 2001. **314**(1-2): pp. 162-175.

17. Man, J., Obrtlik, K., and Polak, J., *Study of Surface Relief Evolution in Fatigued 316L Austenitic Stainless Steel by AFM.* Materials Science and Engineering A-Structural Materials Properties Microstructure and Processing, 2003. **351**(1-2): pp. 123-132.

18. Hussain, K., and Delosrios, E.R., *Application of Short and Long Fatigue-Crack Growth-Behavior in Lifetime Prediction of Mine Auxiliary Ventilation Fans.* Materials Transactions Jim, 1994. **35**(9): pp. 585-590.

19. Liaw, P.K., Yang, C. Y., Palusamy, S. S., Ren, W., *Fatigue Crack Initiation and Propagation Behavior of Pressure Vessel Steels.* Engineering Fracture Mechanics, 1997. **57**(1): pp. 85-&.

20. Liaw, P.K., Leax, T. R., Fabis, T. R., Donald, J. K. Leax, T. R., Fabis, T. R. Donald, J. K., *Fatigue Crack-Growth Behavior in an Mn-Cr Austenitic Steel.* Engineering Fracture Mechanics, 1987. **26**(1): pp. 1-13.

21. Jiang, L., Wang, H., Liaw, P. K., Brooks, C. R., Chen, L., Klarstrom, D. L *Temperature Evolution and Life Prediction in Fatigue of Superalloys.* Metallurgical and Materials Transactions A-Physical Metallurgy and Materials Science, 2004. **35A**(3): pp. 839-848.

22. Saleh, T.A., Yang, B., Liaw, P.K., Buchanan, R.A. and Klarstrom, D.L. *Thermographic Detection of Fatigue Damage in HASTELLOY C-2000 superalloy" Symposium on Materials Lifetime Science and Engineering.* TMS Annual Meeting, 2003.

23. Liaw, P.K., Hartmann, H.R. and Helm, E. J., *Corrosion Fatigue Crack-Propagation Testing with the Krak-Gage in Salt-Water.* Engineering Fracture Mechanics, 1983. **18**(1): pp. 121-&.

24. Kim, J. and Liaw, P.K., *Monitoring Tensile Damage Evolution in Nextel 312/Blackglas (TM) Composites.* Materials Science and Engineering A-Structural Materials Properties Microstructure and Processing, 2005. **409**(1-2): pp. 302-308.

25. Kim, J. and Liaw, P.K., *Characterization of Fatigue Damage Modes in Nicalon/Calcium Aluminosilicate Composites.* Journal of Engineering Materials and Technology-Transactions of the Asme, 2005. **127**(1): pp. 8-15.

26. Yang, B., Liaw, P. K., Huang, J. Y., Kuo, R. C., Huang, J. G., Fielden, D. E., *Stress Analyses and Geometry Effects During Cyclic Loading Using Thermography.* Journal of Engineering Materials and Technology-Transactions of the ASME, 2005. **127**(1): pp. 75-82.

27. Chen, L.J., Liaw, P. K., Wang, H., He, Y. H., McDaniels, R. L., Jiang, L., Yang, B., Klarstrom, D.L.,*Cyclic Deformation Behavior of HAYNES (R) HR-120 (R) Superalloy Under Low-Cycle Fatigue Loading.* Mechanics of Materials, 2004. **36**(1-2): pp. 85-98.

28. Liaw, P.K., Wang, H., Jiang, L., Yang, B., Huang, J. Y., Kuo, R. C., Huang, J. G., *Thermographic Detection of Fatigue Damage of Pressure Vessel Steels at 1,000 Hz and 20 Hz.* Scripta Materialia, 2000. **42**(4): pp. 389-395.

29. Sridhar, N., *Metals Handbook - Corrosion.* 1987. **13**: pp. 643.

30. Ashby, M., and Johnson,.K., *Materials and Design: The Art and Science of Material Selection in Product Design.* 2002: pp. 176.

31. Lloyd, A.C., Noel, J. J., McIntyre, S., Shoesmith, D. W., *Cr, Mo and W Alloying Additions in Ni and Their Effect on Passivity.* Electrochimica Acta, 2004. **49**(17-18): pp. 3015-3027.

32. Meck, S.N., and Crook, P., *Localized Corrosion Susceptibility of Nickel Alloys in Halide Containing Environments.* Corrosion NACE Conference, 2002.

33. Meck, S.N., and Crook, P., *Susceptibility of Nickel and Cobalt Alloys to Localized Corrosion in Fluoride and Iodide Solutions: Comparative Behavior to Chloride and Bromide Solutions.* Corrosion NACE Conference, 2002.

34. Kritzer, P., Boukis, N., and Dinjus,E., *Review of the Corrosion of Nickel-Based Alloys and Stainless Steels in Strongly Oxidizing Pressurized high-temperature solutions at subcritical and supercritical temperatures.* Corrosion, 2000. **56**(11): pp. 1093-1104.

35. Newman, R.C., Corrosion Science, 1985. **25**(331-341).

36. Boudin, S., et al., *Analytical and Electrochemical Study of Passive Films Formed on Nickel-Chromium Alloys - Influence of the Chromium Bulk Concentration.* Surface and Interface Analysis, 1994. **22**(1-12): pp. 462-466.

37. Jabs, T., Borthen, P., and Strehblow, H.H., *X-ray Photoelectron Spectroscopic Examinations of Electrochemically Formed Passive Layers on Ni-Cr Alloys.* Journal of the Electrochemical Society, 1997. **144**(4): pp. 1231-1243.

38. Lorang, G., Noel, J. J., McIntyre, S., Shoesmith, D. W., *AES Depth Profiling of Passive Overlayers Formed on Nickel-Alloys.* Surface and Interface Analysis, 1990. **16**(1-12): pp. 325-330.

39. Stansbury, E.E., and Buchanan, R.A., *Fundamentals of Electrochemical Corrosion.* ASM International, 2000.

40. Ricker, R., and Jones, R., *Environmental Effects on Advanced Materials.* The Minerals, Metals and Materials Society, 1991.

41. Gough, H.J. and Wood, W.A., *The Crystalline Structure of Steel at Fracture.* Proceedings of the Royal Society of London Series A-Mathematical and Physical Sciences, 1938. **165**(A922): pp. 0358-0371.

42. Head, A.K., *The Growth of Fatigue Cracks.* Philosophical Magazine, 1953. **44**(356): pp. 925-938.

43. Stroh, A.N., *The Formation of Cracks as a Result of Plastic Flow.* Proceedings of the Royal Society, 1955. **A223**: pp. 404.

44. Mott, N.F., *A Theory of the Origin of Fatigue Cracks.* Acta Materialia, 1958. **6**: pp. 195-202.

45. Halfpenny, A., *A Practical Discussion on Fatigue*, n-Code International.

46. Schijve, J., *Review Article: Fatigue of Structures and Materials in the 20th Century and the State of the Art.* International Journal of Fatigue, 2003. **25**: pp. 679-702.

47. Inglis, C.E., *Stresses in a Plate Due to the Presence of Cracks and Sharp Corners.* Transactions of the Institute of Naval Architects, 1913. **55**: pp. 219-241.

48. Dowling, N.E., *Mechanical Behavior of Materials: Engineering Methods of Deformation, Fracture, and Fatigue*. 1999: Prentice - Hall.

49. Paris, P.C., Gomez, M. P., and Anderson, W. E., *A Rational Analytical Theory of Fatigue.* The Trend of Engineering, 1961. **13**: pp. 9-14.

50. Irwin, G.R., *Analysis of Stresses and Strains Near the End of a Crack Traversing a Plate.* Transactions of the American Society of Mechanical Engineers Journal Applied Mechanics, 1957. **24**: pp. 361-365.

51. Hertzberg, R.W., *Deformation and Fracture Mechanics of Engineering Materials*. 4th ed. 1996: John Wiley and Sons, Inc.

52. Suresh, S., *Fatigue of Materials*. 2nd ed. 1998: Cambridge University Press.

53. Laue, S., H. Bomas, and F. Hoffmann, *Influence of surface condition on the fatigue behaviour of specimens made of a SAE 5115 case-hardened steel.* Fatigue & Fracture of Engineering Materials & Structures, 2006. **29**(3): pp. 229-241.

54. Patel, C., T. Pyle, and V. Rollins, *Corrosion-Fatigue Crack Initiation in Metals.* Nature, 1977. **266**(5602): pp. 517-518.

55. Boateng, A., Begley, J.A., and Staehle, R.W., *Corrosion Fatigue of Type-304 Stainless-Steel and Inconel 600 in a Boiling (140-Degrees-C) Concentrated Caustic Solution.* Metallurgical Transactions a-Physical Metallurgy and Materials Science, 1983. **14**(1): pp. 67-73.

56. Boateng, A., Begley, J.A., and Staehle, R.W., *Corrosion Fatigue of Type-304 Stainless-Steel in H_2SO_4 and Boiling NaOH.* Corrosion, 1980. **36**(11): p. 633-638.

57. Asphahani, A.I. and Sridhar, N., *Corrosion Fatigue of Nickel and Nickel-Base Alloys.* Corrosion, 1982. **38**(11): pp. 587-595.

58. Inglis, N.P. and Larke, E.C., *Corrosion-Fatigue Properties of an Aluminium Magnesium Silicon Alloy in the Unprotected, Anodized, and Painted Conditions.* Journal of the Institute of Metals, 1954. **83**(4): pp. 117-&.

59. Ryder, J.T. and Gallaghe, J.P., *Temperature Influence on Corrosion Fatigue Behavior of 5ni-Cr-Mo-V Steel.* Journal of Testing and Evaluation, 1974. **2**(3): pp. 180-189.

60. Garcia, C., and Duquette, D. J., *Modeling Environmental Effects on Crack Growth Processes.* 1986: pp. 343.

61. Rosecrans, P.M., and Duquette, D.J., *Formation Kinetics and Rupture Strain of Ni-Cr-Fe Alloy Corrosion Films Formed in High-Temperature Water.* Metallurgical and Materials Transactions A-Physical Metallurgy and Materials Science, 2001. **32**(12): pp. 3015-3021.

62. Harlow, D.G. and Wei, R.P., *Life prediction - The Need for a Mechanistically Based Probability Approach.* Probabilistic Methods in Fatigue and Fracture, 2001. **200**: pp. 119-137.

63. Daeubler, M.A., Warren, G. W., Bernstein, I. M., Thompson, A. W., *Modeling of Corrosion Fatigue Crack Initiation Under Passive Electrochemical Conditions.* Metallurgical Transactions A-Physical Metallurgy and Materials Science, 1991. **22**(2): pp. 521-529.

64. Wei, R.P., him, G., and Tanaka, K., *Corrosion Fatigue and Modeling.* Journal of Metals, 1983. **35**(8): pp. A47-A47.

65. Wei, R.P. and Harlow, D.G., *Mechanistically Based Probability Modeling, life Prediction and Reliability Assessment.* Modeling and Simulation in Materials Science and Engineering, 2005. **13**(1): pp. R33-R51.

66. Mueller, M.P., *Dependence of Corrosion Fatigue Crack Initiation Mechanisms on the Corrosion Behavior of 2 Stainless Chromium Steels.* Corrosion, 1982. **38**(8): pp. 431-436.

67. Muller, M., *Theoretical Considerations on Corrosion Fatigue Crack Initiation.* Metallurgical Transactions A-Physical Metallurgy and Materials Science, 1982. **13**(4): pp. 649-655.

68. Magnin, T., Coudreuse, L, and Lardon, J.M., *A Quantitative Approach to Fatigue Damage Evolution in FCC and BCC Stainless-Steels.* Scripta Metallurgica, 1985. **19**(12): pp. 1487-1490.

69. Wei, R.P., and Landes, J., *Correlation Between Sustained-Load and Fatigue-Crack Growth in High Strength Steels.* Materials Research and Standards, 1969. **9**: pp. 25-32, 44-50.

70. Harlow, D.G. and Wei, R.P., *Probability Modeling and Statistical Analysis of Damage in the Lower Wing Skins of Two Retired B-707 Aircraft.* Fatigue & Fracture of Engineering Materials & Structures, 2001. **24**(8): pp. 523-535.

71. Harlow, D.G. and Wei, R.P., *Probabilities of Occurrence and Detection of Damage in Airframe Materials.* Fatigue & Fracture of Engineering Materials & Structures, 1999. **22**(5): pp. 427-436.

72. Harlow, D.G., and, Wei, R. P., *A Critical Comparison Between Mechanistically Based Probability and Statistically Based Modeling for Materials Aging.* Materials Science and Engineering A, 2002. **323**: pp. 278-284.

APPENDICES
Appendix A: Tables
Appendix B: Figures

APPENDIX A

Table 1. Typical Roughness Values for Various Materials

Specimen	Preparation Method	Roughness (Ra)
Fracture Surfaces	None	100 nm - 5 mm
Steel	Mechanical Polishing (1-mm-diamond paste)	2 - 5 nm
NiAl Single Crystal	Mechanical Polishing (0.25 mm diamond paste)	1 nm
Superalloy	Chemical Etching	3 - 4 nm
Superalloy	Electropolishing	0.8 nm
Microalloyed Steel	Electropolishing	0.6 nm

Source: Goken, Mathias, University of Saarland, Germany, Veeco Technologies, Studies of Metallic Surfaces and Microstructure with Atomic Force Microscopy [9].

Table 2. Nominal Composition of Haynes C2000®

Nominal Chemistry	Nickel	Chromium	Molybdenum	Copper	Carbon	Silicon
Weight Percent	Bal.	23	16	1.6	0.01 Max	0.08 Max

Table 3: Chemical Composition of Various Corrosion-Resistant Nickel Alloys

ALLOY	COMPOSITION (wt.%)
Alloy 59	59Ni-23Cr-16Mo-1Fe
Alloy 686	46Ni-21Cr-16Mo-5Fe-4W
Alloy 625	62Ni-21Cr-9Mo-5Fe
Alloy 22	56Ni-22Cr-13Mo-3Fe-3W
Alloy C2000	60Ni-23Cr-16Mo-1.6Cu

Source: Meck, S. N. and Crook, P. "Localized Corrosion Susceptibility of Nickel Alloys in Halide Containing Environments." Corrosion - NACE Conference 2002 [32].

Table 4: Cyclic Polarization Electrochemical Parameters for Various Corrosion Resistant Nickel Alloys

ALLOY	E_{CORR}(mV)SCE	CPRx10^{-3} (mm/y)	I_{PASS} (mA/cm2)
Alloy 59	-467	4.82	1.15
Alloy 686	-426	2.91	1.36
Alloy 625	-474	2.90	2.28
Alloy 22	-505	1.71	1.75
Alloy C2000	-446	0.2	0.90

Source: Meck, S. N. and Crook, P. "Localized Corrosion Susceptibility of Nickel Alloys in Halide Containing Environments." Corrosion - NACE Conference 2002 [32].

Table 5. Common ASTM Standards Related to Fatigue

ASTM Standard	Standard Description
E466	Conducting Force Controlled Constant Amplitude Axial Fatigue Tests of Metallic Materials
E467	Verification of Constant Amplitude Dynamic Forces in an Axial Fatigue Testing System
E468	Presentation of Constant Amplitude Fatigue Test Results for Metallic Materials
E606	Strain-Controlled Fatigue Testing
E647	Measurement of Fatigue Crack Growth Rates
E739	Statistical Analysis of Linear or Linerarized Stress-Life (S-N) and Strain-Life (ε-N) Fatigue Data
E1012	Verification of Specimen Alignment Under Tensile Loading
E1823	Standard Terminology Relating to Fatigue and Fracture Testing

Source: Shigley, J.E., and Mische, R.M.., *Mechanical Engineering Design*. Fifth ed. 1989, New York: McGraw-Hill Book Company [7].

APPENDIX B

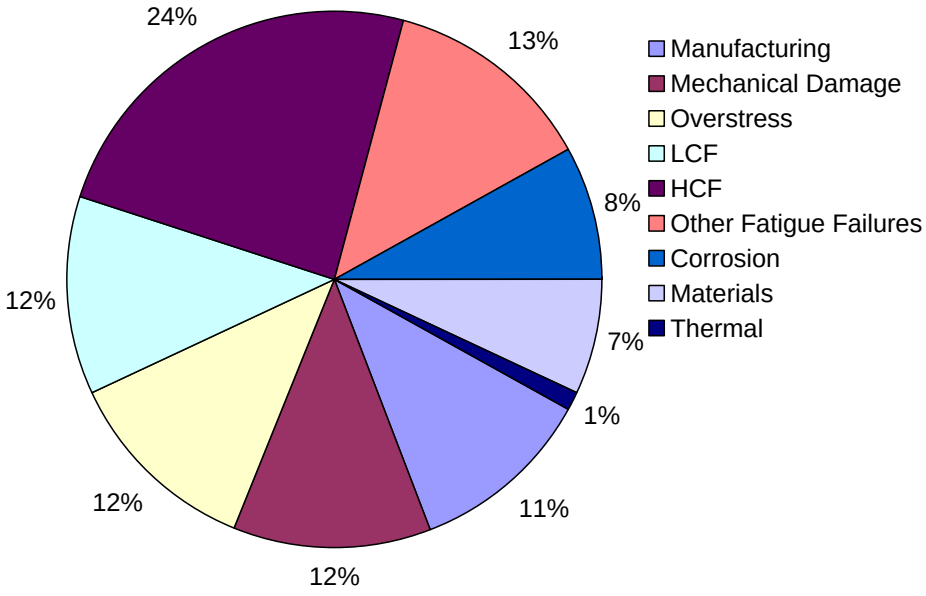


Figure 1. Fatigue Pie Chart: a) Distribution of Different Failure Modes in Jet Engines

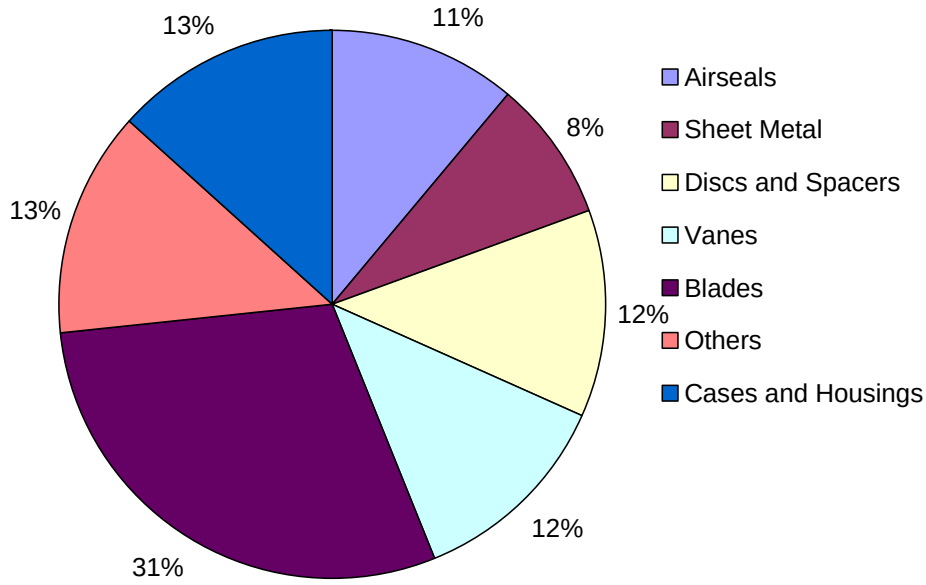


Figure 1. continued: b) Susceptibility of Different Components to HCF Problems

Source: Cowles, B. "High Cycle Fatigue in Aircraft Gas Turbines: An Industry Perspective." International Journal of Fracture. Vol. 80, 1996. (Reprinted from [1] with permission from Kluwer Academic Publisher.)

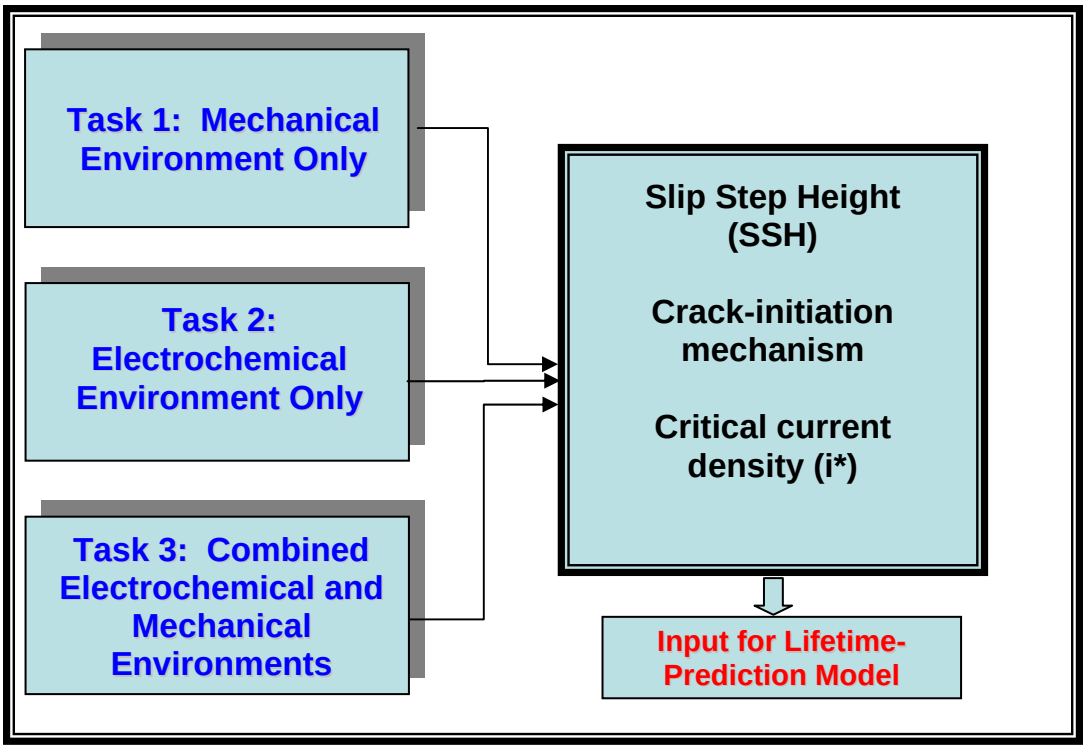


Figure 2. Research Tasks Flowchart

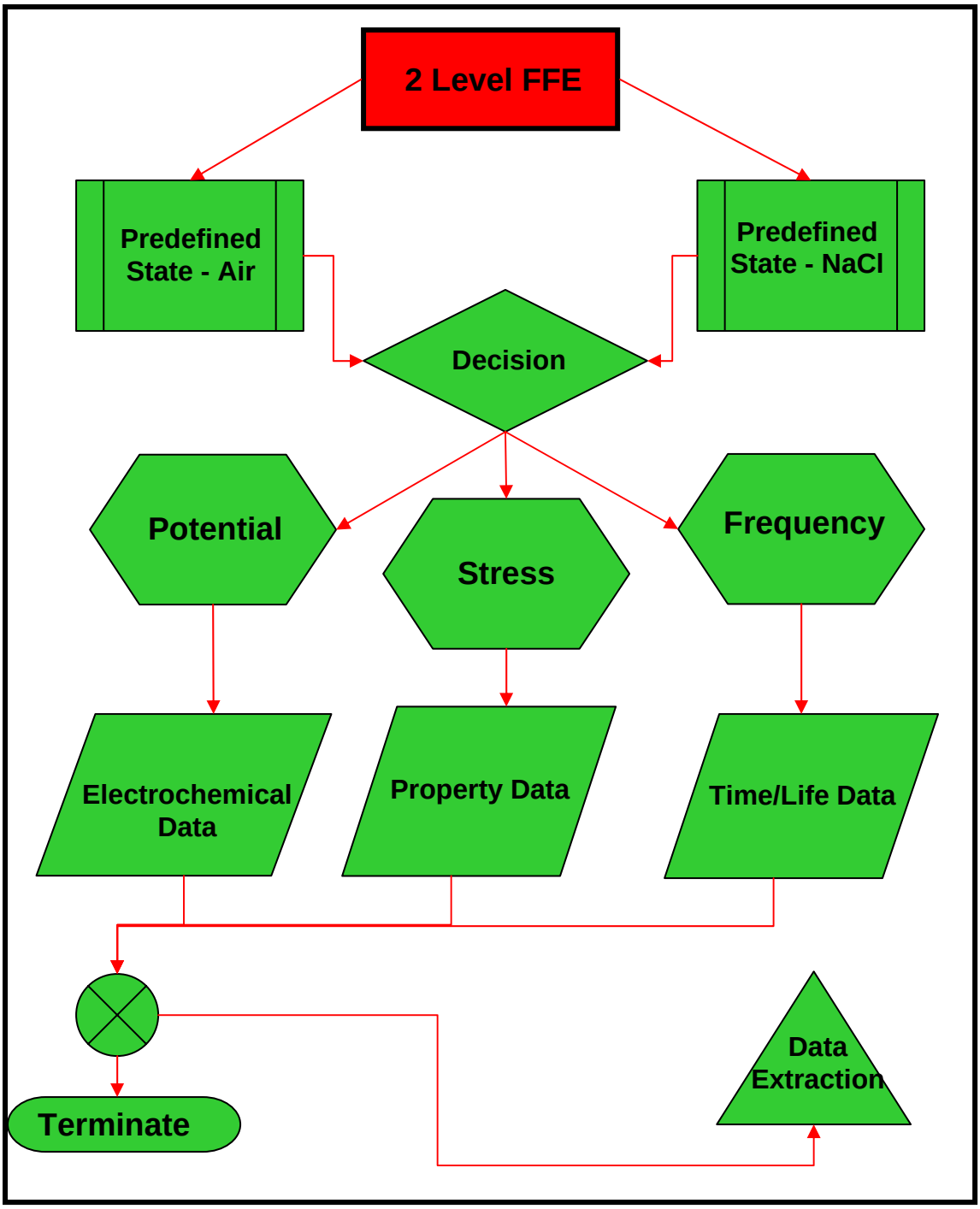
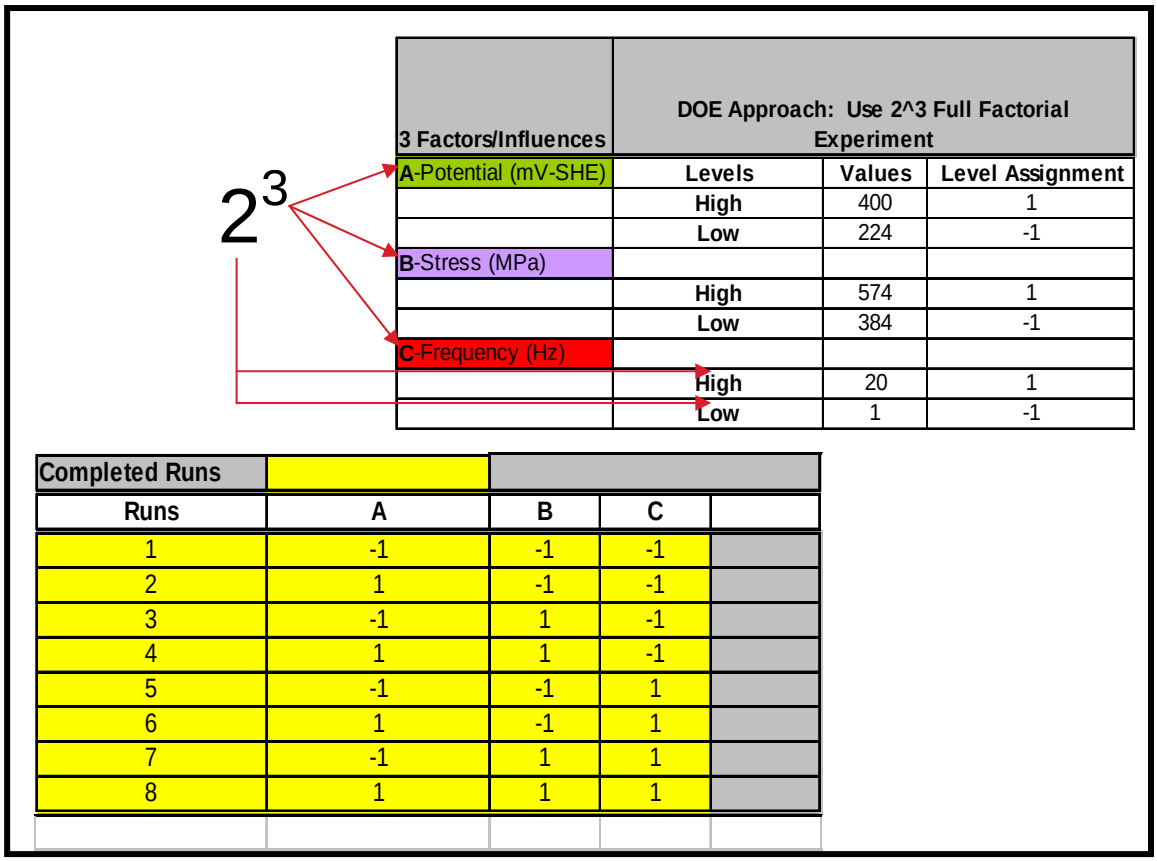


Figure 3. A Depiction of the Logic Process for the Design of Experiments of C2000



3 Factors/Influences	DOE Approach: Use 2^3 Full Factorial Experiment		
A-Potential (mV-SHE)	**Levels**	**Values**	**Level Assignment**
	High	400	1
	Low	224	-1
B-Stress (MPa)			
	High	574	1
	Low	384	-1
C-Frequency (Hz)			
	High	20	1
	Low	1	-1

Completed Runs				
Runs	**A**	**B**	**C**	
1	-1	-1	-1	
2	1	-1	-1	
3	-1	1	-1	
4	1	1	-1	
5	-1	-1	1	
6	1	-1	1	
7	-1	1	1	
8	1	1	1	

Figure 4. The 2^3 Full Factorial Spreadsheet for C2000

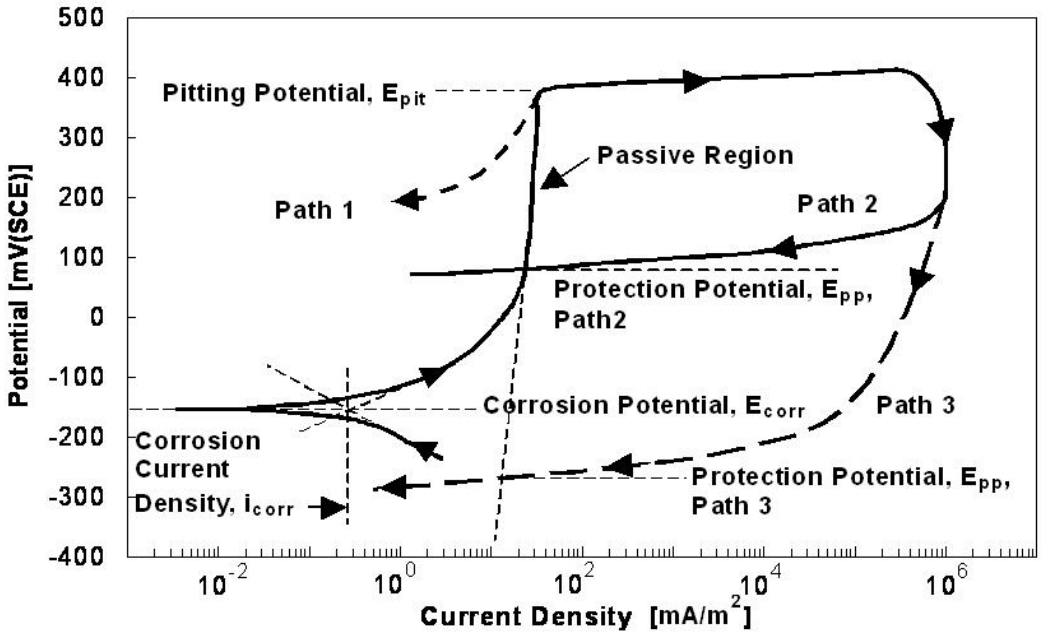


Figure 5. Typical Representation of Cyclic Anodic Polarization Curve

Source: Peter, W.H.; Buchanan, R.A.; Liu, C.T.; Liaw, P.K.; Morrison, M.L.; Horton, J.A.; Carmichael Jr., C.A.; and Wright, J.L. "Localized corrosion behavior of a zirconium-based bulk metallic glass relative to its crystalline state," Intermetallics, 2002; 10:1157-1162. (Reprinted from [4] with permission from Elsevier.)

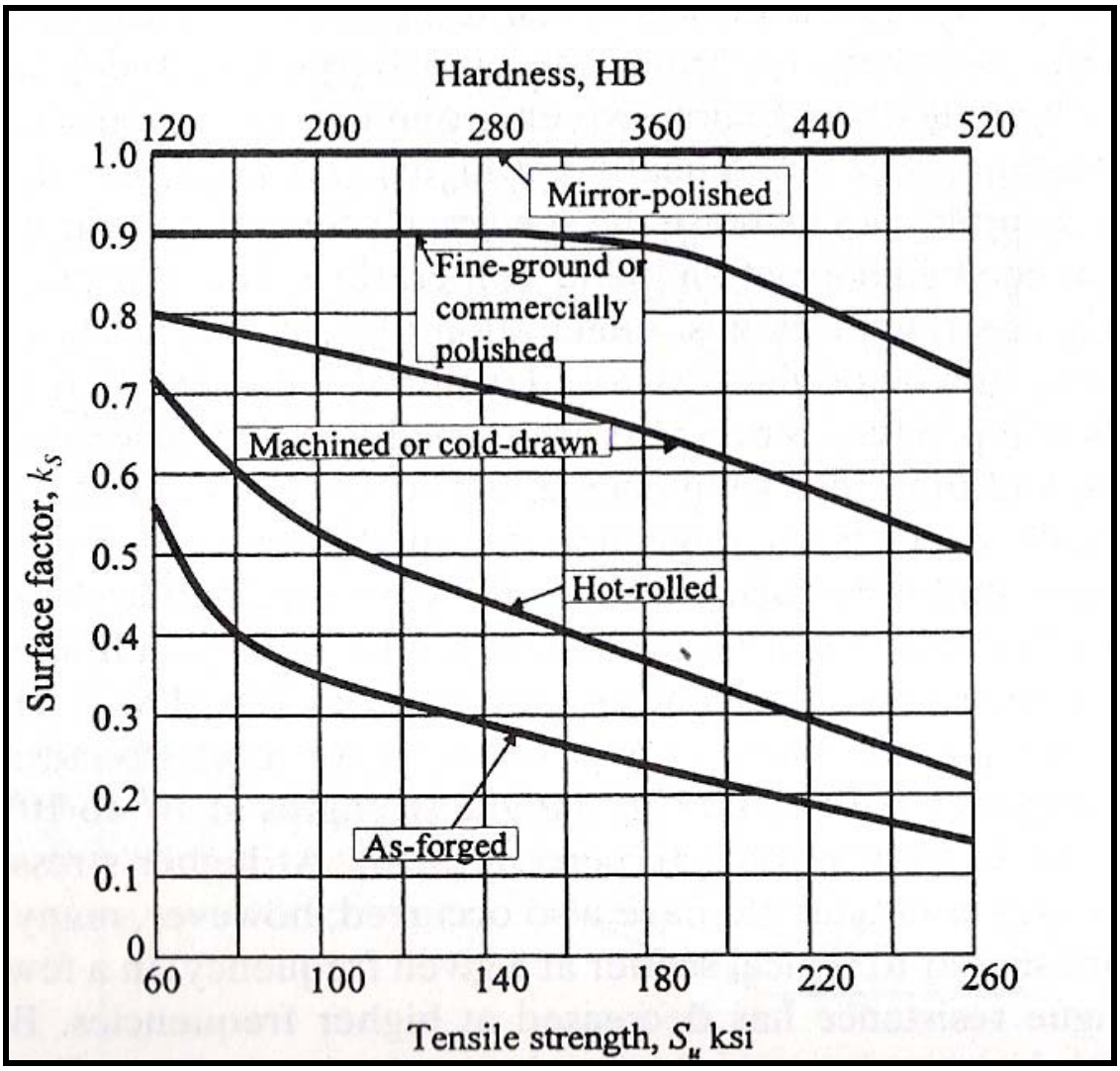


Figure 6. The Fatigue Properties of Materials for Various Surface Finishes

Source: Juvinall, R.C. and Marshek, K.M.., *Fundamentals of Machine Component Design*. Second ed. 1991, New York: John Wiley and Sons. (Reprinted from [5] with permission from John Wiley and Sons.)

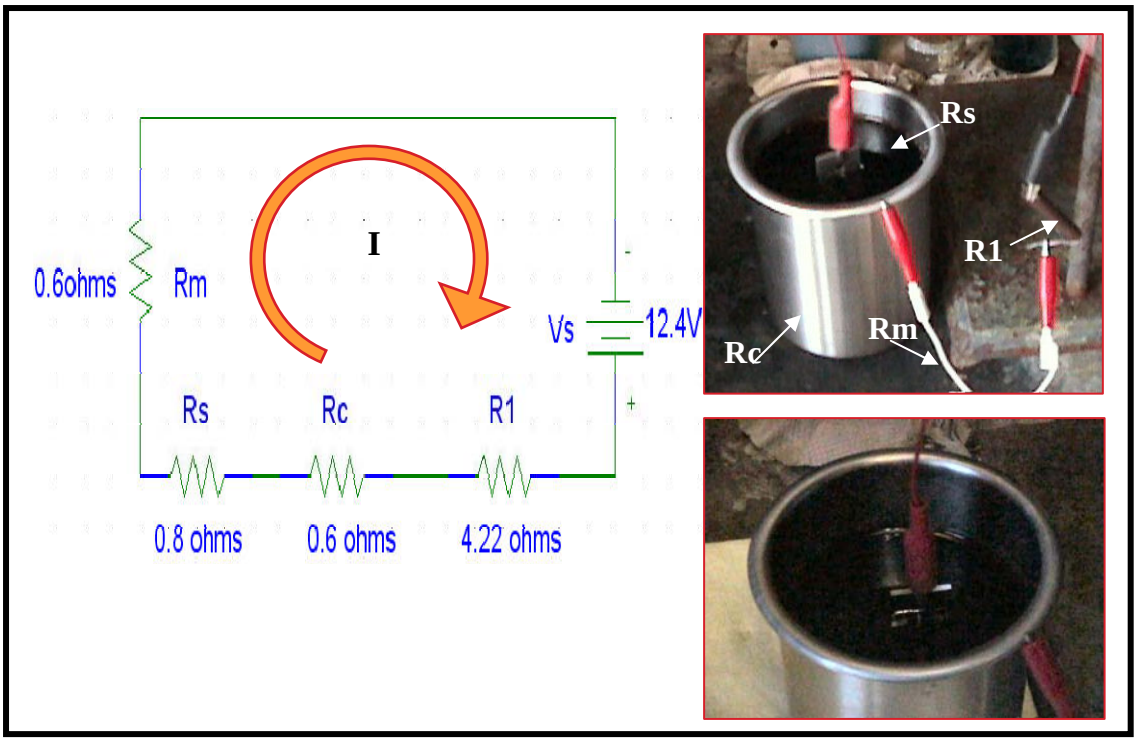


Figure 7. Electrochemical Cell and Circuitry Model for Electropolishing C2000

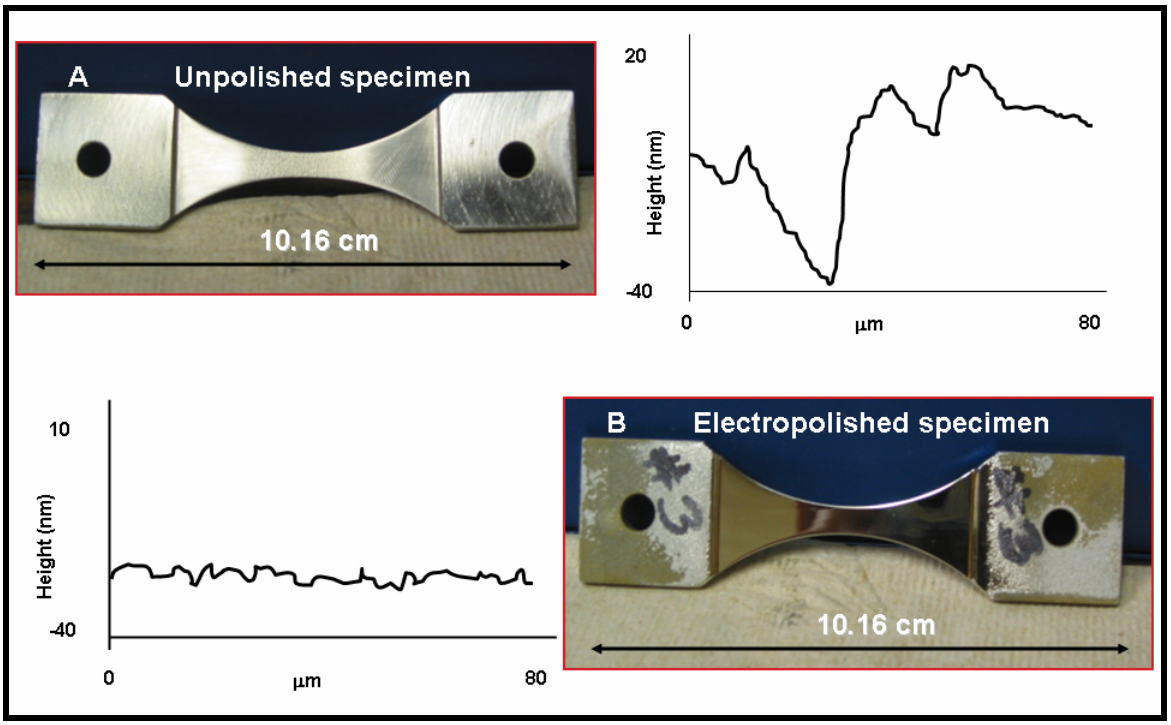


Figure 8. Unpolished and Polished Images of C2000 Samples

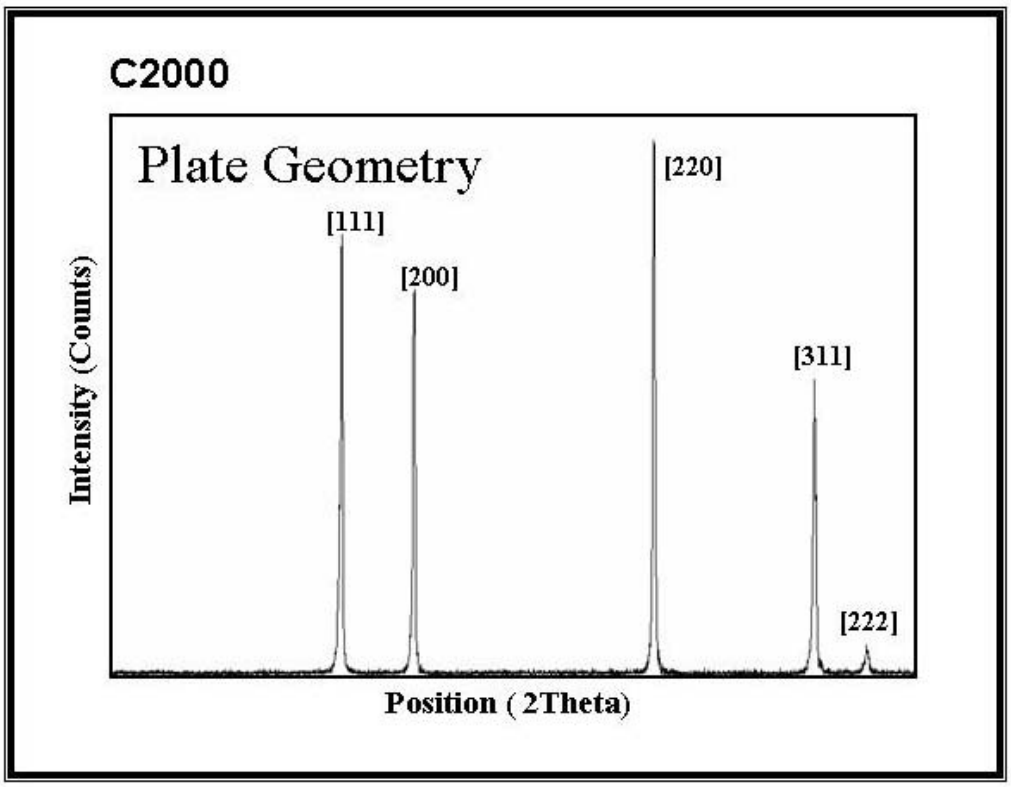


Figure 9. X-Ray Diffraction Data of FCC C2000

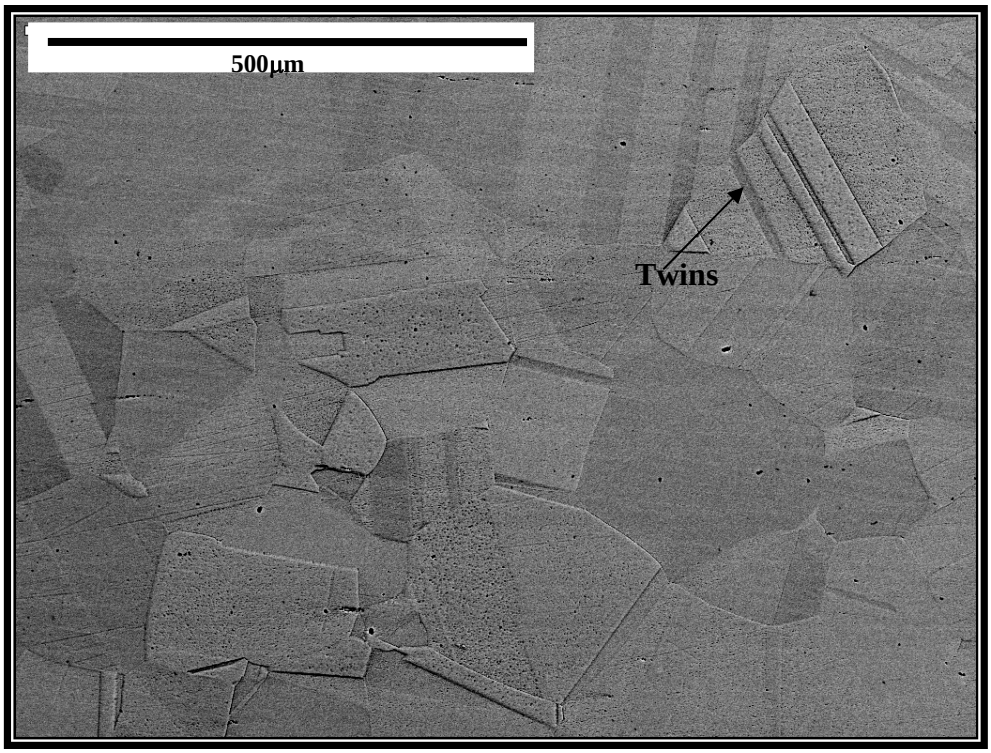


Figure 10. SEM Micrograph of C2000 Grain Morphology

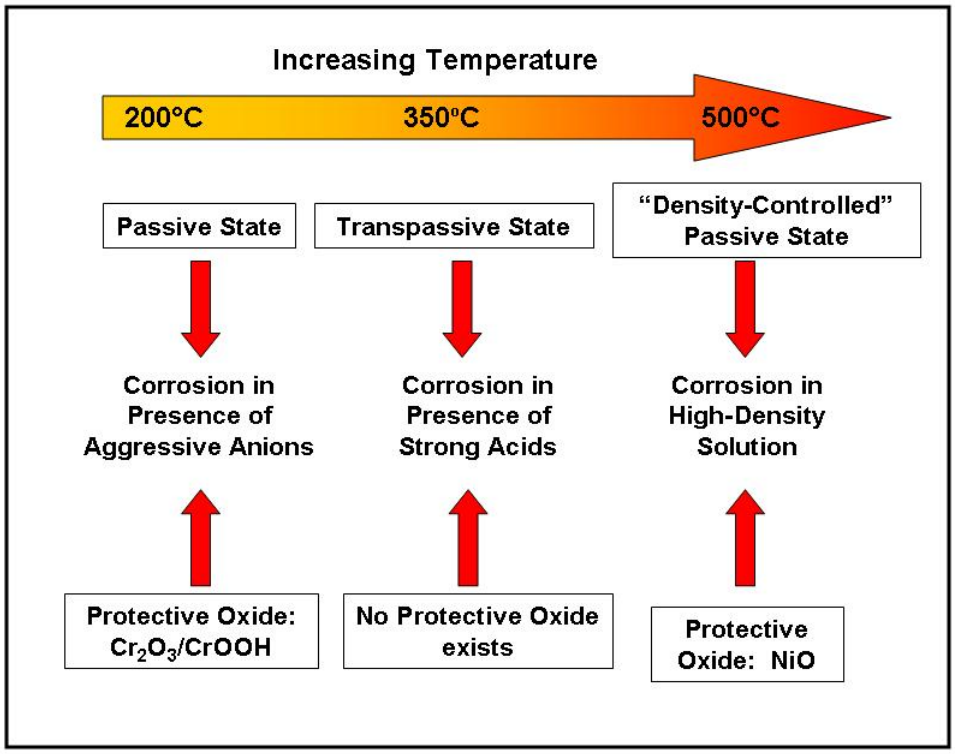


Figure 11. Effects of Increasing Temperature on Protective Oxide

Source: Kritzer P., Boukis N., and Dinjus E., "Review of the Corrosion of Nickel-Based Alloys and Stainless Steels in Strongly Oxidizing Pressurized High-Temperature Solutions at Subcritical and Supercritical Temperatures." Corrosion, Vol. 56, No. 11. (Reprinted from [34] with permission from the National Association of Corrosion Engineers.)

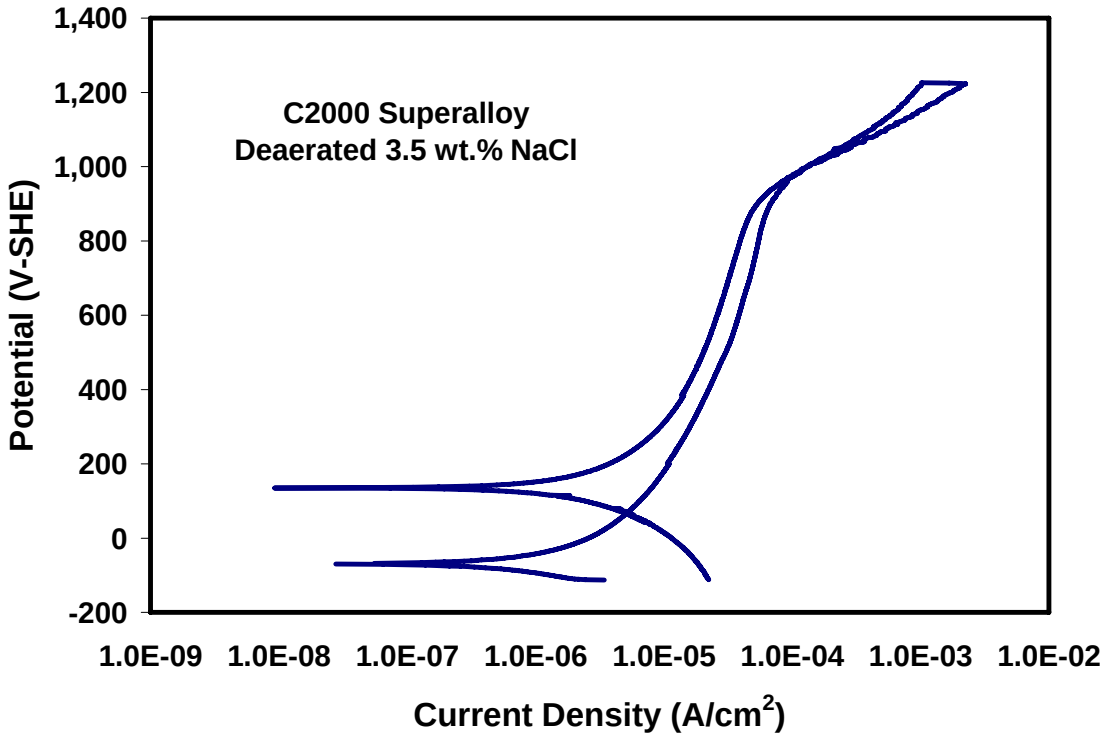


Figure 12. Cyclic Polarization Curve for Haynes C2000® Alloy in Deaerated 3.5 wt.% NaCl

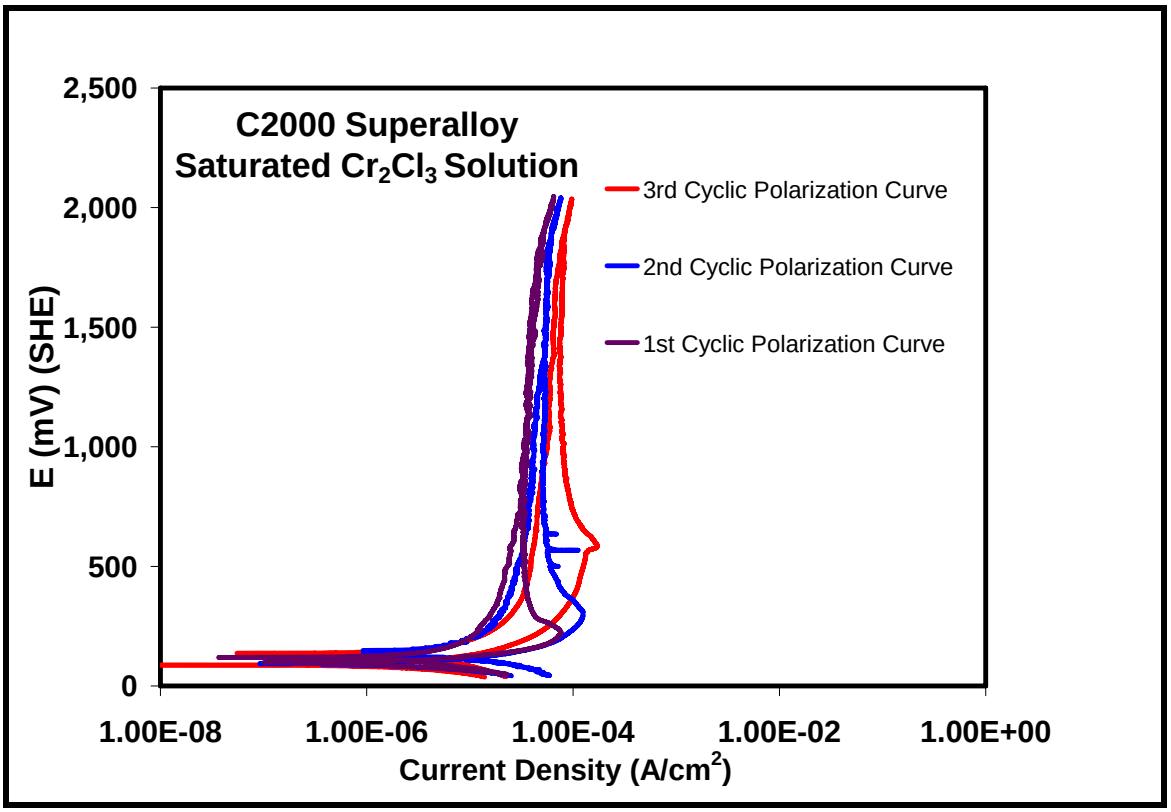


Figure 13. Cyclic Anodic Polarization Curve for Haynes C2000® in a Concentrated Metal-Ion Solution

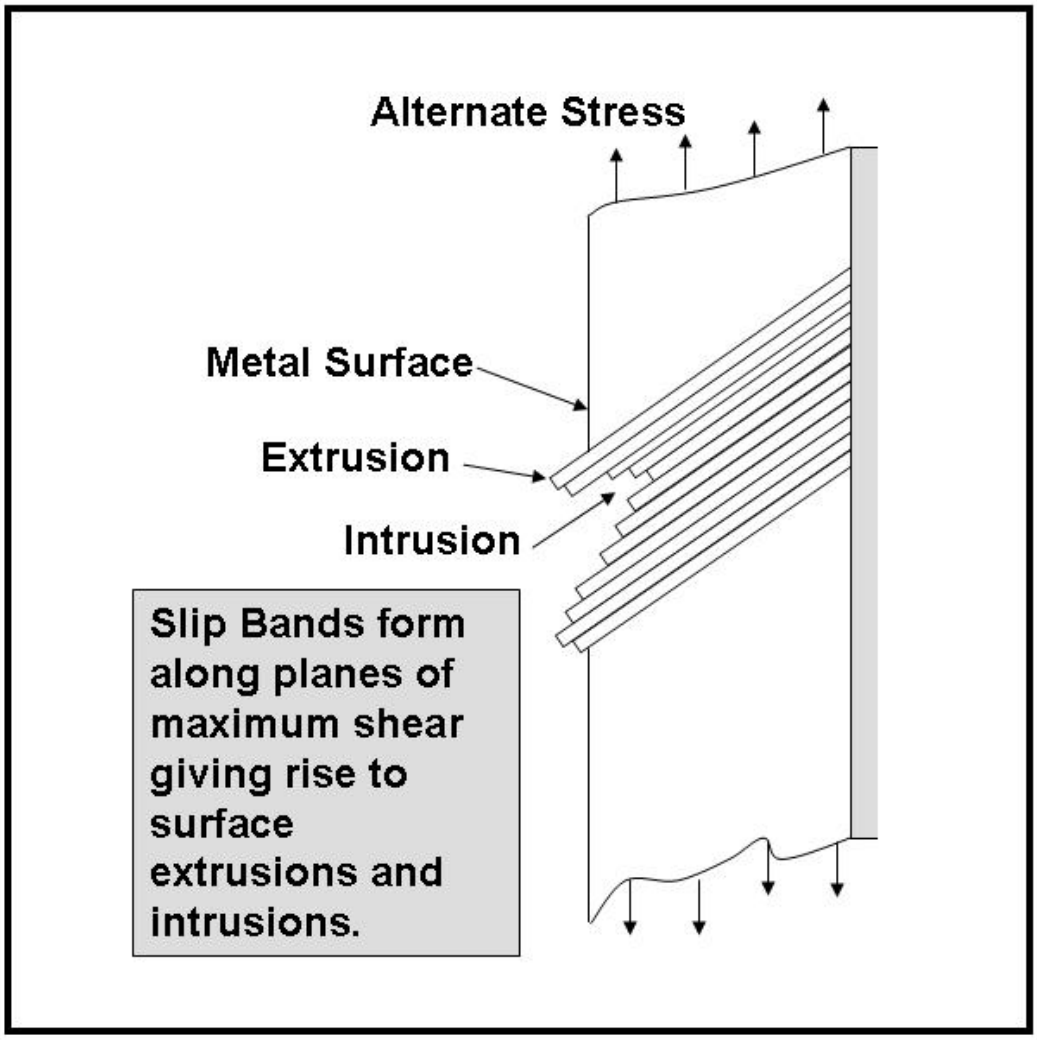


Figure 14. A Schematic of Persistent Slip Bands (PSB)

Source: Halfpenny A., A Practical Discussion on Fatigue, nCode International, Sheffield, UK [45].

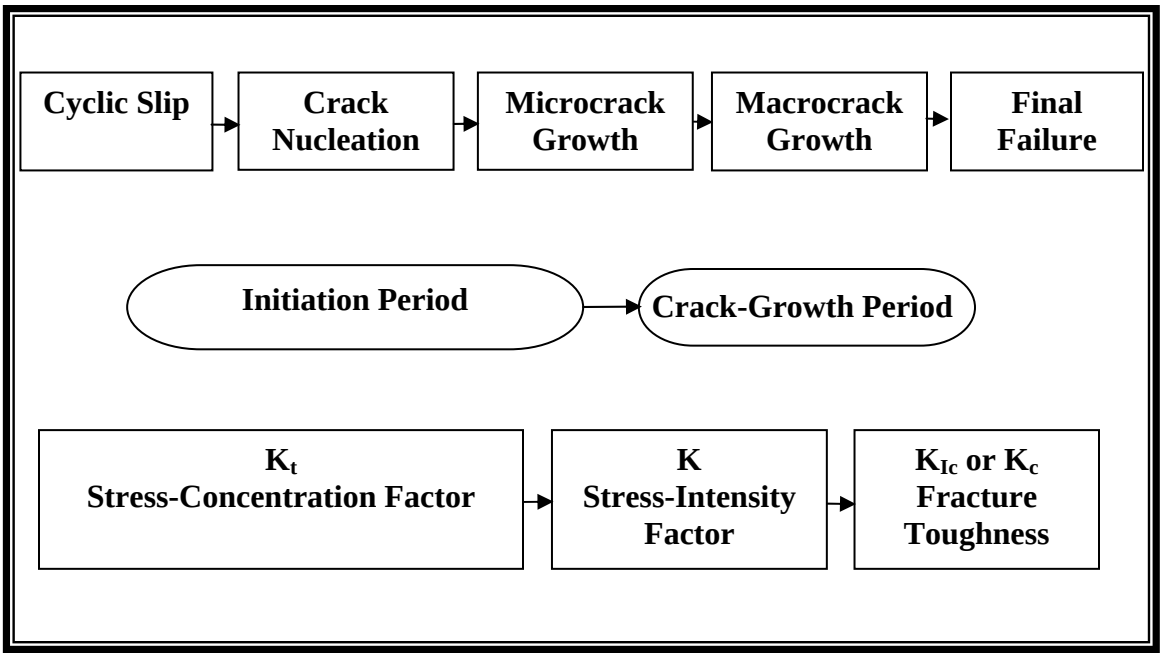


Figure 15. Different Phases of Fatigue Life and Relevant Factors

Source: Schijve J., Fatigue of Structures and Materials in the 20th Century and the State of the Art, International Journal of Fatigue, Vol. 25, 2003, pp. 679-702. (Reprinted from [46] with permission from Elsevier.)

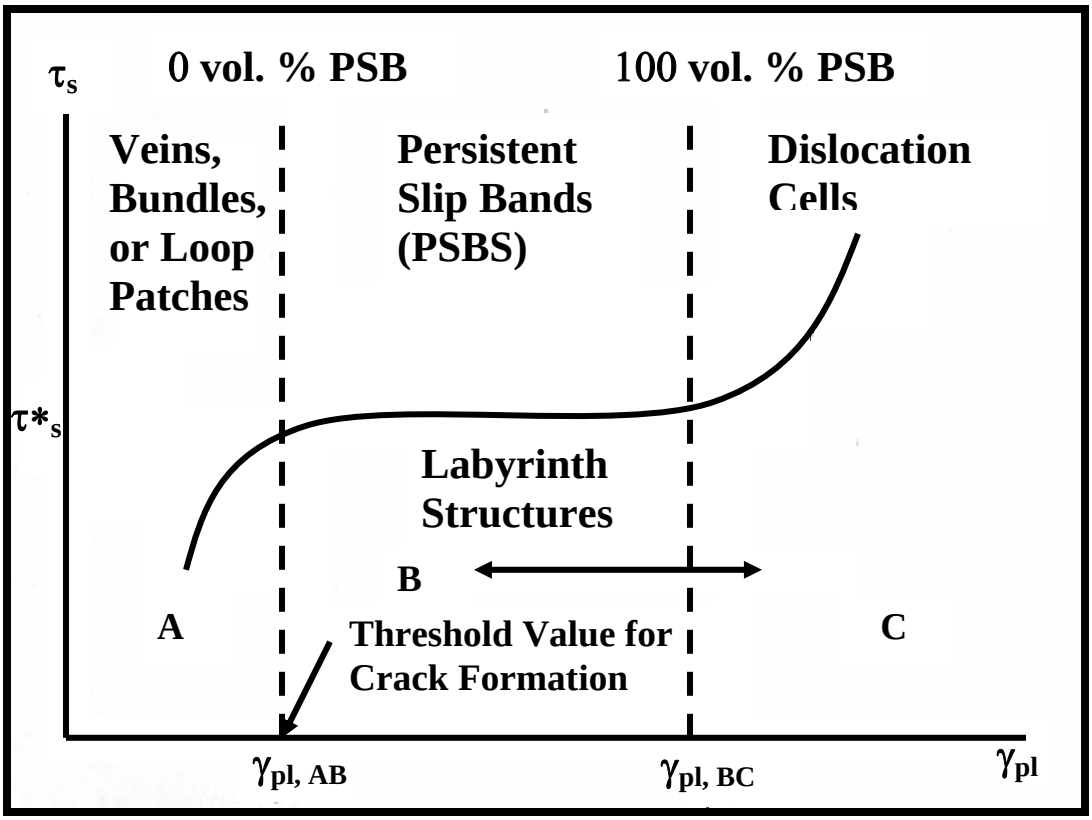


Figure 16. Different Regimes of Saturation Stress-Strain

Source: Suresh S., Fatigue of Materials, Second Edition, Cambridge University Press, 1998, pp. 42. (Reprinted from [52] with permission from the Cambridge University Press.)

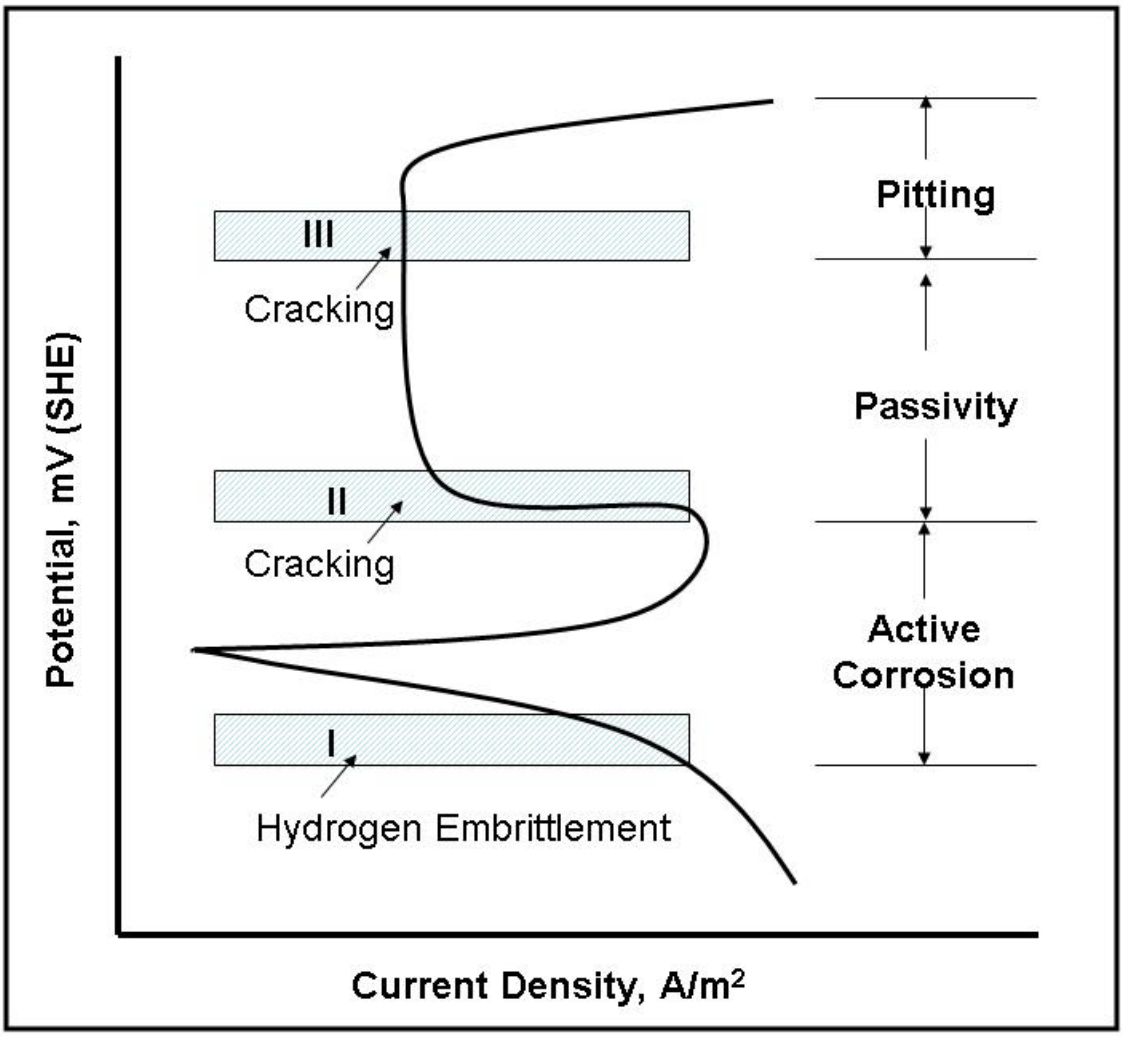


Figure 17. A Schematic for the Stress-Corrosion Cracking Behavior for Active Corrosion (Region I), Passivity (Region II), and Pitting (Region III)

Source: Stansbury, E. E., and Buchanan, R. A., Fundamentals of Electrochemical Corrosion, ASM International, 2000, pp. 371. (Reprinted from [39] with permission from the American Society of Materials.)

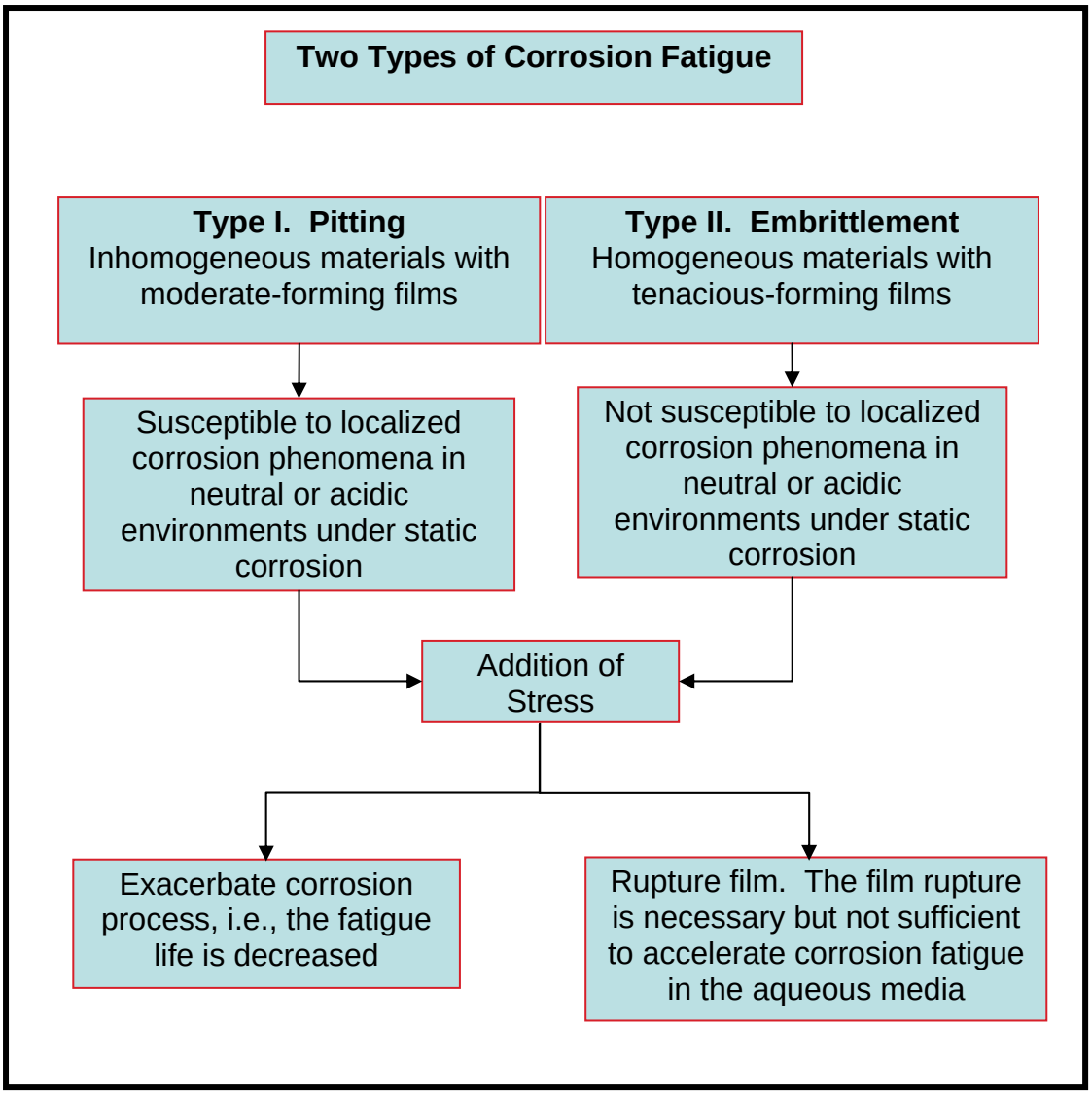


Figure 18. Types of Corrosion-Fatigue: a) Categories of Corrosion-Fatigue for Passivating Materials

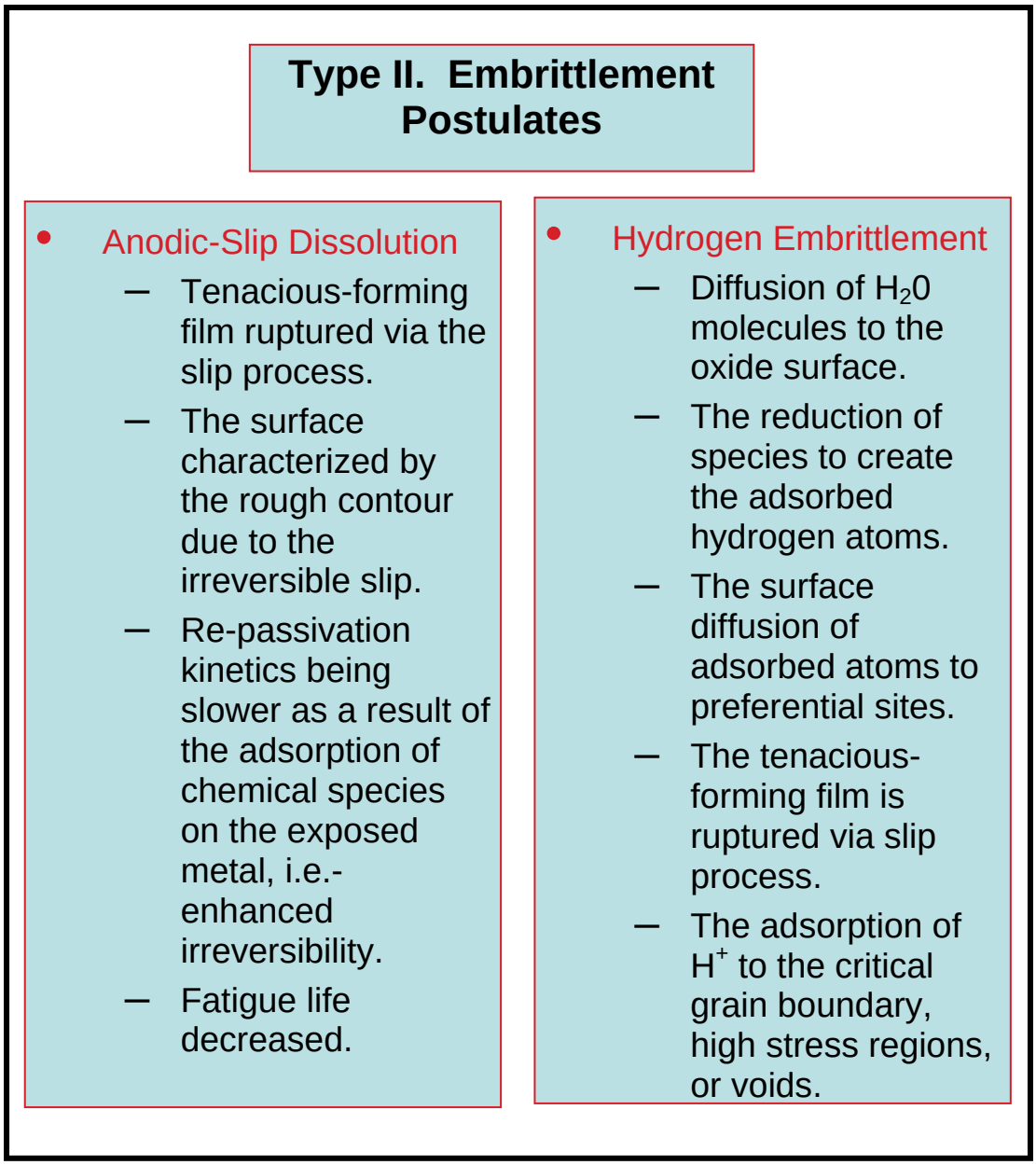


Figure 18. Continued. b) Type II Embrittlement Postulates for Passivating Materials

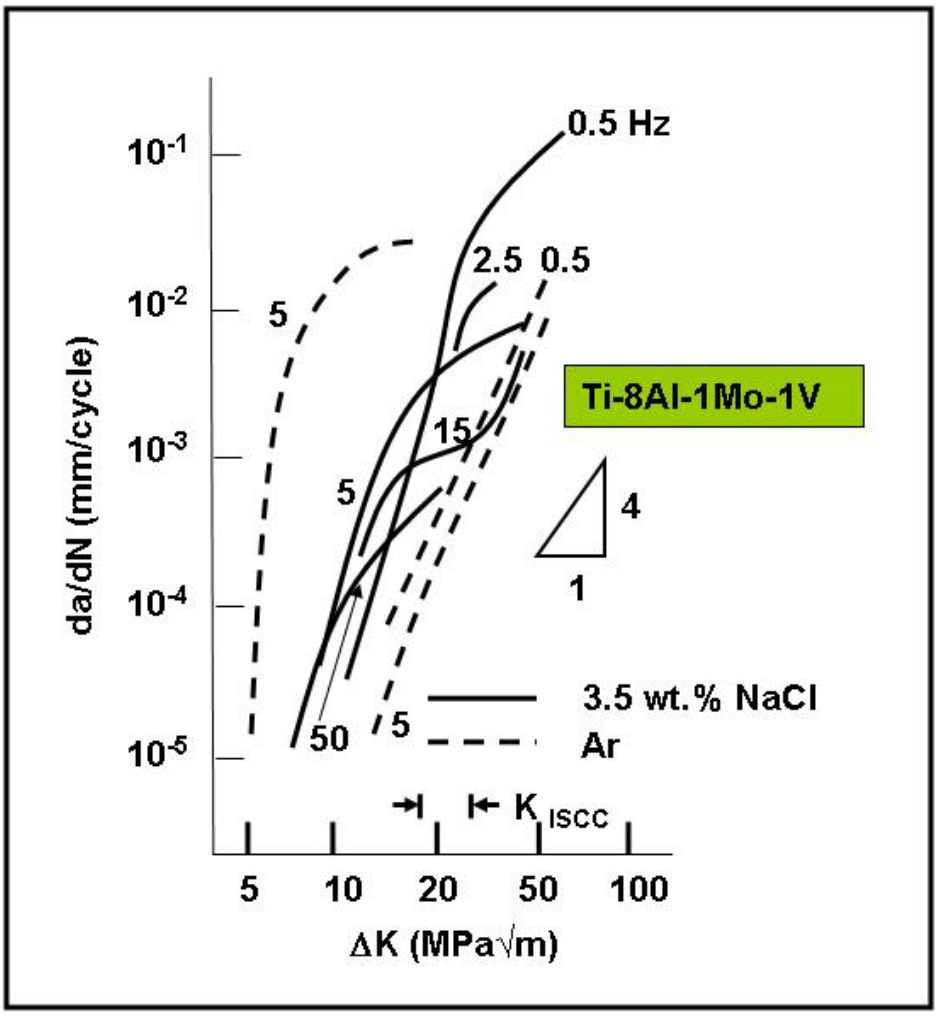


Figure 19. Frequency Effects on Corrosion Fatigue

Source: Suresh S., Fatigue of Materials, Second Edition, Cambridge University Press, 1998, pp. 583. (Reprinted from [52] with permission from the Cambridge University Press.)

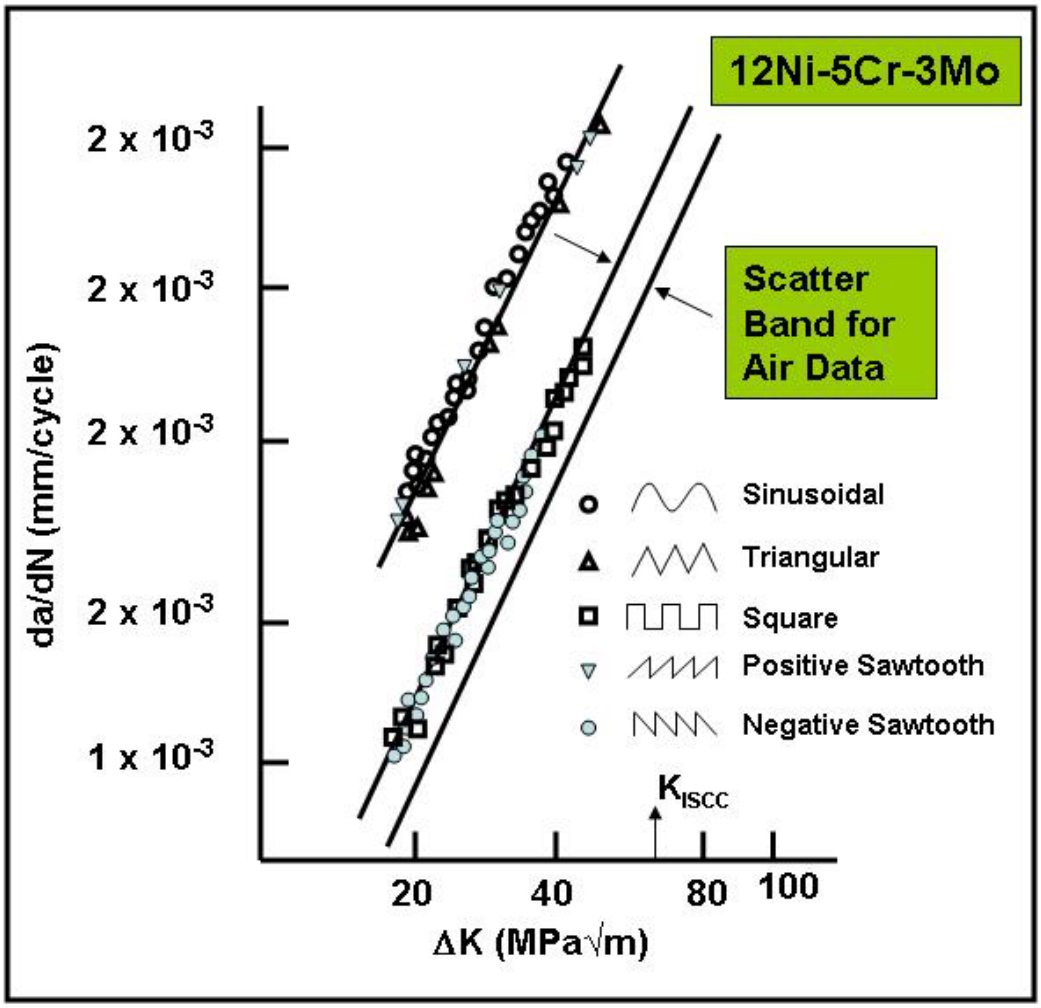


Figure 20. Waveform Effects on Corrosion Fatigue

Source: Suresh S., Fatigue of Materials, Second Edition, Cambridge University Press, 1998, pp. 584. (Reprinted from [52] with permission from the Cambridge University Press.)

PART II

In-Situ Electrochemical Investigations of a Nickel-Based Alloy Subjected to Fatigue

1. Introduction

The Hastelloy C2000 is a nickel-based alloy rich in chromium and molybdenum to yield a high-corrosion-resistance performing alloy for piping, repositories, and valve fixtures. Fatigue behavior in adverse solutions, namely 3-4 weight percent (wt.%) NaCl was determined by Asphanani [1] for Ni-Cr with additions of molybdenum or other elements to determine the effects of a sodium-chloride solution on the fatigue-endurance limit. Although many papers have been published in the literature to study the effects of corrosive media on the fatigue behavior of conventional materials, such as stainless steels [2-6], the research manifesting the fatigue behavior of nickel-based alloys is limited for the monitoring of corrosion-fatigue behavior [1, 7, 8]. Additionally, most corrosion-fatigue studies are performed on materials that have moderate-forming protective films; and, thus, these materials are susceptible to the localized corrosion at a critical potential, E_p, above the natural potential of the material. When cyclic stresses are imposed, the materials susceptible to corrosion experience a subcritical potential value to pitting. Therefore, the deterioration of the fatigue life is observed due to the coupling of the corrosive environment and the cyclic stresses, and the localized corrosion has caused the material to fail severely.

Most materials that possess a strong passive current density with no pitting potential will withstand a premature fatigue-failure when studied in room-temperature conditions. However, reports in the literature show a deterioration of the fatigue life in the presence of 4 wt. % NaCl for nickel-chromium-molybdenum alloys possessing a 16 wt.% of chromium or less. Therefore, studies on materials with extremely

tenacious passive films, which usually have a chromium content greater than 16 wt.%, are of interest. Currently, there are no publications known to the author on the fatigue behavior of chromium-rich alloys possessing a wt.% greater than 22 wt.% in NaCl solutions, especially those monitoring corrosion-fatigue characteristics. In this investigation, the potential, frequency, and exposure times in 3.5 wt.% NaCl are studied to determine the transition in which electrochemical influences dominate the fatigue behavior.

2. Experimental Setup

2.1 Metallographic Preparations and Electrochemical Experiments: The Hastelloy C2000 superalloy is a face-centered cubic structure at all temperatures. The material has a nominal composition in wt. % consisting of 23 wt.% Cr, 16 wt. % Mo, 1.6 wt. % Cu, and balance Ni. The ultimate tensile strength is approximately 750 MPa for a sheet form. The natural potential of C2000 in 3.5 wt.% NaCl solutions is approximately -224 mV on a standard hydrogen-electrode scale.

For static electrochemical measurements, Hastelloy ® C2000 samples were coarse ground to a 800 grit finish using silicon-carbide grinding pads manufactured by Buehler. A final fine polish was achieved using a diamond paste slurry for 4 hours on a Buehler Vibromet 2 vibratory polisher to produce a 1 micron finish.

2.2 Electrochemical Cell: The electrochemical analysis was conducted in a 2-liter cell consisting of a platinum-counter electrode to support the corrosion reactions in Figure 1. The sample is firmly mounted in epoxy. An electrical contact was made with the sample by tapping a brass screw through the epoxy holder to the sample or working electrode. The working electrode is secured to the u-tube by screwing the sample into a brass screw inset of the u-tube. The sample is submerged into the 2-liter cell via the suspension of the u-tube from an orifice located at the top of the glass container. A polymeric washer placed around the tapped brass screw extending from the back of the epoxy holder helps preclude contact with the 3.5 wt.% NaCl electrolyte. Yet, the washer does not interfere with the electrical contact made by the brass screw with the brass inset located in the u-tube. A saturated calomel electrode

(SCE) connected by a saturated potassium chloride salt bridge served as the reference electrode, which allowed the charge passage for potential measurement readings.

Cyclic-anodic-polarization and potentiodynamic experiments were initiated at a potential of 50 mV below the free potential of the alloys investigated at a scan rate of 0.167 mV/s. A Princeton Applied Research Model 263A potentiostat/galvanostat was interfaced with the electrochemical apparatus to control voltages, monitor currents, and record responses for data analyses using an EG&G 352 SoftCorr III software. All potential values recorded during electrochemical measurements were converted to the standard hydrogen-electrode (SHE) scale for scratch and cyclic-anodic polarization results.

2.3 Mechanical Scratch Tests: Experimental mechanical scratch tests were also performed in a 2-liter cell with a platinum electrode as the counter electrode. The C2000 sample served as the working electrode. As in the cartoon depicted in Figure 1 (All figures and tables are listed in the appendices), the working electrode is secured to the u-tube via a brass screw making an electrical contact with the sample through the epoxy holder and brass screw inset. The sample is submerged into the 2-liter cell via the suspension of the u-tube from an orifice located at the top of the glass container. A saturated calomel electrode connected by means of a salt bridge acted as the reference electrode. While monitoring the current-density response to increasing potentials, scratch tests were conducted with a diamond-tip stylus to mechanically scratch the oxide film. Scratch tests were initiated at 25 mV intervals up until approximately 1,000 mV for 10 seconds during each interval to observe the repassivation kinetics.

2.4 Corrosion-Fatigue Experiments and Surface Preparations: Fatigue experiments were performed with a closed-loop servo-hydraulic Materials Testing System (MTS). Figure 2 shows a picture of the experimental setup for the corrosion-fatigue chamber used to conduct corrosion-fatigue experiments on C2000. The samples were affixed to grips via a ceramic pin-joint assembly to isolate the sample from grips, i.e., to prevent galvanic coupling. A free-floating Teflon top allowed the connection of the working electrode, which is the sample, the platinum counter electrodes, and the salt bridge for electrochemical testing. Experiments were conducted at frequencies of 20 Hz, 5 Hz, and 1 Hz with a constant R-ratio (minimum stress/maximum stress) of 0.1. All fatigue tests were performed under uniaxial tension-tension conditions. Experiments were conducted at each frequency in both the air and 3.5 wt.% NaCl solution. The free potential or natural potential of C2000 and a potential value of 350 mV against a SCE reference electrode were the two potential values controlled during fatigue testing.

The specimens for the C-2000 superalloy were machined from blanks into a flat geometry according to guidelines outlined in the American Society for Testing and Materials (ASTM) E8-M and E-466 specifications [9]. The final geometry was a 50% reduction of the dimensions stated in the ASTM guidelines (Figure 3). The dimensions of the specimen were machined to 101.6 mm in length with a center thickness of 1.59 mm and a hole diameter of 6.6 mm. Each sample consisted of a continuous radius to ensure crack initiation within the center area and the ease of the crack identification under the scanning-electron microscope (SEM). To generate the stress versus fatigue life cycle (S-N) data, 600 grit, 800 grit, and 1,200 grit silicon-

carbide papers were used to bevel the edges of the samples. For careful examinations of the fatigued surface under SEM, additional samples were given an optimal surface finish by electropolishing the sample for seventy-five minutes at 5V and 1.5 amps in a methanol and a sulfuric acid bath.

2.5 Characterization: The characterization of the as-received material was done with a transmission-electron microscope**.** Transmission-electron-microscopy (TEM) observations were carried out, using a Schottky field-emission gun FEI Tecnai F20 UT microscope with a spatial resolution of 0.14 nm operating at 200 kV. The TEM thin-foil specimens were prepared by the conventional twin-jet electro-polishing technique using a 25 volume percent (vol.%) nitric acid + 75 vol.% methanol solution at -30°C and 10 V. The observation of the fracture morphologies and crack-initiation phenomenon was visualized, using a Leo scanning-electron microscope operating at 20 kV with energy-dispersive-x-ray-spectroscopy (EDS) capabilities.

3. Results

Figure 4 shows the S-N curves for C2000 (Ni-23 wt.%Cr- 16 wt.%Mo) having a coarse-ground finish in both 3.5 wt.% NaCl solutions and air, and a nickel (Ni-16 wt.%Cr-16 wt.%Mo) alloy studied by Asphanani in both air and 4 wt.% NaCl. For both alloys, the fatigue behavior in air is similar, while the fatigue endurance limit of the C2000 in NaCl is higher than that observed for the Ni-16 wt.%Cr- 16wt.%Mo alloy. However, relative to the fatigue life in air, the fatigue life of C2000 in NaCl shows an innocuous trend, while the fatigue life of the 16 wt.% Cr alloy exhibits a decrease in NaCl. Evidently, the higher concentration of chromium is beneficial to maintaining the fatigue life in the C2000 than the Ni-16wt.%Cr- 16 wt.% Mo alloy.

The ability for a material to repassivate or protect the underlying material by providing an oxide film is necessary to impede localized corrosion, such as pitting. Simulated mechanically-perturbation tests provide an indication of the repassivation behavior, as shown in Figure 5. Using a potentiostat, a potential versus current-density curve is generated. A diamond-tip stylus is used to scratch the surface for 10 seconds before removing. The response to the scratched line is represented by an increase in the current density. After 10 seconds, the current density returns to the passivation-current density, i_p. Since the current excursions observed during the scratch tip-unloading segment of the curve are retraceable with that observed during the scratch tip-loading, a rapid repassivation kinetics is inferred (Figure 5).

Experiments to determine the current responses to the in-situ corrosion-fatigue performed at a stress amplitude, σ_a, of 574 MPa and a frequency of 20 Hz are depicted in Figure 6. Region A is in the potential range of -75 mV – 150 mV, which

represents the early stages of fatigue where the cycle range is from 0 – 60,000 fatigue cycles. The critical potential region, ~ 150 mV – 550 mV, represents the portion of the fatigue behavior where 60,000 – 120,000 fatigue cycles have accrued, and it is also a susceptible region to localized corrosion attack. Unlike the results from those shown in Figure 5, a delay in the current response upon the scratch tip-unloading is indicated by the current transients outlined with a square box known as the critical potential region. The presence of current transients suggests that there are locations where fresh metal is exposed for localized corrosion to occur. Passing the critical potential region is Region B, ~550 mV – 800 mV, where the cycle range is from 120,000 – 200,000 cycles. An SEM micrograph of the slip events on the fatigue surface associated with the critical potential range and the corresponding fatigue cycles is captured via an SEM image, which is shown in Figure 7. Since the amount of the bare material exposed during the slip activities is related to the current density through Faraday's law, a current density versus time diagram can provide a better understanding of the repassivation kinetics for the fatigue sample in 3.5 wt.% NaCl. Thus, the critical-current data associated with the critical potential range can provide useful information concerning the repassivation and subsequent film-rupture time scales for the surface-damage events. Figure 8 shows a current versus time plot where the time axes represent the total time span for the current transients within the critical potential range. The dotted line represents the absence of stresses whereas the solid line represents the response to increasing potentials during cyclic loading. In Region 1 of Figure 8, the time for the repassivation is approximately one minute or 60 seconds. In Region 2, the time for a subsequent event to occur can take as long as 5

minutes or 300 seconds. Overall, the time frame for the incipient surface-damage-event activities vary as well as the time required to repair the ruptured film associated with the collective surface-damage events.

Each current transient is believed to be correlated with the slip-steps emerging on the surface, since these are the only visible features observed under SEM examinations during interrupted fatigue intervals. Hence, the current rise is associated with the film rupture imposed by the material's intrinsic slip mechanisms. To better substantiate the notion of slip steps being the only contributor to the observed current transients, a potential of 350 mV was chosen as the constant potential value to monitor the current responses without the addition of stresses over time. Figure 9 shows the results of holding the potential constant at 350 mV. In Region 1, the current is steady over times. The dashed lines demarcate a deviation from a steady-state current behavior to the onset of a sharp increase in the current. The current decay associated with the repassivation occurs over seconds at which time a steady-state behavior is once again achieved, albeit it is at a higher current. In Region 2, current-transient peak values are not as high as those observed in Region 1. However, the repassivation time appears to be slightly longer. Region 2s shows that the steady-state current achieved after the repassivation is stable for some time period. Notice that in Region 2s, the steady-state current is higher than the steady-state current in Region 1. Further monitoring of the current over time manifests another sharp current spike associated with the exposure of surface-damage events. Unlike the current behavior in Region 2, the repassivation kinetics is faster but the steady-state current is approximately 30 microamps higher. The inspection of Region

4 yields a current trend similar to Region 3, with the exception of the inability to reach a steady-state value with increasing times. Thus, the non-steady state current behavior appears to dominate at times greater than 90,000 seconds. The behavior in Region 4 infers that an electrochemical influence can govern the fatigue life for C2000, if the material is subjected to a constant potential of 350 mV for approximately 90,000s before performing fatigue. The reason for the introduction of a hold time at a constant potential of 350 mV in the electrolyte before commencing fatigue is to induce a corrosion-fatigue effect, which will provide a better understanding of the possible controlling variables if C2000 were to be placed in an electrolyte having a similar oxidizing power. Thus, a non-steady state current response observed in Region 4 of Figure 9 implies that the protective oxide is less protective than at times below 90,000s. Without a good protective oxide layer, the material becomes more susceptible to anodic dissolution. For time periods less than 90,000s, a steady-state current is recovered, even if current transients appear. Consequently, the surface-damage events plotted in Figure 8 must be strongly associated with the exposure of the bare material upon the emergence of slip steps to the surface. Thus, it appears that a reasonable oxide film is most likely maintained even with the addition of cyclic stresses and increased potentials for short electrolyte exposure times.

SEM micrographs revealing the fractographs for C2000 fatigued at a stress amplitude of 574 MPa in 3.5 wt.% NaCl at frequencies of 20 Hz, 5 Hz, and 1 Hz are displayed in Figures 10 and 11 along with the representative EDS patterns. EDS profiles were taken from the crack-initiation site to the edges of the propagation

region. From EDS, chlorine is possibly forming an undetermined chloride at the crack-initiation site, which requires the usage of X-ray photoelectron spectroscopy (XPS) or Raman spectroscopy. In each figure, the EDS profiles at the crack-initiation site are shown. Since chromium is more favorable to forming an oxide than nickel, a normalized representation of the chloride counts with that of the nickel was tabulated. Table 1 shows the normalized count trend for the measurements taken at 20 Hz, 5 Hz, and 1 Hz. As the frequency decreases from 20 Hz to 5 Hz and 1 Hz, the normalized count at the crack-initiation site is decreasing. The means by which the chlorides are being transported may be assisted by chloride channels. Possible secondary chloride channels were observed on C2000 studied in 3.5 wt.% NaCl at a frequency of 1 Hz and a stress amplitude of 574 MPa. Figure 12 shows an SEM micrograph of the features, which are believed to be secondary chloride channels that were observed on the surface of the C2000 sample.

The fracture surface of C2000 fatigued in air at a frequency of 20 Hz is shown in Figure 13. In the absence of the corrosive media, the fracture appearance of C2000 manifests a ductile appearance with three fairly distinctive regions: A) crack initiation, B) crack propagation or growth, and C) fast fracture region. Conversely, C2000 held at a potential of 350 mV over a period of seven days in 3.5 wt.% NaCl at a frequency of 20 Hz reveals a strikingly different fracture morphology. Figure 14 reveals a washed-out surface morphology where there are no distinct fracture regions. The washed-out fracture morphology is most likely associated with the anodic-dissolution behavior of various chloride channels merging to create an eroded or indistinct appearance on the fractured surface.

The crack-initiation site is captured during an interval within the corrosion-fatigue cycles. The enclave of the crack width is much wider at the center as compared to the edges. This behavior suggests that the crack initiation originated at the center of the crack shown in Figure 15. The nucleation of small flaws along the slip bands or steps was observed under the transmission-electron microscopy (TEM). Figure 16 shows a TEM image of a flaw along a slip band having a length of approximately 300 nm.

4. Discussion

Both slip dissolution and film rupture are mechanisms commonly associated with the removal or disturbance of oxide films on metallic materials. Sophisticated scratch tests [10] have been performed to better understand the repassivation kinetics, and models have been derived to capture the behavior of oxides during and following scratch tests. These conventional tests provide useful insights into the time necessary to reform a protective layer. However, scratch tests conducted by a diamond stylus on coupons submerged in an aqueous corrosion solution do not adequately account for the interaction of the bare material with the cleaved oxide layers. Hence, a more ideal experiment is needed to account for such interactions to provide a clearer understanding of how emerging slip steps affect the oxide repassivation. If a material is not susceptible to pitting under static corrosion conditions due to a strong tendency to maintain passivity, the influence of an electrochemical environment will not be observed if the passive film is not ruptured. Once a film rupture has occurred due to emerging slip steps, the mass transport of detrimental ions from the bulk solution can cause adverse effects on the fatigue behavior. Otherwise, the environment does not have an effect on the fatigue life.

As shown in Figure 6, a critical potential range exists whereby the repassivation-kinetics behavior is slower. Slip emergences before the critical potential range are mostly reversible slip steps, which quickly come back into registry upon unloading. The notion of the slip-reversibility dominating at potentials before the critical potential range is substantiated by the absence of current transients in this region, and, hence, null or little bare material is exposed. If the summation of the

bare material over the entire sample is too small, the scan rate may be too fast to detect the fresh metal with increasing potentials. It is apparent that within the critical potential region (150 mV – 550 mV) in Figure 6, the slip irreversibility is more prevalent due to the pronounced increase in the current and the slower repassivation-kinetics trend indicated by the current transients in Figure 6. A detectable slip-step height must be a critical height to allow for an ample exposure of the bare material over the entire surface. Therefore, the charge transfer associated with the anodic and cathodic reactions must be sufficient to detect a measurable current response due to increases in potentials. The detectable current transients are associated with the amount of the bare material loss or dissolution through Faraday's law by integrating the area underneath the decay response. The current responses in Figure 6 also correspond with the total amount of slip-step events occurring at various locations over the deformed gage area (Figure 7).

Once the critical current regime has been passed, a trend similar to that observed at lower potentials is restored (Region B in Figure 6). The trend shown in Region B is most likely due to a quasi-permanent surface formed by the irreversibility of slips, in which the response is expected to be similar to that found for an undisturbed surface or one experiencing the slip reversibility. Thus, in Region A, before the critical potential regime, the ease of slip reversibility permits a virtually smooth surface finish to exist until the critical regime is reached. Within the critical regime, dislocation multiplication and mobility continue until dislocation pile-ups occur due to the number of dislocations generated along with the prevalence of favorable slip planes oriented for an easy slip. Thus, the tendency for slip

reversibility becomes less likely. At some point within the critical range, saturation occurs in which slip reversibility is no longer possible. Consequently, the new surface contour is attributed to a more diffused surface created as a result of cycling. This surface is fairly uniform or undisturbed until the impediment of further dislocation motion promotes the crack initiation at the interface of microstructural barriers, such as twin boundaries, grain boundaries or precipitates. Once a primary crack propagates throughout the sample, continuous fatigue makes failures inevitable.

Figure 8 shows the current response of C-2000 to increasing potentials with and without cyclic stresses within the critical potential regime. The time between subsequent events provides an estimate for the average time necessary to initiate another series of transient bursts. Within a forty-minute span, at least ten current transients account for a given number of deformation events at a stress amplitude of 574 MPa and a frequency of 20 Hz in 3.5 wt.% NaCl. For comparison purposes, the cyclic anodic-polarization currents, as represented by the dotted lines, for C-2000 coupons are plotted to validate the presence of current transients observed during fatigue. Without the presence of stresses, a steady current rise should occur over times as the potential increases. The addition of stresses cause the slip activity, which exposes the bare material, to produce a current rise that is captured in the data reported in Figure 8.

Figure 9 depicts the response of the current to a potential held at 350 mV against a saturated calomel electrode (SCE). Over times, the steady-current response is interrupted, as indicated by the sharp rise in the current between Regions 1 and 2. In this experiment stress is not prevalent; thus, the gradual increase in the current

response is not due to film rupture produced by slip steps emerging to the free surface. The local oxide break-down, possibly attributed to local defects within the oxide, appears to be occurring. However, the examination for tiny pits under an optical microscope was not apparent. The reason may result from the strong propensity for the formation of the chromium oxide, which acts as a protective barrier to corrosion. Additionally, a good mapping scheme is necessary to compare the as-received sample with one exposed at 350 mV for long times to indisputably resolve defects over the surface.

Between Regions 2 and 3, the current response is marked by the rapid increase in the current not observed at shorter times. The sharp rise and rapid decay suggest many small openings, i.e., defects, happening over the gage area. Large or step-like regions formed by emerging slip steps expose more areas for electrochemical attack as compared to defect openings located in the oxide layer; consequently, more time is required to allow for the repassivation of a larger area, as compared to a smaller one. Another apparent observation is the inability to maintain the original current response, while holding the sample at 350 mV. The dashed lines separate incommensurable responses. At each dashed-line interval, the steady-state current response is higher than the previous state. This behavior continues until Region 4 is reached; in which the non-steady state behavior dominates. The observation in Region 4 suggests the depletion of chromium from the sample. Thus, the acceleration of corrosion for C-2000 subjected to cyclic fatigue appears to occur for potentials within the critical potential range, lower frequencies, such as 20 Hz, 5 Hz, and 1 Hz, and exposure times greater than 200,000 seconds in chloride solutions. At a potential

chosen from the critical potential range, the depletion of chromium over time occurs more rapidly. Without the sufficient chromium content, the oxide-reformation kinetics is not as protective. At frequencies less than 5 Hz, more time is permitted to allow for the transport of detrimental ions, such as chlorides, to be transported along the direction of crack propagation. The transition from purely mechanical to electrochemical influences is most notable at exposure times of 200,000s where the chlorides have more opportunities to be transported into the oxide layer or attracted to local defect inhomegeneities in the oxide layer. Additionally, the local acidification will expedite the dissolution process to create chloride channels (Figure 12) for a crack-propagation effect governed by electrochemical influences.

The effect of chloride species on C2000 is dependent upon factors including the oxide-film thickness, oxide-film-rupture strain, and kinetics of foreign ions to assailable regions on the surface. Consequently, the dissolution of the oxide film must occur for the aqueous-corrosion attack under static and dynamic loading. The dissolution of the tenacious oxide layer of C2000 is not possible in room-temperature conditions. The reason is partly due to key constituents, such as the high chromium content and the addition of molybdenum. The addition of molybdenum to nickel alloys, such as C2000, is believed to preferentially locate to local defect sites within the oxide barrier, which decreases the propensity for anodic dissolution due to the molybdenum's ability to act as a strong bond former with surrounding neighbors [11, 12]. Other theories suggest that the presence of MoO_4^{2-} acts as a repelling barrier for detrimental ions, such as OH- and Cl- [11, 13]. An electrolyte hold-time test was performed to determine the effects of the chloride-layer buildup at the surface after

the exposure to chloride concentrations over time. The chloride transport into the sub-layer is indisputable if chlorides are found below the surface at various sites around the fracture circumference. SEM with EDS provides some idea as to chlorides being transported along the fractured surface. However, whether the transport mechanism(s) is by the competitive ion adsorption or ion penetration is arguable [14, 15]. One clear observation is that a sufficient time is necessary to allow the transport of chlorides into the fractured regions. At higher frequencies like 20 Hz, the chloride concentration is very high at the crack-initiation site, as compared to other regions on the fractured surface. As the frequency is decreased, more time is allotted for the transport of chlorides from the crack-initiation site along the crack propagation or growth direction. Staehle [16] postulated the crack growth by anodic dissolution due to emerging slips at the crack core, as described in Figure 17. Once a critical crack size is achieved, the subsequent chemical reactions in the occluded region are at a lower pH, which increases the local acidity. The acidic solution is more aggressive than that in the bulk solution. Consequently, the repassivation kinetics can be severely affected at the location where slips emerge into the core of the occluded region. The core-lining is now rough because of the dissolution and the irreversibility of dislocations on favorable slip planes protruding to the inner layer. Secondary cracks on the surface are capacious due to chloride channels propagating from the anodic dissolution region at emerging slip steps from the sub-layer (Figure 12) at a frequency of 1 Hz and stress amplitude of 574 MPa. Thus, this trend provides a strong evidence that chloride channels, a pit formed by progressive anodic dissolution, are plausible means of promoting crack propagation in 3.5 wt.% NaCl.

Figures 10 and 11 reveal the results of corrosion-fatigue experiments in 3.5 wt. % NaCl solutions at frequencies of 20 Hz, 5 Hz, and 1 Hz to determine the chloride buildup and transport from the crack-initiation site to the edge of the propagation region of the fracture surface. At frequencies of 5 Hz and 1 Hz, the ratio of chloride to nickel counts is less than that calculated at higher frequencies, such as 20 Hz. Thus, it reasonable to surmise that with decreasing frequencies more time is allotted for the chlorides to be transported along the direction of propagation, as determined by line profiles measured from the crack-initiation site to the edge of the propagation region. The chloride content at the crack-initiation site has decreased from above 3,000 counts for a frequency of 20 Hz to slightly below 250 counts for a frequency of 5 Hz. For C2000 fatigued at 20 Hz, an EDS profile was taken at the edge of the propagation region in the area delineated by the box, as shown in Figure 10, to obtain a qualitative estimation of 200 counts for the chloride content. Table 1 lists the normalized EDS data for C2000.

Figure 14 manifests the appearance of the fracture surface after exposing C2000 to a 3.5 wt.% NaCl electrolyte for seven days before commencing the corrosion-fatigue experiment. In air or at frequencies of 20 Hz, 5 Hz, and 1 Hz in 3.5 wt.% NaCl, the fatigue or corrosion-fatigue behavior is governed strictly by the mechanical process, such as the crack initiation at slip interfaces or steps (Figures 15 and 16). Thus, at the natural potential of C2000, reducing frequencies from 20 Hz to 1 Hz do not significantly affect the fatigue life in both air and 3.5 wt.% NaCl (Table 2). However, a longer exposure time of seven days to 3.5 wt.% NaCl induces an electrochemical effect on fatigue of C2000. The reason is attributed to the chloride

layer buildup, which attacks the local inhomogeneities in the oxide film. The coupling of the mechanical stresses and the dissolution associated with the longer exposure to chlorides promotes a deleterious effect on the fatigue life of C2000 (Table 2). The reason is that the distinctive regions normally observed in 3.5 wt.% NaCl upon the fresh exposure or in air are clearly indistinguishable after the long-term exposure. The coupling of the anodic dissolution and crack propagation occurring simultaneously produces an eroded or washed-out fracture appearance. This washed-out phenomenon suggests that the electrochemical process dominates the corrosion-fatigue behavior at the long-term exposure in 3.5 wt.% NaCl. Thus, the combination of a critical potential value of 350 mV and increased exposure times promote the depletion of the chromium oxide layer. As a result, the repassivation kinetics upon fatiguing the sample is not as protective. Therefore, the material becomes susceptible to anodic dissolution, and thus, the creation of chloride channels form and propagate to manifest a washed-out fracture morphology.

5. Conclusion

The corrosion-fatigue behaviors of C2000 at a frequencies of 20 Hz, 5 Hz, and 1 Hz in 3.5 wt.% NaCl and air were studied. The fatigue characteristics for C2000 in air and 3.5 wt. % NaCl are similar at all three frequencies tested, which implies no corrosion dependence on the fatigue properties. Thus, reducing frequencies from 20 Hz to 1 Hz does not significantly affect the fatigue life at the natural potential of C2000. However, the combination of a critical potential value of 350 mV and increased exposure times to 3.5 wt.% NaCl before commencing fatigue induces failures dominated by electrochemical influences. After seven days, the chlorides in the bulk solution have longer times to form a chloride-buildup layer around the C2000 sample. Chloride channels are believed to be the means at which chlorides are transported along the crack-propagation direction. The presence of chloride channels was observed at secondary crack-initiation sites. Consequently, the propagation of the crack via chloride channels produces a washed-out fracture surface that is attributed to the anodic dissolution and crack propagation occurring simultaneously.

REFERENCES

1. Asphahani, A.I. and Sridhar, N., *Corrosion Fatigue of Nickel and Nickel-Base Alloys.* Corrosion, 1982. **38**(11): pp. 587-595.

2. Mueller, M.P., *Dependence of Corrosion Fatigue Crack Initiation Mechanisms on the Corrosion Behavior of 2 Stainless Chromium Steels.* Corrosion, 1982. **38**(8): pp. 431-436.

3. Muller, M., *Theoretical Considerations on Corrosion Fatigue Crack Initiation.* Metallurgical Transactions A-Physical Metallurgy and Materials Science, 1982. **13**(4): p0. 649-655.

4. Murtaza, G. and Akid, R., *Empirical Corrosion Fatigue Life Prediction Models of a High Strength Ssteel.* Engineering Fracture Mechanics, 2000. **67**(5): pp. 461-474.

5. Boateng, A., Begley, J. A., and Staehle, R.W., *Corrosion Fatigue of Type-304 Stainless-Steel in H_2SO_4 and Boiling NaOH.* Corrosion, 1980. **36**(11): pp. 633-638.

6. Boateng, A., Begley, J.A., and Staehle, R.W., *Corrosion Fatigue of Type 304 Stainless-Steel in Sulfuric-Acid.* Corrosion, 1977. **33**(4): pp. 152-152.

7. Patel, C., Pyle, T., and Rollins, V., *Corrosion-Fatigue Crack Initiation in Metals.* Nature, 1977. **266**(5602): pp. 517-518.

8. Boateng, A., Begley, J. A., and Staehle, R.W., *Corrosion Fatigue of Fe-Cr-Ni Alloys in Hot Concentrated NaOH Solution.* Journal of Metals, 1979. **31**(12): pp. 56-56.

9. (ASTM), *Metals Test Methods and Analytical Procedures*. Metals - Mechanical Testing; Elevated and Low - Temperature Tests, ed. J.L.C. R. A.

Storer, D. F. Savini, S. R. Powell, S. H. Hart, K. W. O'Brien, D. Paz, A. L. Stanton, E. C. Cannon, L. A. Loux, R. E. Craig, and M. Osvald. Vol. 3.01. 1986, Philadelphia: ASTM.

10. Barbosa, M., *A Model for the Kinetics of Repassivation .2. Scratching Electrodes.* Corrosion, 1988. **44**(3): pp. 149-153.

11. Lloyd, A.C., Noel, J. J., McIntyre, S., and Shoesmith, D. W., *Cr, Mo and W alloying additions in Ni and their effect on passivity.* Electrochimica Acta, 2004. **49**(17-18): pp. 3015-3027.

12. Mueller, M.P., *Influence of Alloy Composition and Microstructure on Corrosion-Fatigue Properties of Ferritic Chromium Steels.* Metals Technology, 1982. **9** (JUN): pp. 235-239.

13. Loi, S., Sun, G, Franz, V., and Butt, H. J., *Rupture of Molecular Thin Films Oobserved in Aatomic Force Microscopy. II. Experiment.* Physical Review E, 2002. **66** (3).

14. McBee, C.L, and Kruger, J., *Localized Corrosion.* NACE, 1974: p. 252.

15. Strehblow, H.H., Werkst Korrosion, 1976. **27**: pp. 792.

16. Staehle, R.W., Begley, J.A., and Boateng, A., *Corrosion Fatigue of Type 304 Stainless-Steel in a Boiling 17.5N Sodium-Hydroxide Solution.* Journal of Metals, 1976. **28** (12): pp. A34-A34.

APPENDICES

Appendix A: Tables
Appendix B: Figures

APPENDIX A

Table 1. Chloride Content for C2000 in 3.5 wt.% NaCl

R = 0.1			
Frequency / Normalized Counts	**20 Hz**	**5 Hz**	**1 Hz**
Chloride Counts / Nickel Counts	**2.00**	**1.80**	**0.77**

Table 2. Corrosion-Fatigue Data for C2000 in 3.5 wt.% NaCl

R = 0.1				
Frequency / Chloride Content	**20 Hz**	**5 Hz**	**1 Hz**	**Long-term Exposure @ 20 Hz**
Cycles to Failure $\sigma_{a\ max}$ = 574 MPa	109,282	205,440	110,584	74,805
Cycles to Failure $\sigma_{a\ min}$ = 384 MPa ***- no failure**	5,000,000*	3,683,891*	1,015,246	——

APPENDIX B

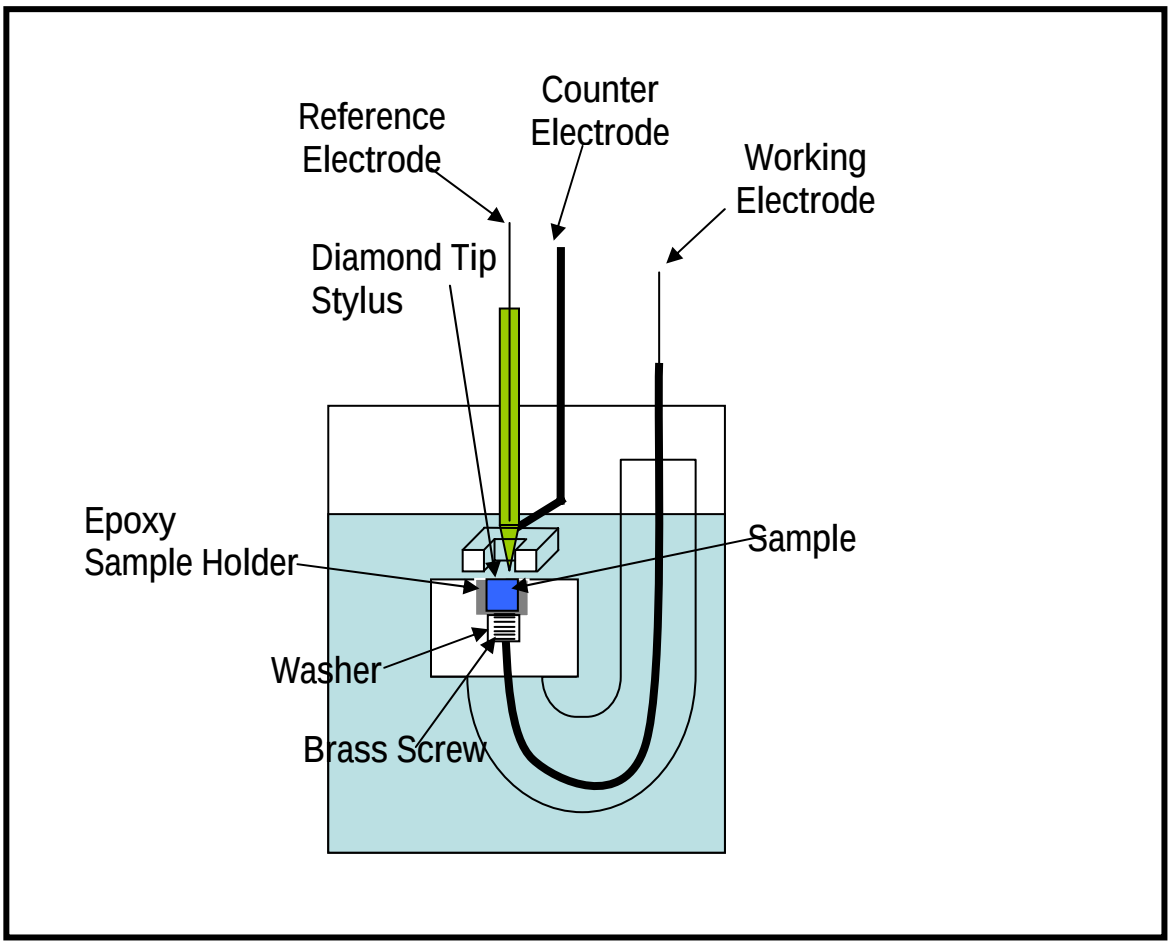


Figure 1. Electrochemical-Cell Apparatus for Scratch Tests

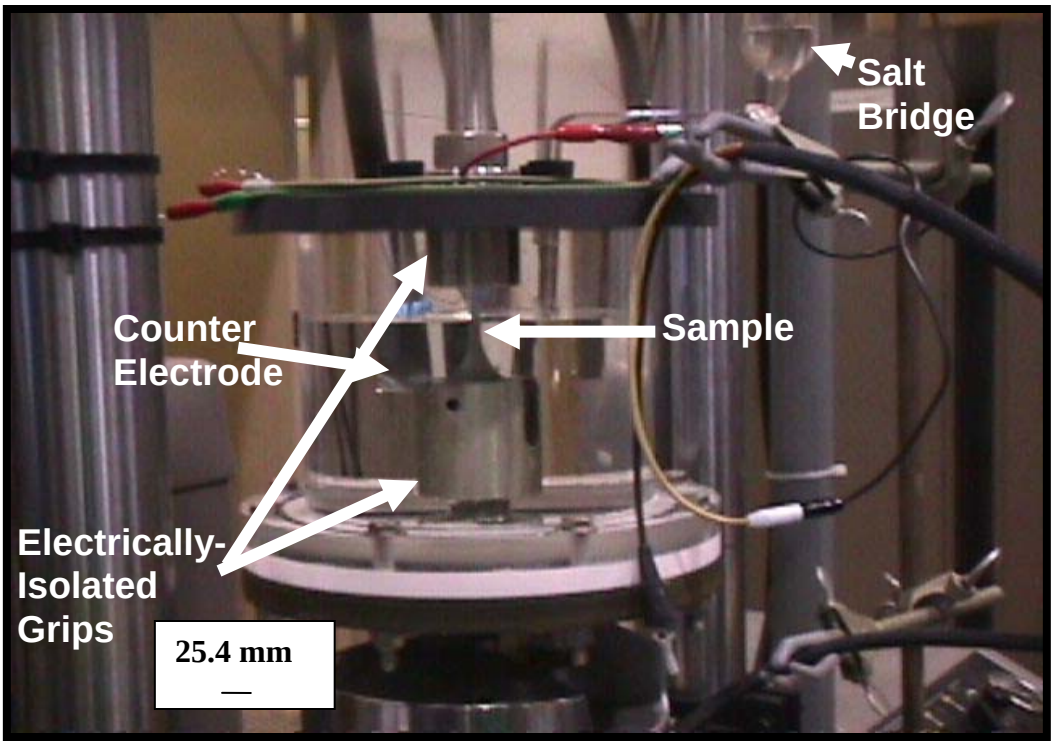


Figure 2. Corrosion Cell Interfaced with a MTS Fatigue Machine

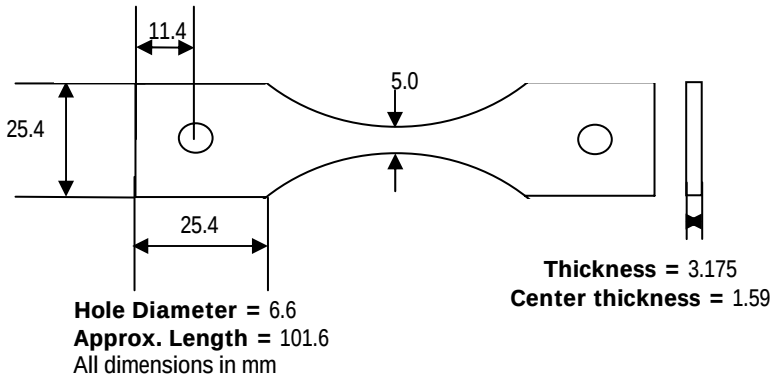


Figure 3. Schematic of Flat Tensile Specimen Geometry [1]

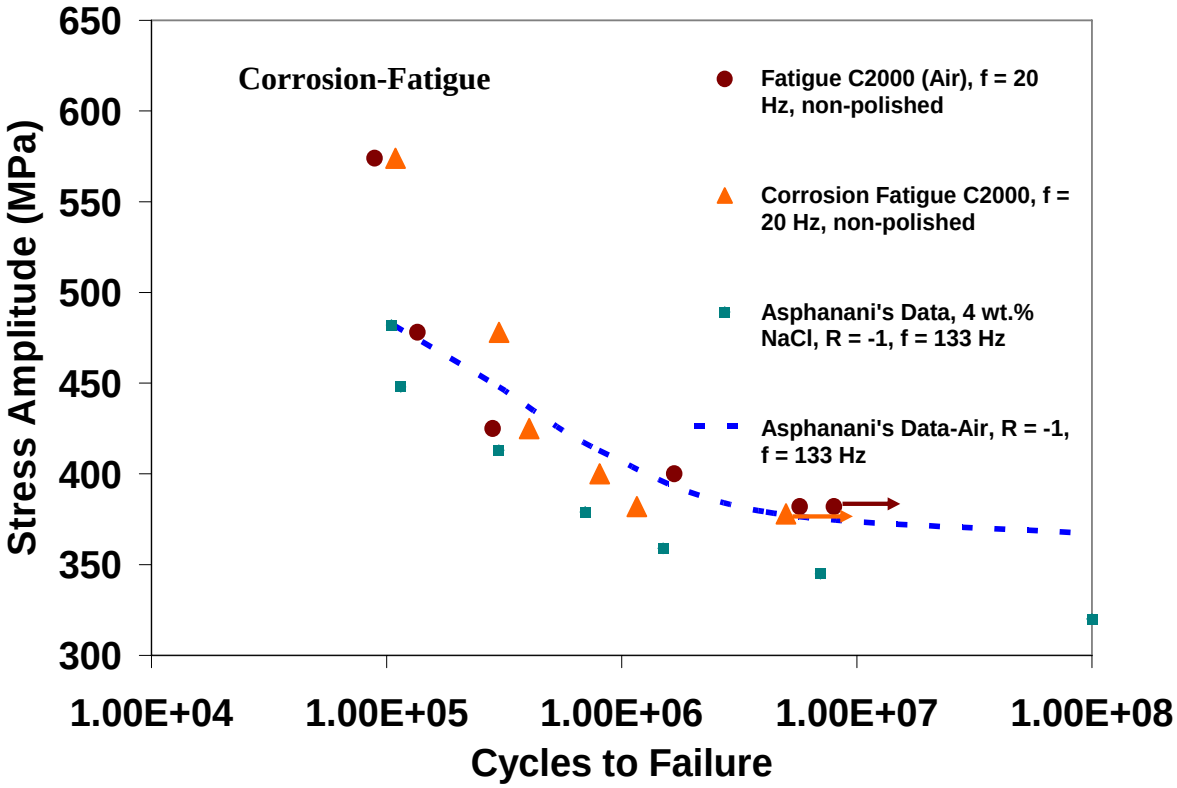


Figure 4. S-N Curve for C2000 and a Nickel Alloy Studied by Asphanani [2].

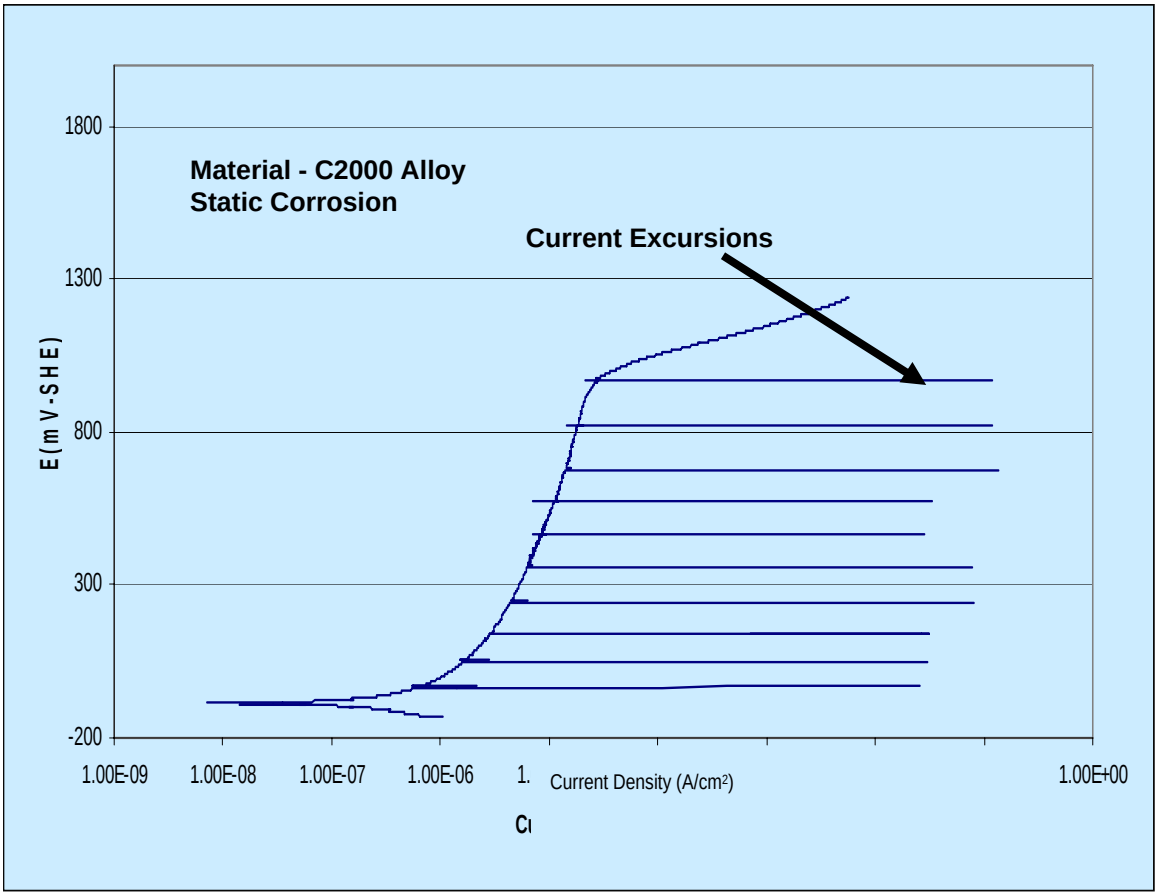


Figure 5. Potentiodynamic Scratch Test Curve in 3.5 wt. % NaCl

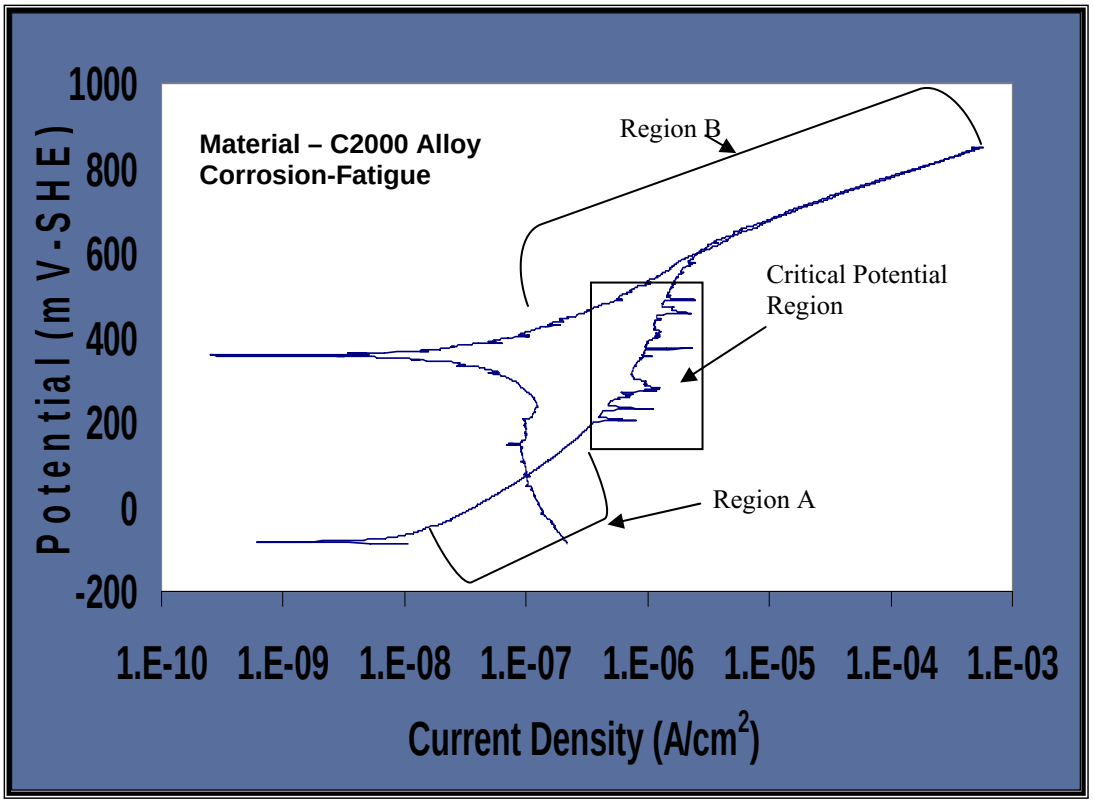


Figure 6. Cyclic-Anodic Polarization Corrosion-Fatigue Curve in 3.5 wt. % NaCl at a Frequency of 20 Hz and a Stress Amplitude of 574 MPa.

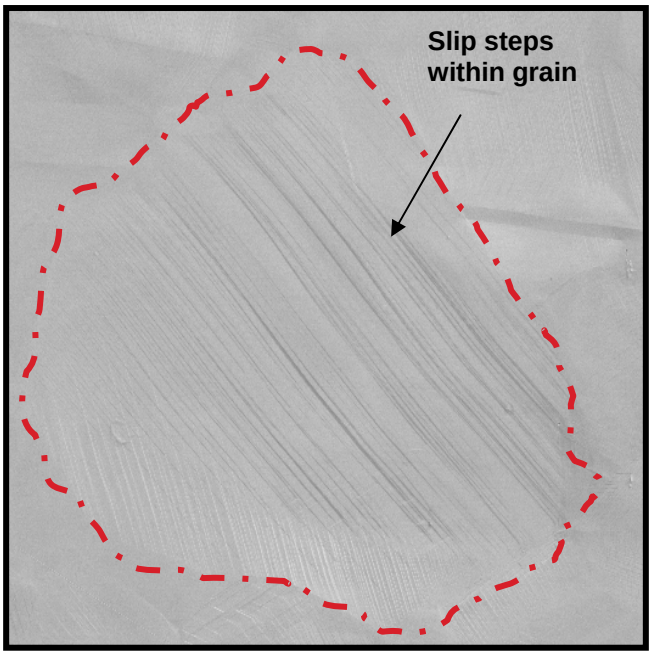


Figure 7. Slip Steps Emerging to the Surface Throughout the Gage Volume for C2000

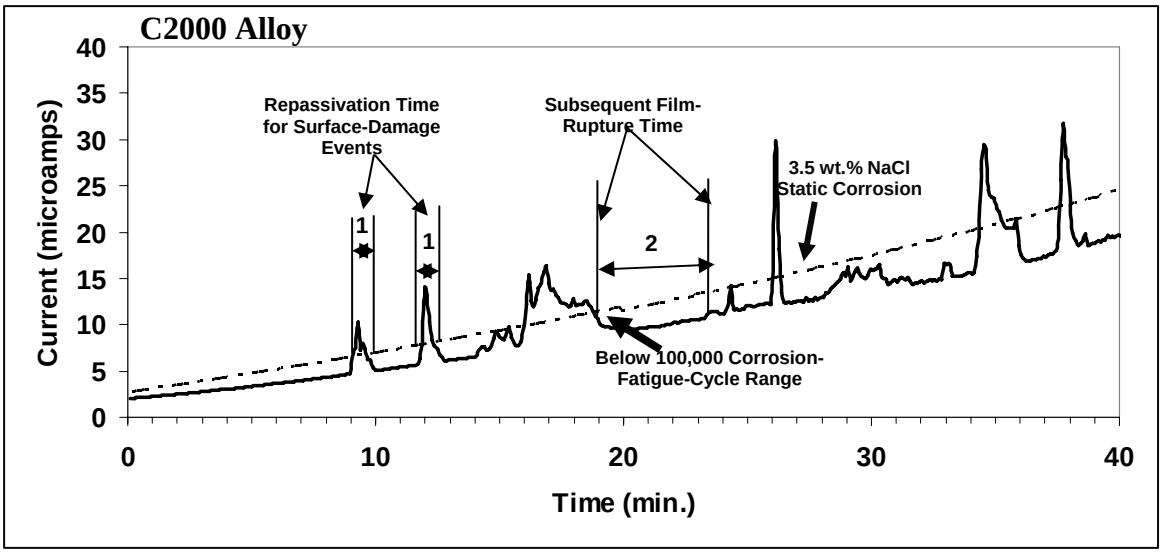


Figure 8. Critical Current Range Corresponding to the Critical Potential Range

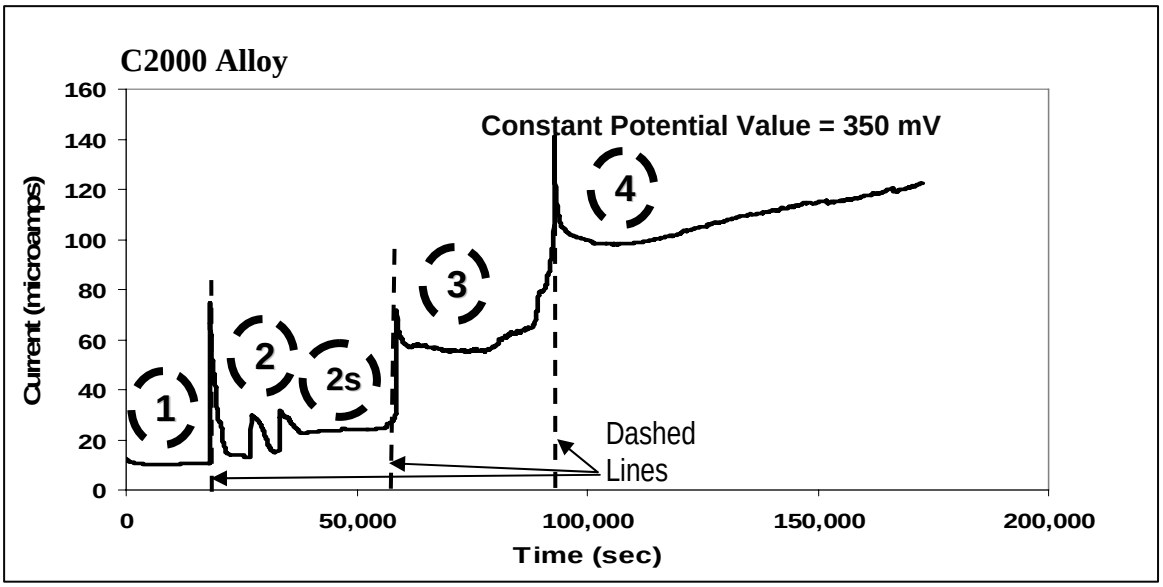


Figure 9. Constant Potential of 350 mV Against SCE Graph Monitoring Current vs. Time for C2000

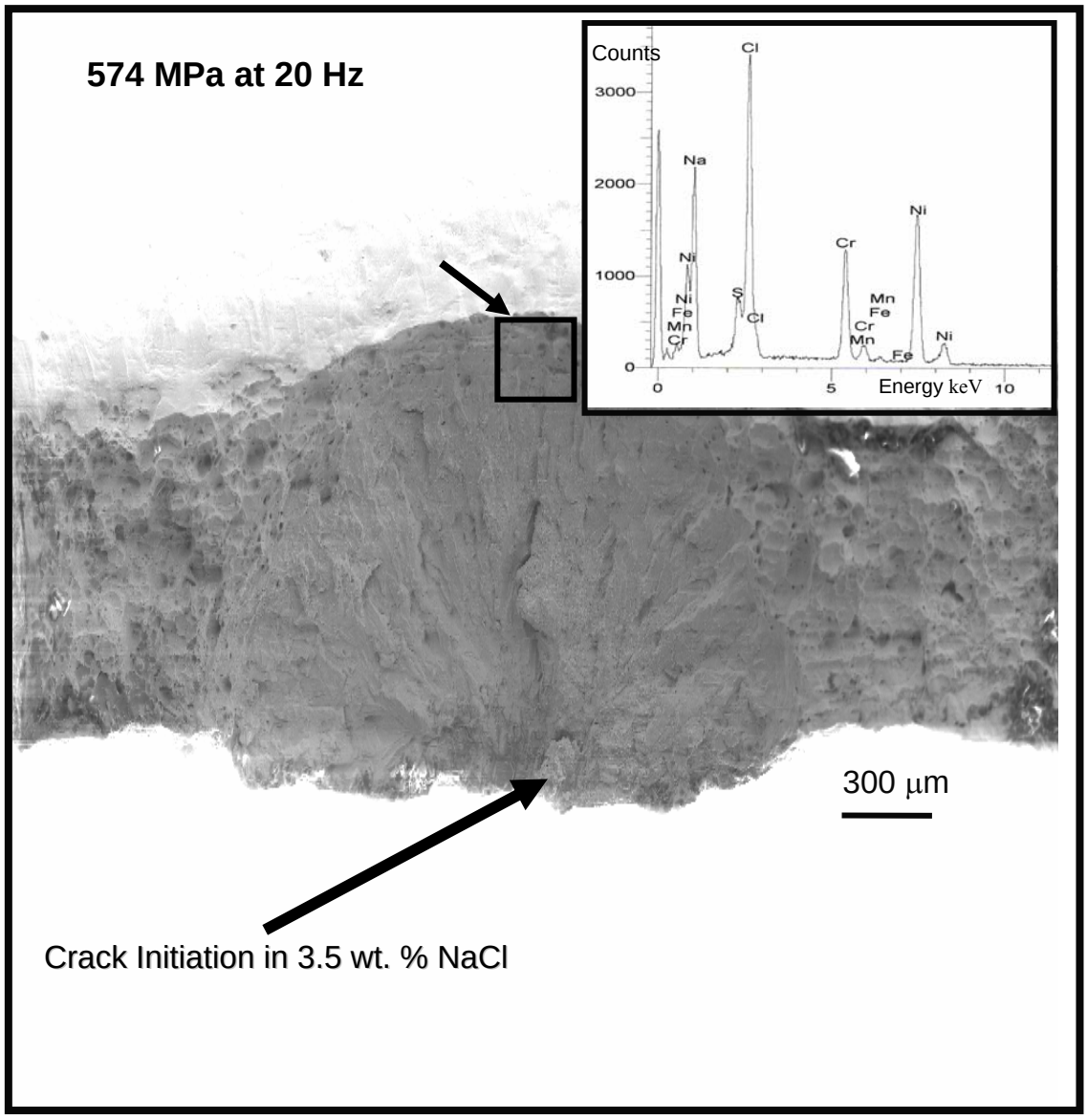


Figure 10. Fracture Morphology and Corresponding EDS Spectrum for Corrosion-Fatigue of C2000 in Air at R = 0.1, f = 20 Hz, and σ_a = 574 MPa

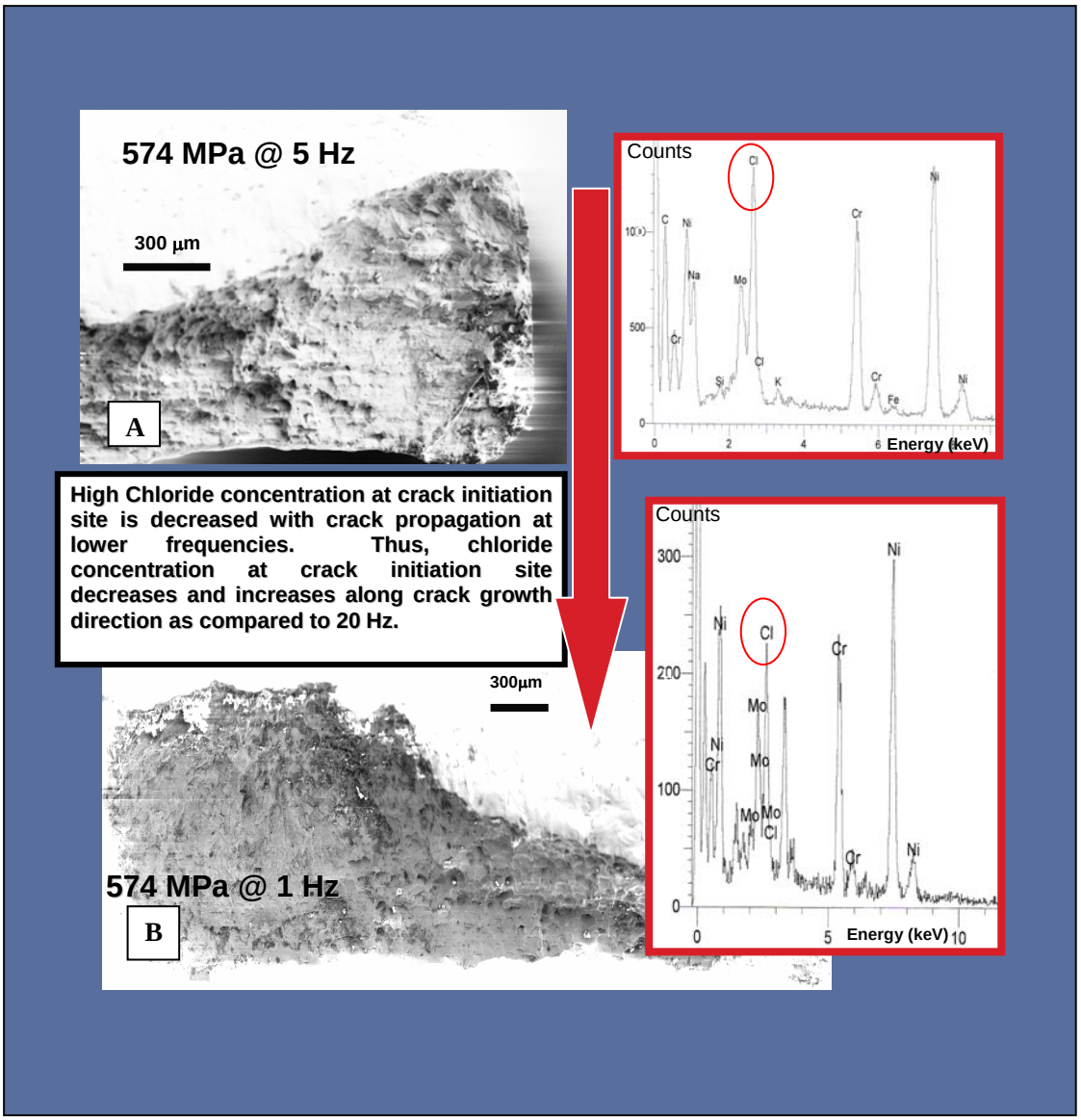


Figure 11. Fracture Morphology: A) Fracture Morphology and Corresponding EDS Spectrum for Corrosion-Fatigue of C2000 in 3.5 wt.% NaCl at R = 0.1, f = 5 Hz, and σ_a = 574 MPa B) Fracture Morphology and Corresponding EDS Spectrum for Corrosion-Fatigue of C2000 in 3.5 wt.% NaCl at R = 0.1, f = 1 Hz, and σ_a = 574 MPa

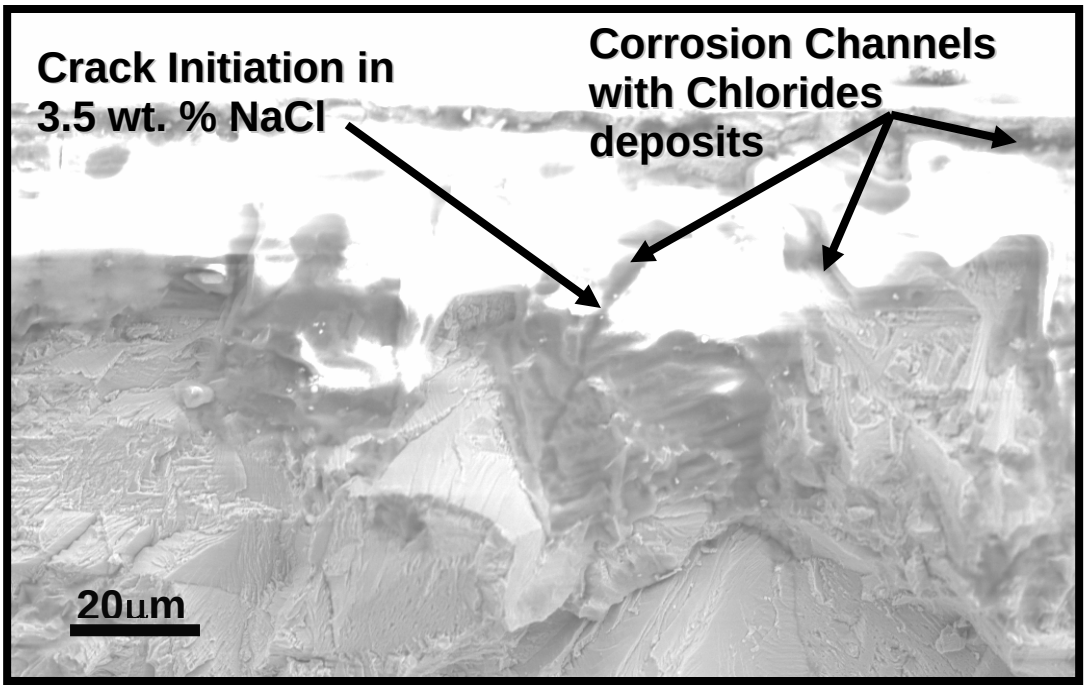


Figure 12. Chloride Channels at Secondary Crack-Initiation Sites

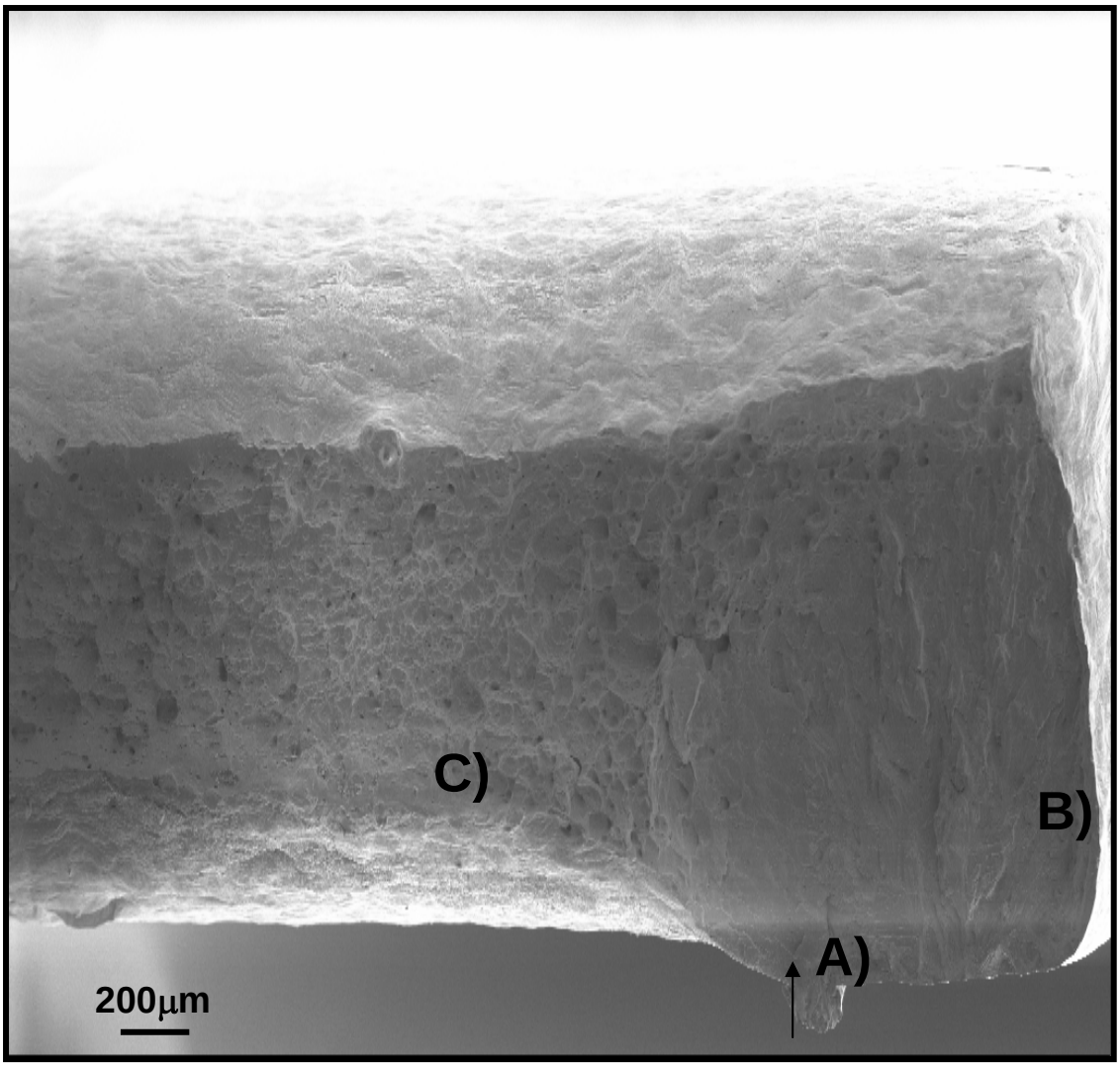


Figure 13. Distinctive Fracture-Morphology Regions Associated with Fatigue of C2000 in air at R = 0.1 and f = 20 Hz

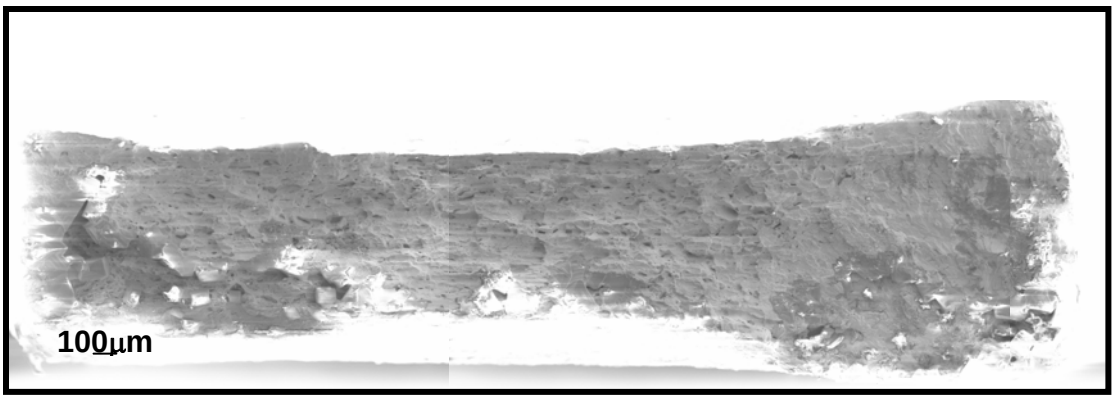


Figure 14. Distinctive Fracture Regions Washed-Out Due to the Anodic Dissolution after Long-Term Exposure Times (7 days) to 3.5 wt.% NaCl Before Commencing Corrosion-Fatigue at R = 0.1, f = 20Hz

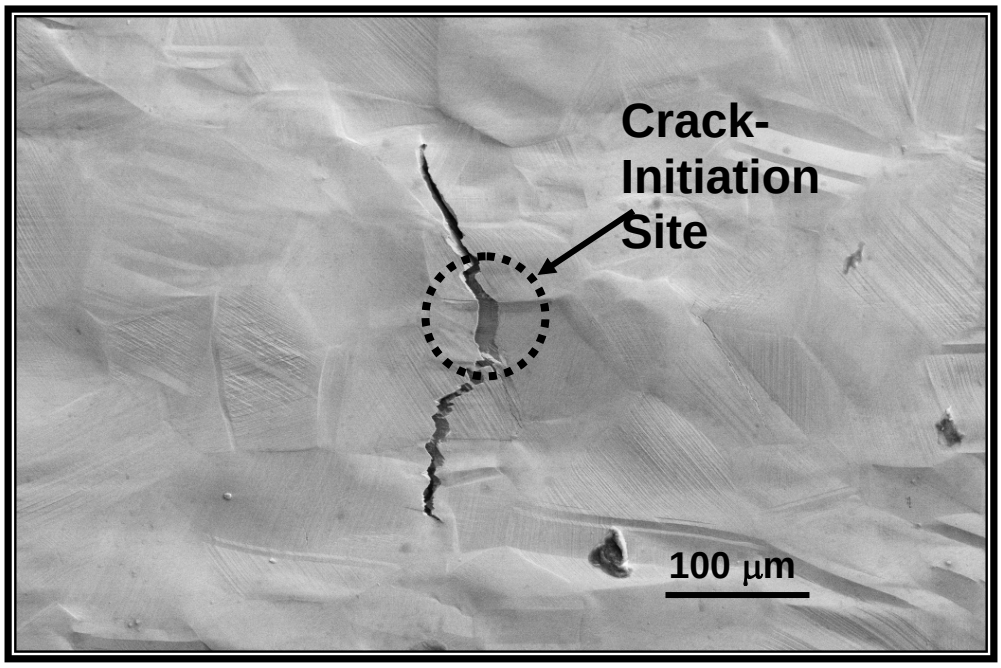


Figure 15. Crack-Initiation Site for C2000 at Slip Bands.

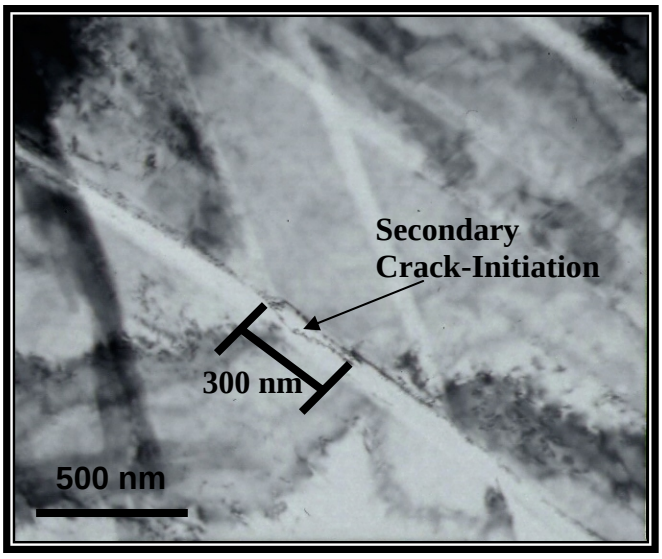


Figure 16. Transmission-Electron-Microscopy Image of a Secondary Crack at a Slip Interface

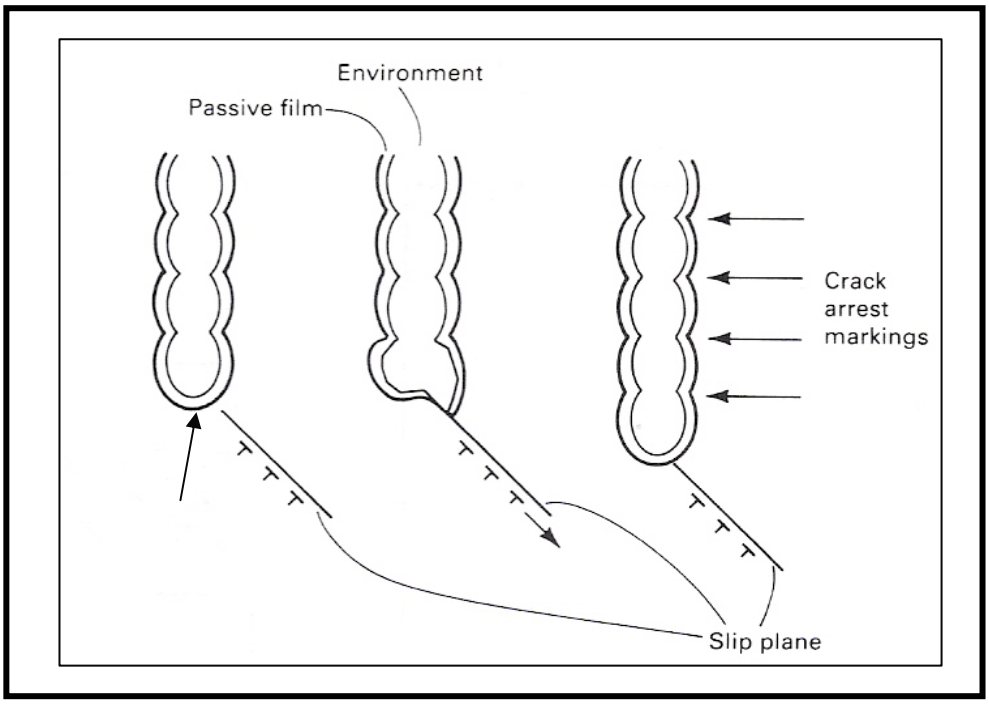


Figure 17. Stahle [16] Model for Crack Propagation in a Corrosive Environment

PART III

Validation of an Electrochemical Model for a Passivating Nickel Alloy

1. Introduction

Fatigue-crack initiation is a subject that is of concern to industry. In the aviation industry, crack-initiation is frequently ascribed to microstructural variables and foreign debris. Attempts to derive equations or models to predict the crack-initiation life for structural materials is limited. Mura, Tanaka, and Naksone [1] have created models that account for the contribution of dislocations along favorable slip bands to crack initiation. Attempts to revamp their models to include other crack-initiation mechanisms such as crack-initiation at inclusions and grain boundaries [2], have been performed. Models to represent the corrosion-fatigue influence on the crack initiation within the active, passive, or pitting regions have been treated [3]. All of the models identify parameters that are believed to characterize the response of the material system under corrosion-fatigue and fatigue environments.

Predicting the crack-initiation life for structural materials is challenging because data on the mechanical and electrochemical properties are limited, or unavailable. Additionally, the crack-initiation process depends upon the material [4] and electrolyte-exposure times [5]. Moreover, designing an experimental platform to investigate conjoint influences presents difficult, since the pertinent parameters must be experimentally measurable. Hence, repeatable testing is required to give credence to model solutions.

In this part, a refined model to determine the number of cycles to crack initiation for a passivating material, C2000, is presented. Experimental procedures are highlighted to provide the reader with insight into how the experimental parameters were determined, and pertinent constants extracted from the literature are

described. The section also discusses the theoretical basis on which the model was conceived.

2. Experimental Procedure

2.1 Corrosion-Fatigue Experiments and Surface Preparations: Cyclic-anodic-polarization and potentiodynamic experiments were initiated at a potential of 50 mV below the free potential of the alloys investigated at a scan rate of 0.167 V/s. A Princeton Applied Research Model 263A potentiostat/galvanostat was interfaced with the electrochemical apparatus to control voltages, monitor currents, and record responses for data analyses using an EG&G 352 SoftCorr III software. All potential values recorded during electrochemical measurements were converted to the standard hydrogen-electrode (SHE) scale for scratch and cyclic-anodic polarization results.

Fatigue experiments were performed with a closed-loop servohydraulic Materials Testing System (MTS). Figure 1 (All figures and tables are listed in the appendices) shows a picture of the experimental setup for the corrosion-fatigue chamber used to conduct corrosion-fatigue experiments on C2000. The samples were affixed to grips via a ceramic pin-joint assembly to isolate the sample from grips, i.e., to prevent the galvanic coupling. A free-floating Teflon top allowed the connection of the working electrode, which is the sample, the platinum counter electrodes, and the salt bridge for electrochemical testing. Experiments were conducted at frequencies of 20 Hz with a constant R-ratio (minimum stress/maximum stress) of 0.1. All fatigue tests were performed under uniaxial tension-tension conditions. Corrosion-fatigue experiments were conducted in a 3.5 wt.% NaCl solution. Accelerated corrosion experiments were performed for

C2000 by increasing the potential value to 350 mV against a SCE reference for all fatigue testing.

3. Background on C2000

Corrosion-fatigue involves the deterioration of the fatigue life produced in an inert environment with that observed in a non-inert environment. In general, fatigue involves the formation of extrusions and intrusions on the surface of a material [6]. These intrusions and extrusions form recesses that can potentially serve as local stress risers for the initiation of a crack. For corrosion-fatigue, at the point where the primary crack forms, it is believed that the advent of anodic slip-step dissolution occurs simultaneously. Subsequently, deformation is controlled by mechanical and electrochemical influences, which depends on the exposure time and the electrolyte. A commercially-available material known as C2000 does not undergo localized corrosion at room temperature in 3.5 wt.% NaCl solutions [7]. An in-situ electrochemical-fatigue study implies that the material's intrinsic slip process influences the current responses [8], which makes this material an ideal material for validation of a corrosion-fatigue model. With a sufficient exposure time to the 3.5 wt.% NaCl electrolyte, chlorides can be transported along the direction of crack propagation [8]. These chlorides participate in the anodic dissolution process, and hence, chloride channels are created as depicted by the blue dotted lines in Figures 2a and 2b.

4. Formulation of Corrosion-Fatigue Crack-Initiation Model

4.1 Mueller's Model Approach: Mueller [9] attempted to develop a model that would predict the corrosion-fatigue behavior for materials within various states of corrosion, such as the active or passive states. Muller's theory suggested that a critical notch depth begins along a favorable slip-plane during the fatigue process. The critical notch depth occurs at a critical stress range, where the critical depth is only possible, if the passive layer thickness is less in dimensions than the slip-step height. Thus, below the fatigue-endurance limit, the stress range is too low to surface slip steps greater than the passive film thickness, and film rupture will not occur. While Muller's work identified useful correlations between the passive film thickness and the slip-step height, and the critical current density and critical depth, the model uses a conservative fracture-mechanics approach, the Dugdale model, for describing the primary flaw.

4.2 Daeubler's Model Approach: Daeubler et al. [3] further refined Muller's model to describe the initiation of a given crack along a favorable slip band by using a Griffith model from fracture mechanics to describe the critical crack size length/depth. The notion that the flaw length/depth was attributed to the progressive dissolution of the bare material was again used to formulate the model. In the model, the authors' describe the crack-initiation phenomenon for passive materials, and they identify some pertinent correlations between mechanical and electrochemical phenomena. However, the inception of a critical crack depth occurring due to the progressive dissolution theory has not been observed experimentally. In most cases, for materials within the passive regime, the nucleation of flaws requires the rupturing

of the oxide films. Also, the oxide regrowth kinetics must occur at a much slower rate in comparison to the exposure of the material to detrimental species within the electrolyte. Within the critical stress range, film rupture permits bare material exposure to the electrolyte upon successive fatigue cycles, where the amount of material exposed to the electrolyte for a given time depends upon the ease of slip. Once irreversible slip is achieved, the repassivation time or passive film kinetics is affected more severely due to the frustration of oxide growth during fatigue, and hence, successive film ruptures.

Thus, Daubler's work attempted to present a more representative lifetime-prediction model of the corrosion-fatigue process for passivating materials. Perhaps the most important parameter in Daeubler's equation is the fatigue exponent, (α), since it appears to control the shift of the curve on the stress versus the number of cycles to crack initiation (S-Ni) diagram. Therefore, α may possibly serve as a useful parameter for a material's susceptibility to crack initiation. The final mechanical-electrochemical model derived by Daeubler yields the following equation for the number of cycles to crack initiation, Ni. Table 1 is a legend of all the parameters used in Equations 1 - 10.

$$N_i = \frac{SSH_c \upsilon}{nbk}\left[\frac{zF\rho(1+\alpha)nbka_c}{Mi^*(SSH_c - h_f)}\right]^{\frac{1}{(1+\alpha)}}\left(\frac{\sigma_a}{\sigma_{fl}}\right)^{\frac{-2}{(1+\alpha)}} \quad \textbf{(1)}$$

4.3 Chan's Model Approach: In the work of Chan [2], the number of dislocations required to contribute to the initiation of a crack can be described by considering when the crack formation is energetically favorable. This trend would be the case when the surface energy to form the crack is balanced by the strain energy due to the obstruction of further dislocation mobility. Thus, the energy associated with the creation of a crack, W_{eq}, is determined by the product of the two new surfaces of a particular length, c, and the surface energy required to produce the crack enclave. The strain energy, γ_s, associated with the onset of the formation of the crack, a_c, can be correlated with the surface energy associated with the creation of two new surfaces, the crack length, and the slip-band width, d (Equation 2).

$$2a_c\gamma_s = \frac{cW_{eq}}{d} \quad \textbf{(2)}$$

Also, the actual number of dislocations, n_c, necessary to produce the local rise in the strain energy, and hence, the creation of a flaw of length c, can be described using the following equation, where b is the burger's vector.

$$a_c = n_c b \quad \textbf{(3)}$$

The number of dislocations, n, in a given slip band, along with the combinations of Equations 2 and 3, can be used to derive Equation 4 for the critical number of dislocations [10].

$$n_c = 0.05\left(\frac{d}{bh}\right)\sqrt{\frac{cWeq}{d\mu}} \quad \textbf{(4)}$$

Therefore, the final equation to describe the crack size, a_c, for a primary crack depth is given by Equation 5:

$$a_c = 0.005\left[\frac{d}{h}\right]^2\left[\frac{\gamma_s}{\mu}\right] \quad \textbf{(5)}$$

Once the description for the critical depth is identified, an energy balance equation relating the response variables to the applied stress range can be formulated. Chan's model for the life-prediction of structural materials at a grain-boundary is described below in Equation 6.

$$\left(\Delta\sigma - 2M_t k\right)N_i^{\ \alpha} = \left[\frac{8M_t^{\ 2}\mu^2}{\lambda\pi\left(1-\nu\right)}\right]^{\frac{1}{2}}\left(\frac{h}{d}\right)\left(\frac{a_c}{d}\right)^{\frac{1}{2}} \quad \textbf{(6)}$$

5. Refined Model Approach

In Daeubler's model, a dimensional analysis approach is proposed to derive an equation that describes the number of cycles to crack initiation. An energy balance approach is employed to construct a microstructure-based model in Chan's model. Although both models have microstructural and other key parameters, the platforms on which these models were proposed are questionable or incomplete for crack-initiation in corrosive media. Consquently, an attempt to develop a model that adequately describes the crack initiation in real systems is presented in a refined model, which uses both Daeubler's and Chan's models.

There are two possibilities to increase the local strain energy along a given slip band oriented for favorable slip. Case 1a is the increase in local strain energy at the intersection of a grain or twin boundary due to dislocation pile-ups. Case 1b represents the occurrence of a crack by dislocation pile-ups at precipitates. Ensuing crack initiation, the film-reformation kinetics does not occur at the same rate since the core of the crack has a more diffuse character. Additionally, secondary slip planes within the proximity of the original or primary crack site further frustrates the reformation of the protective oxide. Figure 2 is a cartoon of how the crack initiates in both cases.

Of all the models for corrosion-fatigue or fatigue, the aforementioned are the best relationships for describing the intrinsic micro-features and electrochemical contributions to corrosion-fatigue-crack initiation. In the corrosion-fatigue of passive films, both film rupture and dissolution must occur simultaneously at the critical nucleation depth. Since both Chan's and Daeubler's models allot for a defect tolerant

term, the crack depth term, a, from Equations 1 and 6, respectively, can be equated. The point at which the crack depths are equivalent is known as the critical depth for the formation of a stable crack. The present model to describe the number of cycles to create a critical depth is shown in Equation 7:

$$N(\sigma) = x^{1/\alpha} \cdot (\sigma - 2 \cdot M_t \cdot k)^{\frac{-2}{\alpha(1+\alpha)}} \cdot \left(\frac{d}{y^2} \right)^{-1/\alpha(1+\alpha)} \quad \textbf{(7)}$$

where x and y represent the following constants.

$$x = \frac{SSH \cdot \nu}{n \cdot b \cdot k} \cdot \left[\frac{z \cdot F \cdot \rho \cdot (1 + \alpha) \cdot n \cdot b \cdot k}{M \cdot I \cdot (SSH - hf)} \right]^{\frac{1}{(1+\alpha)}} \quad \textbf{(8)}$$

$$y = \left[\frac{8 \cdot Mt^2 \cdot \mu^2}{\lambda \cdot \pi (1 - \nu)} \right]^{\frac{1}{2}} \cdot \left(\frac{h}{d} \right) \quad \textbf{(9)}$$

The substitution for Chan's estimation of the stable crack size or the critical crack depth can be justified for two reasons. First, film rupture must occur for materials exhibiting the passive behavior before anodic currents can be detected. This trend requires that a critical slip-step height associated with the applied stress

must be achieved to allot for the bare material exposure to the electrolyte. It also must hold true that the beginning of the progressive dissolution occurs simultaneously with the formation of a stable crack depth. With Chan's model, the nucleation of the critical crack depth is not restricted to the slip band, but may occur at any material barrier.

6. Discussion

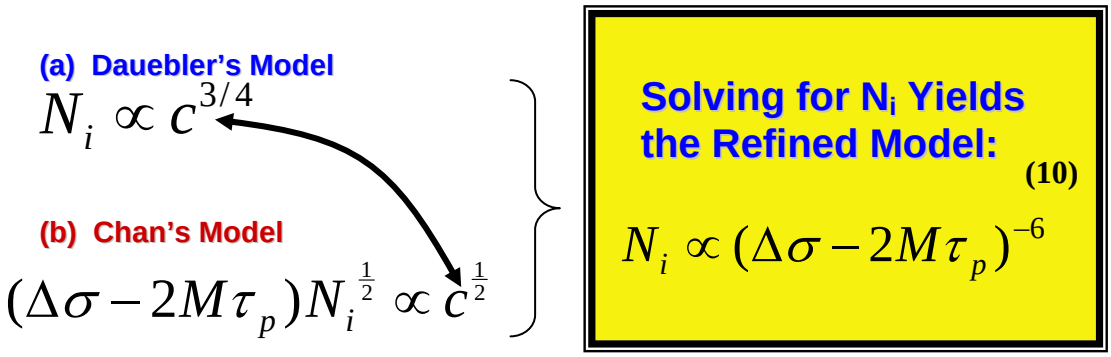
Since the current response increases upon exposure of the bare material to the rupture process experienced during fatigue, cyclic-anodic-polarization tests coupled with fatigue tests provide an indication of the critical potential range for the onset of fracture due to accelerated corrosion conditions. For a stress amplitude of σ_1 = 574 MPa and a frequency of 20 Hz, the current transients occur intermittently, whereas the current excursions are more regular for lower frequencies, such as 1 Hz. The parameters extracted from the experiments include the slip-step height and the critical-current density.

For this research, the slip-step height is measured with a laser interferometer. The grain size is measured using the conventional optical-microscopy-measuring techniques, and the current density is judiciously selected by generating a histogram of the number of anodic current transients occurring within increasing time intervals. The histogram is generated by averaging the magnitude of the current transient occurrences over time. These magnitudes are then graphed to observe the current-transient trend. The time for crack initiation is selected as the highest response value measured by the most pronounced anodic-current response represented by the trend. For example, if a modal distribution is present, the highest point is chosen as the crack-initiation site. If a bimodal distribution is observed, the point exhibiting the largest average magnitude is chosen. In Figure 3, diagram (a) represents a modal distribution of the corrosion-fatigue behavior at σ_1 = 574 MPa. Figures 3 (b) and 3 (c) represent the intermediate and the lowest stress amplitudes of σ_2 = 485 MPa and 384 MPa, respectively.

At an intermediate stress of 485 MPa a modal behavior is plotted, and at the fatigue endurance limit a steady-state current response is observed. The film thickness and material constants are chosen to be reasonable with those found in literature. Table 2 lists the values selected for this study.

The incipient crack-initiation forms when the instability criterion [2] is satisfied. Since the experimental current response can be monitored versus the number of cycle, the estimated number of cycles required for the onset of crack initiation can be determined, although the approach is conservative in two respects. First, the approach is conservative due to the instability criterion and, secondly, the approach is conservative because the number of fatigue cycles to initiate a detectable crack is based on mostly current response data from optical microscopy.

In the refinement of Dauebler's model, an attempt has been made to better account for microstructural contributions to the corrosion-fatigue crack-initiation model. As a result of monitoring the current response under corrosion-fatigue conditions, a reasonable estimate can be estimated for the number of cycles required for the onset of crack nucleation. Thus a relation between the number of cycles to initiate a crack and the crack-size power relation can be generated according to equation 10. Figure 4 shows the experimental corrosion-fatigue S-N_i curve as measured by the aforementioned method for determining the crack-initiation site. The solid line represents the theoretical fit to the curve. Figure 5 shows a cartoon comparing the improvement in the electrochemical models up to the present. As can be seen, the present model is an improvement due to Ni's higher power exponent dependence to the critical crack size.


(a) Dauebler's Model
$N_i \propto c^{3/4}$
(b) Chan's Model
$(\Delta\sigma - 2M\tau_p)N_i^{\frac{1}{2}} \propto c^{\frac{1}{2}}$
Solving for N_i Yields the Refined Model:
(10)
$N_i \propto (\Delta\sigma - 2M\tau_p)^{-6}$

7. Conclusion

C2000 is a nickel-based superalloy that is resistant to localized corrosion in 3.5 wt.% NaCl solutions at the natural potential of the material. In the case of C2000, a critical potential within the passive range of the material is held constant to determine the electrochemical influences on fatigue. The critical current associated with onset of primary fracture is used in the refined model along with the measurement of the average critical slip-step-heights to determine the response to corrosion-fatigue in a potentially detrimental electrolyte. The extracted experimental values are used in the model along with collected data to verify the validity of the refined model approach. Thus, the refined model:

- Provides a better estimate of the electrochemical and mechanical responses for C2000.
- Serves as an improvement of Mueller's and Dauebler's models.

REFERENCES

1. Tanaka, K. and Mura, T., *A Dislocation Model for Fatigue Crack Initiation.* Journal of Applied Mechanics-Transactions of the Asme, 1981. **48**(1): pp. 97-103.

2. Chan, K.S., *A microstructure-based fatigue-crack-initiation model.* Metallurgical and Materials Transactions a-Physical Metallurgy and Materials Science, 2003. **34**(1): pp. 43-58.

3. Daeubler, M.A., Warren, G. W., Bernstein, I. M., Thompson, A. W., *Modeling of Corrosion Fatigue Crack Initiation under Passive Electrochemical Conditions.* Metallurgical Transactions a-Physical Metallurgy and Materials Science, 1991. **22**(2): pp. 521-529.

4. Vehoff, H., Laird, C., and Duquette, D.J., *The Effects of Hydrogen and Segregation on Fatigue Crack Nucleation at Defined Grain-Boundaries in Nickel Bicrystals.* Acta Metallurgica, 1987. **35**(12): pp. 2877-2886.

5. Gough, H.J., *Corrosion-fatigue of metals.* Journal of the Institute of Metals, 1932. **49**: pp. 17-92.

6. Schijve, J., *Review Article: Fatigue of Structures and Materials in the 20th Century and the State of the Art.* International Journal of Fatigue, 2003. **25**: pp. 679-702.

7. Meck, S.N., and Crook, P., *Localized Corrosion Susceptibility of Nickel Alloys in Halide Containing Environments.* Corrosion NACE Conference, 2002.

8. Steward, R.V., Wang, G., Buchanan, R.A., Liaw, P.K., Saleh, T.A., Klarstrom, D.L., and Meck, S.N., *In-Situ Electrochemical Investigations of a*

Nickel-Based Alloy Subjected to Fatigue. Metallurgical and Materials Transactions A-Physical Metallurgy and Materials Science. **in press**.

9. Muller, M., *Theoretical Considerations on Corrosion Fatigue Crack Initiation.* Metallurgical Transactions a-Physical Metallurgy and Materials Science, 1982. **13**(4): pp. 649-655.

10. Venkataraman, G., Chung, Y.W., Nakasone, Y., Mura, T., *Free-Energy Formulation of Fatigue Crack Initiation Along Persistent Slip Bands - Calculation of S-N Curves and Crack Depths.* Acta Metallurgica Et Materialia, 1990. **38**(1): pp. 31-40.

APPENDICES

Appendix A: Tables
Appendix B: Figures

APPENDIX A

Table 1. Parameter Descriptions

Parameter	Definition
SSH_c	Slip-step Height
ν	Frequency
n	Number of Slip Steps on the Surface
b	Burger's Vector
h_f	Passive Film Thickness
z	Charge
F	Faraday's Constant
ρ	Density
α and k	Fitting Parameters
a_c	Critical Crack Length
M	Atomic Weight
c	Chan's Critical Crack Length
i*	Maximum Current Density
σ_a	Applied Stress Amplitude
σ_{fl}	Fatigue Limit
d	Grain Size
M_T	Taylor Factor
t	Geometrical Constant
μ	Shear Modulus
h	Slip-band Width
λ	Universal Constant
τ_p	Plastic Shear Stress
Ni	Number of Cycles to Crack-Initiation
Gs	Surface Energy of the Crack
W_{eq}	Strain Energy Stored in the Dislocation Dipoles
n_c	Number of dislocations that Contribute to the Crack Formation
$\Delta\sigma$	Stress Range

Table 2. Values Used in the Calculation of the Present Model

Mt = 2	$\nu = 0.3$
$\mu = 8 \times 10^4$ MPa	$h_f = 2 \times 10^{-9}$ m
$M = 6.72 \times 10^4$ Mpa	$I = 1283 \times 10^{-6}$ A/cm
$SSH = 1240 \times 10^{-9}$ m	$d = 200 \times 10^{-6}$m
z = 2 1/mol	$M = 8 \times 10^4\ 10^6$ kg/m·s^2
F = 96,500 A/s	f = 20 Hz
n = 5	$\alpha = -0.35$
$\rho = 8.34$ g/cm^3	k = 175
$b = 0.25 \times 10^{-9}$ nm	$\gamma = 0.005$ Hz
$h = 4 \times 10^{-5}$ m	

APPENDIX B

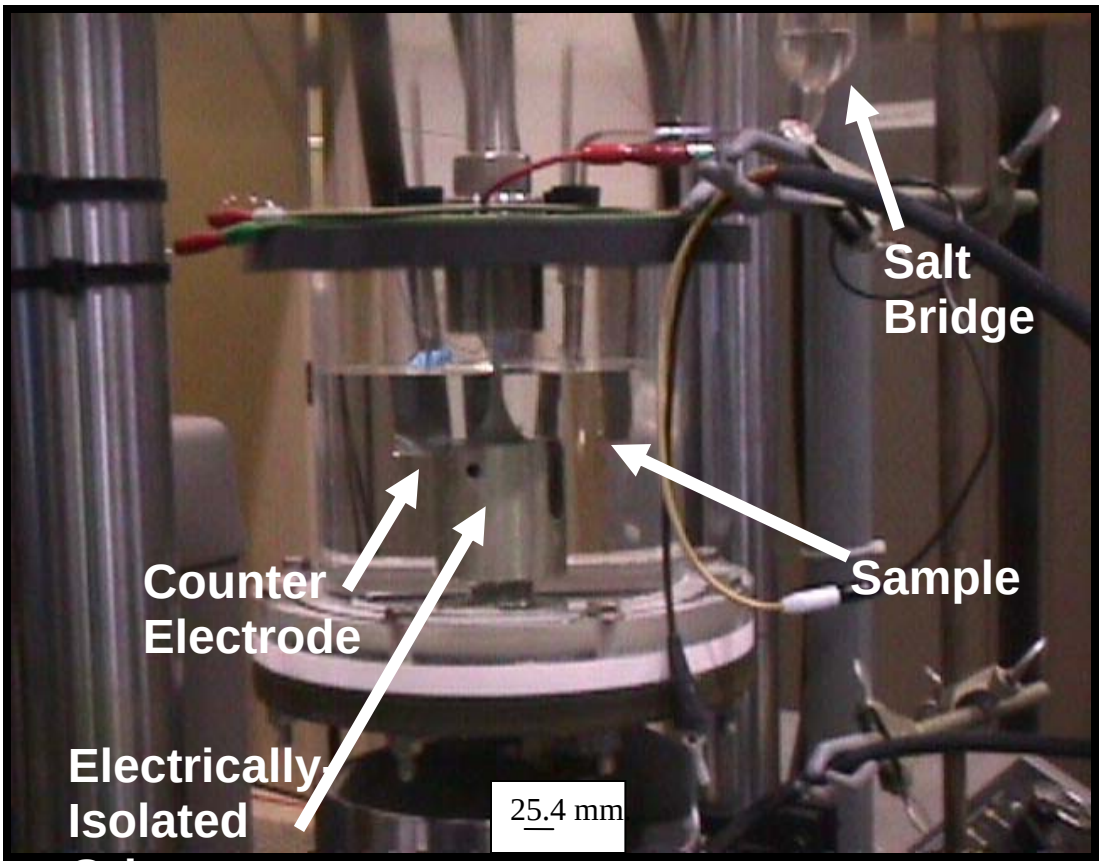


Figure 1. Electrochemical Chamber Interfaced with Electrohydraulic Fatigue Testing Machine.

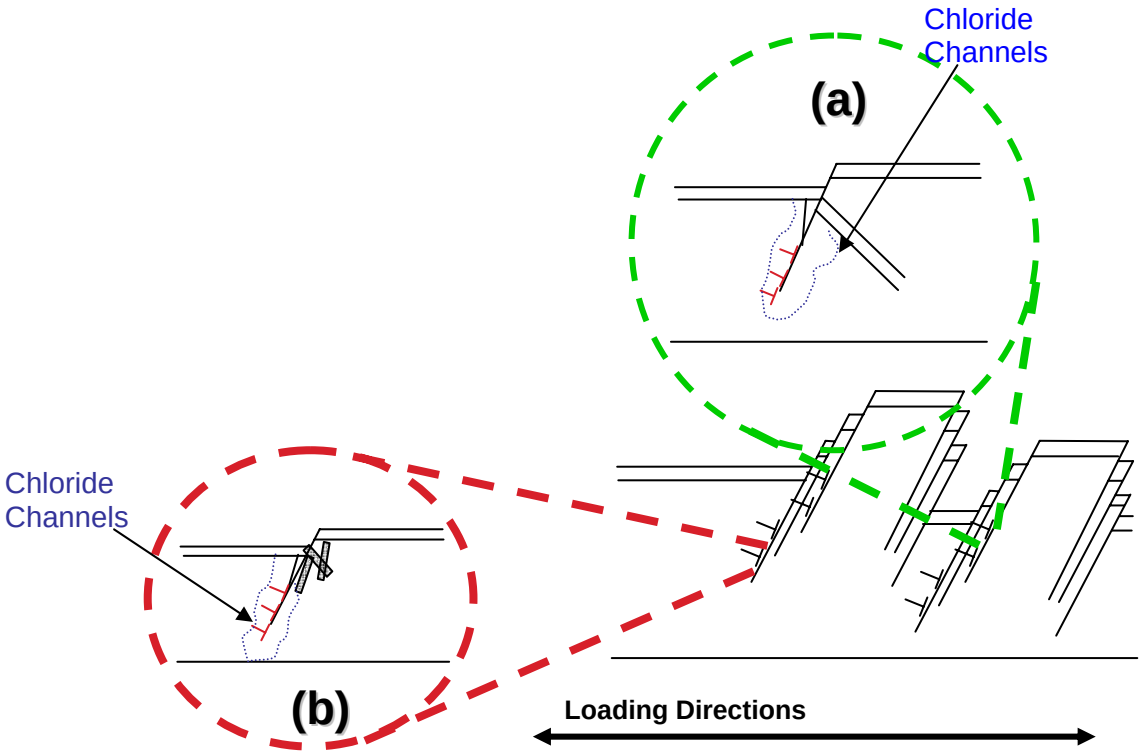


Figure 2. Rupture Process: Case (a): The Nucleation of a Crack Due to Dislocation Pile-up at a Twin or Grain Boundary; Case (b): The Nucleation of a Crack Due to Pile-up at Precipitates

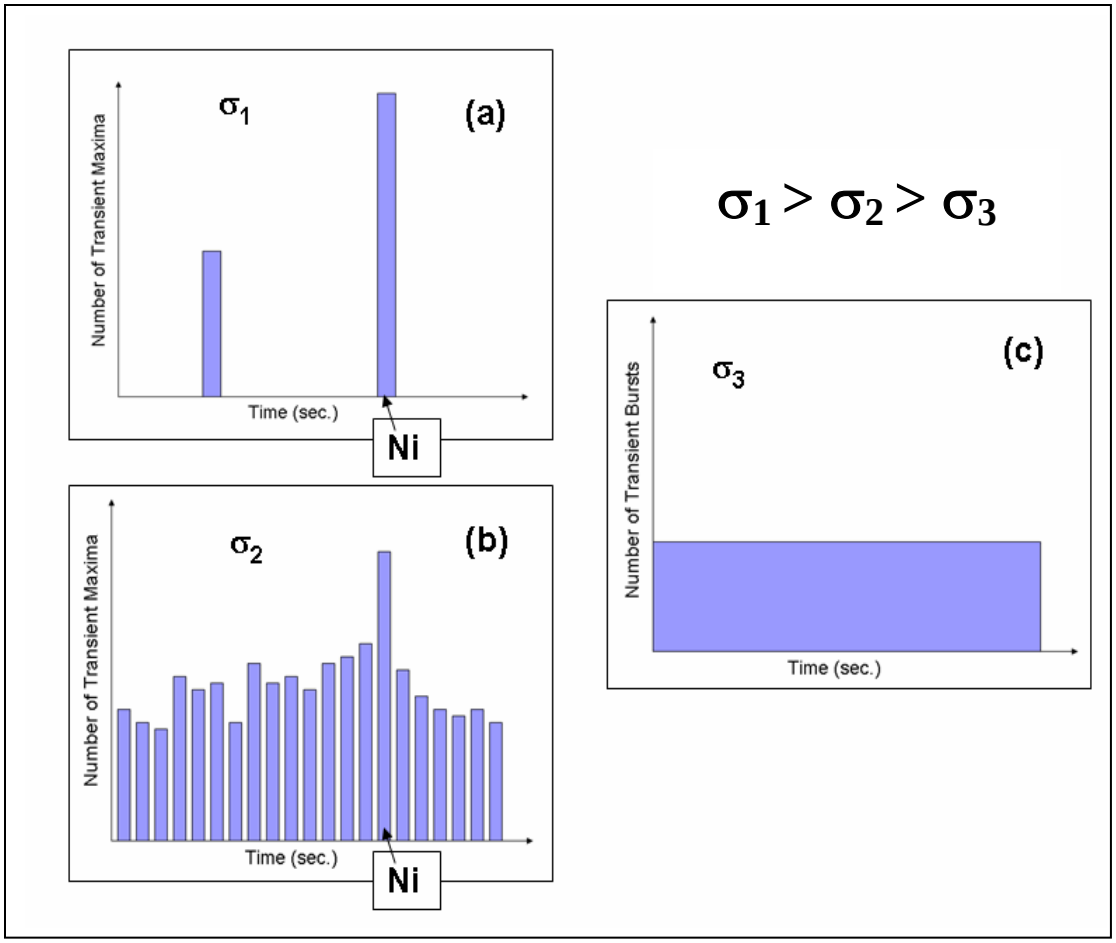


Figure 3. Temporal Representation of Fatigue Events: a) Number of Current Transients Recorded Over Time at a High Stress Amplitude of 574 MPa; b) Intermediate Stress Amplitude of 485 MPa; c) and at the Endurance Limit of 384 MPa at a Frequency of 20 Hz

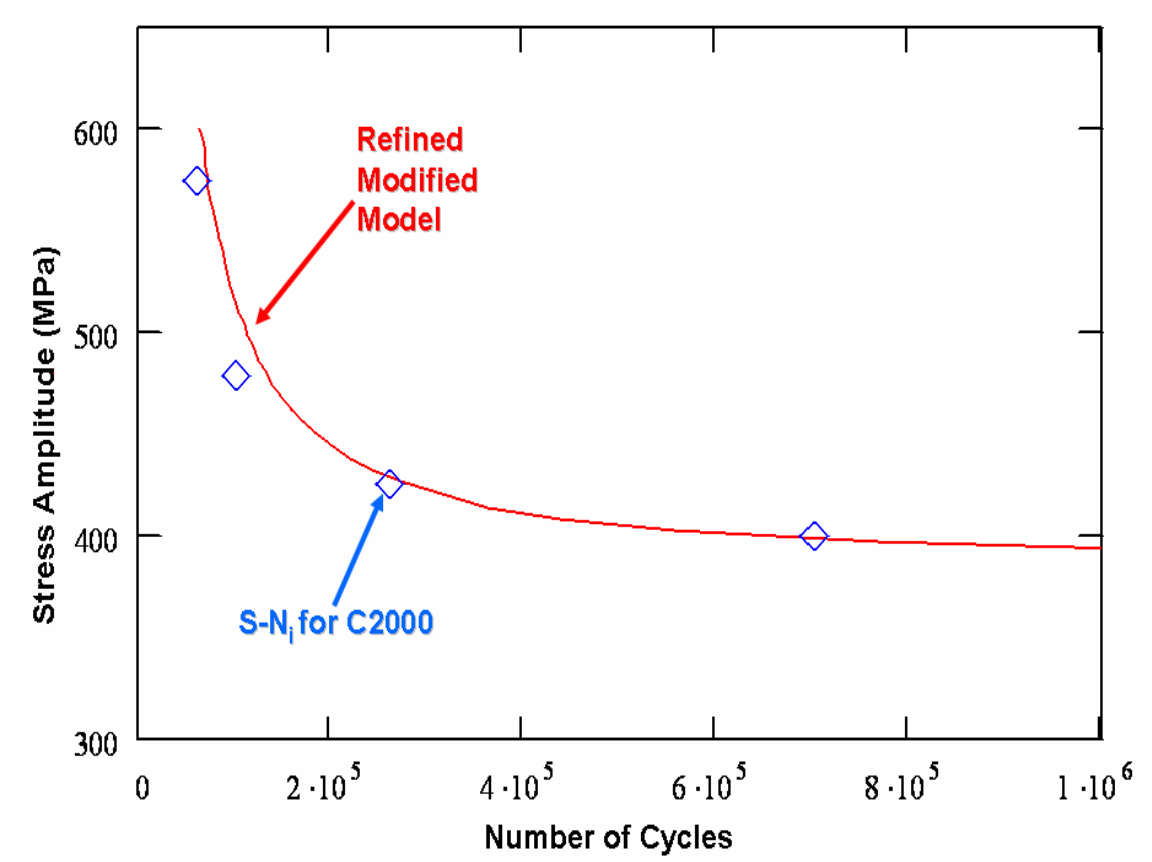


Figure 4. Refinement of Mueller's and Daeubler's Model for Predicting the Lifetime for C2000

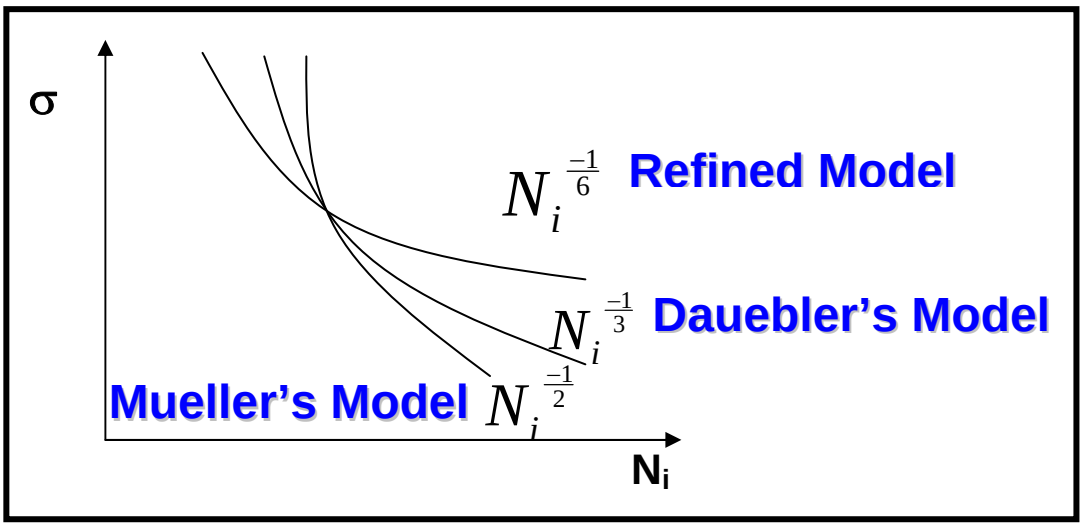


Figure 5. A Cartoon Showing the Various Refinement Effects of Mueller's Model Fit for Predicting the Lifetime for Crack-initiation in Structural Materials

PART IV

Pitting of a Bulk Ni-18 wt.% Fe Nanocrystalline Alloy

1. Introduction

Grain size is known to be inversely proportional to the material strength via the widely-known Petch [1] and Hall [2] relationship established in the 1950s. Although the metallurgical community was privy to the notion of the improved strength with the decreasing grain size, the advent of bulk nanocrystalline (nc) materials emerged later due to the lack of successful bulk-fabrication methods. Interests in nc materials debuted in the 1980s [3-7] . Recently, techniques, such as electrodeposition and mechanical attrition, are promising techniques for producing nc materials. The breakthrough for the vast commercialization of bulk nc materials is predicated upon a good understanding of both the material's mechanical and electrochemical properties to compete with advanced high-strength materials like bulk metallic glasses [8] and superalloys [9].

Intuitively, pitting corrosion of nc alloys are not expected to exhibit good corrosion behavior, considering that many grain boundaries are available for the occurrence of intergranular corrosion, a reasonable suspect. The fabrication method for the production of nc materials is of great importance. For instance, powder-metallurgical nc materials have porosity issues, which compromise the bulk integrity. Substantial voids in ball-milled nc materials promote easy coalescence and provide channels for chloride ions from the bulk electrolyte or hydrogen produced via hydrolysis to be transported quickly into vacancy portals. Hence, excessive hydrogen gas or chloride ions can potentially produce swelling.

The aim of this paper is to report findings of the electrochemical behavior available on a binary nickel-based bulk nc material, Ni-18 wt.% Fe, as a function of microstructure, and provide an explanation of the cracking-phenoma observed in the pit

core. Moreover, the comparisons of the electrochemical properties among the as-received and annealed nc alloys are discussed.

2. Experimental Procedure

2.1 Specimen Preparation: The nc Ni-18Fe alloy was prepared by an electrodeposition technique on a stainless-steel substrate, and was provided by Integran Technologies, Inc. The as-received nc material dimensions were 70 mm (length) x 70 mm (width) x 3 mm (thickness). The nc coupons for the electrochemical studies comprised of an approximate 30.7 mm^2 area. Three nc alloys were heated treated in an air furnace at a temperature of 400ºC for 3 hrs., 8 hrs., and 24 hrs. The as-received nc sample was fine polished to a 0.5 μm finish. The annealed nc coupons were mechanically grinded with silcon-carbide grinding pads to a 800 grit finish. Afterwards, each coarse-ground sample was finished through a series of fine polishes until a 0.5 μm finish was achieved. The etchant used to reveal the grain morphology consisted of a 35 ml hydrochloric acid, 15 ml of glycerol, and 10 ml of nitric acid. The samples were held under hot water for a few seconds before performing a swab etch.

2.2 Optical Microscopy (OM): The characterization was done with a Reichert – Jung MeF4 Metallograph microscope system to visualize and capture optical micrographs of the as-received and corroded samples.

2.3 X-Ray Diffraction: The bulk nc samples were placed on a SiO_2 single-crystal slide to keep the sample firmly mounted to the sample holder during testing. X-ray diffraction data was taken with a Phillips diffractometer. The scan step size was 0.04 (steps/second), and the target wavelength used was 1.54 Å Cu Kα.

2.4 Scanning-Electron Microscopy (SEM): The observation of the localized corrosion phenomenon was carried out with a LEO SEM with energy-dispersive-spectrum (EDS) capabilities by JEOL. The accelerating beam used to image the structure was 20 KeV.

2.5 Transmission-Electron Microscopy (TEM): A transmission-electron microscope (TEM) was used to image the grains at high magnifications and verify the nc size-distribution of the grains. The TEM observations were carried out using a Schottky field-emission gun FEI Tecnai F20 UT microscope with a spatial resolution of 0.14 nm operating at 200 kV. The TEM thin-foil specimens were prepared by the conventional twin-jet electro-polishing technique using a 25 volume percent (vol.%) nitric acid + 75 vol.% methanol solution at -30°C and 10 V.

2.6 Electrochemical Experiments: Electrochemical experiments were conducted within a glass cell with an epoxy lid containing orifices for working, counter, and reference electrodes. A platinum foil was used as the counter electrode, and a saturated calomel electrode served as the reference electrode. All electrochemical experiments were performed under aerated conditions. The electrolyte consists of a 0.6 M solution of NaCl. The open circuit potential and potentiodynamic-polarization tests were measured with a potentiostat in the circuitry with the reference, counter, and working electrodes. The nc coupon comprised of an approximate 30.7 mm^2 area was finished to a 0.5 μm polish. All cyclic-anodic polarization experiments were conducted at a scan rate of 0.167 mV/s using a PARC Parstat 2263 pontentiostat equipped with the POWERCORR software. Before commencing a cyclic-anodic polarization test, the open-circuit or free potential of the material under study was monitored until a steady state was achieved. Actual cyclic-anodic-polarization experiments began 20 mV below the open-circuit potential, and initially scanned in the noble direction.

2.7 Atom-Probe Tomography: NC samples were prepared by the atom-probe tomography on an Imago LEAP microscope system by machining a 1 mm x 1 mm square

plate from the bulk material with a mechanical wire saw. The samples were electropolished to a sharp tip radius for the operation below a 14 KV threshold. Each sample was cryogenically cooled before the ionization. A pulse fraction of 20% of the standing voltage was used during operation.

3. Results

3.1 Optical Microscopy: The optical micrographs were captured for the as-received nc material, the 3 hrs., 8 hrs., and 24 hrs.-annealed nc materials (Figures 1-4) (All figures and tables are listed in the appendices). The grain morphology of the as-received nc alloy were equiaxed and uniformly distributed. There was no difference in the grain morphology and grain-size distributions for the as-received and 3 hrs.-annealed nc materials. Both the 8 hrs. and 24 hrs. nc materials exhibited similarities in the grain morphologies (Figure 3 and 4). The optical micrographs for the four nc materials were captured after performing cyclic-anodic-polarization experiments. For the samples annealed for times longer than 3 hrs., micrometer and nanometer grains were observed. After performing cyclic-polarization tests, optical images were taken to observe the effects of the corrosive media on the nc material.

3.2 Transmission -Electron Microscopy: Transmission-electron microscopy confirms that the as-received material is nanocrystalline. Figure 5a shows the TEM image of the as-deposited nc material. The as-deposited sample contained equiaxed grains. The average grain size is 23 (Figure 5b).

3.3 X-ray Diffraction: The X-ray diffraction profiles were taken for the 3 hrs., 8 hrs. and 24 hrs.-annealed nc materials to determine whether a change in the crystal structure occurred during the annealing treatments (Figure 6). The data in Figure 6 shows no change in the crystal structure for the three heat-treated nc samples.

3.4 Electrochemical Experiments: Various properties about the material under study can be retrieved from cyclic-anodic polarization curves (Figure 7) [10]. The free potential or corrosion potential, commonly referred to as E_{corr}, is the natural potential,

with respect to the reference electrode, of a material within a given electrolyte without impressing a potential. The protective potential is the potential value at which the passivation is maintained. A passive trend on the cyclic-anodic-polarization diagram is an indication of the material's ability to resist dissolution or passive film breakdown within a given electrolyte. The point at which the oxide/hydroxide layer experiences dissolution is referred to as the pitting potential, E_{pit}. Although the pitting potential is commonly taken as the potential at the onset of pitting, pitting or localized corrosion may actually occur at potential values lower than those manifested on the cyclic-polarization curve. Hence, a more accurate definition of E_{pit} is the potential representing a pit or another form of the localized corrosion of a critical size. The intersection of the passive potential range and the reversed potential marks the protection or repassivation potential, E_{pp}, of the material. In some cases, the protection potential does not follow path 2. Thus, the protection potential is not in the anodic region. There is a possibility that the protection potential can intersect the cathodic (negative) region of the curve. If such an event occurs, the material is extremely sensitive to the localized corrosion induced by inadvertent events, such as scratches incurred during handling.

Figure 8 shows the cyclic-anodic-polarization behavior for the as-received nc material and the nc materials heat treated for 3 hrs., 8 hrs., and 24 hrs. In Figure 8, the as-received nc material exhibits the best Icorr value, and the annealed nc materials experience a decrease in Icorr with increasing grain size (Table 1). The Ecorr values for the as-received and the nc alloys annealed for 3 hrs. were similar. However, the 24-hrs. sample experienced a slight decrease, while the 8-hrs. sample exhibited a much lower Ecorr value. The pitting-potential values, Epit, for the as-received and the 3 hrs. and 8

hrs. are shown in Table 1. Unlike the aforementioned, Epit for the 24-hrs. sample was difficult to measure from the cyclic-anodic-polarization graph, since there is a steady increase in the current density. Hence, it is reasonable to assume that the pitting potential is within the range of Ecorr.

The scanning-electron microscopy (SEM) images for the tested as-received nc alloy (Figure 9), and the qualitative X-ray mapping images were taken for the tested as-received nc material to identify the location of iron oxides, chlorides, and elemental constituents or compounds that are likely present due to the anodic polarization. Qualitative mapping results, which appear as the brightest regions, verified the presence of chlorides (Figure 10a), an iron oxide (Figure 10b), and nickel (Figure 10c). In Figure 10a, X-ray mapping results show the mass transport of chlorides from the bulk electrolyte to the pit core. A deposited iron-oxide layer formed an enclosed ring around the pit core (Figure 10b). The iron oxide is believed to be Fe_2O_3, since optical microscopy revealed the presence of a burnt-orange colored ring. The nickel tends to remain uniformly distributed, with the exception of the depleted Ni region indicated by the arrows on Figure 10c. Figures 11a and 11b show both a lower and higher resolution of the etched 24 hrs.-nc material after the cyclic-anodic-polarization. Unlike the as-received nc alloy, a random distribution of the localized pits is observed throughout the sample.

In Table 1, the natural corrosion potential, E_{corr}, of both the nc and the annealed-materials are similar. However, the current density, Icorr, is higher for the 24-hrs. anneald nc alloy. A decline in the passivation properties is apparent from the shift to the right on the cyclic-anodic-polarization data, and the steady increase in the current density. Additionally, there is not a protective potential, E_{PP}, for any of the alloys. The pitting

potential, E_{Pit}, for the as-received nc alloy is higher than those observed for the 3-hrs., 8-hrs., and 24-hrs. alloys. Electrochemical data (Table 1) are compared with those measured for the as-received nc alloy and annealed Ni-18 wt.% Fe materials. An SEM image was captured at a high resolution (Figure 12) to carefully observe the grain pattern, and EDS was used to verify that the larger and smaller grains were the same composition. Figures 13a and 13b manifest similar EDS profiles, which confirms that the alloy remains homogenous.

3.5 Atom-Probe Tomography: The atom-probe tomography was employed to monitor the evolution of the grain-boundary segregation. Figure 14 reveals the results of an atom probe tomography reconstruction of the material for the 3- and 24-hrs. annealed samples. It is evident that there is no grain-boundary segregation occurring over time. Thus, the nc material's chemistry remains uniform and is stable at elevated temperatures up to 400ºC. Additionally, the electrodeposition process is optimal considering the absence of impurities detected within the bulk of the nanocrystalline material. Only surface contaminants of oxygen and carbon were detected.

4. Discussion

4.1 Pit Initiation: Two reasons may be responsible for the decrease in passivation properties for the annealed nc alloys. The first could be associated with either a structure change, which can be verified via X-ray diffraction, or heterogeneities, which can be verified via an energy dispersive spectroscopy (EDS) analyses. Since there is no structure change (Figure 6) nor compositional heterogeneities present (Figure 14), structure dependence does not seem to be a plausible reason for the passivity breakdown. Therefore, the reduced electrochemical properties are most likely attributed to the second most likely cause: the nature of the passive film [11] and the nc order arrangement within the grains.

The cyclic-anodic-polarization data manifests a short passivity range for nanocrystalline materials. Longer annealing times for the nanocrystalline material further reduce the passivity range and increase the corrosion rate. Finally, after annealing for 24 hrs., the nanocrystalline material does not exhibit any appreciable passivity; and, thus, the material has a strong propensity for pitting. Overall, for the as-deposited nanocrystalline material, within a 150 mV range above the free potential, the passivity range for the nanocrystalline Ni-18 wt.% Fe is resistant to the localized corrosion. This trend is unusual since one would expect the grain-boundary population for the nanocrystalline material to be greater than the annealed nc materials. With this in mind, the localized corrosion attributed to intergranular corrosion would appear to be the most probable suspect, given the large volume fraction of grain-boundaries present.

4.2 Pit Propagation: For the as-received nc alloy, the pit depth increases due to the depletion of oxygen and the increased pH. Increasing potentials exacerbate the

autocalytic growth of pits; and, thus, massive pits form. Upon returning the material to the proximity of the natural potential, i.e., returning to the open-circuit potential, cracking occurs due the possible presence of residual stresses, which can accelerate dissolution. Subsequent transport of excessive detrimental chlorides from the bulk electrolyte to the pit core, or the increased hydrogen content within the localized pit may induce expansion or swelling of the nc material. The formation of cracks within the pit core due to residual-stress cracking or mud cracking have been reported for other materials exposed to salt environments [12].

Research in the literature [13-15] reports that the hardness properties are temperature dependent, within a 1-hour exposure to an elevated temperature of 300ºC. Therefore, the mechanical properties of nanocrystalline materials are dependent upon the temperature. Additionally, the strength of nanocrystalline grains consisting of sizes smaller than 10 nm does not follow the Hall-Petch relationship. To continue to produce high-strength materials with a reduced grain-size, another mechanism must be employed. Grain-boundary segregation is among the most popular means to achieve further improvement in the strength with the decreased grain size. Lui et. al [16, 17] first showed how the addition of boron promotes grain segregation in Ni_3Al systems, which improves the strength.

According to the Ni-Fe phase diagram, a gamma prime (γ) phase is in equilibrium at a temperature slightly below the heat treatment temperature. Instead of adding smaller constituents, such as boron, it is plausible to assume that the segregation of γ particles to the grain boundaries can occur at an elevated temperature of 400ºC, if the transformation has not reached an equilibrium. Consequently, EDS results were performed to study

compositional variations between the smaller and larger grains within the bulk nc material. If the grain-boundary segregation is prevalent, the segregated particles are not a property-enhancing mechanism for corrosion as with strengthening due to the local chemical-potential gradient present at the grain-boundary junction. Indeed, the electrochemical results show a reduction in the passivity range with increasing grain size (Figure 8). Such results infer a breakdown of the passive film integrity, which implies that there are an increased number of defects present due to annealing. If there are an increased number of defects, there are an increased number of sites available for the deposit of detrimental chloride species from the bulk electrolyte. As a result, there are a uniform number of pit-incubation sites. However, the propagation of pits for the annealed nc alloys is believed to be attributed to the increased surface area availability on the larger grains for cathodic reactions to occur as opposed to those for the smaller grains.

For corrosion to occur, the current densities associated with the anodic and cathodic reactions must be balanced. Consequently, the cathodic and anodic sites are necessary to create a concentration cell, i.e., pitting. Within the bulk electrolyte, detrimental-chloride species are attracted to metal ions. Subsequent, metal hydrolyse occur, which increases the local hydrogen-ion concentration, i.e., the local acidification. The chloride species are uniformily dispersed due to the large degree of defects within the grains of the nc materials. The initial stage of localized corrosion is believed to commence at the grain-boundary interface of the larger and smaller grains possessing the greatest grain-boundary mismatch and defect density. Within the matrix of the larger grains, a long-range packing order is more prevalent as compared to the grain boundary, which is comprised of defects associated with a short-range order of atoms and loosely-

packed atoms. Thus, corrosion propagation may easily occur preferentially within the larger grains due to the larger surface area available, which increases the total number of cathodic reactions available to consume electrons released by the dissolution of metal to metal ions.

Since the corrosion behavior of the nc materials is more resistant than the annealed samples, the growth of the pits is constrained due to the lack of susceptibility to corrosion. At the smaller grains, the localized-corrosion proliferation is impeded because of the limited cathodic sites. Additionally, the possible presence of defects within the grain boundary may create a higher resistance to the current. Hence, the corrosion rate is decreased, and the spread of corrosion to similar-size neighboring grains is impeded.

The atom-probe tomography was employed to monitor the evolution of grain-boundary segregation. Figure 15 reveals the results of an atom-probe-tomography reconstruction of nickel for the 3- and 24-hrs.-annealed samples. It is evident that there is no grain-boundary segregation occurring over time. Thus, the nc material's chemistry remains uniform and is stable at elevated temperatures up to 400ºC. Additionally, the electrodeposition process is optimal considering the absence of impurities detected within the bulk of the nc material. Only the surface contaminants of oxygen and carbon were detected. Hence careful re-inspection of the metallographic surface under the SEM appears to show that the larger grains are more susceptible for the aforementioned reasons (Figure 11b).

5. Conclusion

A binary Ni-18 wt. % Fe nanocrystalline material undergoes localized corrosion when immersed in 3.5 wt.% NaCl solutions during potentiodynamic-polarization experiments. The possible formation of Fe_2O_3 deposits surround the pits for the as-received nc material. The cracking phenomena is most likely associated with the coupling effects of possible residual stresses and detrimental species, such as chlorides or hydrogen, into the pit core. The atom-probe-tomography validates that the compositon of the nc material remains uniform after ageing for 3 hrs., 8 hrs., and 24 hrs. The absence of the γ segregation to the grain boundary suggest that the material does not exhibit grain boundary segregation. Overall, the corrosion behavior of the as-depostited nanocrystalline material is the best compared to those reported for the aged nc materials. The reason is believed to be the lack of surface area available for the completion of cathodic reactions by the consumption of electrons released from the oxidation of metal to metal ions in the aged nc materials.

REFERENCES

1. Petch, N.J., *The Cleavage Strength of Polycrystals.* Journal of the Iron and Steel Institute, 1953. **174**(1): pp. 25-28.

2. Hall, E.O., *The Deformation and Ageing of Mild Steel .3. Discussion of Results.* Proceedings of the Physical Society of London Section B, 1951. **64**(381): pp. 747-753.

3. Gleiter, H., *Nanocrystalline Materials.* Progress in Materials Science, 1989. **33**(4): pp. 233-315.

4. Mishra, R. and Balasubramaniam, R., *Effect of nanocrystalline grain size on the electrochemical and corrosion behavior of nickel.* Corrosion Science, 2004. **46**(12): pp. 3019-3029.

5. Wang, S.G., Shen, C.B., Long, K., Yang, H.Y., Wang, F.H., Zhang, Z.D., *Preparation and Electrochemical Corrosion Behavior of Bulk Nanocrystalline Ingot Iron in HCl Acid Solution.* Journal of Physical Chemistry B, 2005. **109**(7): pp. 2499-2503.

6. Inoue, A. and Takeuchi, A., *Recent Progress in Bulk Glassy, Nanoquasicrystalline and Nanocrystalline Alloys.* Materials Science and Engineering A-Structural Materials Properties Microstructure and Processing, 2004. **375-77**: pp. 16-30.

7. Suryanarayana, C., *Structure and Properties of Nanocrystalline Materials.* Bulletin of Materials Science, 1994. **17**(4): pp. 307.

8. Peter, W.H., Buchanan, R.A., Liu, C.T., Liaw, P.K., Morrison, M.L., Horton, J.A., Carmichael Jr., C.A., and Wright, J.L., *Localized Corrosion Behavior of a*

Zirconium-Based Bulk Metallic Glass Relative to its Crystalline State. Intermetallics, 2002. **10**: pp. 1157-1162.

9. Jiang, L., Wang, H., Liaw, P. K., Brooks, C. R., Klarstrom, D. L., C*haracterization of the Temperature Evolution During High-Cycle Fatigue of the ULTIMET Superalloy: Experiment and Theoretical Modeling.* Metallurgical and Materials Transactions A-Physical Metallurgy and Materials Science, 2001. **32**(9): pp. 2279-2296.
10. Stansbury, E.E., and Buchanan,.R.A., *Fundamentals of Electrochemical Corrosion.* ASM International, 2000.
11. Inturi, R.B., and Szklarska-Smialowska, Z., *Localized Corrosion of Nanocrystalline 304 Type Stainless Steel Films.* Corrosion, 1992. **48**(5): pp. 398.
12. Kim, T.G., Lee, H. C., Choi, J. M., Hwang, Y. H., *Failure Analysis of Air Interceptor Missile Rocket Motors.* Engineering Failure Analysis, 2005. **12**(2): pp. 307-315.
13. Wang, Y.M., Cheng, S., Wei, Q. M., Ma, E., Nieh, T. G., Hamza, A., *Effects of Annealing and Impurities on Tensile Properties of Electrodeposited Nanocrystalline Ni.* Scripta Materialia, 2004. **51**(11): pp. 1023-1028.
14. Huang, X.X., Hansen, N., and Tsuji, N., *Hardening by Annealing and Softening by Deformation in Nanostructured Metals.* Science, 2006. **312**(5771): pp. 249-251.
15. Fan, G.J., Choo, H., and Liaw, P. K., *Embrittlement in a Bulk Nanocrystalline Alloy Induced by Room-Temperature Aging.* Applied Physics Letters. **in press**.

16. George, E.P., Liu C.T., and Pope, D.P., *Mechanical Behavior of Ni3Al: Effects of Environment, Strain Rate, Temperature, and Boron Doping.* Acta Materialia, 1996. **44**(5): pp. 1757.

17. George, E.P., Liu C.T., Lin H., and Pope, D.P., *Environmental Embrittlement and Other Causes of Brittle Grain-Boundary Fracture in Ni_3Al.* Materials Science and Engineering A - Structural Materials Properties, Microstructure, and Processing, 1995. **193**: pp. 193.

APPENDICES

Appendix A: Tables
Appendix B: Figures

APPENDIX A

Table 1. Electrochemical Data for Nickel and Nickel-based Materials

Alloy	Icorr (A/m^2)	Ecorr (mV-SCE)	Epit (mV-SCE)
Ni-18wt.% Fe As-Received	0.05	-231	-142
Ni-18wt.% Fe – 3 hr.	0.10	-219	-175
Ni-18wt.% Fe – 8 hr.	0.40	-280	-153
Ni-18wt.% Fe – 24 hr.	0.90	-246	–

APPENDIX B

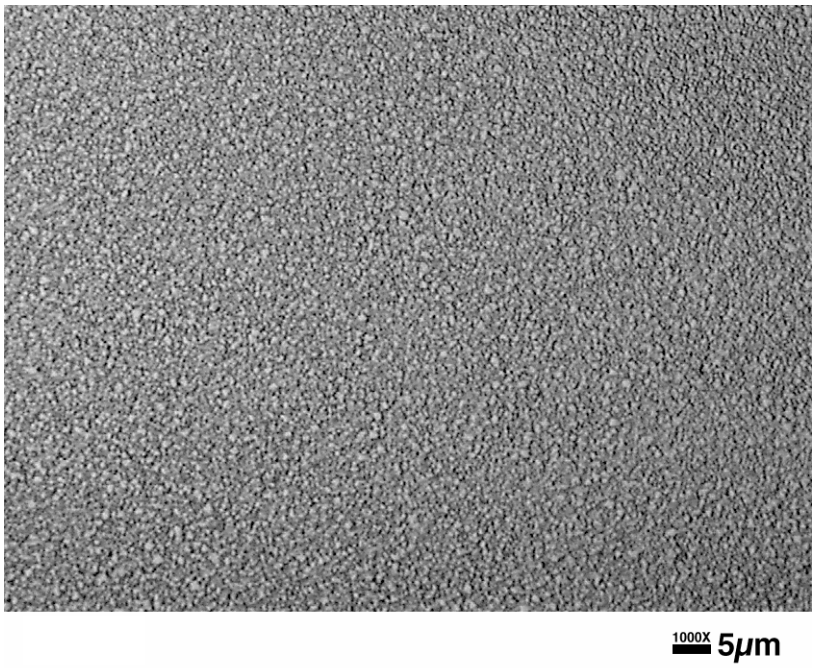


Figure 1. Nanocrystalline Ni-18wt.%Fe As-received Material.

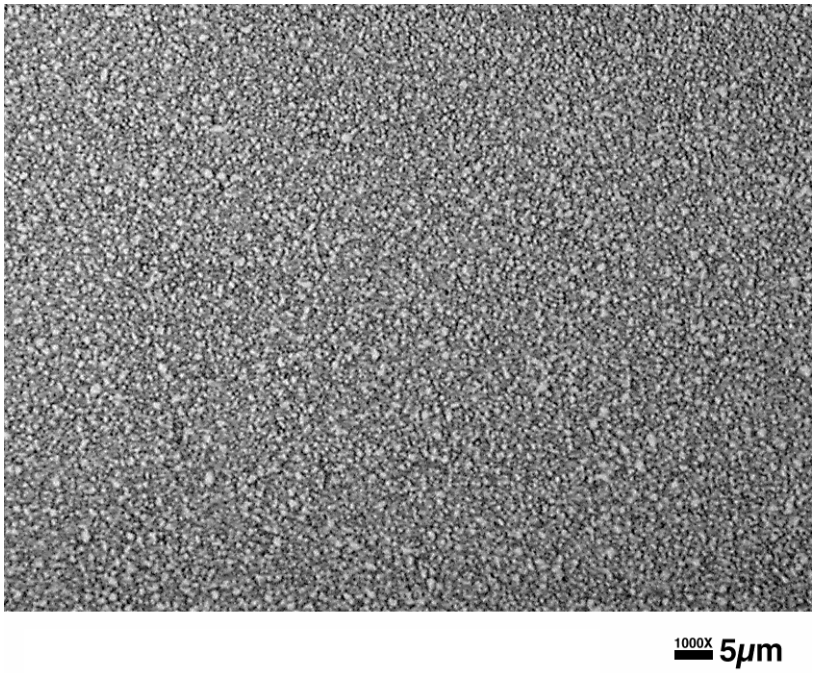


Figure 2. 3 hrs. Anneal at 400ºC of Nanocrystalline Ni-18wt.%Fe

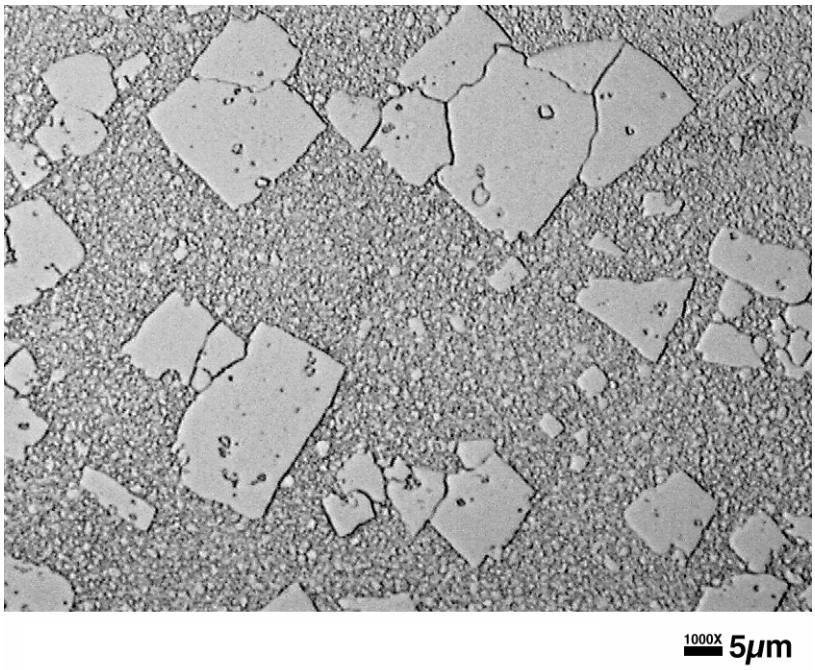


Figure 3. 8 hrs. Anneal at 400ºC of Nanocrystalline Ni-18wt.%Fe

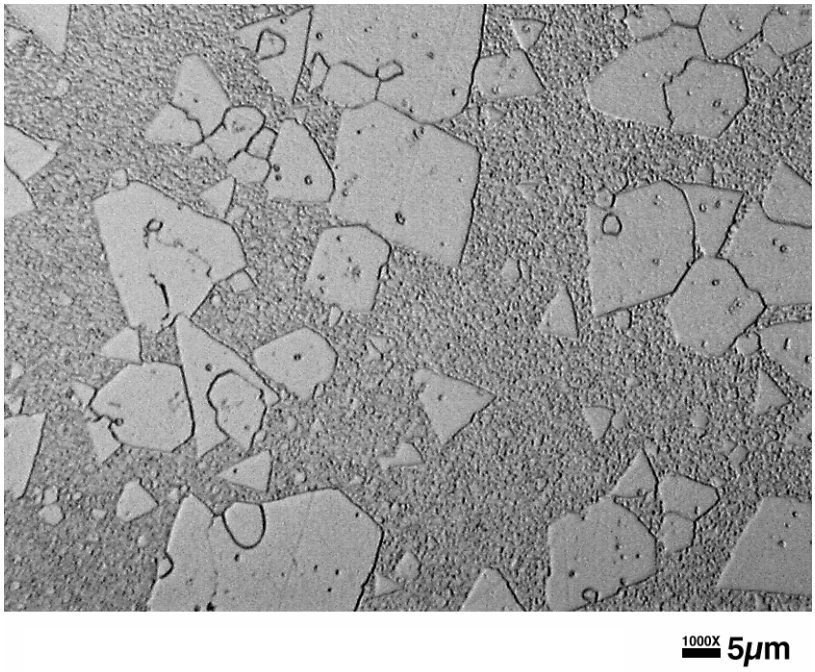


Figure 4. 24 hrs. Anneal at 400ºC of Nanocrystalline Ni-18wt.%Fe

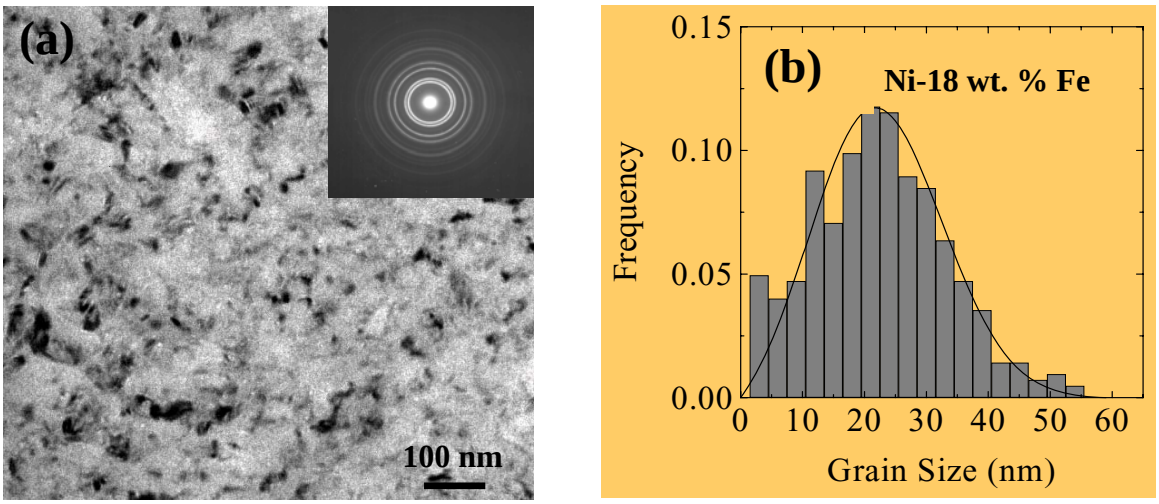


Figure 5. Nanocrystalline Ni-18wt.%Fe: a) Transmission Electron Micrograph, and b) Grain-Size Distribution.

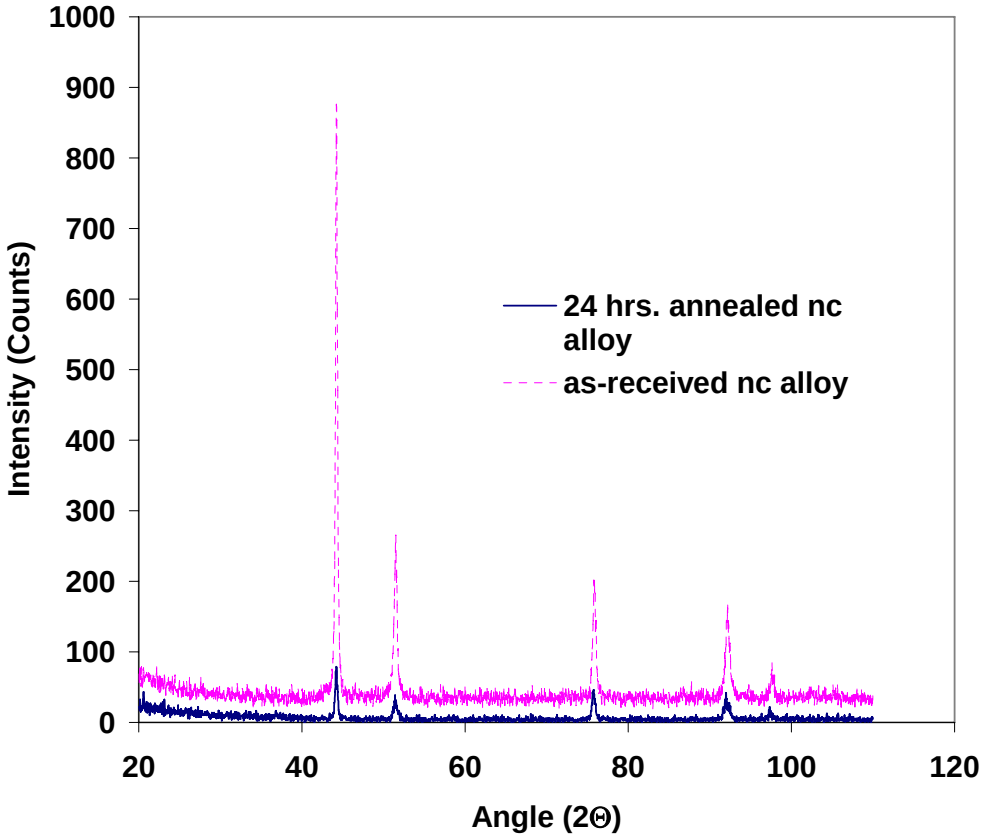


Figure 6. X-ray Diffraction results for Ni-18wt.% Fe Nanocrystalline Samples after 3 hrs., 8 hrs., and 24 hrs. annealing

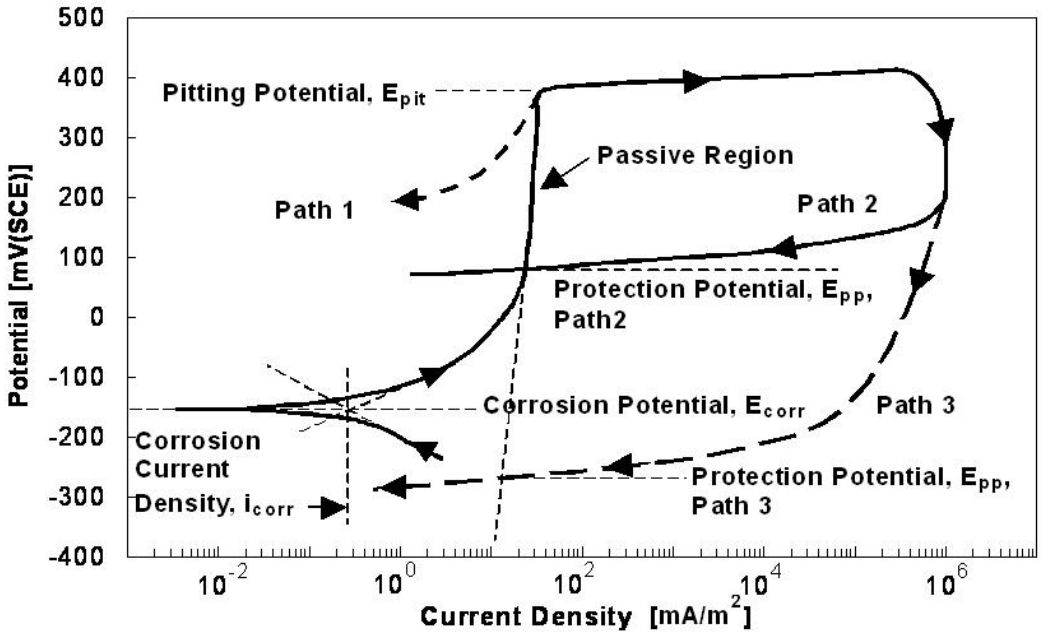


Figure 7. Typical Representation of Cyclic Anodic Polarization Curve

Source: Peter, W.H.; Buchanan, R.A.; Liu, C.T.; Liaw, P.K.; Morrison, M.L.; Horton, J.A.; Carmichael Jr., C.A.; and Wright, J.L. "Localized corrosion behavior of a zirconium-based bulk metallic glass relative to its crystalline state," Intermetallics, 2002; 10:1157-1162. (Reprinted from [8] with permission from Elsevier.)

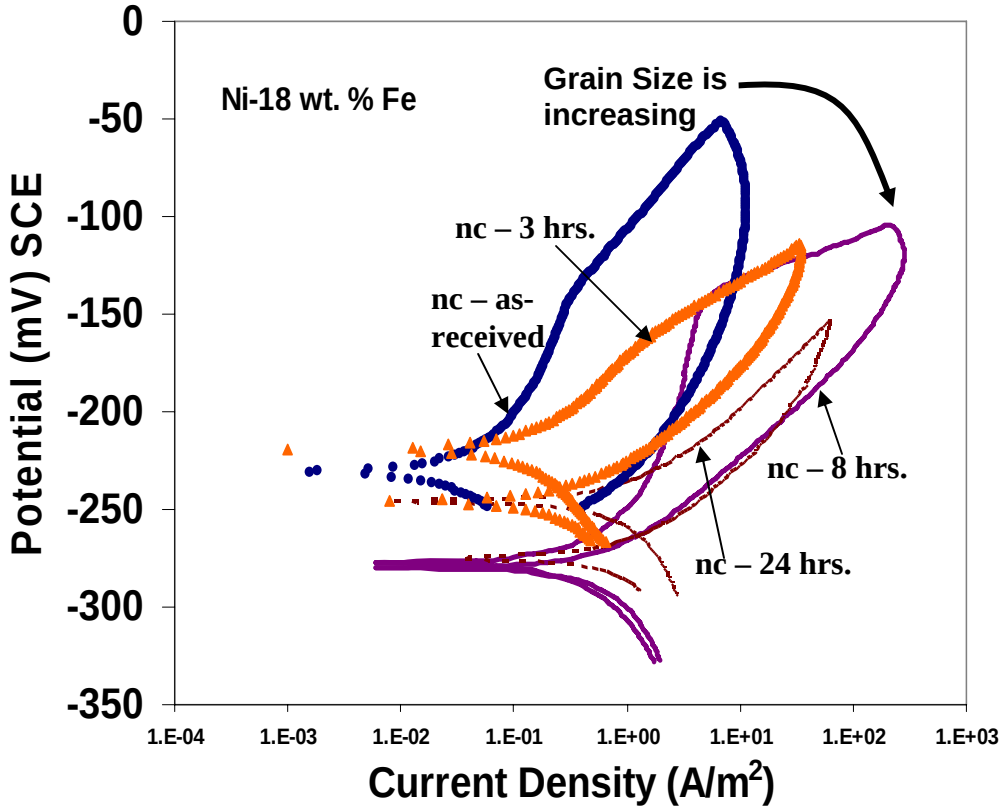


Figure 8. Cyclic-Anodic Polarization Curve for Ni-18wt.% Fe Nanocrystalline Sample in 3.5 wt.% NaCl Solution

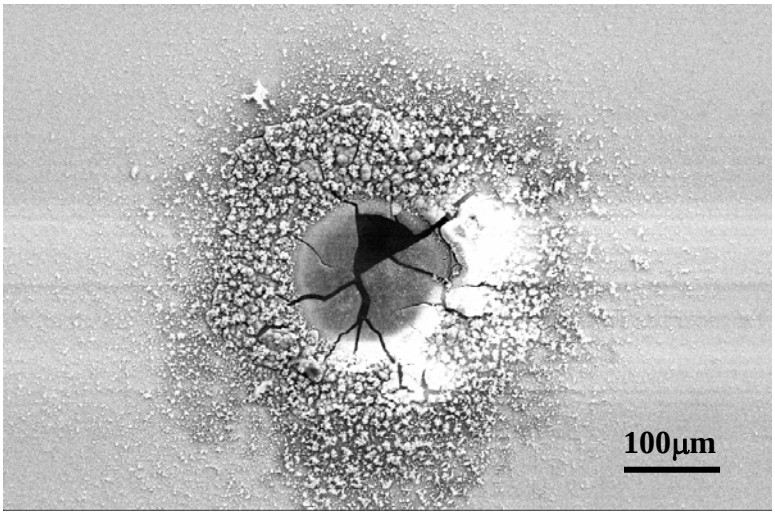


Figure 9. SEM Micrograph of Mud Cracking in Pit on Ni-18wt.% Fe Nanocrystalline Surface

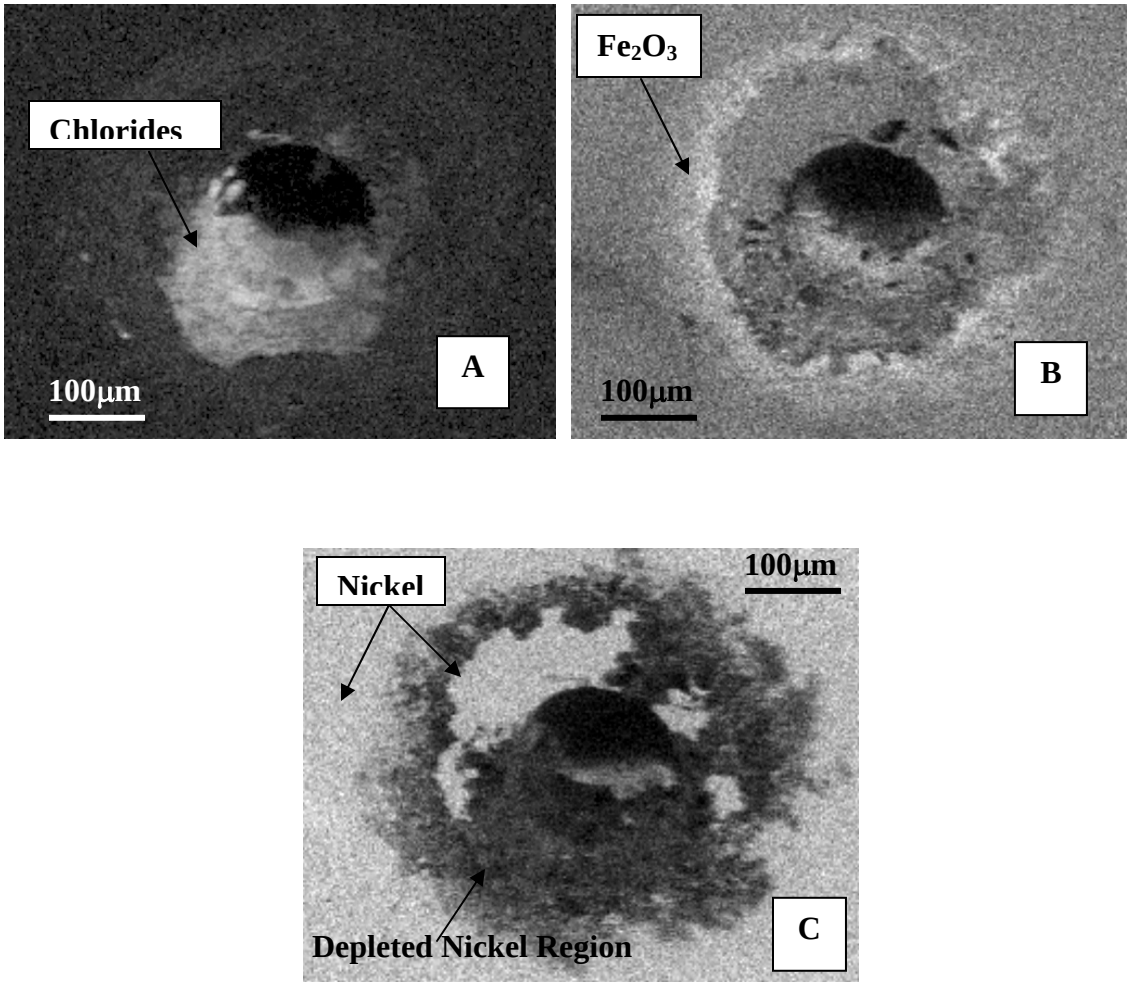


Figure 10. Qualitative X-ray Mapping Data: A) Chloride Concentrations; B) Fe_2O_3 Concentrations; and C) Nickel Concentrations.

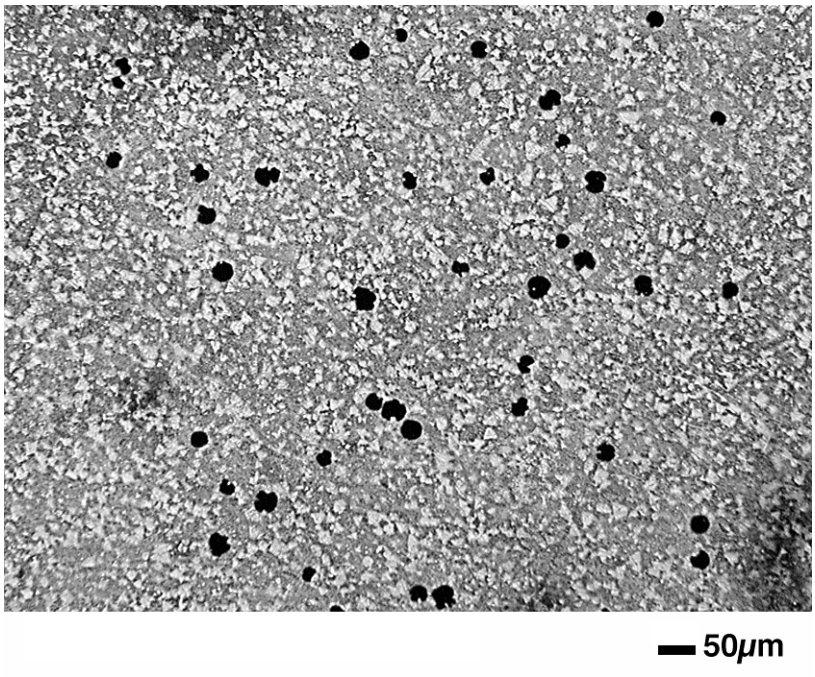


Figure 11. Magnification of Localized Corrosion in 3.5 wt.% NaCl Solution for Nanocrystalline Ni-18wt.%Fe Annealed for 24 hrs. at 400ºC

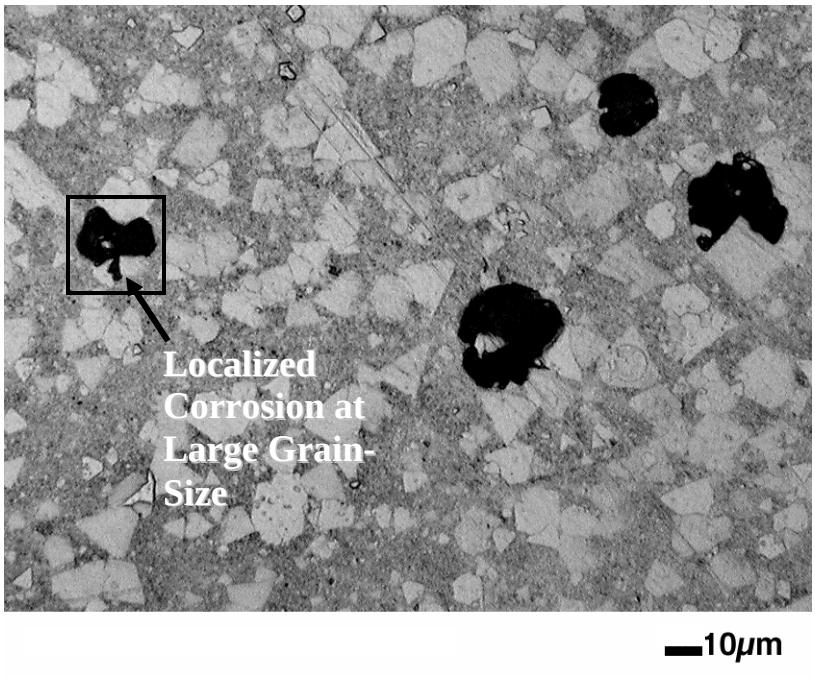


Figure 12. Magnification of Localized Corrosion in 3.5 wt.% NaCl solution for Nanocrystalline Ni-18wt.%Fe Annealed for 24 hrs. at 400ºC

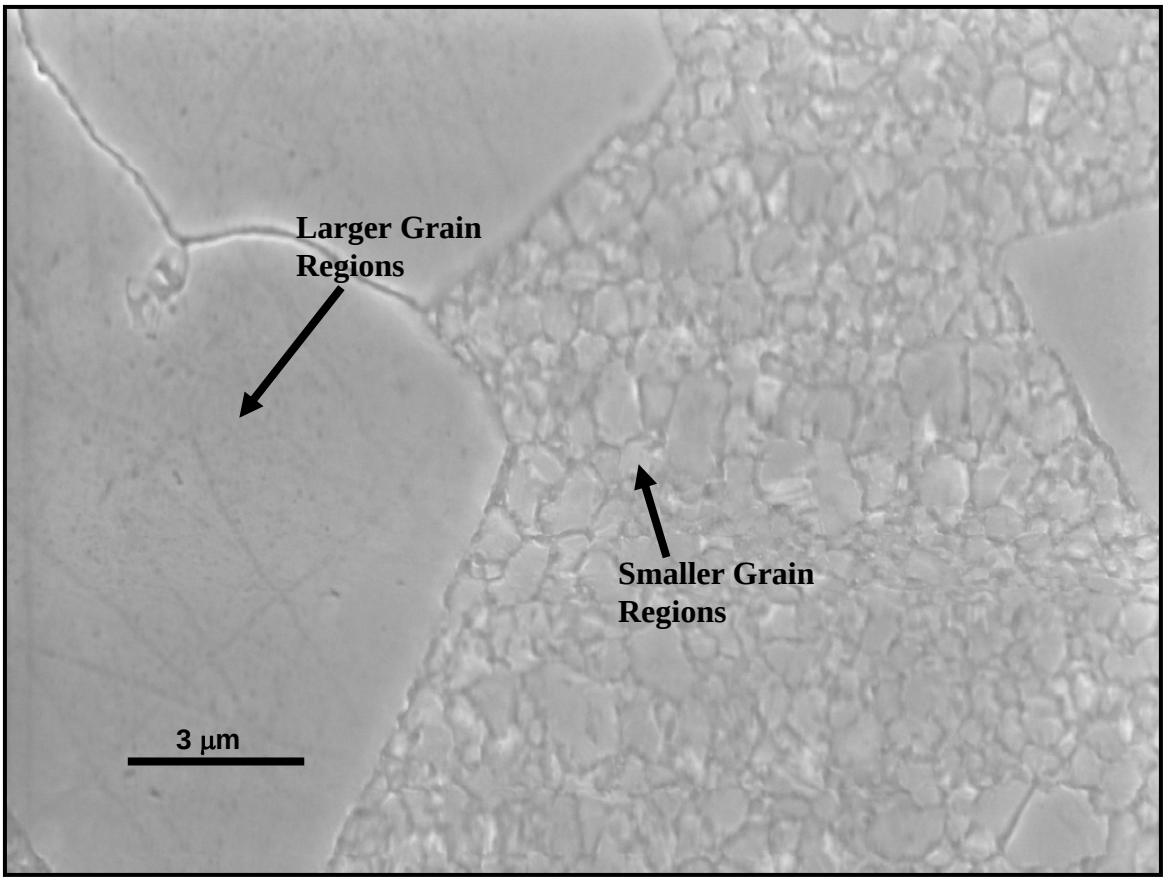
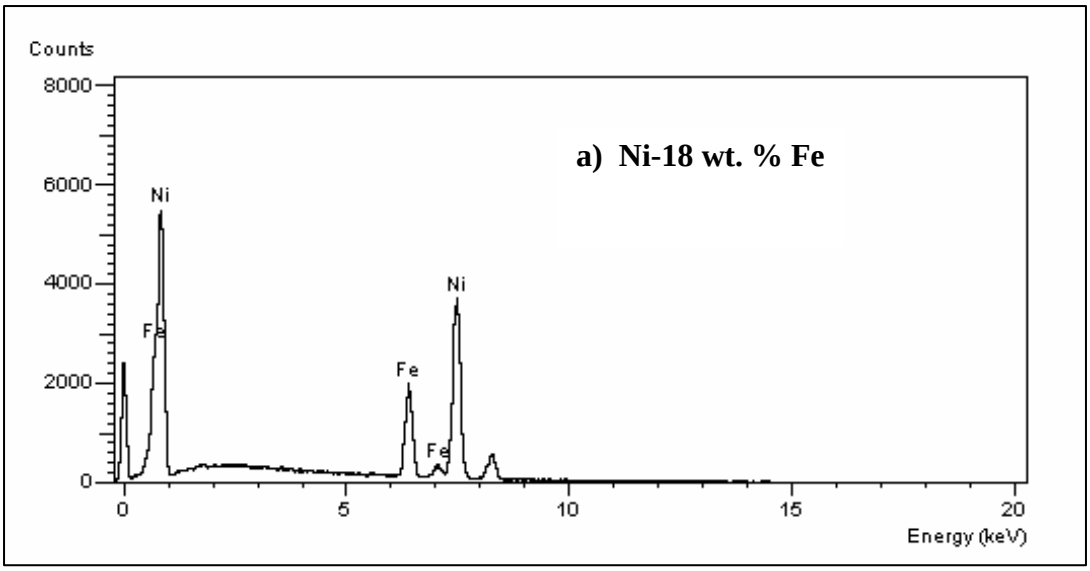


Figure 13. Secondary Electron SEM Image of Nanocrystalline Ni-18wt.%Fe Annealed at 400°C for 24 hrs. with EDS Profile



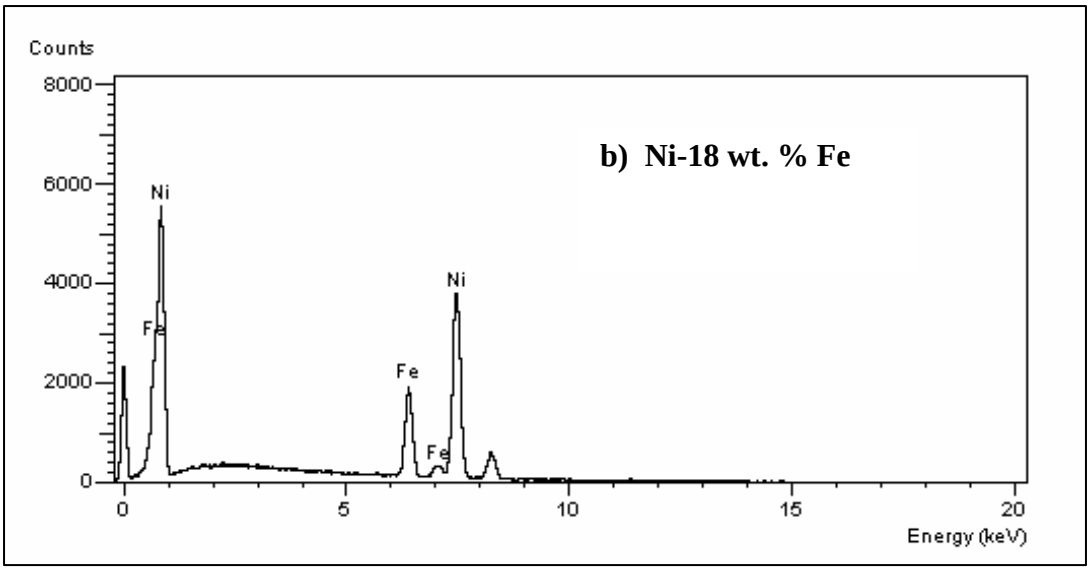


Figure 14. EDS Profiles for the 24-hrs. Annealed NC Material: a) Larger Grain Region. b) Smaller Grain Region

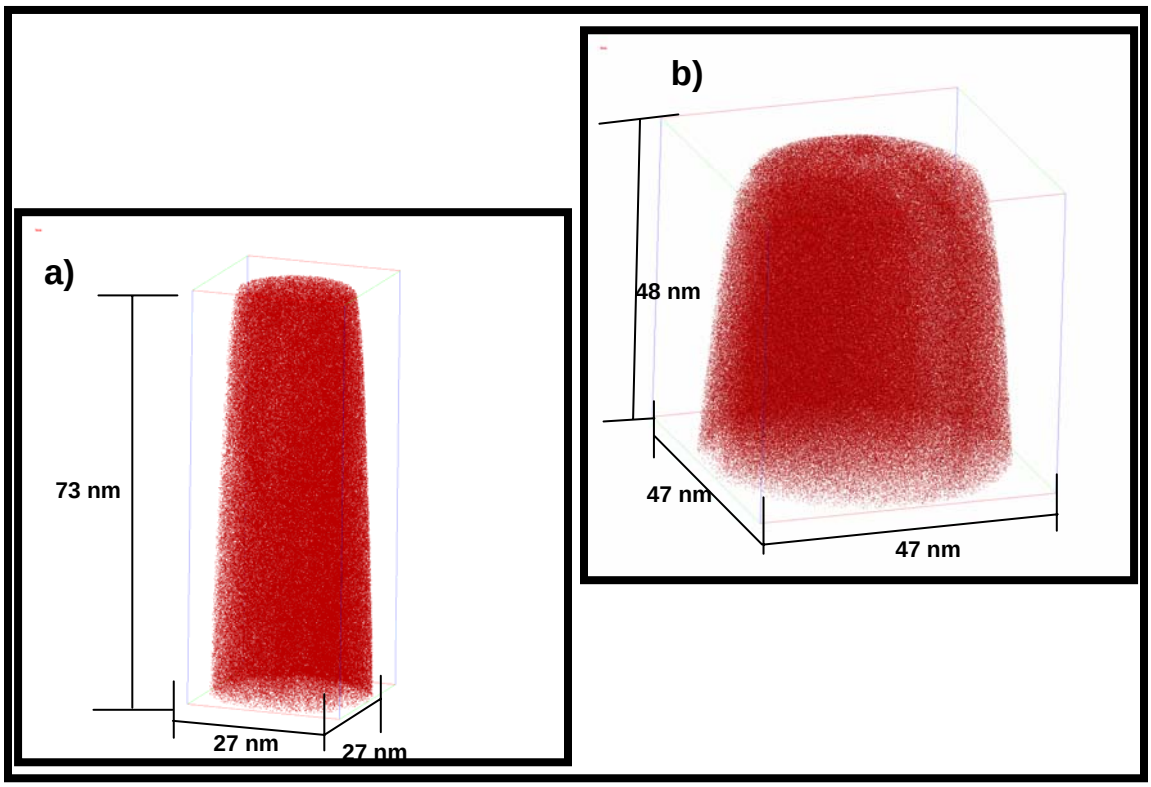


Figure 15. Atom-Probe Reconstruction: a) Ni-Compositional Matrix for the 3-hr. Post Treatment of Ni-18wt.%Fe; b) Ni-Compositional Matrix for the 24-hr. Post Treatment of Ni-18wt.%Fe

DISSERTATION APPENDICES
Appendix A: C2000 Research
Appendix B: Nanocrystalline Research

Appendix A

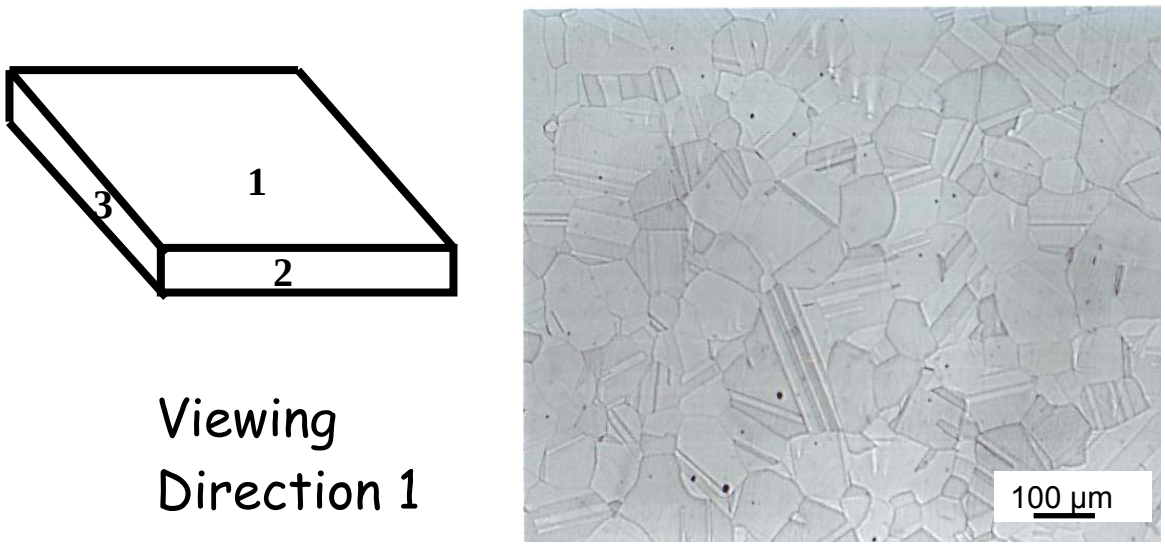


Figure 1. Optical Micrograph of the As-Received C2000 in Viewing Direction 1

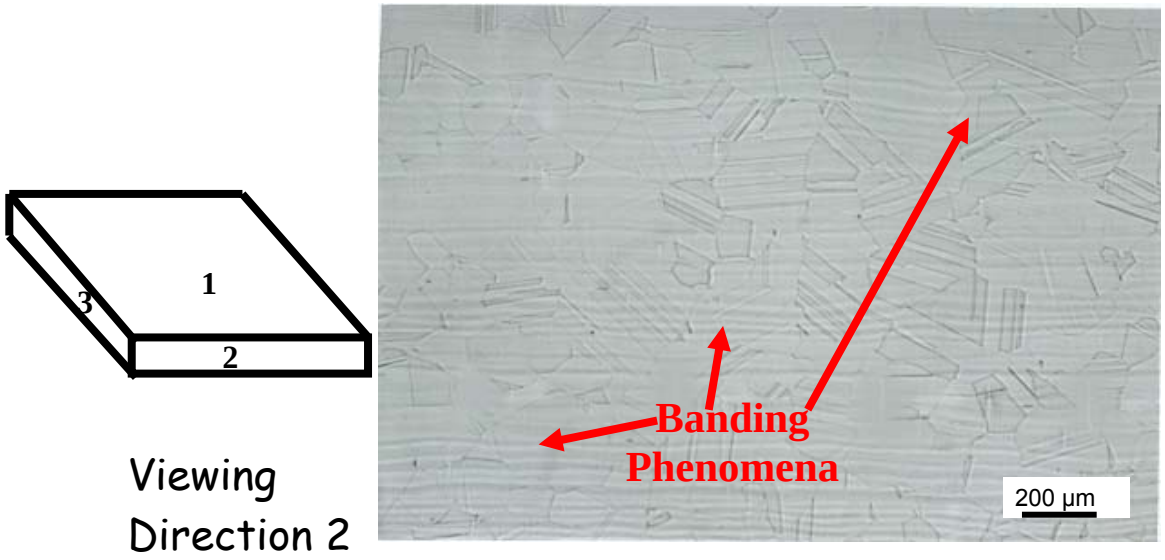


Figure 2. Optical Micrograph of the As-Received C2000 in Viewing Direction 2

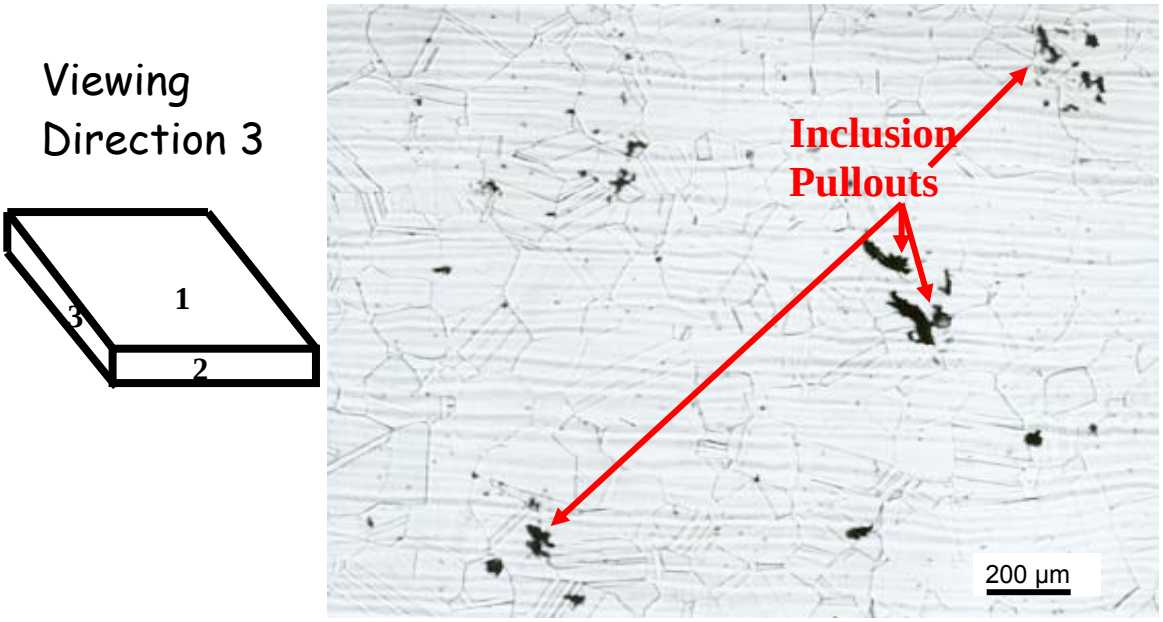


Figure 3. Optical Micrograph of the As-Received C2000 in Viewing Direction 3

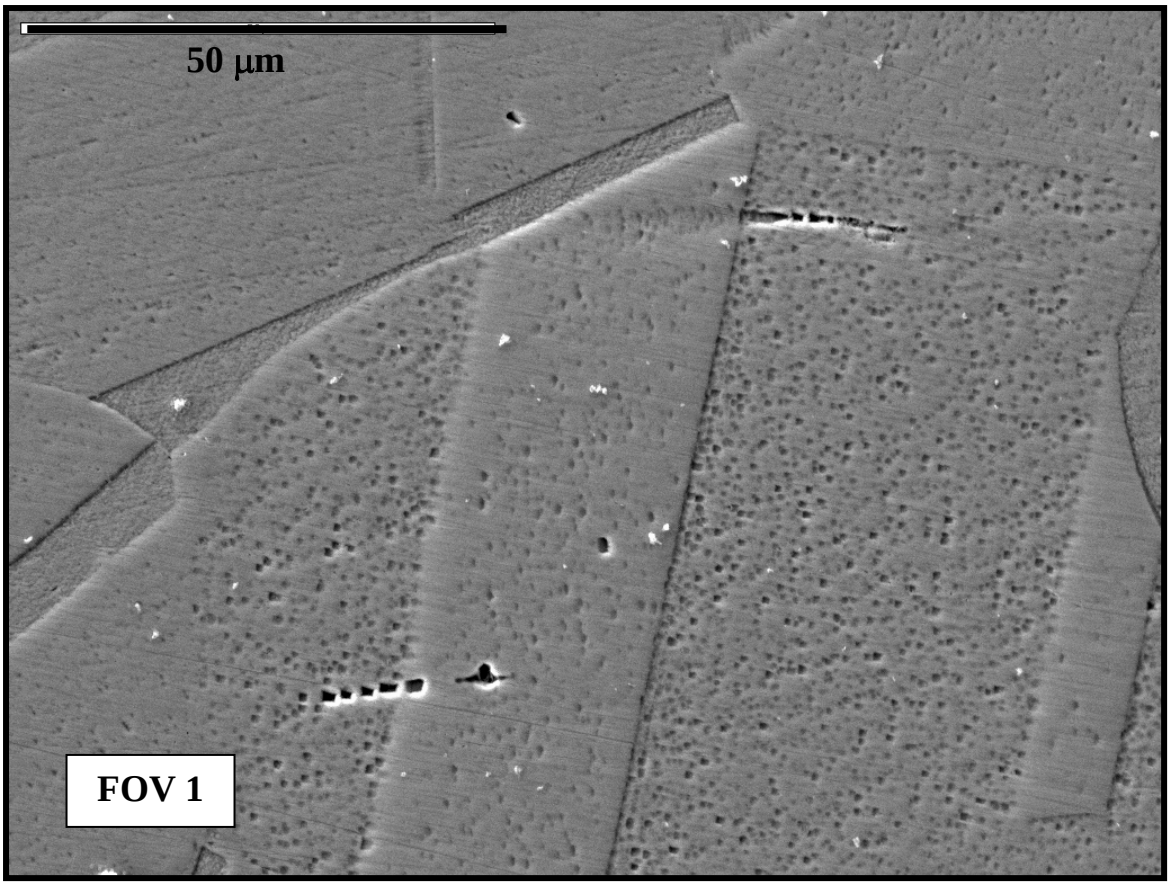


Figure 4. SEM Micrograph of the As-Received C2000 at Field of View (FOV) 1

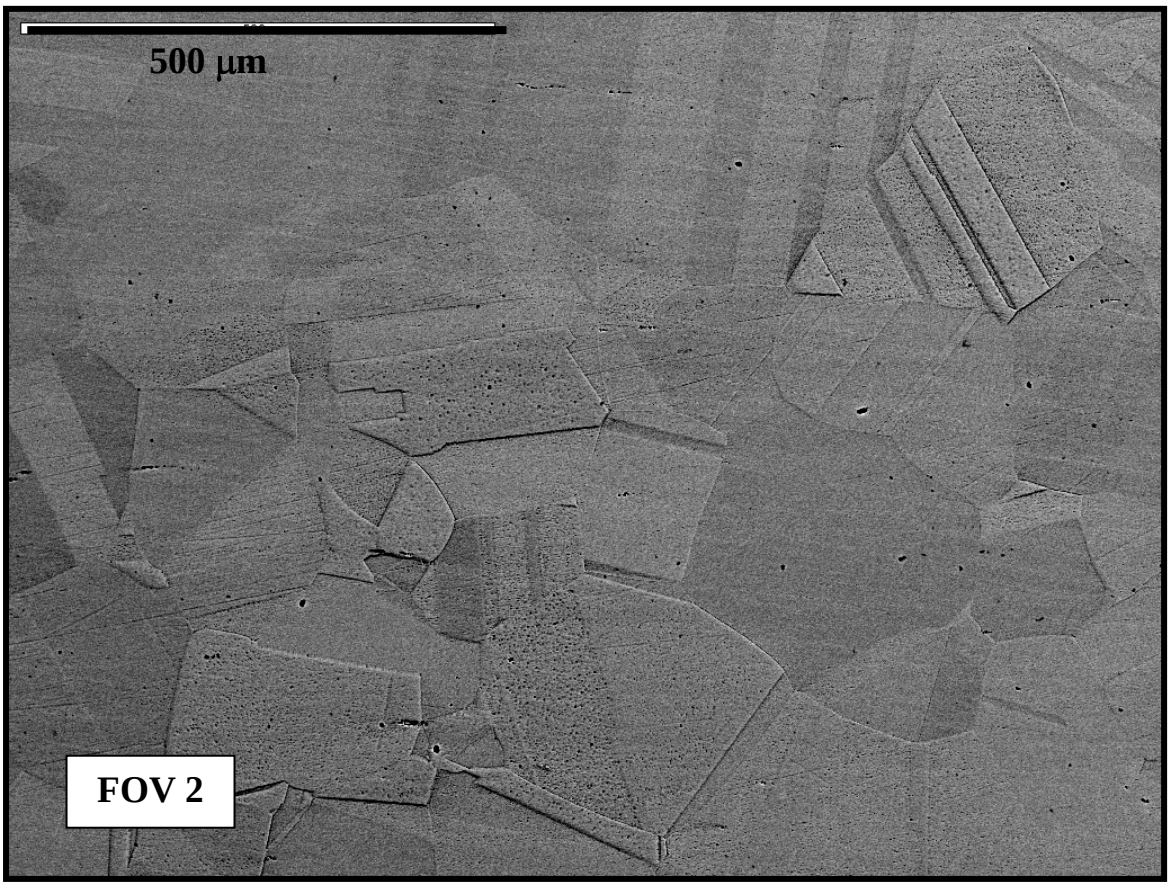


Figure 5. SEM Micrograph of the As-Received C2000 at FOV 2

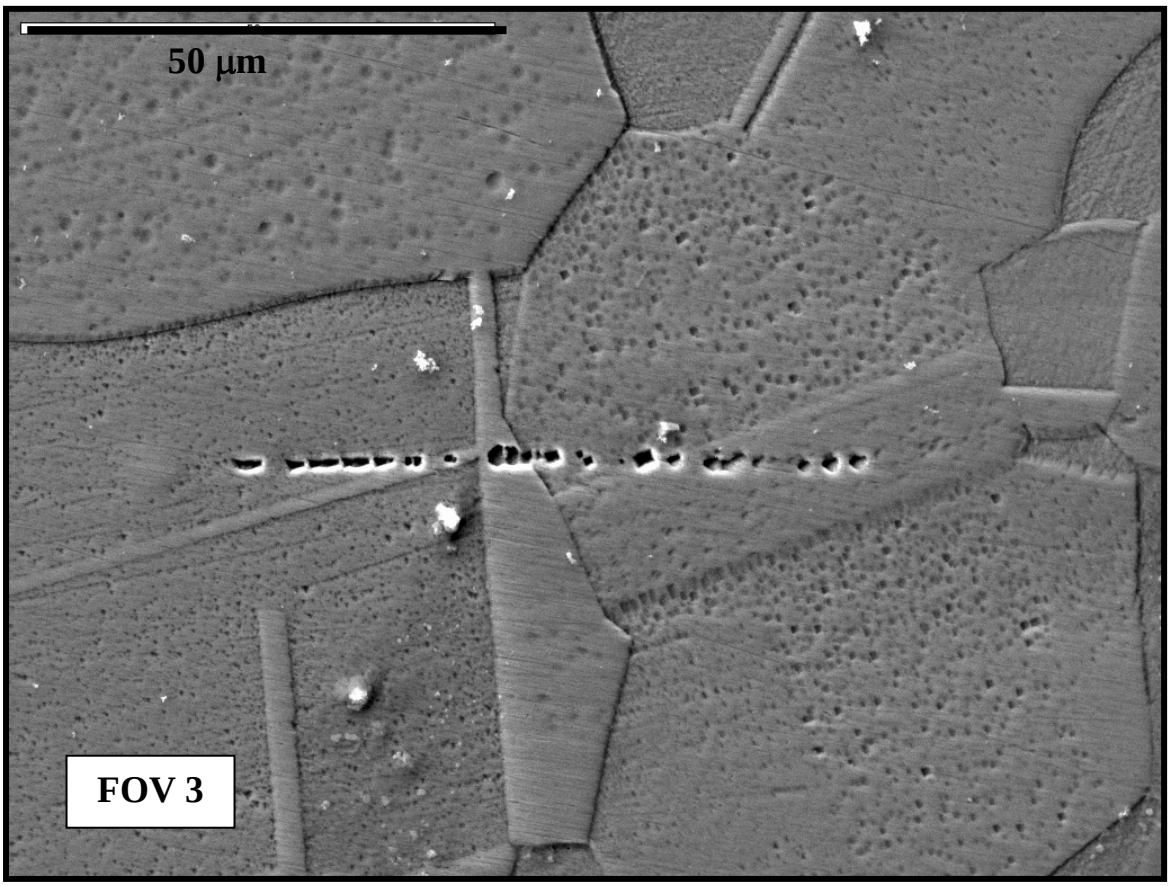


Figure 6. SEM Micrograph of the As-Received C2000 at FOV 3

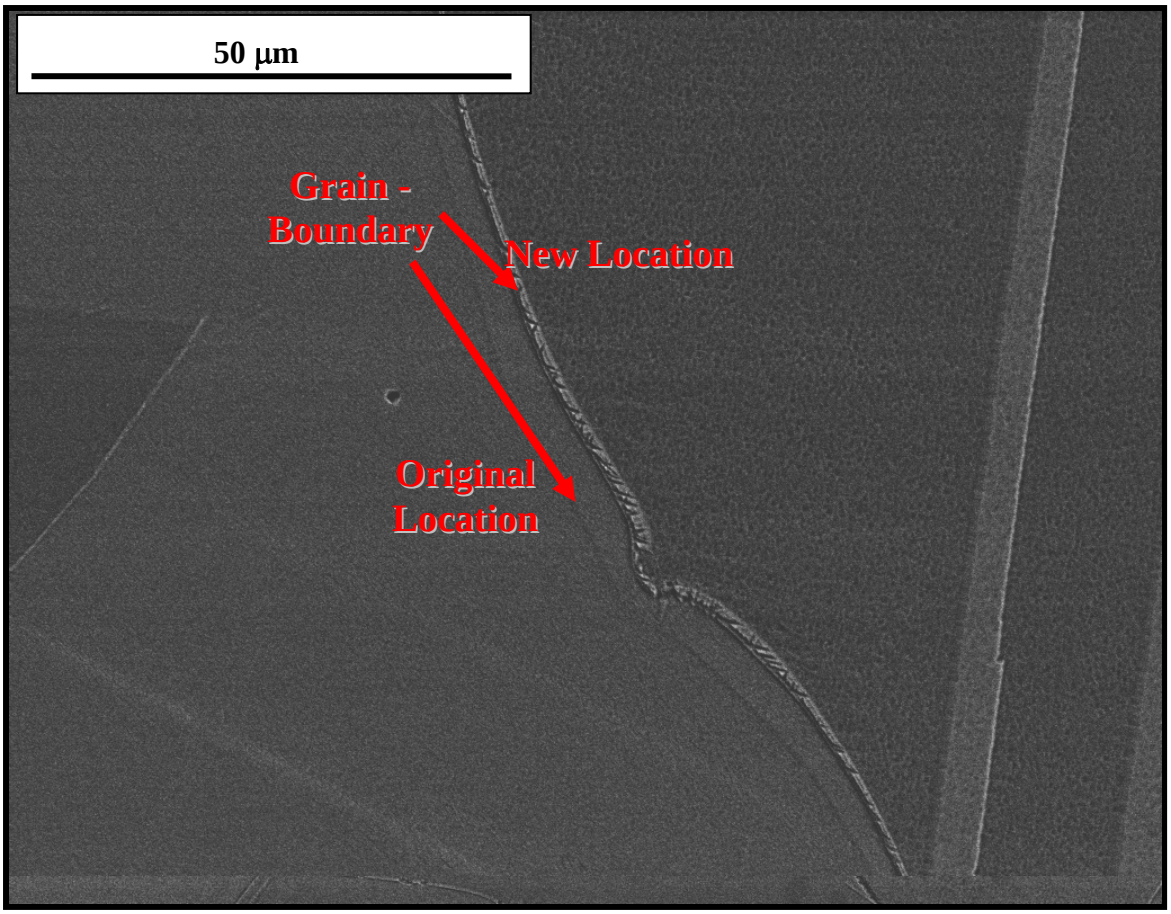


Figure 7. Grain-Boundary Mobility Region in the As-Fabricated C2000

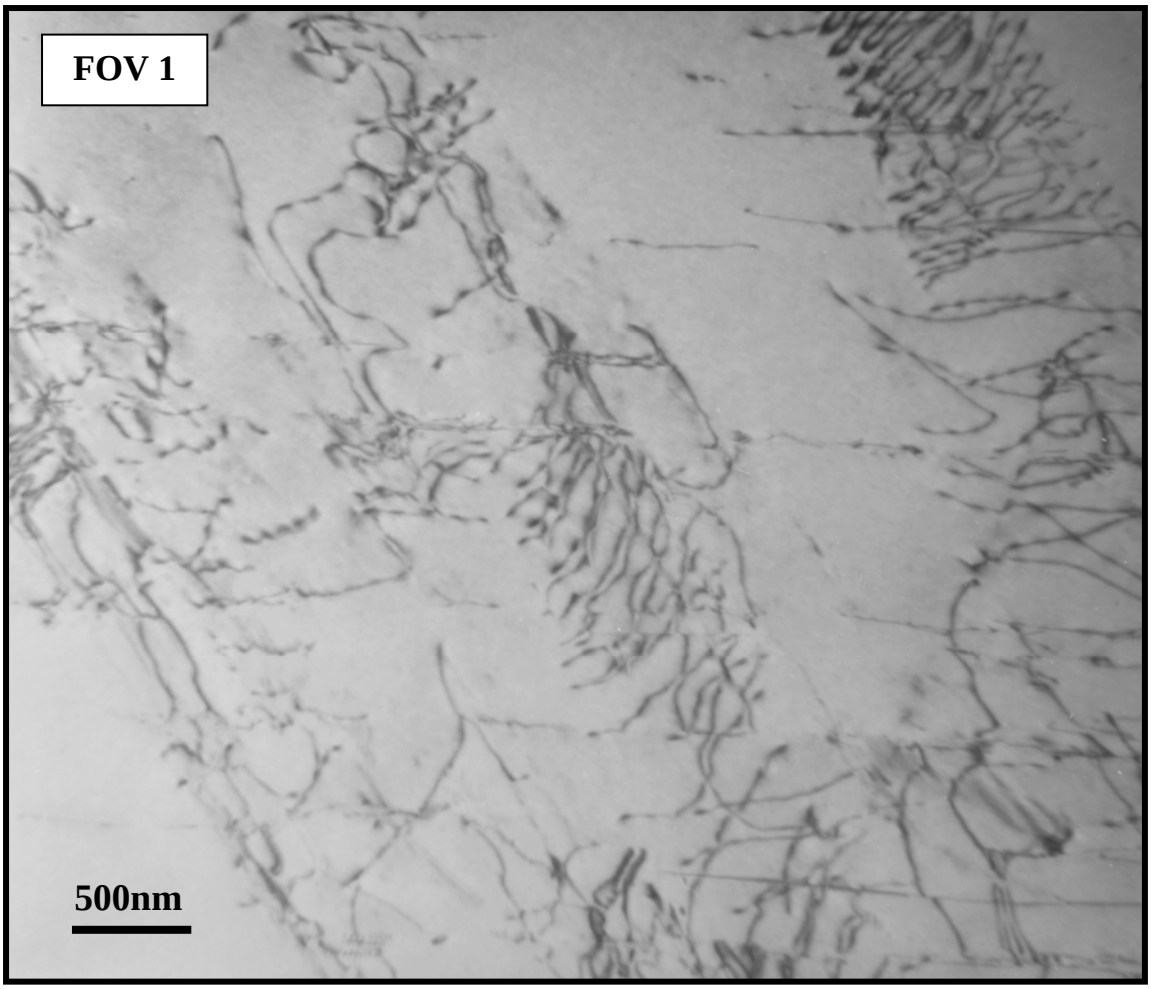


Figure 8. TEM Micrograph of the As-Received C2000 in FOV 1

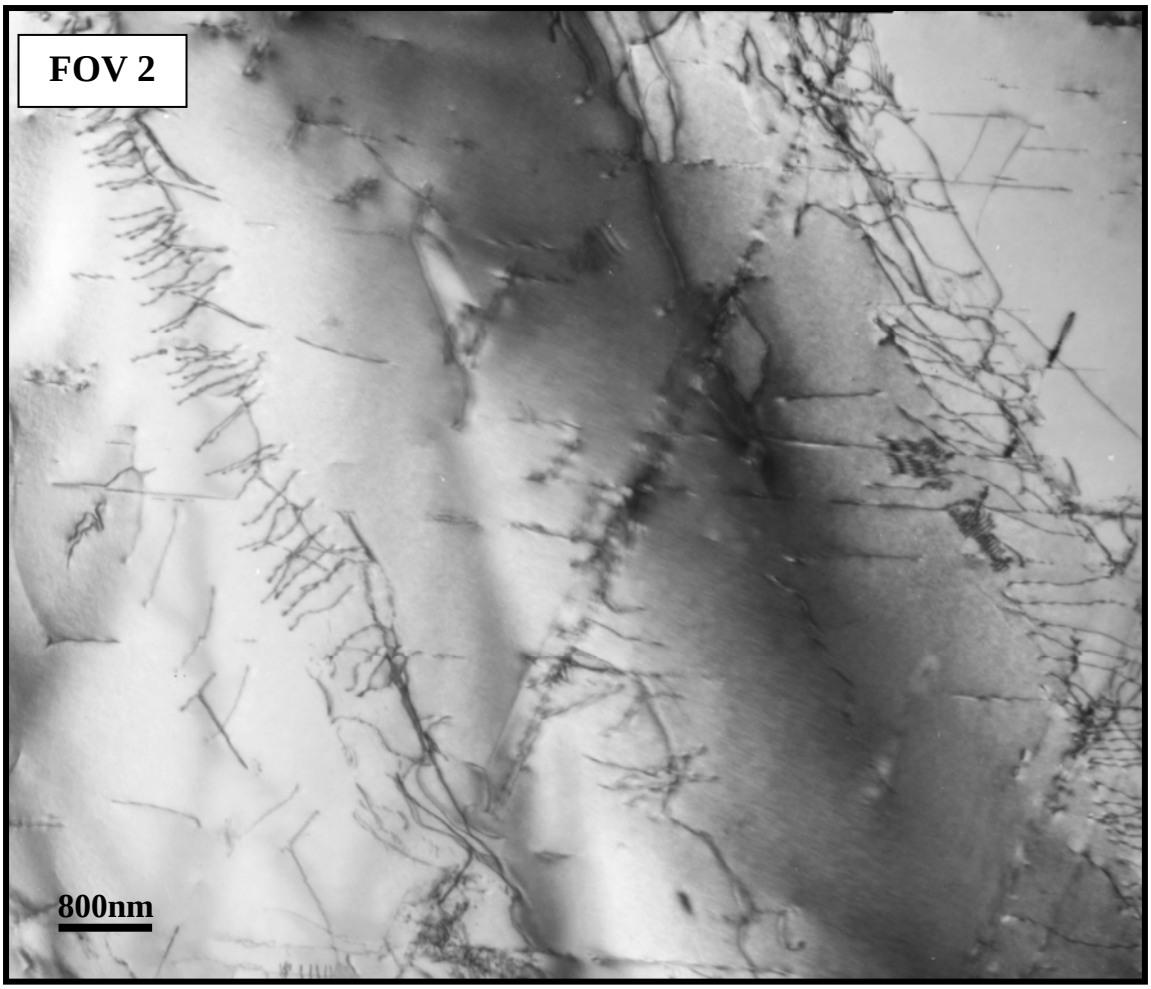


Figure 9. TEM Micrograph of the As-Received C2000 in FOV 2

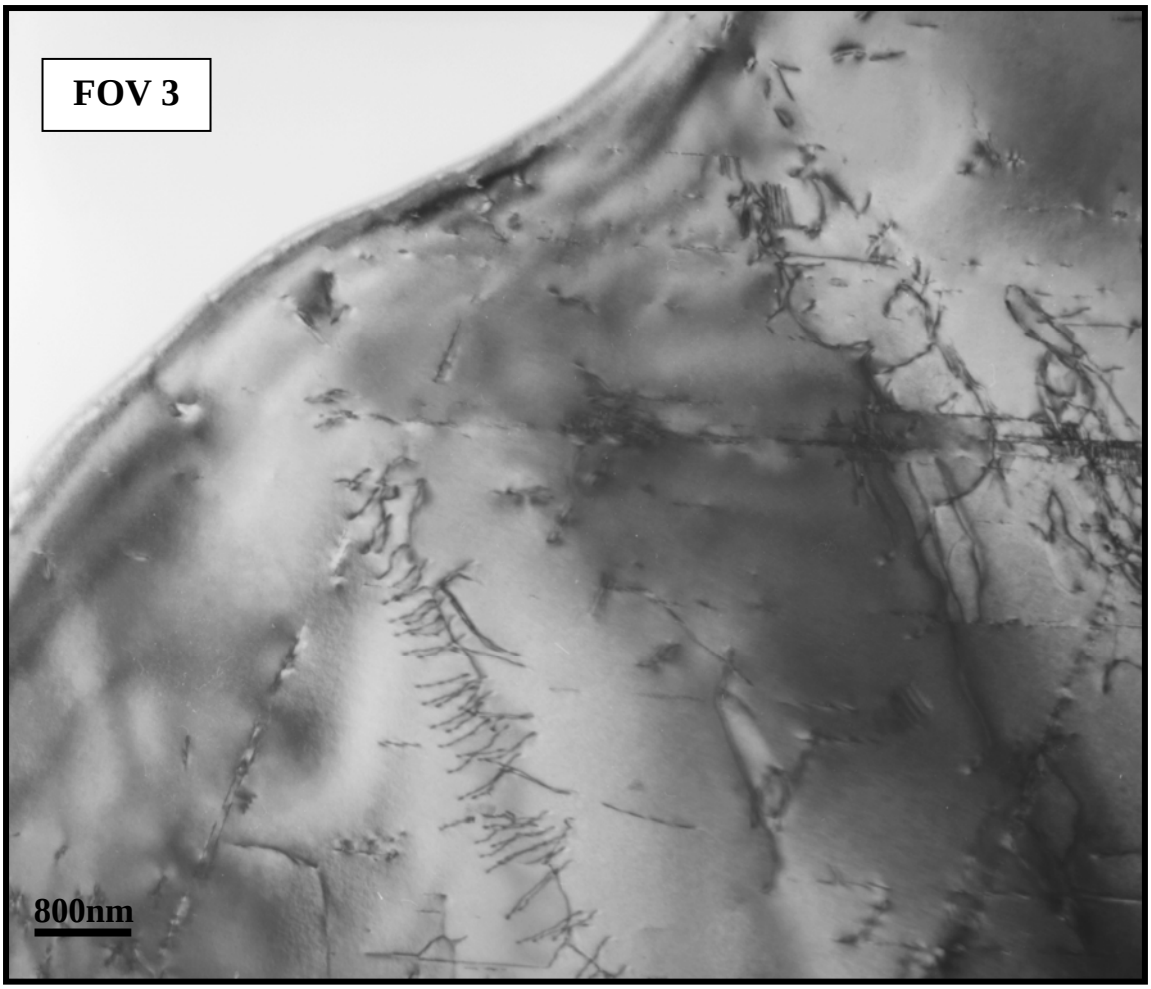


Figure 10. TEM Micrograph of the As-Received C2000 in FOV 3

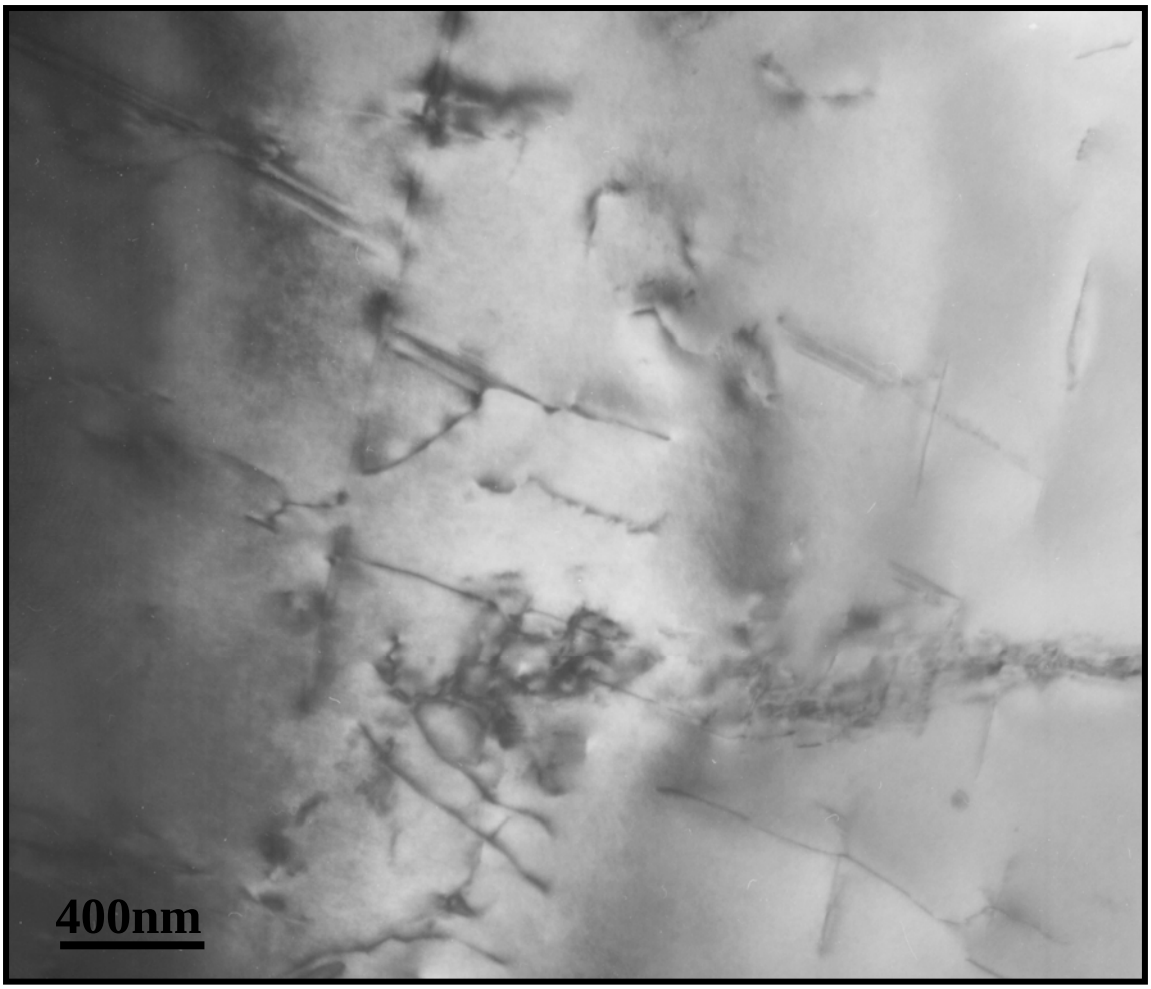


Figure 11. Higher-Resolution TEM Micrograph of the As-Received C2000

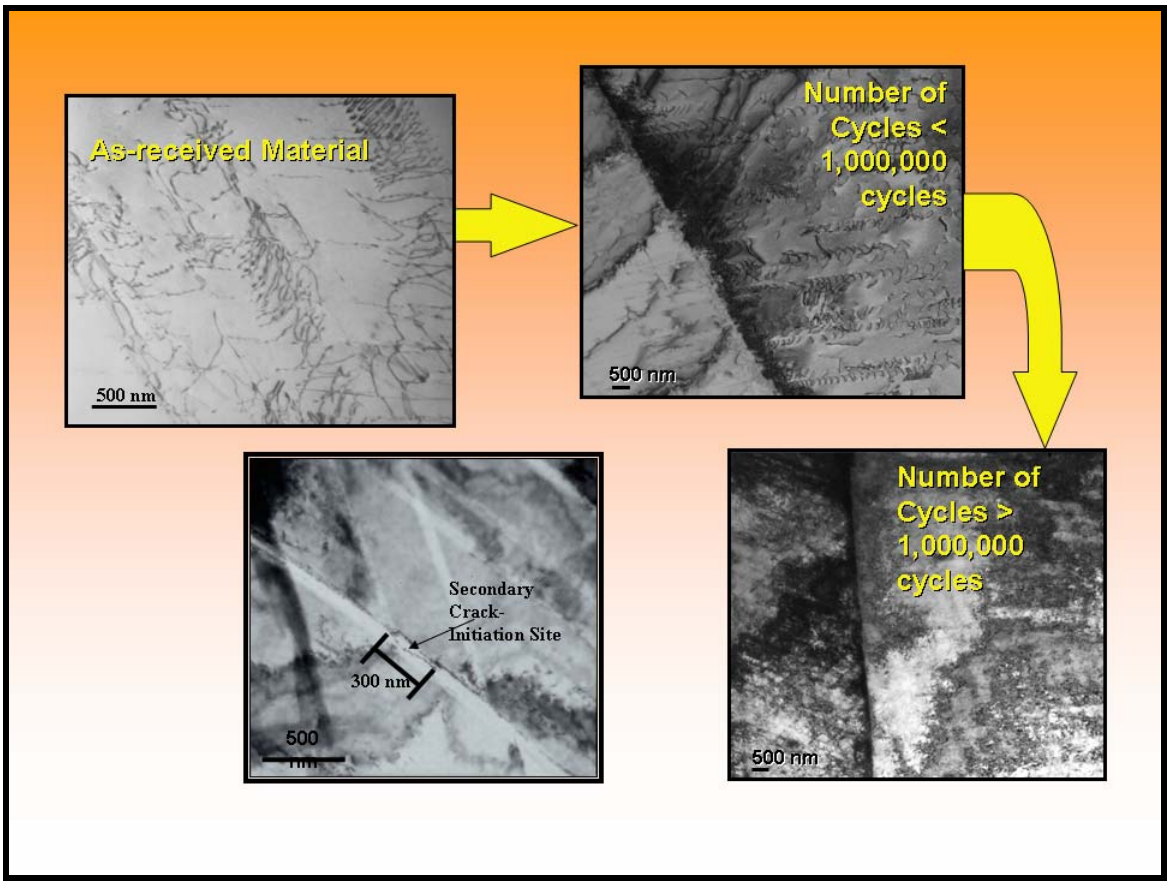


Figure 12. The Evolution of Dislocations: a) As-Received C2000, b) Less Than 1,000,000 Cycles, c) Greater than 1,000,000 Cycles, d) A Secondary Crack Observed After 1,000,000 Cycles

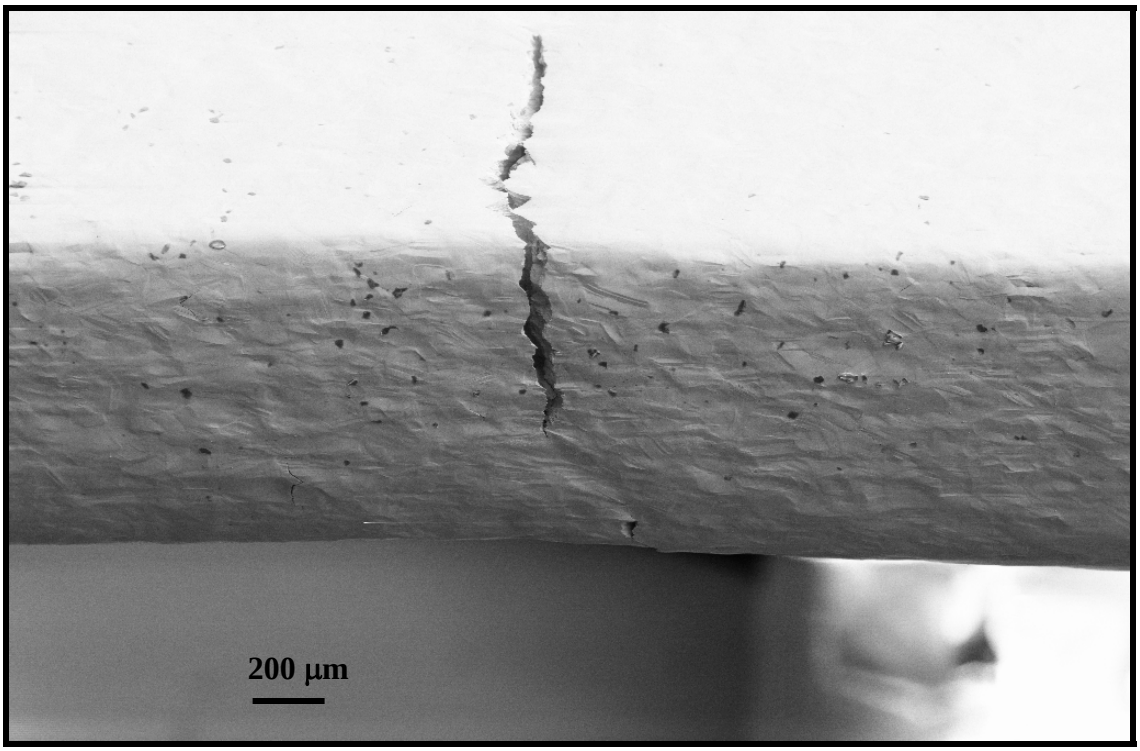


Figure 13. Crack Propagation of C2000 Fatigued at 574 MPa in 3.5 wt.% NaCl and an R-Ratio of 0.1

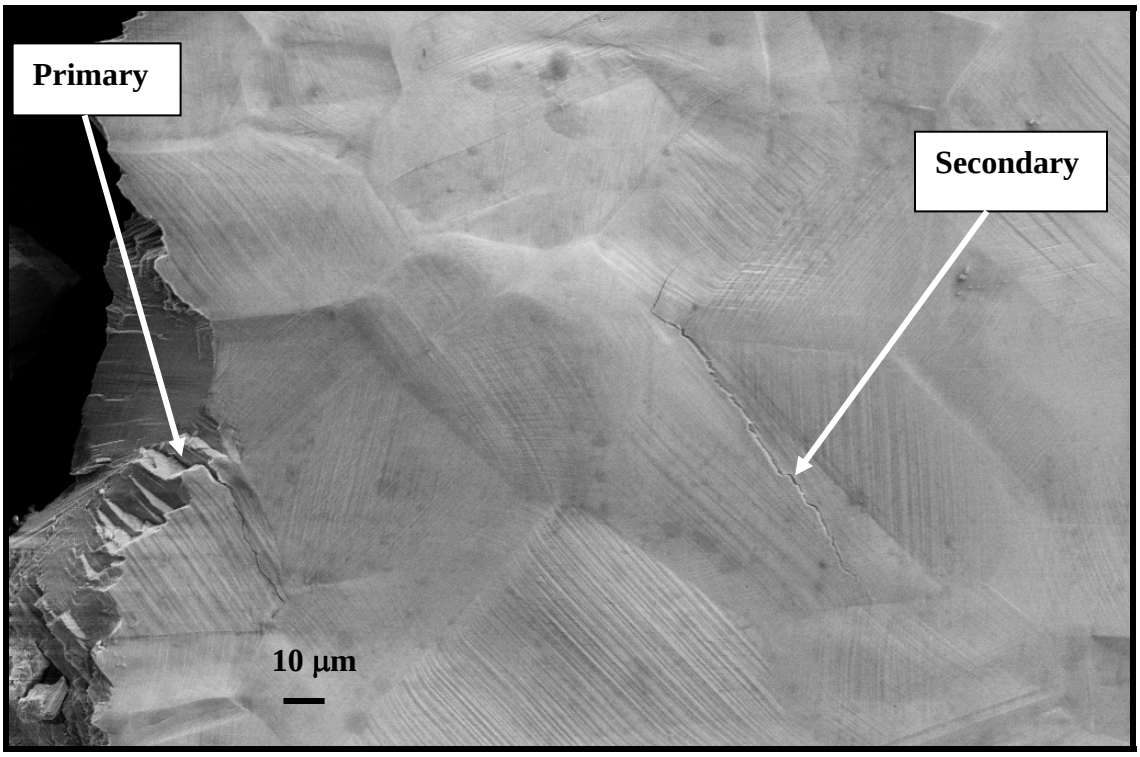


Figure 14. FOV Showing Primary and Secondary Crack-Propagation of C2000 Fatigued at 574 MPa 3.5 wt.% NaCl and an R-Ratio of 0.1

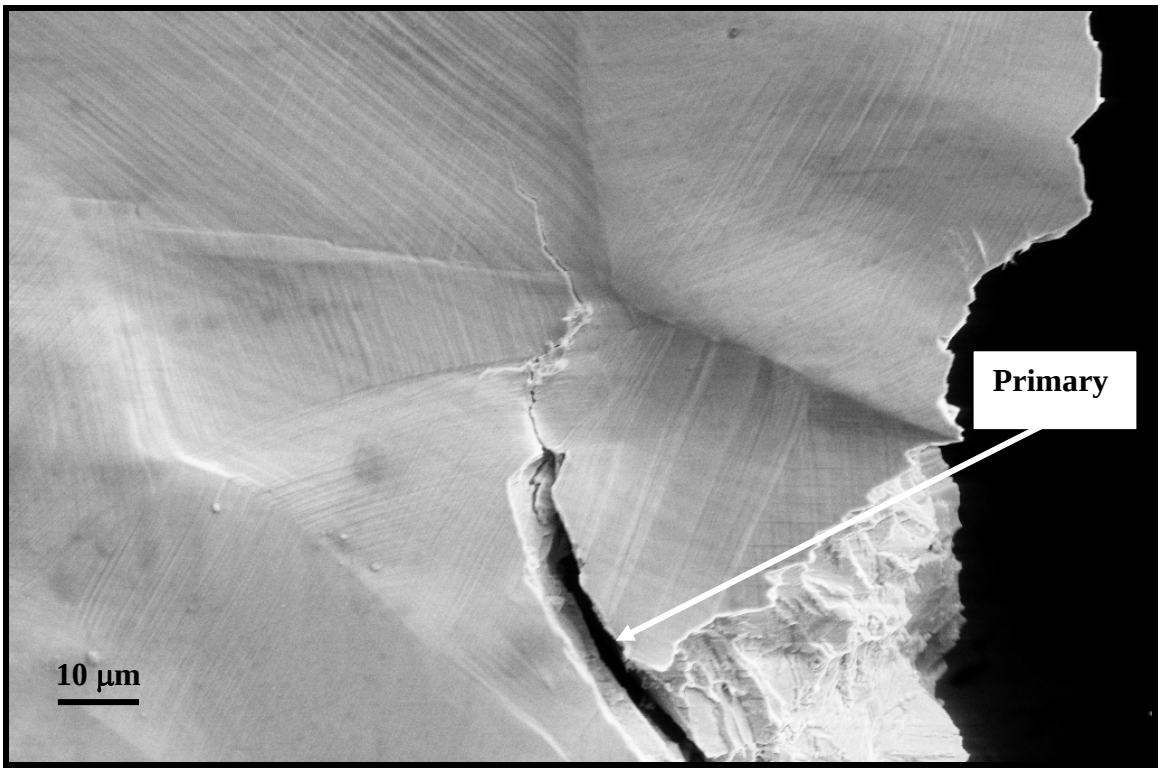


Figure 15. Primary Crack-Propagation of C2000 Fatigued at 574 MPa 3.5 wt.% NaCl and an R-Ratio of 0.1

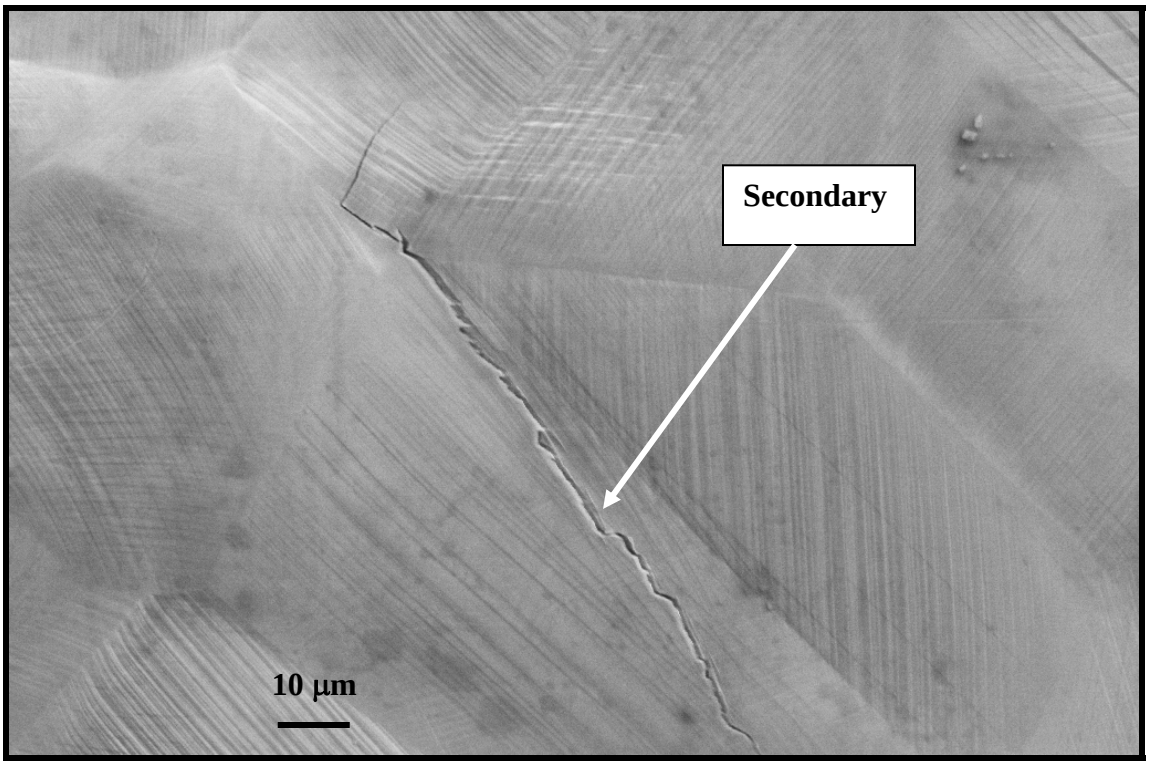


Figure 16. Secondary-Crack Propagation of C2000 Fatigued at 574 MPa 3.5 wt.% NaCl and an R-Ratio of 0.1

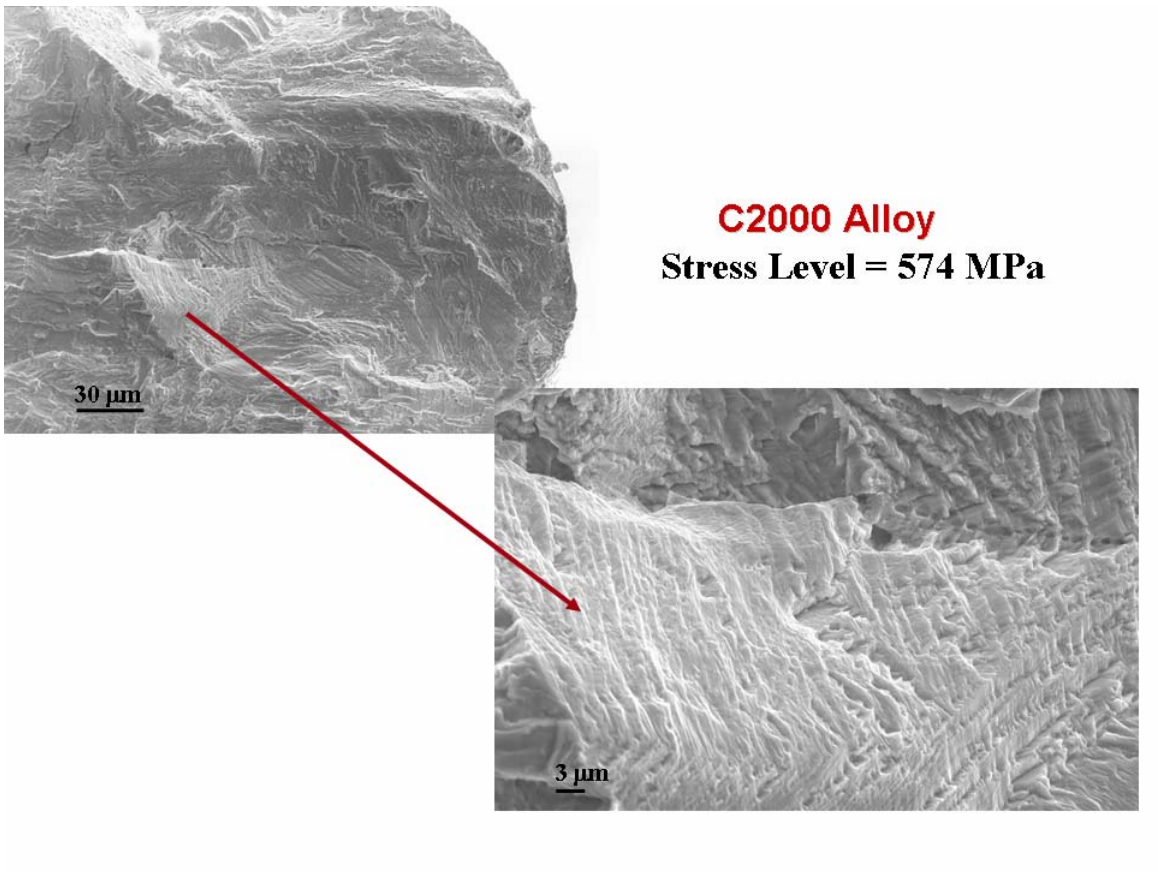


Figure 17. Fractographs of C2000 Fatigued at 574 MPa in Air and an R-Ratio of 0.1

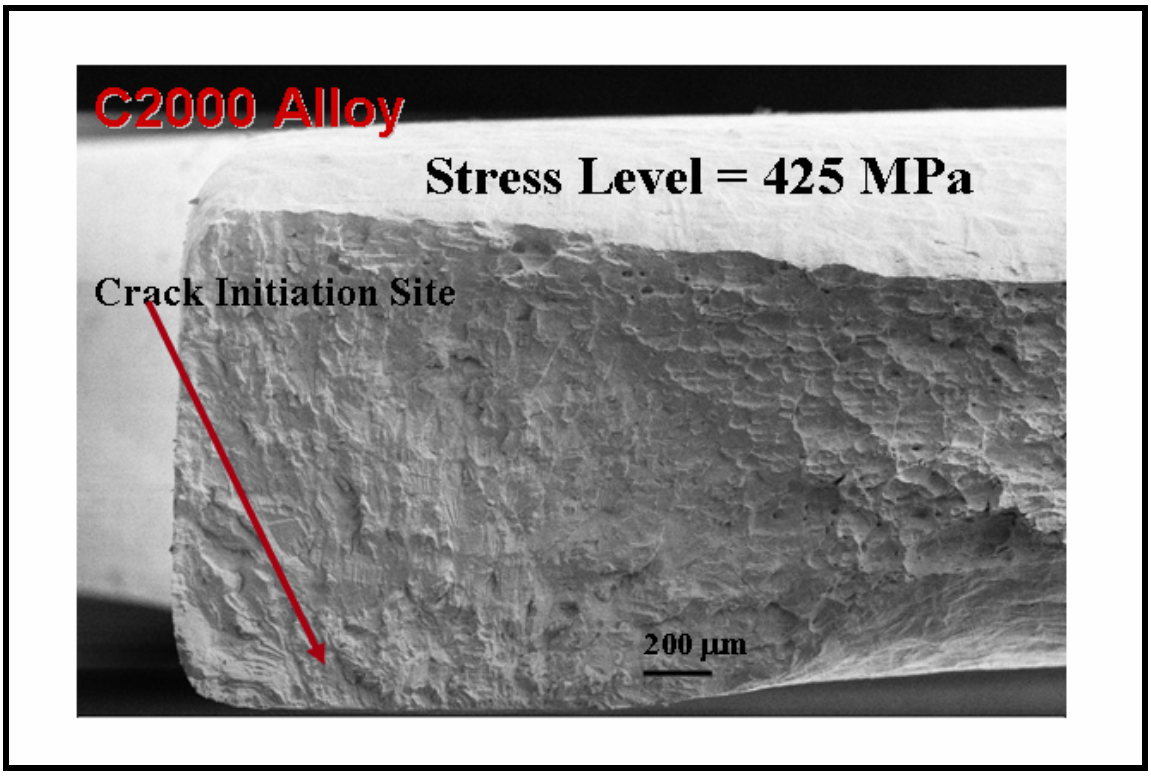


Figure 18. Fractographs of C2000 Fatigued at 425 MPa in Air and an R-Ratio of 0.1

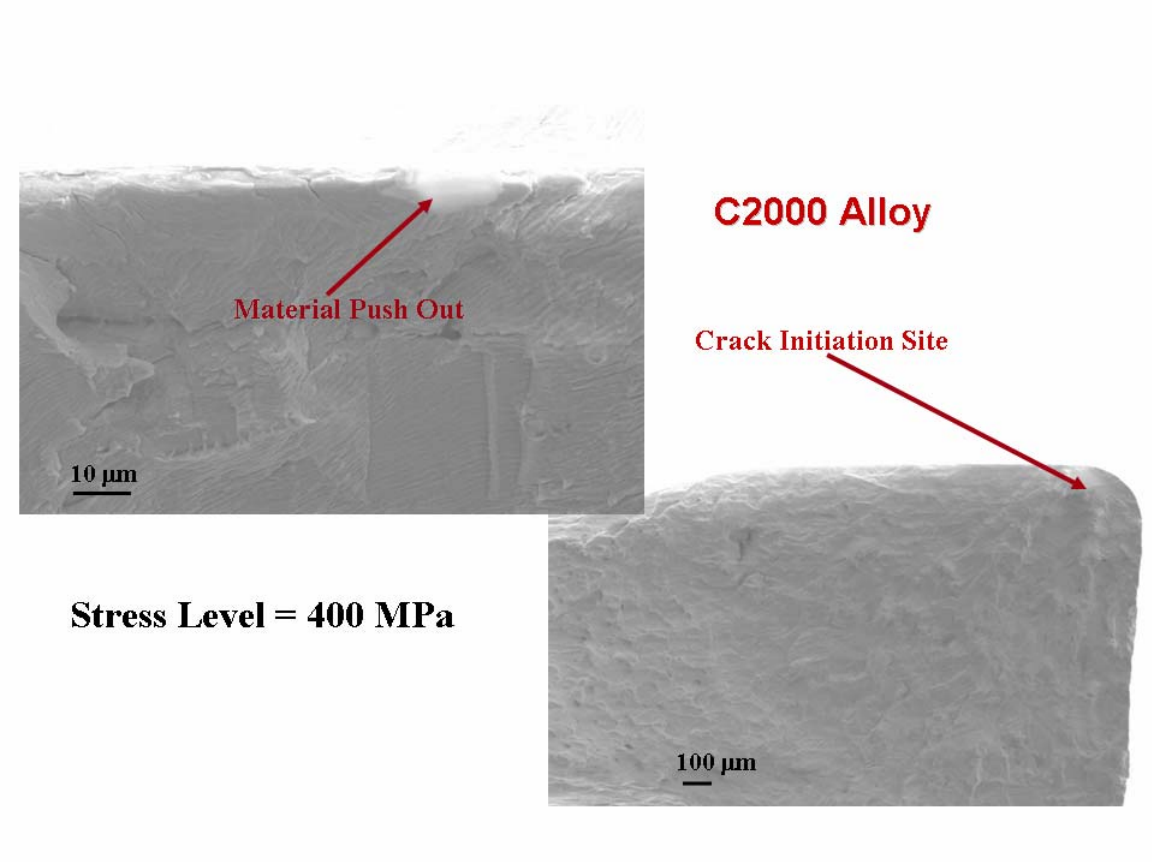


Figure 19. Fractographs of C2000 Fatigued at 400 MPa in Air and an R-Ratio of 0.1

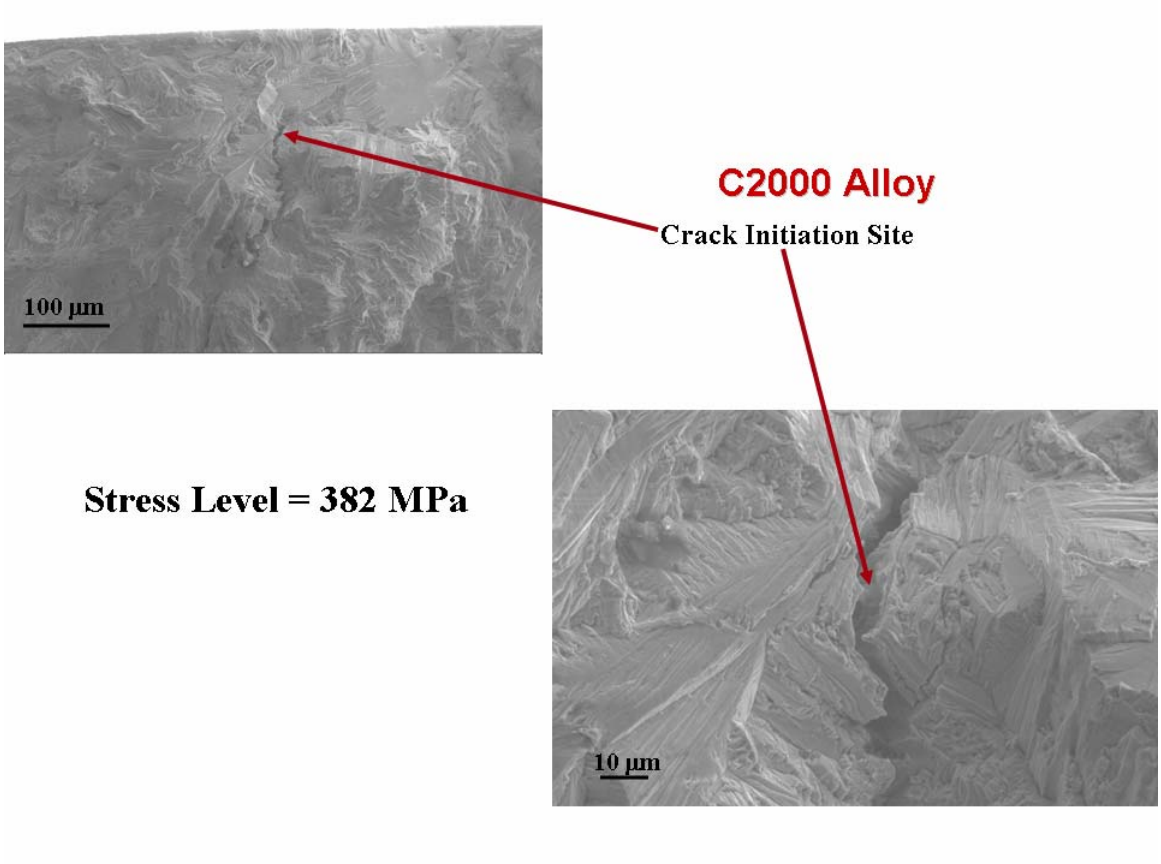


Figure 20. Fractographs of C2000 Fatigued at 382 MPa in Air at and an R-Ratio of 0.1

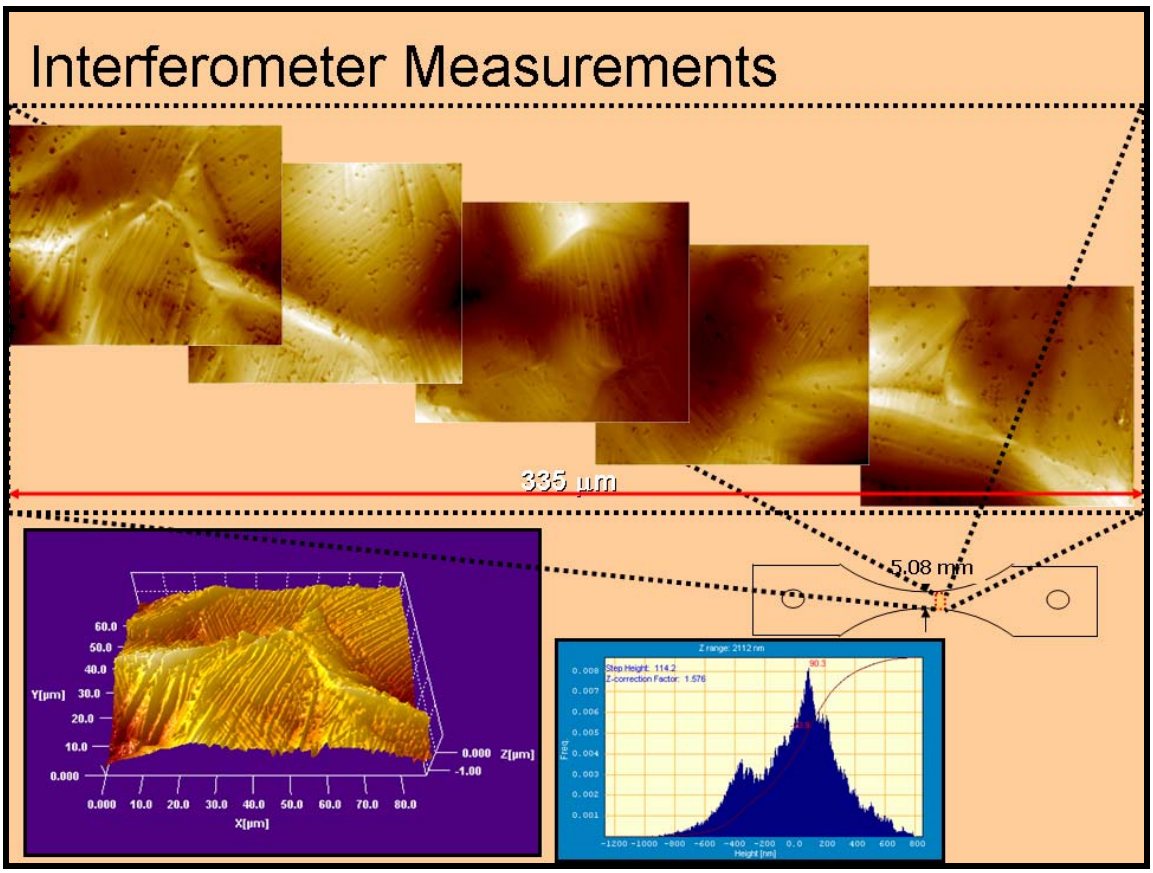


Figure 21. Interferometer Measurements of C2000 Gage Area Deformed at 574 MPa and a R-Ratio of 0.1

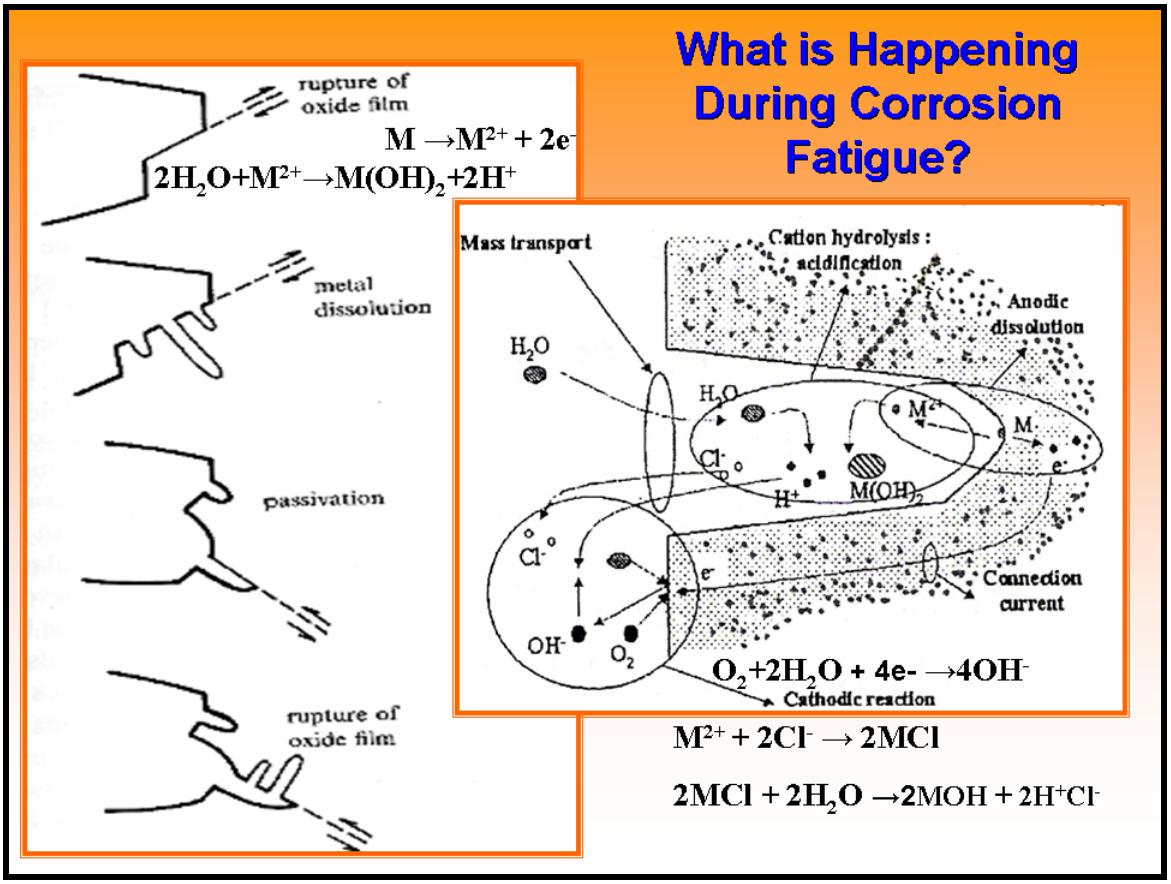


Figure 22. A Cartoon of the Possible Events that Transpire during Corrosion-Fatigue

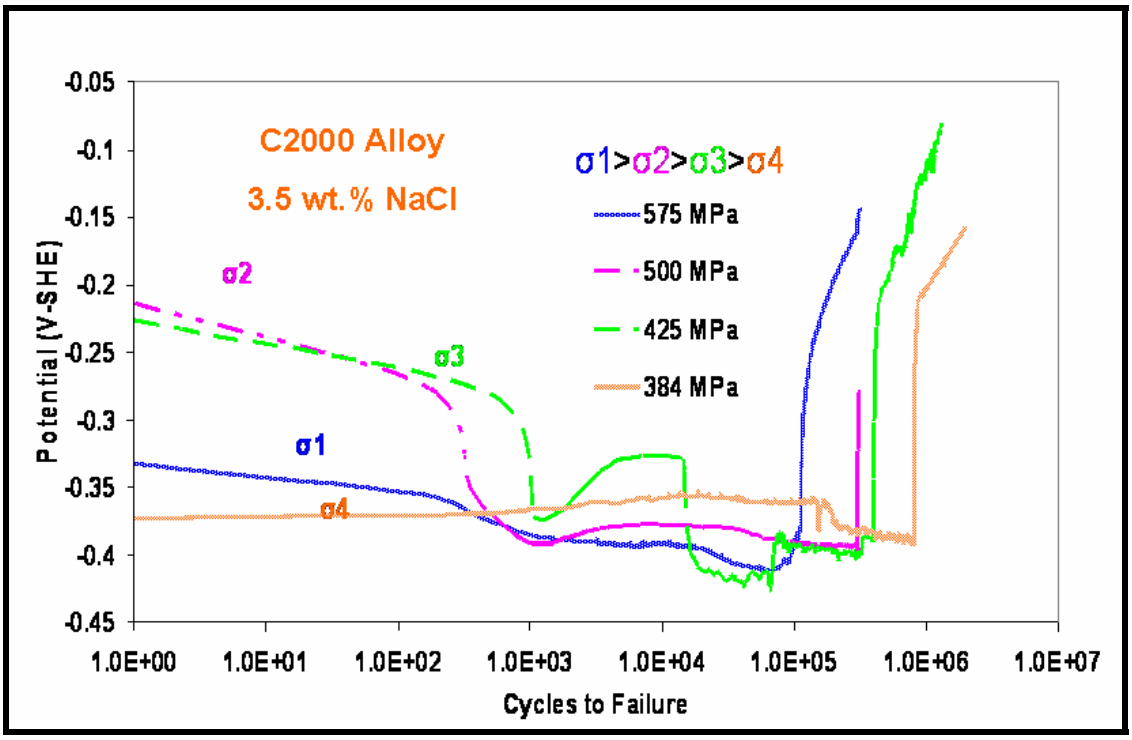


Figure 23. Potential vs. Cycles to Failure for C2000 Subjected to Fatigue at an R-Ratio of 0.1

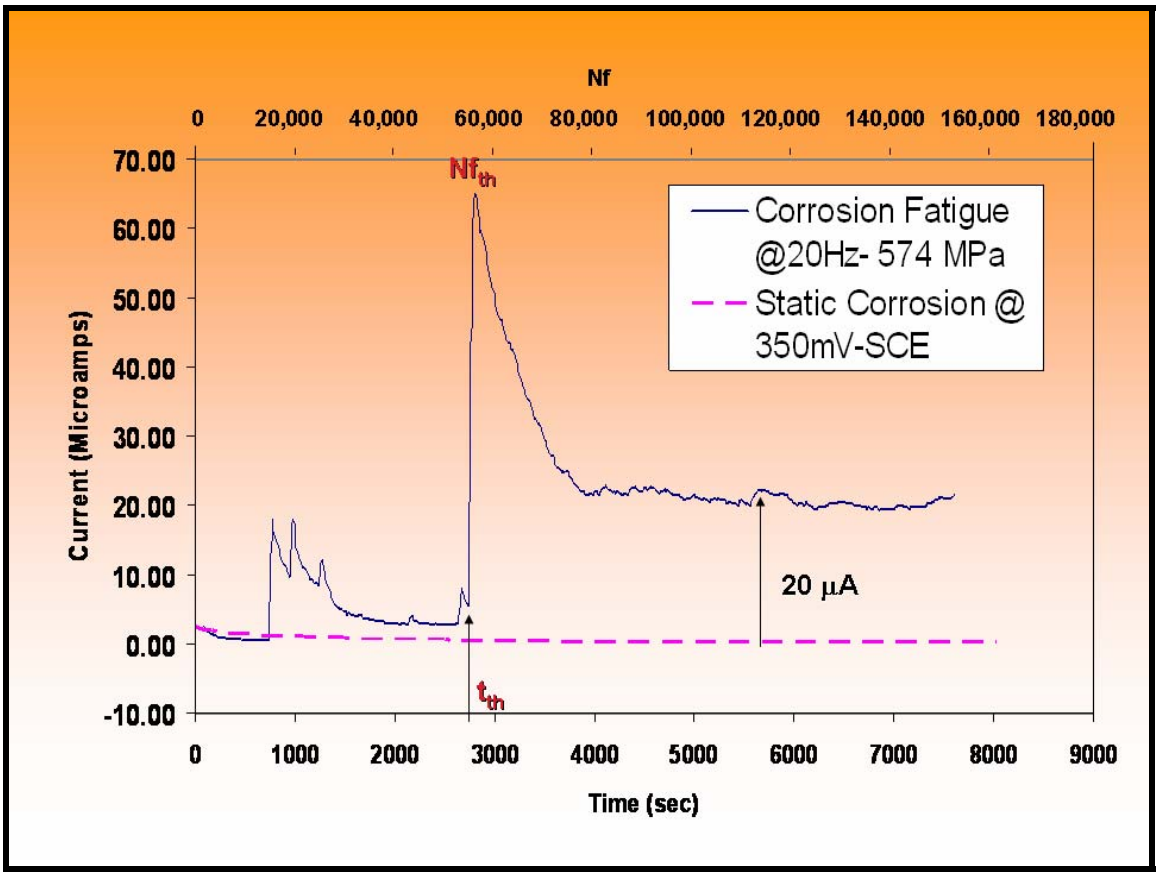


Figure 24. Current vs. Time and Number of Cycles, Nf, for C2000 Subjected to Fatigue at 574 MPa and an R-Ratio of 0.1 While Maintaining a 350 mV Potential

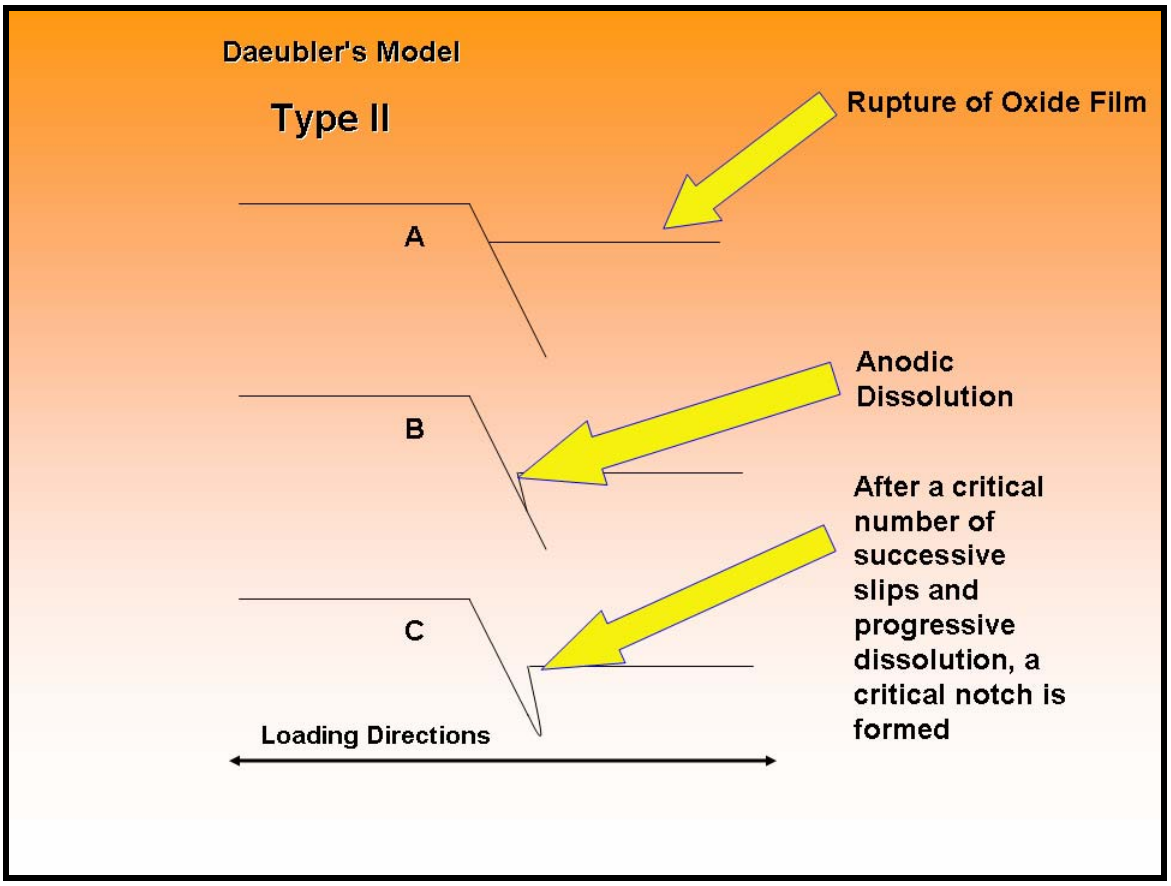


Figure 25. A Cartoon Showing the Progressive Anodic Dissolution During Corrosion-Fatigue

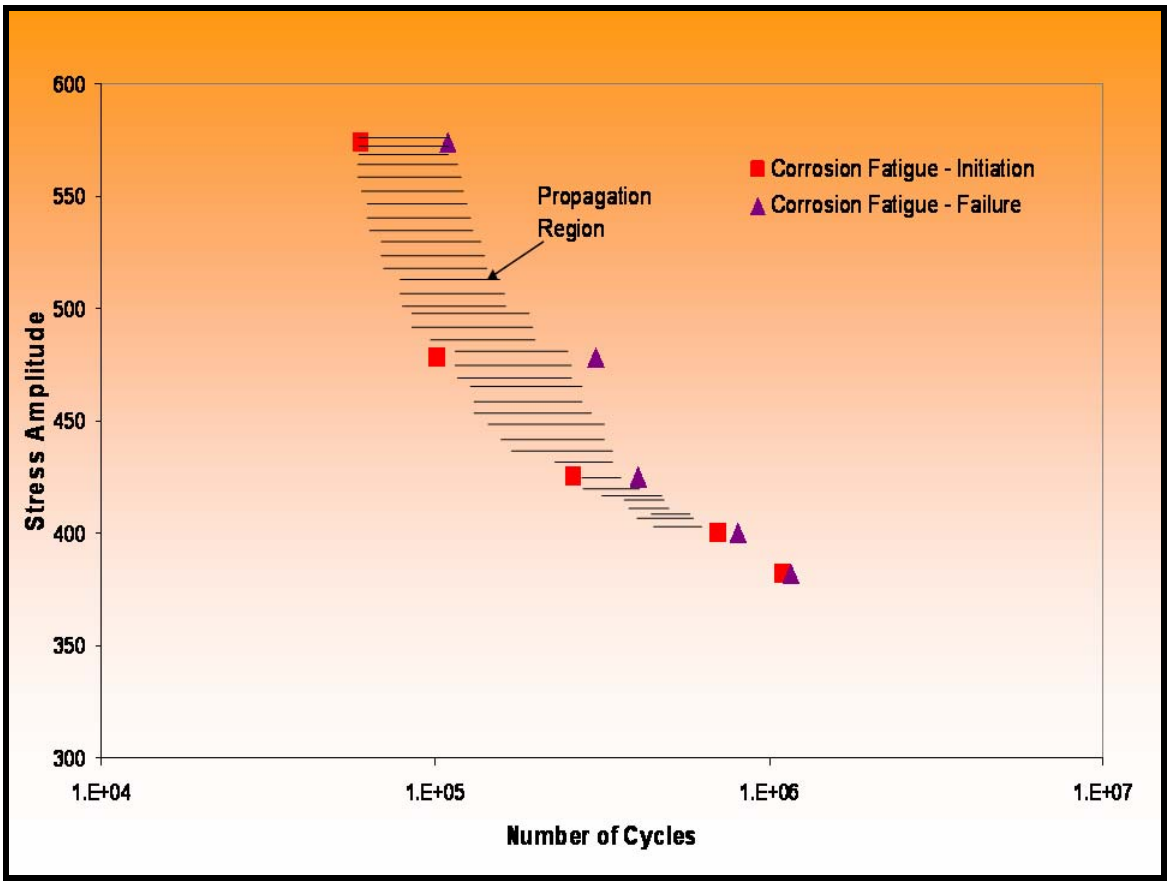


Figure 26. The S-Ni and S-N Curves for C2000

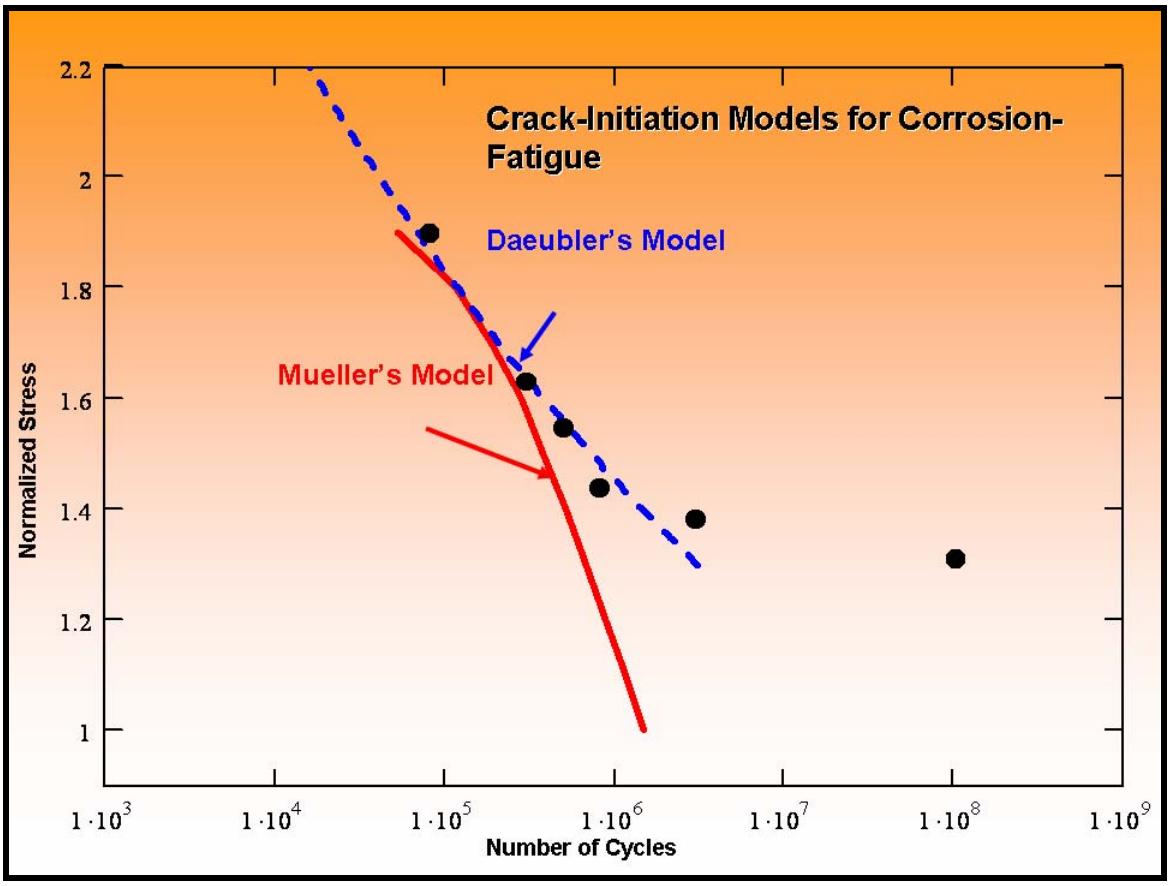


Figure 27. Daeubler and Mueller's Models Plotted With the Experimental Data

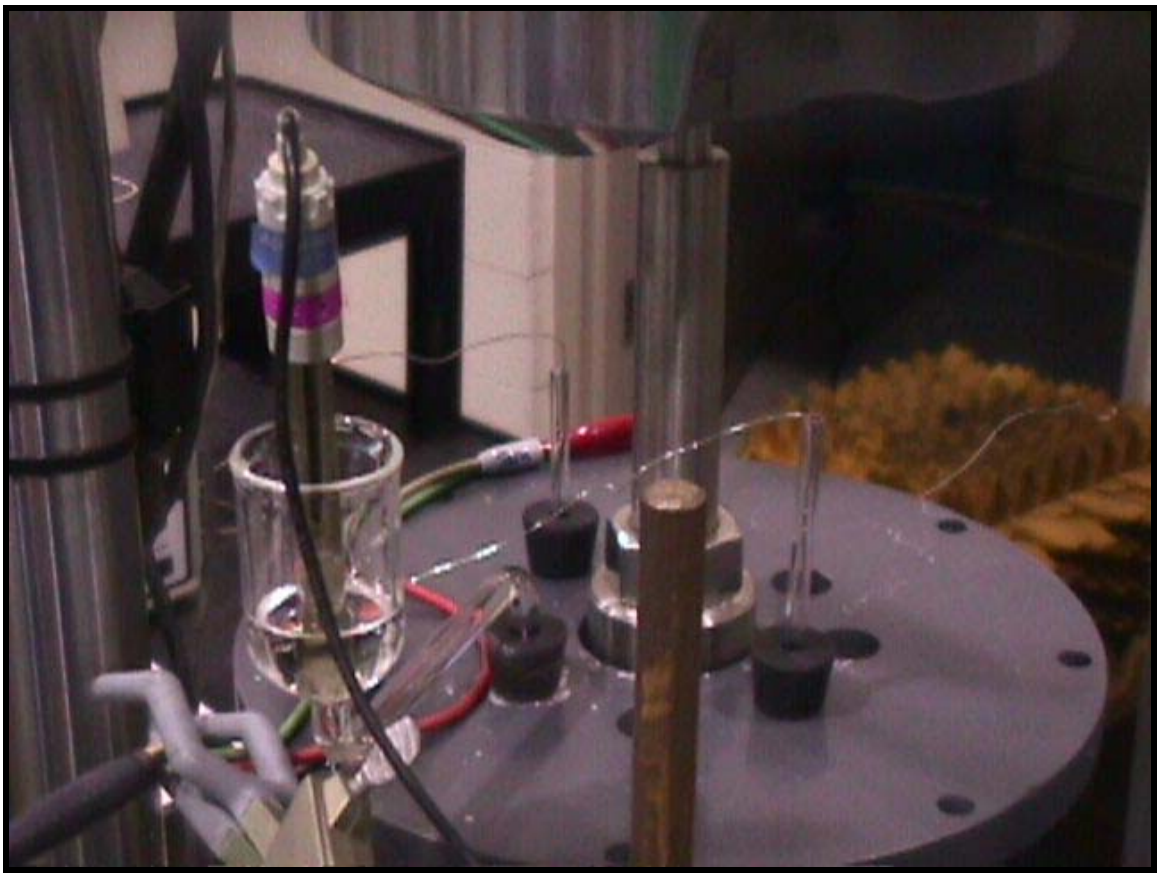


Figure 28. Top View of the Corrosion Cell Chamber

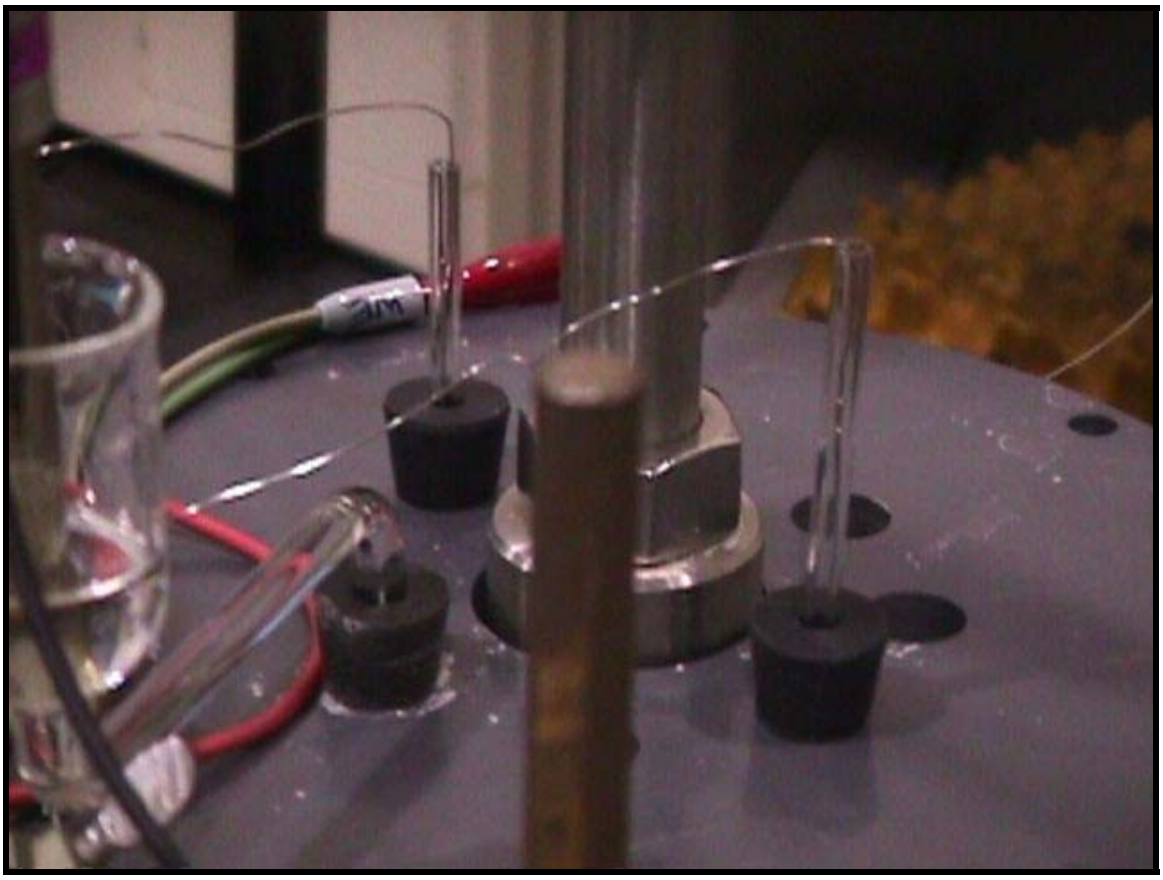


Figure 29. A Zoom Image of the Top View of the Corrosion Cell Chamber

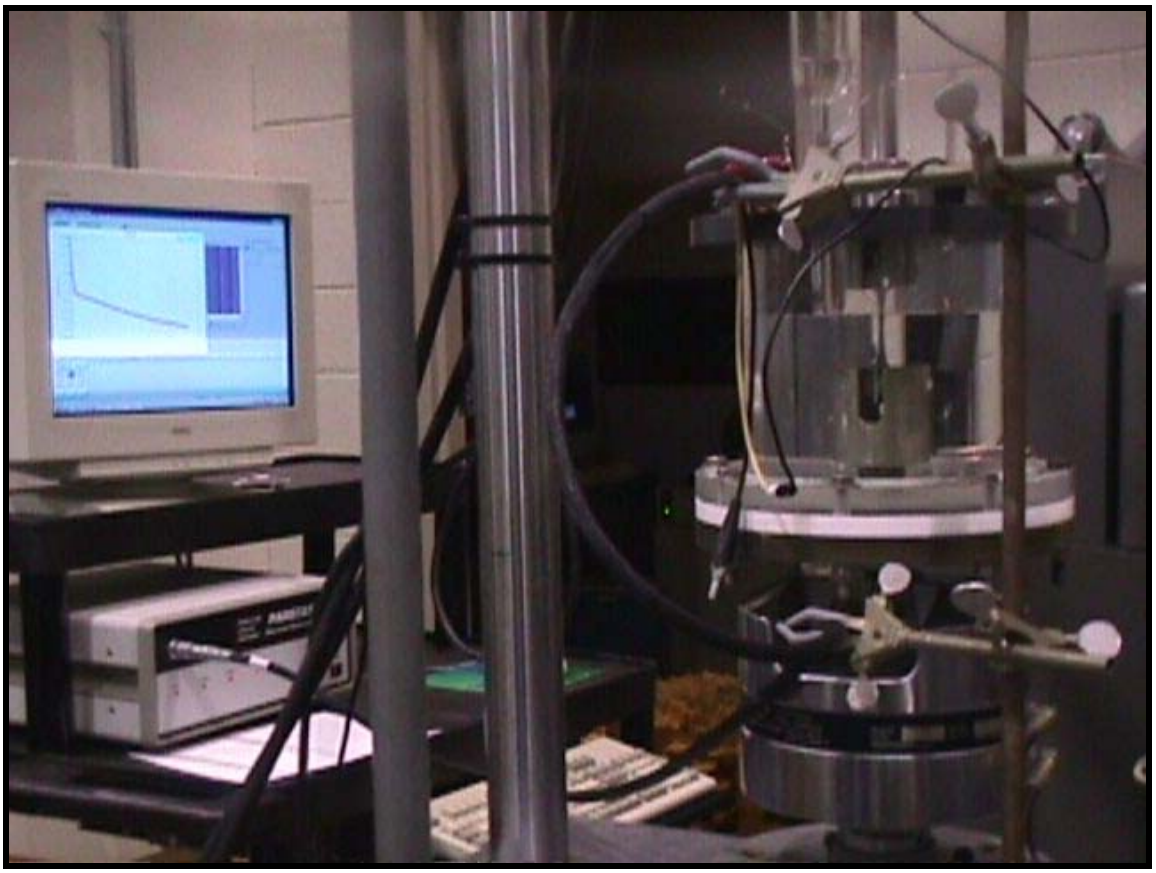


Figure 30. Side View of the Corrosion Cell Chamber

Appendix B

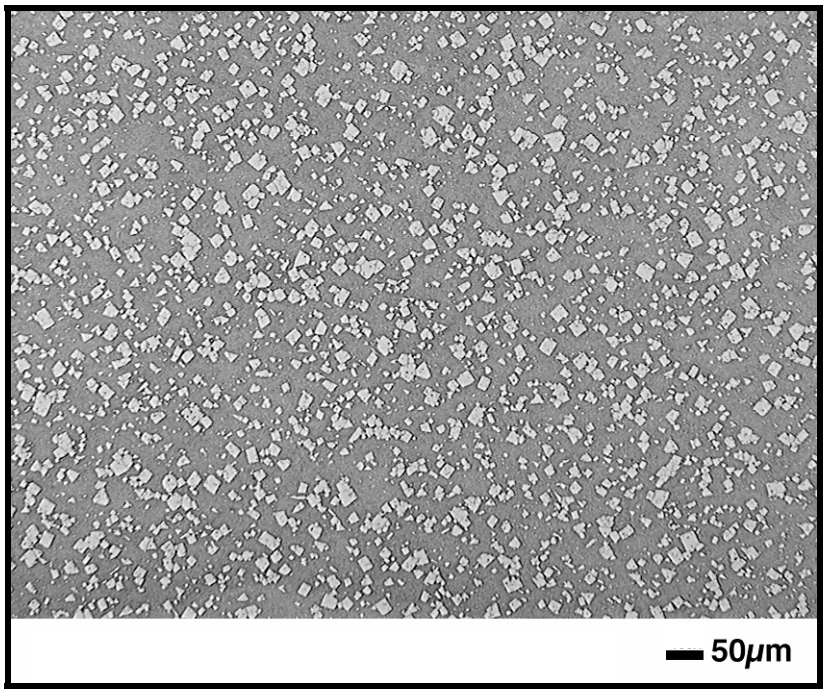


Figure 1. SEM of the 8 hrs. Anneal at 400ºC of Nanocrystalline Ni-18wt.%Fe at Field of View 1 (FOV 1)

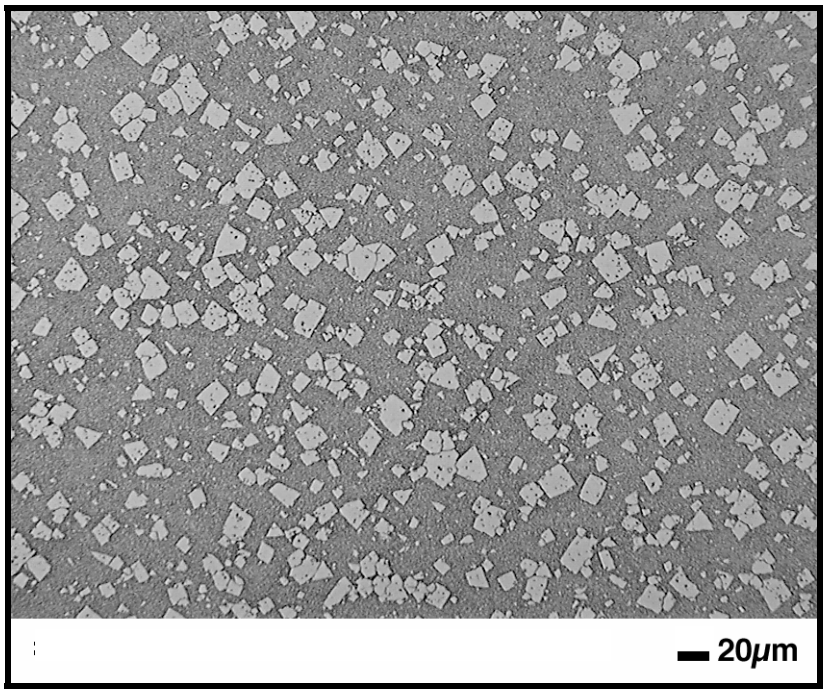


Figure 2. SEM of the 8 hrs. Anneal at 400ºC of Nanocrystalline Ni-18wt.% at FOV 2

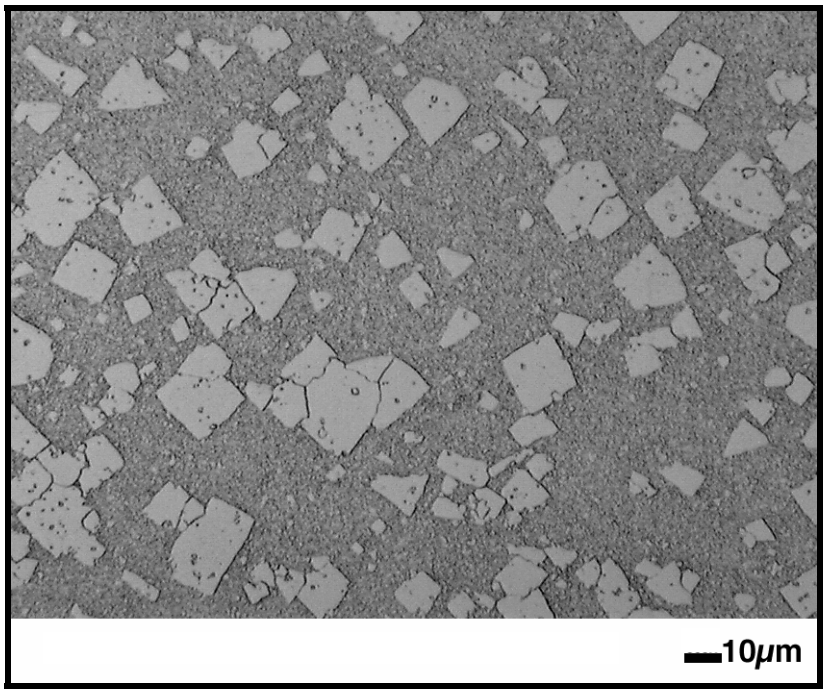


Figure 3. SEM of the 8 hrs. Anneal at 400ºC of Nanocrystalline Ni-18wt.%Fe at FOV 3

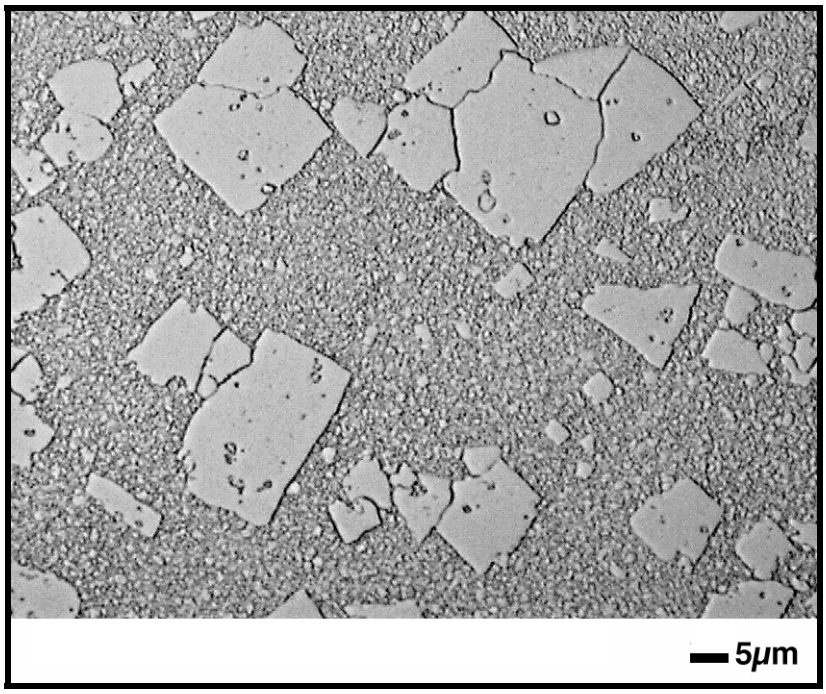


Figure 4. SEM of the 8 hrs. Anneal at 400ºC of Nanocrystalline Ni-18wt.%Fe at FOV 4

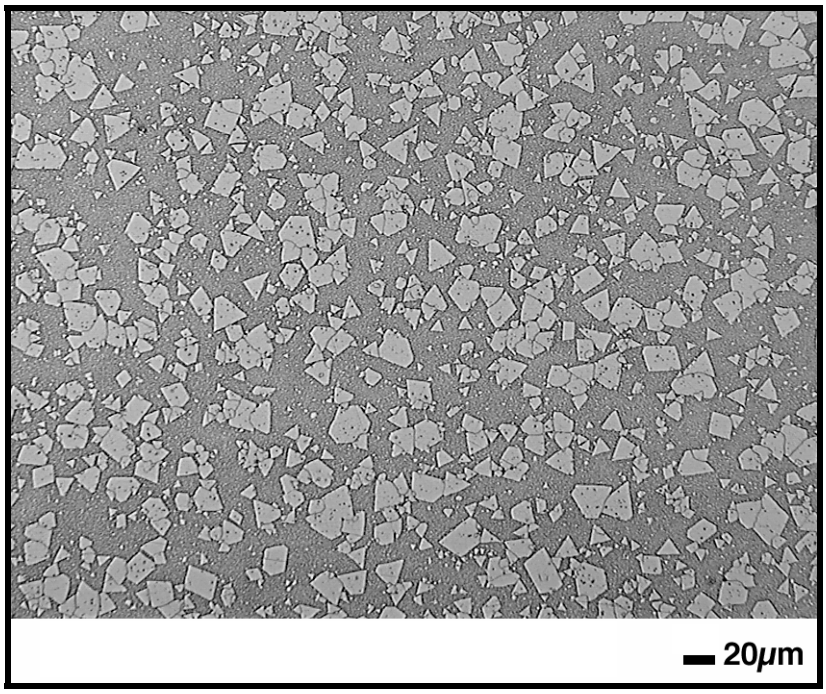


Figure 5. SEM of the 24 hrs. Anneal at 400ºC of Nanocrystalline Ni-18wt.%Fe at FOV 1

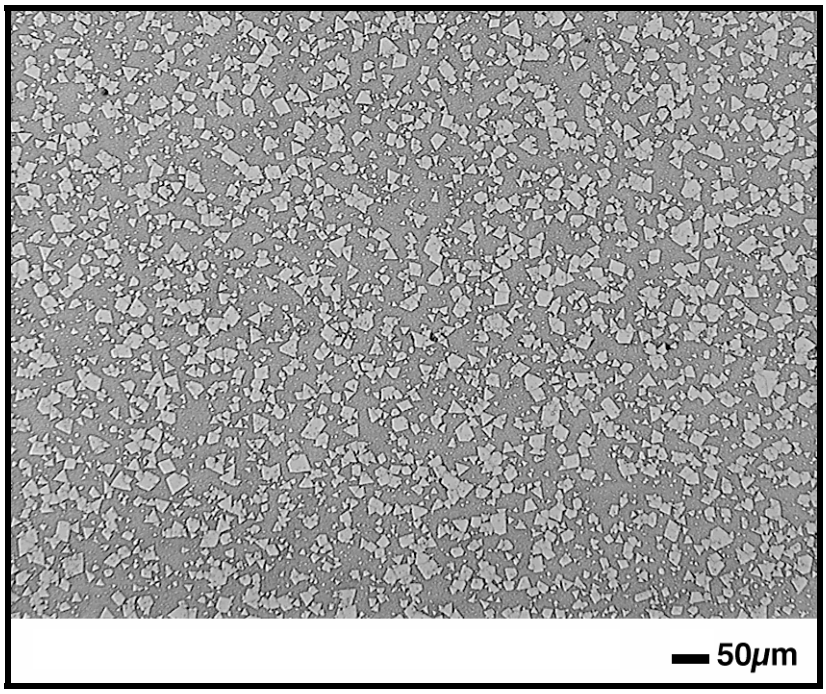


Figure 6. SEM of the 24 hrs. Anneal at 400ºC of Nanocrystalline Ni-18wt.%Fe at FOV 2

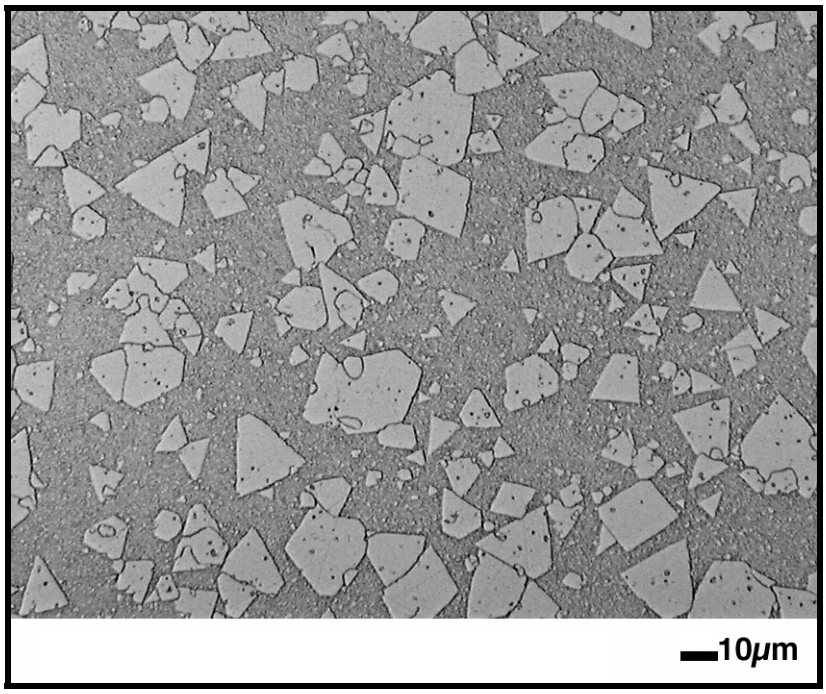


Figure 7. SEM of the 24 hrs. Anneal at 400ºC of Nanocrystalline Ni-18wt.%Fe at FOV 3

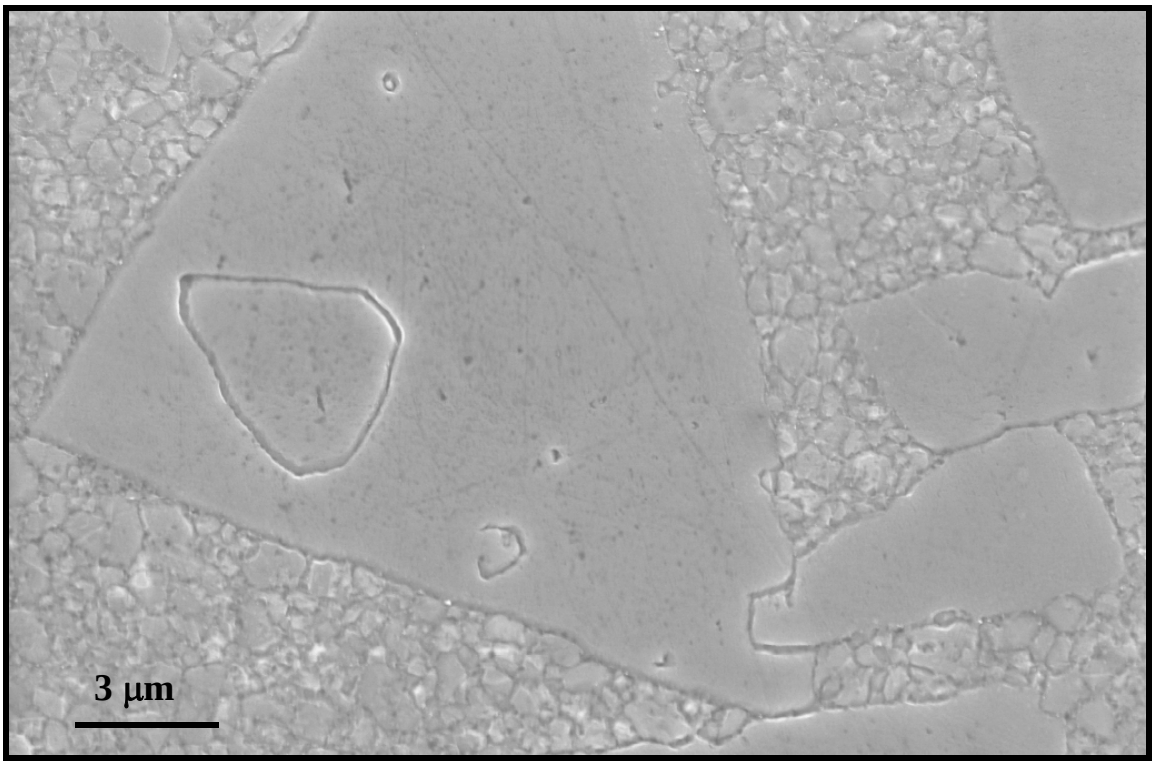


Figure 8. SEM of the 24 hrs. Anneal at 400ºC of Nanocrystalline Ni-18wt.%Fe at FOV 4

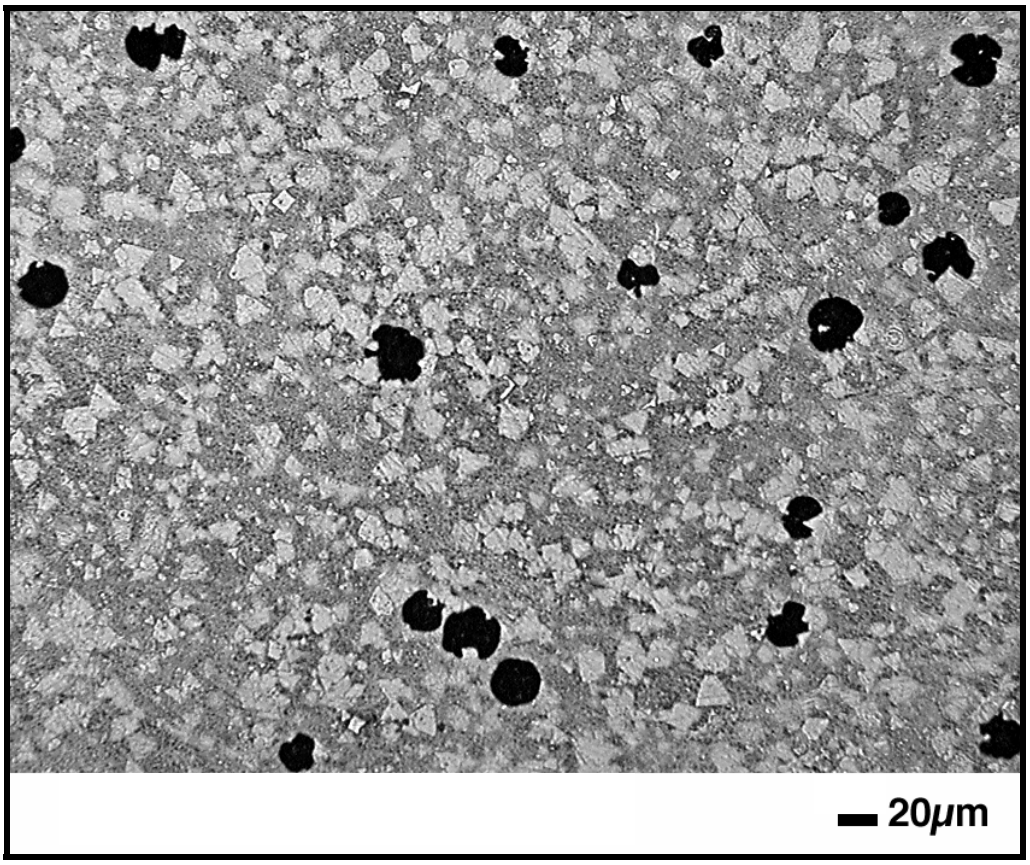


Figure 9. Magnification of Localized Corrosion in a 3.5 wt.% NaCl Solution for Nanocrystalline Ni-18wt.%Fe Annealed for 24 hrs. at 400ºC at FOV 1



Figure 10. Magnification of Localized Corrosion in a 3.5 wt.% NaCl Solution for Nanocrystalline Ni-18wt.%Fe Annealed for 24 hrs. at 400ºC at FOV 2

VITA

Ms. Rejanah Steward is a native of Alcorn State, MS. She is the daughter of Mr. and Mrs. Harry and Yvonne Steward. She completed a B.S. degree in Mechanical Engineering from Mississippi State University as a Whitman "Grady" Mayo Scholar, a M.S. degree from Auburn University as a Graduate (GEM) Fellow. Ms. Steward began her Ph. D. studies at the Georgia Institute of Technology as a GEM Fellow for two years. She completed her Ph.D. studies in the Department of Materials Science and Engineering at the University of Tennessee-Knoxville, and further studies at the Oxford University, Oxford, England. Ms. Steward has earned many awards over her academic tenure. Her most recent honors include the Emerald Honors Student Leadership Award for Minorities in Science, where she will be featured in the Science Spectrum Magazine; the 2006 International TMS Structural Materials Division (SMD) graduate student poster winner for her research on the "Corrosion Fatigue of a Nickel-based Superalloy"; and she was selected as one of two TMS representatives chosen to represent TMS at Junior EUROMAT, a European Materials Science Conference hosted in Lausanne, Switzerland. Most importantly, she is a recipient of God's grace and a persevering saint and servant of Jesus Christ. In her pastime, Ms. Steward enjoys serving in her church, missions and working with students.